GEOPHYSICAL CHARACTER OF THE MOHICAN CHANNEL GAS HYDRATE, NOVA SCOTIA, EASTERN CANADA

by

Janette Cullen

Submitted in partial fulfilment of the requirements
for the degree of Master of Science

at

Dalhousie University
Halifax, Nova Scotia
August 2014

DEDICATION PAGE

The content and format of this page are up to the student.

TABLE OF CONTENTS

LIST OF TABLES vii
LIST OF FIGURES viii
ABSTRACT xii
LIST OF ABBREVIATIONS USED xiii
ACKNOWLEDGEMENTS xiv
CHAPTER 1 INTRODUCTION 1
1.1 PURPOSE OF RESEARCH INTO GAS HYDRATES 1
1.1.1 Potential Fuel Source 2
1.1.2 Potential Impact on Climate Change 4
1.1.3 Potential Geohazard 6
1.2 RATIONALE AND OBJECTIVES 6
1.3 CHAPTER ORGANISATION 7
CHAPTER 2 BACKGROUND 9
2.1 GEOLOGICAL SETTING 9
2.1.1 Regional Geology 9
2.1.2 Geology of the Study Area 15
2.2 STRUCTURAL FEATURES 19
2.2.1 Polygonal Fault Systems 19
2.2.2 Fluid Flow Features 21
2.3 NATURAL GAS HYDRATE 24
2.3.1 Natural Gas Hydrate Structure 24
2.3.2 Natural Gas Hydrate Stability 26
2.3.3 Factors Affecting Gas Hydrate Formation 30
2.3.4 Types of Gas Hydrate Accumulation 30
2.3.5 Bottom Simulating Reflection (BSR) 32
2.3.6 Acoustic Properties 34
2.4 PREVIOUS WORK IN THE STUDY AREA 36
CHAPTER 3 DATA AND METHODS 41
3.1 INDUSTRY 3D MCS DATA 41
3.1.1 Horizon Picking 43
3.1.2 Attribute Analysis 43

3.1.3 Time – Depth Conversion of Horizons 44
3.1.4 Modeling the Base of the Gas Hydrate Stability Zone 47
3.2 2D Single Channel Data 49
3.3 Core Data 50
3.4 Ocean Bottom Seismometer Data 51
3.4.1 OBS Description 52
3.4.2 OBS Data Preparation 53
3.4.2.1 Shot Table and SEGY File Creation 54
3.4.2.2 Direct Arrival Picking 56
3.4.2.3 Water Velocity Profile 57
3.4.2.4 Water Depths 59
3.4.3 OBS Relocation 59
3.4.4 OBS Travel Time Inversion 63
3.4.4.1 Forward Modeling and Inversion 63
3.4.4.2 Data Filtering 65
3.4.4.3 Identification of Reflections and Refractions 65
CHAPTER 4 MODEL RESULTS 68
4.1 1D Velocity Model Results from OBS Data 68
4.1.1 Introduction 68
4.1.2 Identification of Reflections and Refractions 69
4.1.3 1D Velocity Model Results 71
4.1.4 OBS Site 1, Unit 5 76
4.1.5 Discussion 79
4.2 Model of the Base of the Gas Hydrate Stability Zone 80
4.2.1 Introduction 80
4.2.2 Modeling Results 80
4.2.3 Discussion 82
4.3 Gas Volume Calculations 82
4.3.1 Introduction 82
4.3.2 Gas Hydrate Volume Calculations 84
CHAPTER 5 FLUID FLOW FEATURES IN THE MOHICAN CHANNEL AREA, SCOTIAN SLOPE, EASTERN CANADA 88
5.1 Introduction 88

5.2 Regional Setting and Background 89
5.2.1 Regional Setting 89
5.2.2 Gas Hydrates – Distribution and Stability 90
5.2.3 Bottom Simulating Reflection (BSR) 92
5.2.4 Fluid Flow Pathways and Features 92
5.3 Data and Methods 95
5.3.1 Processed Industry 3D Seismic Volume 95
5.3.2 Cores 96
5.3.3 Seismic Attribute Analysis 96
5.3.4 Time-Depth Conversion 97
5.4 Observations 97
5.4.1 Age Estimation 97
5.4.2 Mapped BSR 98
5.4.3 Fault System 102
5.4.4 Seafloor Pockmarks and Mounds 103
5.4.5 Paleo-Pockmarks and Mounds 109
5.4.6 Gas Analyses 113
5.5 Discussion 116
5.6 Conclusions 118
CHAPTER 6 DISCUSSION 120
6.1 Introduction 120
6.2 Key Results 120
6.2.1 Extent of Gas Hydrate in the Torbrook Area 120
6.2.2 Observed Fluid Flow Features 121
6.2.3 Wide Angle Reflection and Refraction Studies, and Improved Volume Assessments 124
6.2.4 Differences between Modelled BGHSZ and Observed BSR 126
CHAPTER 7 CONCLUSIONS 129
7.1 Summary 129
7.2 Recommendations for Future Work 130
REFERENCES 131
APPENDIX A STUDENT CONTRIBUTION TO MANUSCRIPT 143

APPENDIX B COPYRIGHT PERMISSION FOR SCHLESINGER ET AL. (2012) IN APPENDIX C..... 144

APPENDIX C SCHLESINGER ET AL., 2012. SEISMIC VELOCITIES ON THE NOVA SCOTIAN MARGIN TO ESTIMATE GAS HYDRATE AND FREE GAS CONCENTRATIONS 146

APPENDIX D Clock Calibration for OBS Relocation 185

APPENDIX E Sound Velocity Equations 187

APPENDIX F Misfit Tables for OBS 1D Models 188

LIST OF TABLES

Table 3.1 A simplified time-depth table used to convert all picked horizons. 47

Table 3.2 A section of the dataset tested using a variety of sound velocity equations. 58

Table 3.3 OBS drop and retrieval locations and water depths extracted from a GSC(A) multibeam survey for those locations. 60

Table 3.4 Table showing relocated latitude, longitude and water depth for each OBS in the study area. 62

Table 4.1 Gas volume calculations for the Mohican Channel BSR. 87

Table 5.1 A simplified time-depth table 97

Table 5.2 Results from cores for site 2006-046-PC006 and for cores from Hudson cruise 2004-030 showing the main compositional gases found 115

Table A.1 Clock readings at deployment and retrieval of the OBS during CCGS Hudson cruise 2004-030. 185

Table E.1 Misfit tables for 1D velocity models derived from Site 1 OBS data. 189

Table E.2 Misfit tables for 1D velocity models derived from Site 2 OBS data. 190

Table E.2 Misfit tables for 1D velocity models derived from Site 2 OBS data. 190

LIST OF FIGURES

Figure 1.1 Estimated global methane hydrate stability zone thickness in seafloor sediments (from Wood and Jung, 2008). 4

Figure 2.1 Generalized stratigraphic chart for the Scotian margin, offshore Nova Scotia (Weston et al., 2012). 10

Figure 2.2a Map of the Scotian Margin showing the location of major structural features. 11

Figure 2.2b Map of the Scotian Margin showing the location of shallow salt structures, the Abenaki Carbonate Platform and exploration wells throughout the area. 12

Figure 2.3a Seismic reflection profile through the study area showing the Shubenacadie Drift. 17

Figure 2.3b Seismic stratigraphy in the study area as developed by Campbell (2011). 18

Figure 2.4 Planform and cross-sectional characteristics of polygonal fault systems. 20

Figure 2.5 Examples of the subsurface features visible in seismic data that result from sediment mobilisation or fluid flow, taken from Andresen (2012). 23

Figure 2.6 Global distribution of gas hydrates. 25

Figure 2.7 Three crystalline structures which gas hydrate can form. 27

Figure 2.8 Phase diagram describing the conditions necessary for gas hydrate development in oceanic sediments. 29

Figure 2.9 Three types of gas hydrate accumulations as described by Milkov and Sassen (2002). 31

Figure 2.10 Properties of a bottom-simulating reflection (BSR). 34

Figure 2.11 Locations of velocity models developed within the Torbrook study area (blue polygon). 37

Figure 2.12 a) Waveform tomography velocity model for GXT line 5300. 39

Figure 2.13 a) Waveform tomography velocity model for GXT line 1400 superimposed on the pre-stack depth-migrated reflection image. 40

Figure 3.1 Dataset Locations. 42

Figure 3.2 The result of automatic picking program 3D Hunt is shown in blue. 44

Figure 3.3 Amplitudes shown on picked horizons in the 3D MCS dataset. 45

Figure 3.4 Dip of maximum similarity shown on picked horizons in the 3D MCS dataset. 46

Figure 3.5 Example of the filtered 2D SCS reflection profile available in the study area. 50

Figure 3.6 Piston Core unit ready for deployment on the CCGS Hudson 2004-030 cruise 51

Figure 3.7 Modified Dalhousie University OBS with an externally mounted geophone used in the CCGS Hudson 2004-030 cruise. 52

Figure 3.8 A flow chart showing the steps necessary to reach the stage of instrument relocation. 54

Figure 3.9 A schematic showing the physical positions of the GPS antenna and the seismic gun array relative to the center line of the CCGS Hudson. 55

Figure 3.10 An example of direct arrival picking on debiased unfiltered hydrophone data.. 56

Figure 3.11 A graph of the water velocity profile for the Mohican Channel study area using data acquired during the CCGS Hudson 2004-030 cruise. 59

Figure 3.12 The three types of ray families traced by the Rayinvr Program. 64

Figure 3.13 An example of the OBS data amplitude spectrum. 65

Figure 3.14 Example of data matching between OBS data (grey scale plot) and a 3D seismic reflection profile (coloured plot) at Site 1. 67

Figure 3.15 A: An example of OBS data ready for horizon picking. 67

Figure 4.1 A schematic of the acoustic response expected in an area with gas hydrate present above free gas. 69

Figure 4.2 Picked reflections and refractions on hydrophone data at OBS Site 1 and Site 2. 70

Figure 4.3 Reflections picked on OBS dataset matched to reflections visible in the 3D MCS dataset for OBS Site 1 in the west (see figure 3.1 for location)..... 71

Figure 4.4 Reflections picked on OBS dataset matched to reflections visible in the 3D MCS dataset for OBS Site 2 in the east (see figure 3.1 for location)..... 72

Figure 4.5 Top: Raytracing for horizon 7 of an OBS unit. 73

Figure 4.6 Plot of the individual 1D velocity models derived from Site 1 OBS data showing a strong BSR in industry seismic reflection data. 74

Figure 4.7 Plot of the individual 1D velocity models derived from Site 2 OBS data where a BSR is not present in industry seismic reflection data. 75

Figure 4.8 Left: A seismic profile through OBS Site 1 showing the change in character of BSR 1 (OBS horizon 6). 77

Figure 4.9 2004 2 -D velocity model from travel-time tomography using arrivals from the nine OBS stations (triangles) and the corresponding 2D SCS vertical incidence profile. 78

Figure 4.10 A seismic reflection profile through the Mohican Channel BSR showing the position of the calculated base of the gas hydrate stability zone (red line) using model equations of Leon et al. (2009). 81

Figure 4.11 Extent of the interpreted BSR 1 through the Torbrook 3D MCS dataset. 85

Figure 4.12 Extent of the interpreted BSR 2 through the Torbrook 3D MCS dataset. 86

Figure 5.1 Study area location map. 91

Figure 5.2 A profile through the 3D MCS dataset showing age estimation in the area of the Mohican Channel. Horizon 2 is equivalent to the Late Pliocene N60 horizon interpreted by Campbell (2011). 98

Figure 5.3 Seismic character of BSR 1 in the Mohican Channel area. 100

Figure 5.4 Seismic character of BSR 2 in the Mohican Channel area. 101

Figure 5.5 A seismic reflection profile showing the fault system in the study area. 103

Figure 5.6 Map of the dip of maximum similarity on horizon 2 (Figure 5.2). 104

Figure 5.7 Map of the dip of maximum similarity on horizon 3 (BSR 1, Figure 5.2). 105

Figure 5.8 Map of the dip of maximum similarity on horizon 4 (Figure 5.2). 106

Figure 5.9 Pockmarks on the seafloor. 107

Figure 5.10 Seismic reflection profile showing characteristics of the Torbrook seafloor mound. 108

Figure 5.11 Map showing paleo-features on horizon 2. 111

Figure 5.12 Map showing paleo-features on horizon 4. 112

Figure 5.13 An example of pockmark versus fill. 113

Figure 5.14 The two samples analysed for site 2006-046-PC006 (blue diamonds) are plotted on the right side of the graph in the mixed zone (orange dots) and tending towards the biogenic end member (pink squares) rather than the thermogenic end member (yellow triangles). 114

Figure 5.15 Locations of velocity models developed within the Torbrook area. 118

Figure 6.1 A seismic profile showing the change of reflection across the Torbrook area from west to east. 122

Figure 6.2 Instantaneous frequency plotted on a seismic reflection profile through the 3D seismic dataset. 123

Figure 6.3 Velocity-depth profiles for 2002, 2004 and 2006 OBS data. 126

ABSTRACT

Bottom simulating reflections (BSRs) attributed to gas hydrates are described as phase-reversed reflection events that run broadly parallel to the seafloor and can cut across bedding planes. BSRs are understood to be acoustic responses to negative impedance contrasts due to high velocity sediments containing gas hydrate above low velocity sediments containing free gas. Gas hydrates are a unique hydrocarbon trap consisting of a solid ice lattice surrounding hydrocarbon molecules. They form at specific pressure and temperature conditions when free gas undergoes a phase change to gas hydrate. Although BSRs are recognised worldwide, the first reported BSR along the Scotian margin was by Mosher et al. (2004), and the first description of the Mohican Channel site, the focus of this study, was by Mosher et al. (2005). The objectives of this study are to 1) determine the extent of gas hydrate formation in the Mohican Channel area, 2) determine stratigraphic and structural features related to gas hydrate formation, 3) document the geophysical characteristics of the BSR and associated gas hydrate features, and 4) compare volume calculations from this location to regional and global gas hydrate volume estimates. To accomplish these objectives, a 3D seismic reflection volume and a suite of refraction experiments over and proximal to the Mohican Channel BSR were analysed.

Seismic reflection and refraction velocity models in the Mohican Channel area show a distinctive combined high over low velocity signature in the area of the BSR. Stratigraphic and structural interpretation of seismic reflection data shows acoustic blanking, characteristic of sediment-hosted gas hydrate in this same area. Fluid flow features such as vertical pipes and chimneys are scattered throughout the study area. Comparison of the observed depth of the BSR and the modelled base of the gas hydrate stability zone (based on the current pressure and temperature field) shows that the BSR is ~ 200 m shallower than expected. This result suggests that the BSR is not in equilibrium with present pressure and/or temperature conditions, or there is a mis-calculation in the present stability field parameters. For example, the model assumes hydrostatic pressure conditions, and ignores any contribution from lithostatic pressure.

This study interprets the presence of gas hydrate adjacent to the Mohican Channel over an area of 330 km^2. Gas hydrate distribution appears to vary from west to east. Highest concentrations, as estimated from velocity analyses, appear coincident with the strongest observed BSR response in the extreme west of the study area. Overall low gas hydrate concentrations, variable distribution, and poor fit of the observed versus modelled stability field suggests that global estimates of gas hydrate along passive margins are likely exaggerated.

LIST OF ABBREVIATIONS USED

2D	two-dimensional
3D	three-dimensional
BGHSZ	Base of the Gas Hydrate Stability Zone
BSR	Bottom Simulating Reflection
CH_4	methane
CIE	Carbon Isotope Excursion
C-NSOPB	Canada-Nova Scotia Offshore Petroleum Board
CO_2	Carbon Dioxide
Fm	Formation
g/cm^3	grams per centimetre cubed
GHSZ	Gas Hydrate Stability Zone
GSC(A)	Geological Survey of Canada (Atlantic)
H_2O	water
HCO_3	bicarbonate
H_2S	Hydrogen Sulphide
Hz	Hertz
HVZ	High Velocity Zone
IODP	Integrated Ocean Discovery Program
IPCC	International Panel on Climate Change
ka	Thousand years ago
kg	kilogram
kHz	kilohertz
km	kilometres
LVZ	Low Velocity Zone
m	metres
mbsf	metres below the seafloor
Ma	Million years ago
MTD	Mass Transport Deposit
ms	milliseconds
mK/m	millikelvin per metre
mW/m^2	milliwatts per metre squared
MCS	Multi-Channel Seismic
OBS	Ocean Bottom Seismometer
ODP	Ocean Drilling Program
PF	Polygonal Faults
ROV	Remotely Operated Vehicle
s	seconds
SCS	Single Channel Seismic
SO_4	sulphate
tcm	trillion cubic metres (10^{12} m^3)
twtt	two-way travel time
VSP	Vertical Seismic Profile

ACKNOWLEDGEMENTS

I would like to acknowledge my supervisors Dr. David Mosher and Prof. Keith Louden for their continued interest in this research and for allowing me to explore various directions as the study evolved. Thanks also to the members of my examining committee Dr. Andrew MacRae, Dr. Rebecca Jaimeson, Dr. Grant Wach and Dr. John Gosse. Your diverse backgrounds provided invaluable feedback for developing the thesis.

Thanks to EnCana Corporation, Dalhousie University, and the Geological Survey of Canada (Atlantic) who provided the key datasets that made this study possible.

Financial support was provided by an National Science and Engineering Reseach Council (NSERC) Discovery Grant to Dr. David Mosher, and a student scholarship from the Canadian Society of Petroleum Geologists.

I would like to acknowledge various individuals who provided fruitful discussions, reviews and support during my studies, particularly Joanna Gerlings, Angela Schlesinger, Calvin Campbell, Kimberley Jenner, David Piper, John Shimeld, Jane Hawken, Irena Schulten and Yanni Evangelatos.

And finally, thanks to Patrick Dubé for his support over the years, and his ability to keep it all in perspective.

CHAPTER 1 INTRODUCTION

1.1 PURPOSE OF RESEARCH INTO GAS HYDRATES

Gas hydrates are crystalline solids which appear similar to ice. The basic structure is a clathrate consisting of a lattice structure of water molecules which trap guest gas or hydrocarbon molecules. This structure is stable under certain pressure and temperature conditions which are met in polar regions and along large portions of continental margins in the marine environment. Outside of these specific pressure and temperature conditions, the gas hydrate dissociates into its components of water and gas.

Gas hydrates were essentially laboratory curiosities since the 1700's. Practical knowledge began to build from the 1920's when the first hydrocarbon pipelines suffered blockages due to gas hydrate formation in cold weather conditions (Birchwood et al., 2010). Russian scientists first proposed the presence of naturally occurring gas hydrates in permafrost locations in 1946 (Birchwood et al., 2010). Confirmation came in 1968 when drilling at Byrd Station in the Antarctic produced ice cores containing air hydrates (Birchwood et al., 2010). Deep sea drilling expeditions in the 1970's discovered gas hydrates in the deepwater sediments of outer continental margins. Cores containing gas hydrates have been retrieved during deep sea ocean drilling programs (ODP/IODP) such as on the Cascadia margin (Riedel et al., 2006; Torres et al., 2008), India (Collett et al., 2006), and South Korea (Lee et al., 2011). The application of advanced velocity analysis of seismic data has permitted determination of the velocity structure of gas hydrates in marine sediments, and allowed estimation of hydrate saturations and pore space distribution in areas such as the northern Cascadia margin (Dash and Spence, 2011). Studies combining multichannel seismic data, drilling logs and core samples are providing insights into

gas hydrate formation in specific provinces e.g. Andaman Sea, India (Shankar and Riedel, 2013); northern South China Sea (Sun et al., 2012). It is now believed that about 98% of gas hydrates occur in marine sediments while the remaining 2% occur in permafrost regions (Birchwood et al., 2010).

1.1.1 Potential Fuel Source

Gas hydrates contain significant amounts of hydrocarbon gas which could be used as a future fuel resource; therefore, information regarding their extent and gas volume is important to define their exploitation potential. The storage capacity of gas hydrate structures is high. For example, at normal surface temperature and pressure, 1 cubic unit of solid methane hydrate will release approximately 164 cubic units of methane gas (National Energy Technology Laboratory, 2011). Estimates vary widely, but there is general agreement that gas hydrates could potentially collectively contain about twice as much carbon as all known conventional hydrocarbon reserves (Suess et al., 1999). Potential reserves are extensive but due to difficulties delineating the physical extent of deposits and their concentration in formations, the calculations of available gas volumes vary significantly. However growing efforts to better constrain the volume of hydrate-bearing sediments and their gas yields have resulted in a global estimate of $1{,}226 \times 10^{12}$ m^3 (trillion cubic metres, tcm) or $43{,}311 \times 10^{12}$ ft^3 (trillion cubic feet, tcf), with 63.1 tcm or 2,228 tcf possibly occurring in Canadian marine and Arctic sediments (Johnson, 2011).

Seismic studies of gas hydrates at Blake Ridge, eastern USA, and the Cascadia margin, western Canada, have shown that high-resolution seismic data can delineate the base of a gas hydrate layer (Hyndman and Spence, 1992), confirm the presence of free gas beneath the gas hydrate (Hyndman et al., 2001) and provide data to calculate the volume of gas hydrates present (Dash and Spence, 2011). Drilling results in these areas however, have shown actual hydrates to

be more dispersed and of much lesser volume than geophysical evidence indicated. For example, results from U1325 drilled in a depositional basin in northern Cascadia on ODP Leg 311, showed gas hydrate concentrations of 4-8% pore space (Torres et al., 2008), far below the 20% estimated using various geophysical methods (Hyndman et al., 1999; Yuan et al., 1996, 1999). More recently, Wood and Jung (2008) modelled the extent and thickness of the global methane hydrate stability zone (MHSZ) (Fig. 1.1) which they believe to be accurate for regional scale estimates of volume. The results from Wood and Jung (2008) suggest that the bulk of methane hydrate would be found in areas where sediments are thickest, and bottom water temperatures and thermal gradients are lowest, namely continental margins and in polar regions. They estimated an upper boundary of 3 % pore volume at the base of the MHSZ for average concentration in margin sediments.

The first successful intended extraction of gas from gas hydrate deposits occurred in 2002 at the Mallik site in the MacKenzie Delta of the Beaufort Sea (Dallimore and Collett, 2005). Hydrates were first discovered at this site in 1972 by Imperial Oil Ltd. In 1998, the Geological Survey of Canada (GSC) and the Japan National Oil Corporation (JNOC), along with several other institutions, completed the Mallik 2L-38 Gas Hydrate Research Well Program. Studies found interbedded hydrate-rich sands at depths from 890 to 1,106 m with some individual layers greater than 30 m thick. Hydrate saturations exceeded 80 % in some locations. In 2002, one 1,166 m production well and two 1,188 m observation wells were drilled. The research group conducted pressure draw-down tests on six zones containing gas-hydrate bearing sedimentary sections which revealed the presence of “moveable” water in the reservoirs. This result suggested that standard depressurisation methods would be more efficient for hydrate production than the first choice of thermal stimulation. Depressurisation tests completed in 2007 and 2008

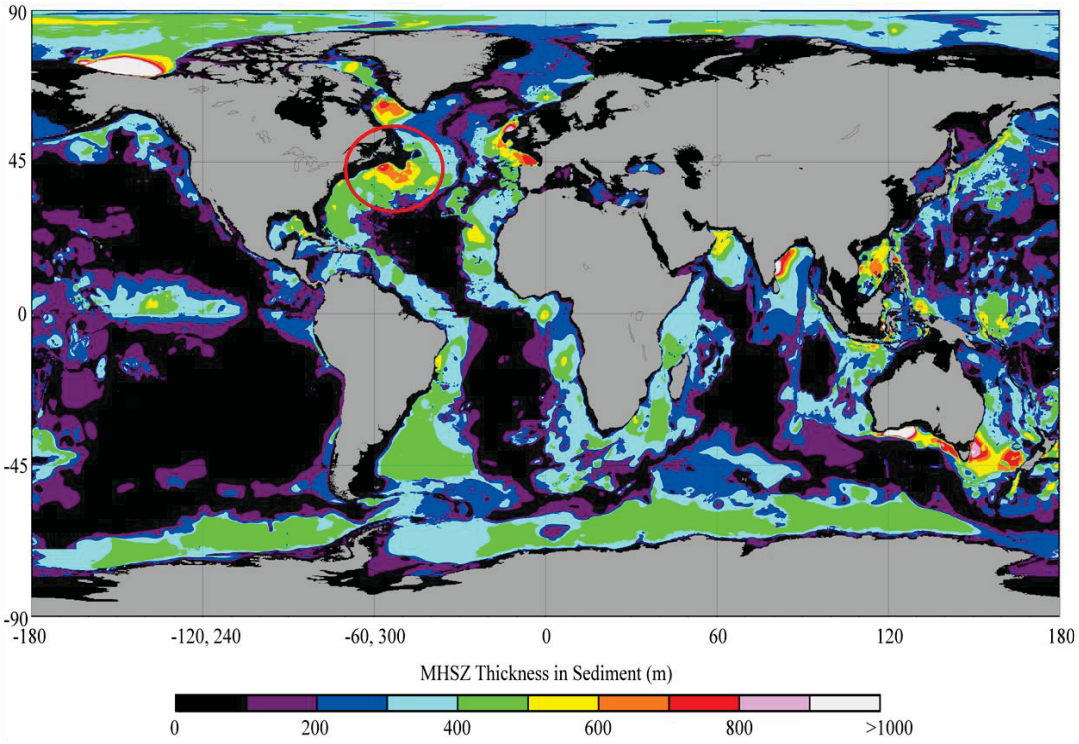

Figure 1.1 Estimated global methane hydrate stability zone thickness in seafloor sediments (from Wood and Jung, 2008). Estimated thickness for the east coast of Canada ranges from 400 to 800 m (red circle).

successfully produced gas from a 12 m interval near the base of a hydrate-rich zone. Sustained gas flow rates of 2,000 – 4,000 m^3 per day were achieved. That test success is viewed as proof of concept for future industrial production of gas from hydrates using established conventional oilfield methods.

1.1.2 Potential Impact on Climate Change

An accurate calculation of methane gas volume currently trapped within gas hydrate is important for understanding the potential impact of gas hydrate dissociation on the carbon cycle and climate change. The release of hydrocarbon gases may significantly modify the global

greenhouse effect because methane is ~23 times more effective at trapping heat in the atmosphere over a 100 year period than carbon dioxide (Ramaswamy et al., 2001). If even a fraction of released methane entered the atmosphere, the presence of the methane and carbon dioxide (an oxidative product of methane) could increase the rate of contemporary climate change.

Gas hydrates are suspected to have played a role in past warming events. The Paleocene-Eocene Thermal Maximum (PETM) at approximately 55 Ma, which saw a rise in global sea surface temperatures of 4 to 8°C over approximately 10,000 years, is the most extensively studied of these warming events (e.g. Winguth et al. 2012). A large negative carbon isotope excursion (CIE) was recorded in both marine and terrestrial sediments during this period. This signal is interpreted as an indicator of large-scale release of light isotope carbon possibly from dissociating marine methane hydrates (Ruppell, 2011a). Negative CIE's are also indicated in repeated Late Quaternary warming events since 400 ka which may have triggered periodic hydrate dissociation events (Ruppell, 2011a).

If the sea bottom temperature rises in the future, locations with gas hydrate will undergo a change in the pressure-temperature regime that keeps the gas hydrate stable in sediments. Models by Majorowicz et al. (2013) show that gas hydrate stability reacts almost instantaneously to water pressure changes, but reacts more slowly to sea bottom temperature changes, due to the heat conductivity effect. Majorowicz et al. (2013) also suggested that methane released from sediments greater than 100 m water depth will dissolve in the water column before reaching the sea surface although breakdown of the methane does deplete the water column oxygen level. Oxygen depletion in turn acidifies ocean waters and eventually leads to carbon dioxide (CO_2) release after some delay, ~50 years for water depths up to 500 m to several hundred years for deeper water. Ruppell (2011a) suggested that northern wetlands appear to be the primary

contributor to atmospheric methane during several Pleistocene (~2.6 Ma to 10 ka) and Holocene warming events (since 10 ka). Therefore, the initial impact of methane release from oceanic sources could be less than that released from onshore sources and may instead contribute to ocean acidification and delayed CO_2 release into the atmosphere.

1.1.3 Potential Geohazard

Dissociating hydrate can increase the risk of seafloor failures. The change in sediment volume and density can destabilize a locality resulting in submarine slides and slumps. Structural failure could result in release of natural gas, further destabilizing the region. From a drilling perspective, dissociating gas hydrates could compromise the integrity of the seafloor and boreholes resulting in shallow water flows, well control problems, and equipment instability. Recent deepwater drilling expeditions which purposefully targeted gas hydrates have been completed successfully without major incidents by using borehole stability and overpressure modeling along with careful drilling fluid management (Ruppell, 2011b). A focus on planned drilling can therefore alleviate safety concerns in areas where gas hydrates are known to exist and where the production of hydrate itself is anticipated. Sudden destabilization of the seafloor however, remains a concern in areas where pipelines or other equipment are on or underneath the seafloor.

1.2 Rationale and Objectives

The presence of a bottom simulating reflection (BSR) is generally interpreted as marking a boundary surface between hydrate-bearing sediments above and gas-bearing sediments below. Although BSRs are recognised worldwide, the first reported BSR on the eastern Canadian continental margin was by Mosher et al. (2004), and the Mohican Channel BSR was first

described by Mosher et al. (2005). The project presented in this thesis attempts to define the geophysical characteristics of gas hydrates in the Mohican Channel area with the goal to determine the gas hydrate physical properties and to calculate gas volumes within the hydrate deposits.

This dissertation has four objectives:

1. To determine the extent of gas hydrate formation including volume assessments in the Mohican Channel area of the Scotian margin;
2. To determine any stratigraphic and structural features specifically related to focusing hydrocarbon gas and subsequent formation of gas hydrate in the study area;
3. To determine if wide-angle reflection and refraction techniques can assist in the detection, characterisation and quantification of in situ gas hydrate;
4. To compare the local gas hydrate volume estimates to regional and global gas hydrate volume estimates.

1.3 CHAPTER ORGANISATION

In this thesis, the chapters are organised as follows:

Chapter 1 – an introductory chapter that outlines the purpose of research into gas hydrates along with the study objectives;

Chapter 2 – a chapter containing background information on the regional geological setting and relevant characteristics of natural gas hydrates;

Chapter 3 – a chapter on data and methods describing the industry 3D multi-channel seismic dataset, the 2D single channel dataset, core data, and ocean bottom seismometer data acquisition and processing;

Chapter 4 – a chapter describing the results from 1) 1D velocity models using OBS data; 2) the calculated base of the gas hydrate stability zone adjacent in the Mohican Channel area; 3) estimated gas hydrate and free gas concentrations in the study area;

Chapter 5 - a stand-alone manuscript for submission to a peer-reviewed journal that describes fluid flow features observed in the 3D MCS dataset;

Chapter 6 – a discussion of the results;

Chapter 7 – conclusions and recommendations for future work;

A complete reference list is included at the end of the thesis.

CHAPTER 2 BACKGROUND

2.1 GEOLOGICAL SETTING

The Scotian Basin is a classic passive margin with over 250 million years of dynamic geological history ranging from the opening of the Atlantic Ocean to recent post-glacial deposition. The basin stratigraphic succession displays several systems including syn-rift, carbonate margin, fluvial-deltaic-lacustrine and deep water depositional systems. The geological history of the Scotian margin was comprehensively described by Jansa and Wade (1975), Wade and MacLean (1990), and in the Play Fairway Analysis (PFA) Report conducted by the Offshore Energy Research Association of Nova Scotia (OERA) in 2011. A brief summary of those reports is contained in the following paragraphs. A generalised stratigraphic chart for the Scotian Basin is presented in Figure 2.1, and location maps are presented in Figure 2.2.

2.1.1 Regional Geology

The eastern Canadian continental margin is a passive margin formed during mid-Triassic rifting ~220 Ma between the African and North American tectonic plates (Jansa and Wade, 1975; Wade and MacLean, 1990). Rifting created as series of interconnected grabens and half grabens named, from west to east, Shelburne, Sable, Abenaki, Laurentian and South Whale subbasins, and the Orpheus graben (Figure 2.2a). Smaller, isolated basement lows such as the Mohican graben and the Naskapi graben complex were also formed by the rift process (Figure 2.2a). The thickest sediment accumulation is found on the outer shelf and slope in the Sable, Laurentian and South Whale subbasins, reaching15 – 20 km thickness due to several periods of subsidence and deposition (Jansa and Wade, 1975; Wade and MacLean, 1990; Shimeld, 2004).

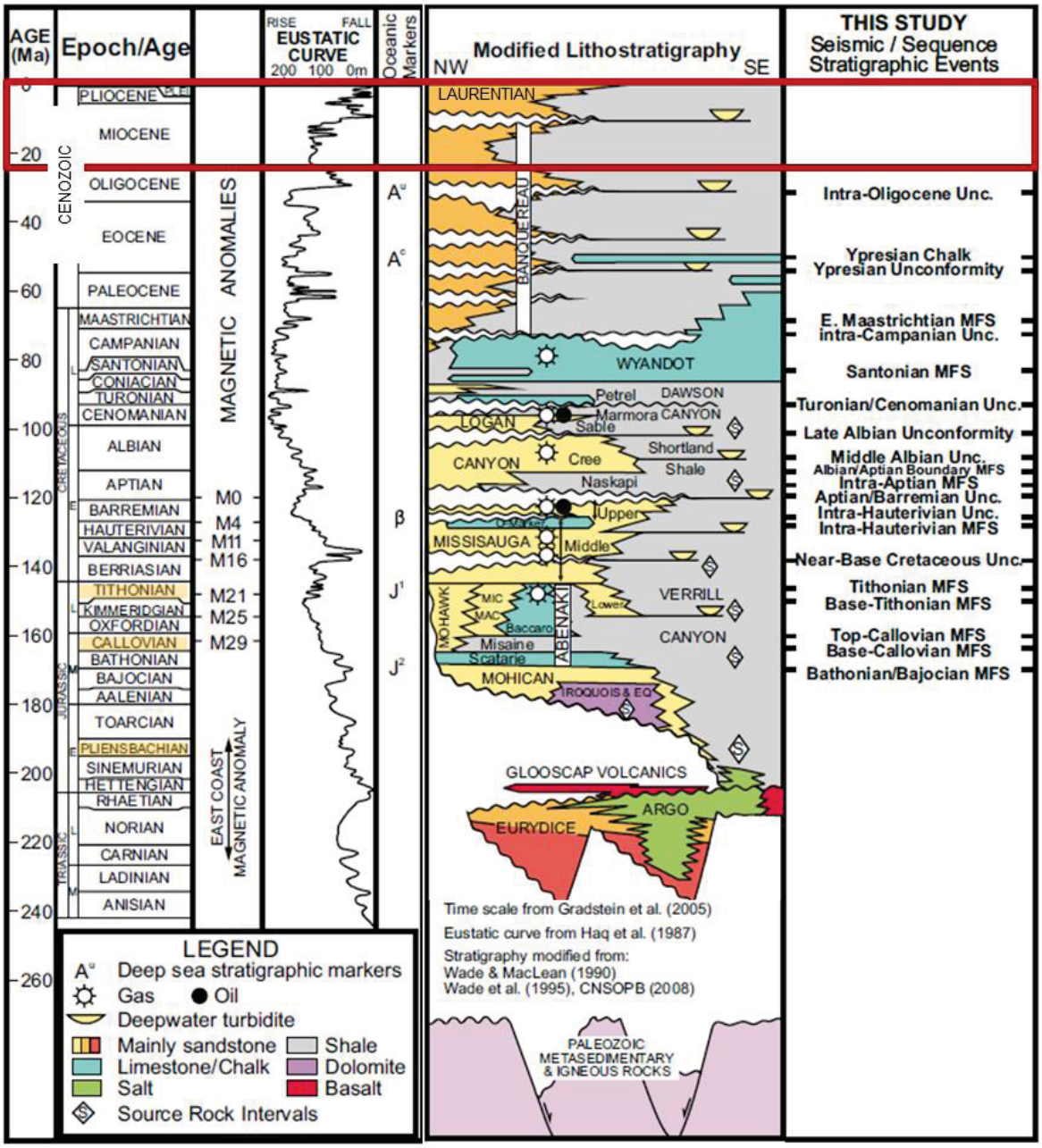

Figure 2.1 Generalized stratigraphic chart for the Scotian margin, offshore Nova Scotia (Weston et al., 2012). The red rectangle marks the study interval. The source rocks identified in the study area by the Play Fairway Analysis (OERA, 2011) are highlighted in yellow on the left.

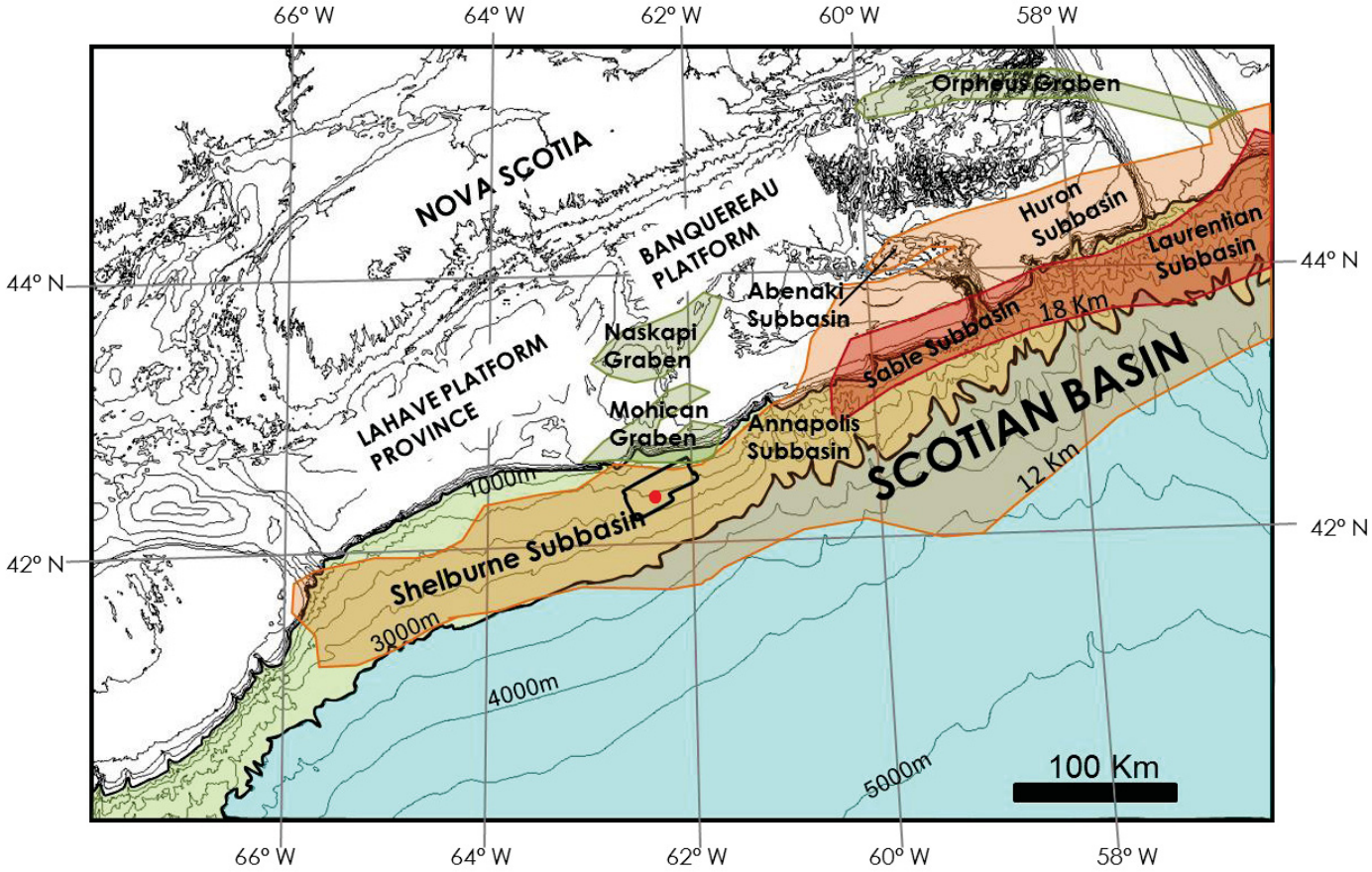

Figure 2.2a Map of the Scotian Margin showing the location of major structural features. The location of the 3D MCS data available for this study is outlined by a black polygon in the center of the figure. The depth to the Mesozoic-Cenozoic basement is shown by the brown shaded regions. Adapted from Weston et al. (2012).

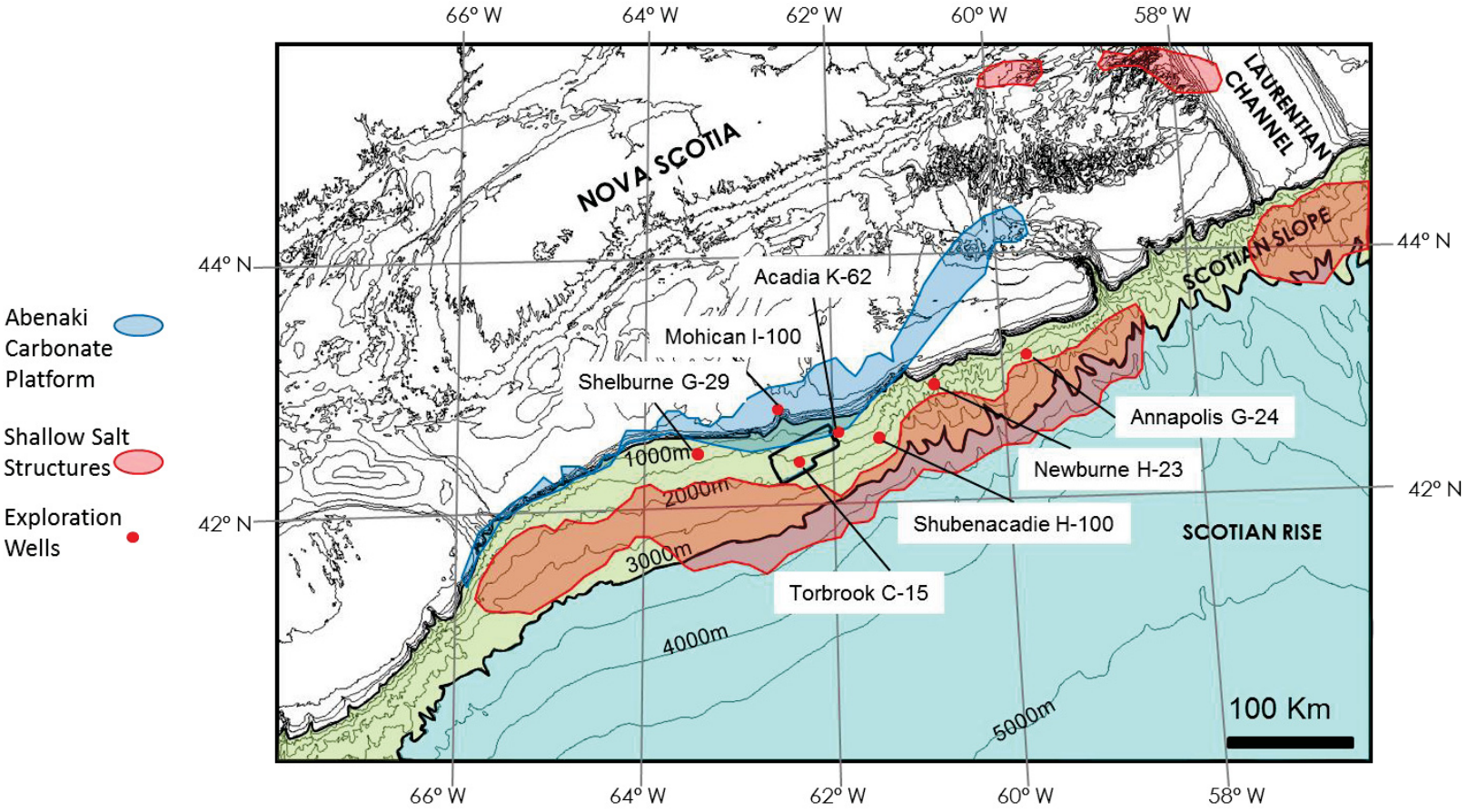

Figure 2.2b Map of the Scotian Margin showing the location of shallow salt structures, the Abenaki Carbonate Platform and exploration wells throughout the area. The location of the 3D MCS data available for this study is outlined by a black polygon in the center of the figure. Adapted from Campbell (2011).

Late Triassic fluvial and lacustrine redbed sediments and volcanic sequences were deposited in the series of narrow, interconnected basins (Wade and MacLean, 1990; OERA PFA, 2011). As the continents moved northwards, marine sediments formed in restricted conditions, along with mixed clastics and minor carbonates were deposited (Eurydice Fm.). Evaporites up to 2 km thick were deposited in central parts of the rift system (Argo Fm.) (OERA PFA, 2011)

In the Early Jurassic, an eastwards pulse of redbed sediments was deposited in the western Central Scotian Basin (OERA PFA, 2011). At this time, renewed tectonism caused complex faulting and erosion of older rocks. The North American and African continents separated and the proto-Atlantic Ocean opened. A marine transgression covered the basins with a shallow sea within which thin sequences of carbonates and clastic sediments accumulated (OERA PFA, 2011). Dolomites and clastics of the Iroquois Fm. were laid down locally on the seaward portion of the margin (Wade and MacLean, 1990; Hansen et al., 2004; OERA PFA, 2011). On the basin margins, a thick succession of coarse-grained clastic sediments and fluvial shales were concurrently deposited (Mohican Fm.) (OERA PFA, 2011).

By the Middle Jurassic, the Atlantic Ocean had become broader and deeper (~1 km) and a carbonate bank, of the Abenaki Fm., had formed in the western part of the basin (Figure 2.2b). Carbonate deposition was occasionally overrun by deltaic depocenters but persisted until the Early Cretaceous (OERA PFA, 2011).

Regional uplift to the east in the Late Jurassic resulted in an influx of clastic sediments and the establishment of the Sable Delta complex in the Huron, Laurentian and Sable sub-basins (OERA PFA, 2011). Each subbasin had periods of rapid subsidence, differentiated by timing (Wade and MacLean, 1990). The sediments were sourced from the ancestral St. Lawrence River region. In the Abenaki and Sable subbasins, alluvial plain and deltaic facies of the MicMac Fm.

were deposited east of the carbonate bank (OERA PFA, 2011). Outboard of the carbonate bank, the MicMac Fm. interfingered with deep marine shales of the Verrill Canyon Fm (Shimeld, 2004). As the St. Lawrence River region became better established, an increasing clastic sediment supply buried the carbonate reefs and banks on the LaHave Platform and later the Banquereau Platform (OERA PFA, 2011). The postulated Shelburn Delta in the southwest may have had a similar history of sedimentation (OERA PFA, 2011).

Early Cretaceous sedimentation was dominated by a series of thick sand-rich deltaic sediments, carbonate shoals and shallow marine shelf successions (Missisauga Fm.) (OERA PFA, 2011). Sediment loading at this time mobilized the Jurassic salts both vertically and laterally in the Sable and Shelburne subbasins resulting in the formation of features such as diapirs, welds and canopies (Shimeld, 2004; OERA PFA, 2011) (Figure 2.2b). Shimeld (2004) identified five syn-rift salt subprovinces through the Scotian Basin both along strike and basinward to landward and concluded that salt tectonics is active throughout the area. Shimeld (2004) interpreted the presence of primary salt basins beneath subprovinces I, II (including the Shelburne Subbasin and Mohican Graben) and V, and landward of subprovince IV (beneath the Sable Subbasin). Diapirs within subprovinces I, II, and V have experienced reactivation during the Cenozoic, most especially in subprovince V where only Quaternary sediments cover several active diapirs. In subprovince III, extensive allochthonous canopy systems were expelled from the Sable subbasin and moved seaward by 80 – 100 km (Shimeld, 2004).

During periods of sea level lowstands, rivers incised exposed shelf sediments and deltas formed at the shelf edges. The deltas provided turbidity currents and mass transport deposits to the slope from the Middle Jurassic to the Cretaceous (OERA PFA, 2011). This movement of sediments deposited potential reservoirs into canyons and mini-basins. A major marine

transgression occurred in the late Early Cretaceous when deltaic sedimentation ceased and thick shales of the Logan Canyon Fm. covered the shelf (OERA PFA, 2011). During the Late Cretaceous, marine shales, chalks and minor limestones of the Dawson Canyon Fm. were deposited throughout the entire shelf of the Scotian Basin. The end of the Cretaceous in the Scotian Basin is marked by a rise in sea level, basin subsidence, and the deposition of marine marls, chalks and chalky mudstones of the Wyandot Fm. The Wyandot Fm. was in turn buried by marine shelf mudstones and later shelf sands of the Banquereau Fm. (OERA PFA, 2011). Although mainly composed of mudstone, units of chalk, sandstone and conglomerate of regional significance occur in the Banquereau Fm. (Shimeld, 2004). Glaciomarine and marine sands, silts and clays were deposited on the outer shelf and upper slope during the Late Pliocene and the Quaternary (Laurentian Fm.).

2.1.2 Geology of the Study Area

The study area lies within the Shelburne subbasin (Figure 2.2a), which is part of the Diapir Province identified by the PFA Report (OERA, 2011). This province is characterized by vertically raised diapirs on top of the autochthonous salt basin (Deptuck, 2011) and corresponds to structural subprovinces I and II as identified by Shimeld (2004). Possible autochthonous salt was encountered at the base of the Mohican H-100 well, just north of the study area (Figure 2.2b). Most of the structural traps in the Diapir Province are related to salt tectonics (OERA PFA, 2011). The LaHave Platform Province lies to the north and a distinct hinge zone, which runs diagonally through the study area, determines its seaward boundary (Deptuck, 2011).

In this part of the margin, the PFA report (OERA, 2011) states that marine source rock could have generated liquid hydrocarbon that was trapped in the salt-related traps, such as

overhangs, or in turbidite-related sedimentary traps in the mini-basins. In this southwestern province, basins typically contain less than 9 km of clastic sediments (OERA PFA, 2011).

The PFA report (OERA, 2011) identified five potential source rocks on the Scotian margin grouped into two major petroleum systems: 1) Early to Middle Jurassic, and 2) Late Jurassic to Early Cretaceous. The basin modeling study by OERA (2011) divided offshore Nova Scotia into 6 zones, with the study area falling mainly into Zone 1 and partially into Zone 2. Three source rocks are present in the study area (Figure 2.1); 1) Tithonian (deposited ~148 Ma), which started to mature very recently in the Late Paleogene and has undergone limited explusion (migration out of the source rock) of hydrocarbons; 2) Callovian (deposited ~160 Ma) which started to mature in the Late Cretaceous and has undergone limited expulsion of hydrocarbons; and 3) Pliensbachian (deposited ~ 196 Ma), an unproven source rock with varied maturity in stages from the Early to Late Cretaceous and locally scattered expulsion zones throughout the study area. The PFA Report (OERA, 2011) concludes that about 2/3 of the total amount of hydrocarbon generated is “in-place” in zone 1. Also zone 1 has a high-ranked Early-Middle Jurassic play system with a source rock without excessive maturity levels. The Annapolis and Newburn wells to the east of the study area both contain gas-bearing sands (Figure 2.2b). The discovery of gas in the region and the recent PFA report (OERA, 2011) confirms the presence of an active slope hydrocarbon system which could provide the hydrocarbon gas necessary for gas hydrate formation.

The study interval lies within the thickest section of the Shubenacadie Drift as identified by Campbell (2011) and formed between horizons of estimated Pliocene age (horizons N50 – Early Pliocene and N60 – Late Pliocene) (Figure 2.3). Campbell (2011) determined that the Shubenacadie Drift exceeds 1500 m thickness near the Torbrook C-15 well and covers a total

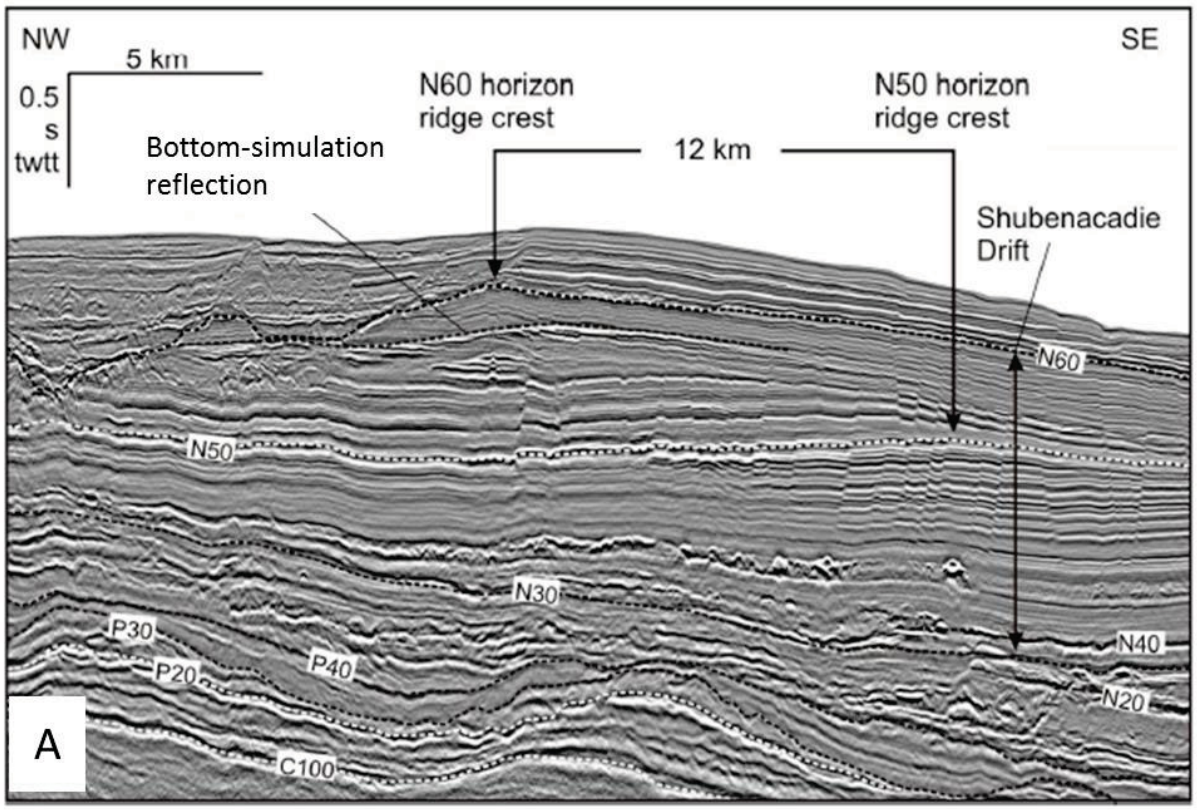

Figure 2.3a Seismic reflection profile through the study area showing the Shubenacadie Drift. The Mohican Channel bottom-simulating reflection is visible at the top of the Drift. Interpretation described in Chapter 5 of this thesis concentrates on the area between the N50 and N60 horizons, with estimated ages of Early and Late Pliocene respectively. Figure adapted from Campbell (2011).

area of 9500 km^2. Sample control in the area is sparse and simply points to mainly mud-based lithology, although Campbell (2011) theorises that muddy turbidities and hemipelagic sediments were the sediment source for the Drift. Alongslope currents have moved and moulded sediments possibly sorting the sediments sufficiently to provide the pore space necessary for gas hydrate formation in parts of the Drift.

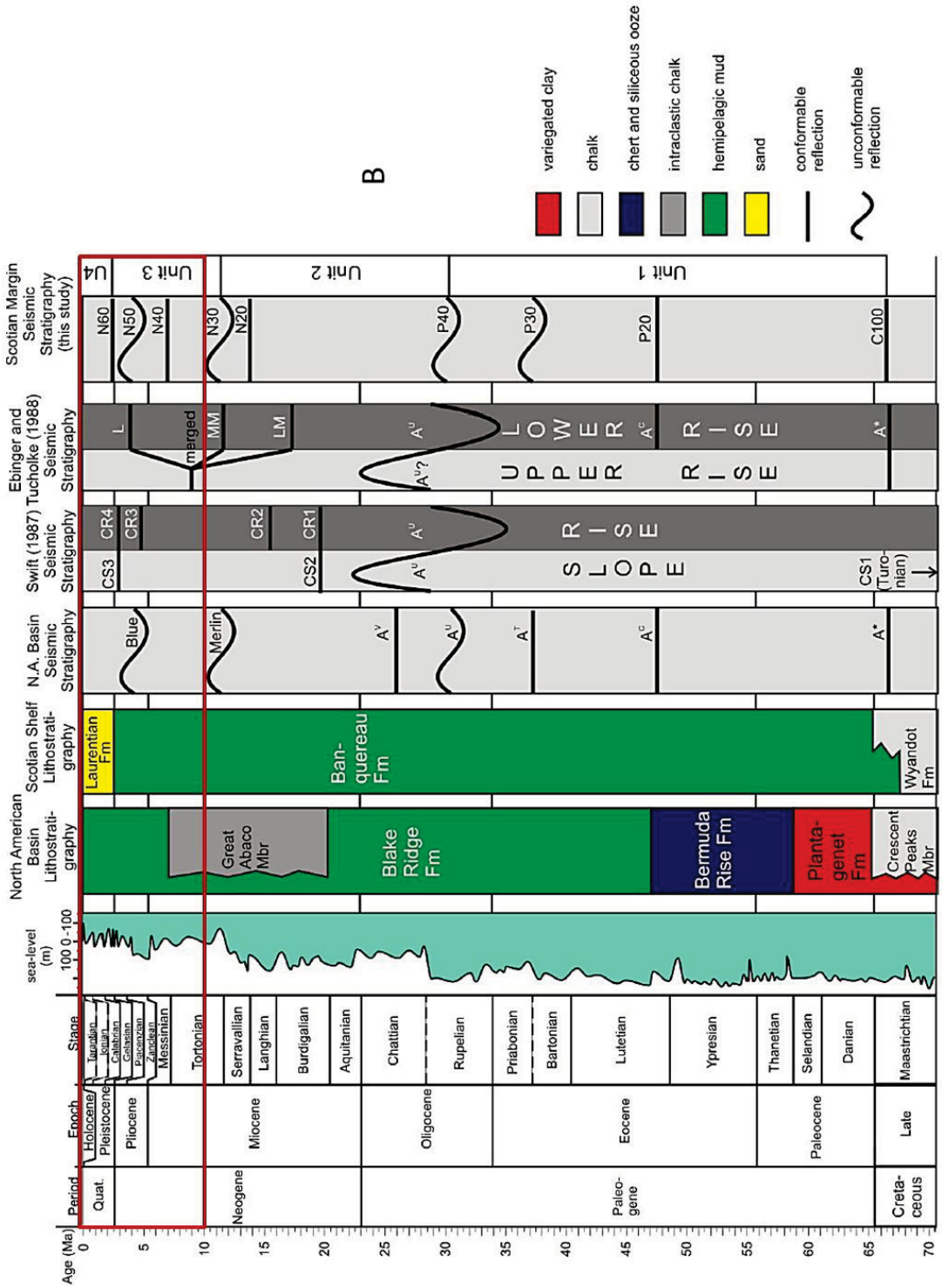

Figure 2.3b Seismic stratigraphy in the study area as developed by Campbell (2011). The red rectangle denotes the study interval. The rightmost column shows the seismic stratigraphic names given by Campbell and used in this thesis.

2.2 Structural Features

Faults can provide pathways for hydrocarbons to move from deep sources upwards into shallow hydrocarbon reservoirs or into the zone where gas hydrate could form. Observations in the Voring Basin, offshore Norway (Berndt, 2005) show that fluid flow tends to focus through discrete pathways such as faults or pipes. A polygonal fault system described by Hansen et al. (2004) in the Sable Subbasin, adjacent to the study area (Figure 2.2a), formed in Cenozoic mudrocks and upper Cretaceous chalks similar to those present in the study area.

2.2.1 Polygonal Fault Systems

A special class of normal, non-tectonic, non-gravitational faulting has been described over the past two decades in basin slope and floor sediments (Cartwright and Dewhurst, 1998; Dewhurst et al., 1999; Hustoft et al., 2007). These are termed polygonal faults (PF) due to their distinctive honeycomb structure in map view (Cartwright, 1994; Lonergan et al., 1998). The definition of a PF system describes "a plan view geometry where planar, curved and sinuous fault traces are distributed in a wide variety of orientations and connect to form both closed and open multi-sided cells" (Lonergan et al., 1998) (Figure 2.4).

Polygonal faulting was first described in the North Sea by Cartwright (1994, 1996) and has since been found in sedimentary basins worldwide such as offshore Norway (Laurent et al., 2012) and the Lower Congo Basin (Gay et al., 2004). PF systems could potentially act as fluid flow pathways from deeper to shallower reservoirs, so understanding their nature and distribution within a basin may enhance understanding of the local or regional hydrocarbon potential of shallow plays (Stuevold et al., 2003). Gay et al. (2006a/b, 2007a/b) related polygonal faulting to fluid transport and dewatering structures such as pockmarks identified on the seafloor of the

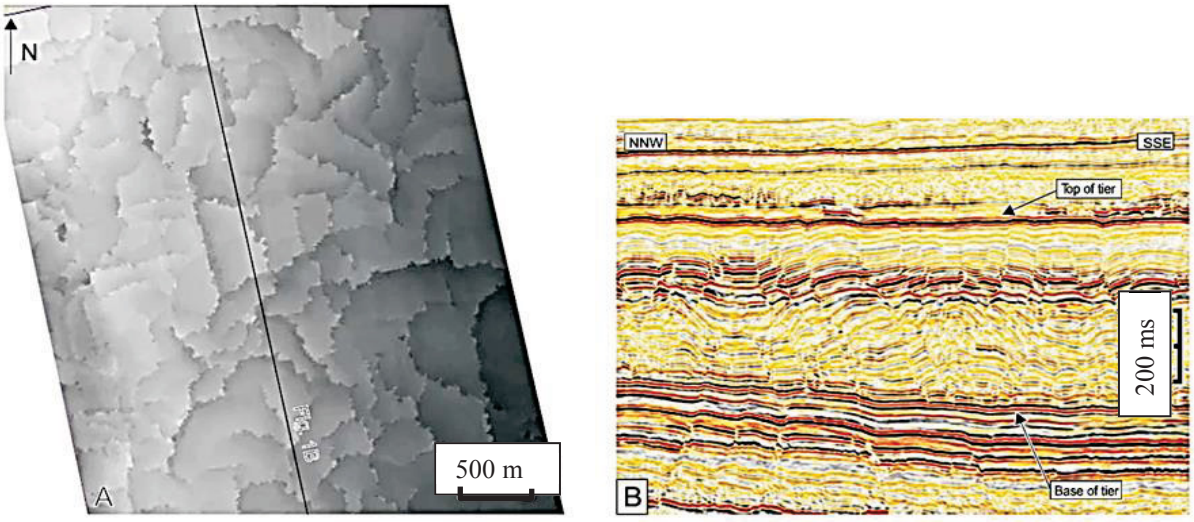

Figure 2.4 Planform and cross-sectional characteristics of polygonal fault systems. (a) Structure map in two-way travel time of part of a polygonal fault system deforming Neogene biosiliceous mudstones offshore Norway, showing the typical planform of the fault network. (B) Part of a seismic profile across the map in (A), showing the layer-bound nature of the faulting, with upper and lower boundaries of the faulted 'tier' clearly shown following stratigraphy. Example from Cartwright (2007).

Lower Congo Basin. Berndt et al. (2003) and Bünz et al. (2005) determined that PFs played a role in focussing fluid flow into a gas hydrate stability zone on the mid-Norwegian margin.

This type of faulting develops in passive margin basins within fine- to very fine-grained sedimentary sequences with high clay content as well as carbonate chalks (Cartwright and Lonergan, 1996; Dewhurst et al., 1999; Hansen et al., 2004). To date, a number of mechanisms have been proposed for their formation such as: 1) syneresis, volumetric contraction and liquid expulsion (Cartwright and Lonergan, 1996; Dewhurst et al. 1999); 2) low coefficients of residual friction (Goulty, 2008); 3) density inversion related to overpressured pore water (Plaza-Faverola et al., 2012); and 4) thermal and chemical contraction due to the opal A to opal CT conversion (Davies et al., 2009; Cartwright, 2011). PF systems are recognized as forming early during burial because of two key observations: (1) Cartwright (1994) found that the edges of the PF systems

usually form where the host stratigraphic unit is less than 100 m thick, and (2) Lonergan et al. (1998) and Stuevold et al. (2003) found evidence of growth faulting at the seabed.

Hansen et al. (2004) described an extensive PF system in the Upper Cretaceous chalk of the Wyandot Formation and Cenzoic mudrocks of the Banquereau Formation in the Sable Subbasin, northeast of the study area (Figure 2.2a). The authors attributed the PF system formation to syneresis and its distribution to distinct lithological changes. In the NW European province, many deepwater sandstone reservoirs have top seals affected by PF systems posing questions about the effect these systems may have on seal integrity (Stuevold et al., 2003).

2.2.2 Fluid Flow Features

Recognition of active or paleo-fluid flow pathways and expulsion features can indicate the status of the hydrocarbon system in a location of interest. Vertical fluid flow through marine sediments occurs globally on passive and active continental margins and is a widespread dynamic process. Fluid migration in sedimentary basins is an important process and the nature of focused fluid flow in gas hydrate formation remains under examination worldwide (Crutchley et al., 2011; Plaza-Faverola et al., 2012; Vadakkepuliyambatta et al., 2013).

The migration and subsequent expulsion of pressurised fluids in sediments produce features such as pockmarks, mounds, pipes and chimneys. Expulsion of overpressured fluids onto the seafloor results in pockmarks or mounds. Pockmarks are defined as concave, crater-like depressions ranging in diameter from a few metres to several hundred metres and were first described on the Scotian Shelf by King and MacLean (1970). Most seafloor pockmarks appear dormant, suggesting their activity may be episodic and implying multiple phases of fluid flow, although the timing is generally unknown. Mounds can reach considerable height above the seafloor having relief of several 10's of metres (Gay et al., 2007b; Matsumoto et al., 2011), and

some have active fluid flow. Active seeps frequently attract diverse benthic and chemosynthetic communities which can host unique specialized species (Herbozo et al., 2013; Marcon et al., 2014).

Ascending gas and fluid can leave subsurface traces in seismic datasets in the form of amplitude anomalies or disturbed zones (Figure 2.5). These are caused by contrasting acoustic impedence across the surrounding rock due to velocity and density changes. Stacked or columnar acoustic disturbances are termed seismic pipes and are understood to represent vertical gas and fluid pathways (Figure 2.5) (Cartwright, 2007; Loseth et al., 2011). They are circular to sub-circular in map view and can have vertical to sub-vertical geometry over 1km in length (Cartwright, 2007). Seismic pipes may terminate in pockmarks on the seafloor depending on their pressure regime (Cartwright, 2007; Andresen, 2012). Seismic pipes can be distinguished from seismic processing artifacts because their development shows both structural and stratigraphic control, such as formation above structural traps or faults (Cartwright, 2007; Huuse et al., 2010). Seismic pipes are also recognisably different from gas chimneys which exhibit wide zones of deteriorated seismic signal (wipe outs, velocity pull downs) due to the presence of low velocity gas pockets (Figure 2.5) (Loseth et al., 2009; Andresen, 2012). The presence of traceable reflections into the chimneys indicates the chimney sediments are not reworked as opposed to mud volcanoes which carry reworked sediments through the conduits up to the seafloor (Figure 2.5) (Matsumoto et al., 2011; Andresen, 2012). In some locations such as the northern US Atlantic margin, gas plumes have been identified in the water column and directly related to seeps found at water depths within the limits of the regional gas hydrate stability zone (Skarke et al., 2014).

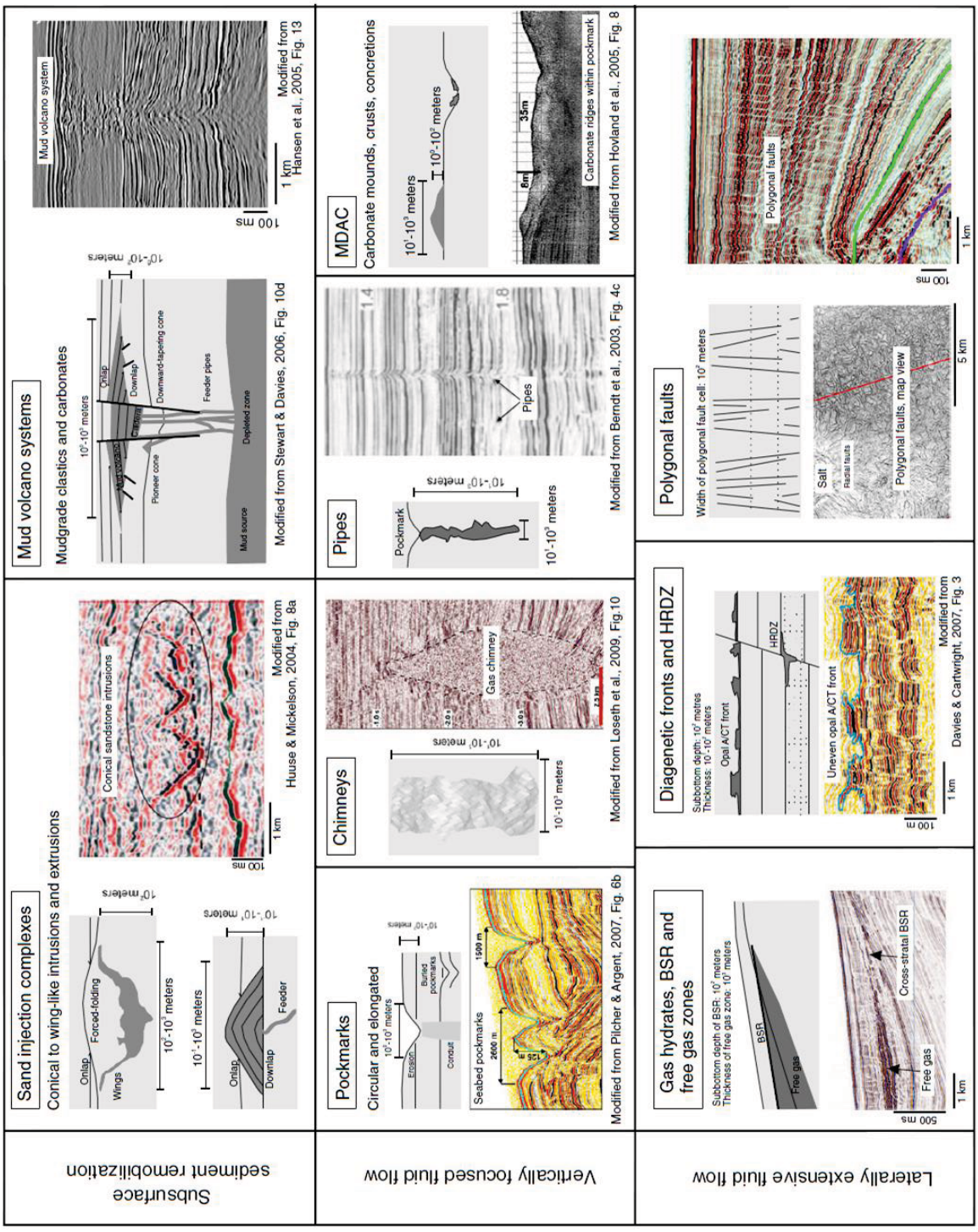

Figure 2.5 Examples of the subsurface features visible in seismic data that result from sediment mobilisation or fluid flow, taken from Andresen (2012). Pockmarks, chimneys, and pipes are all indicative of vertically focused fluid flow, while polygonal faults and gas hydrates influence lateral fluid flow.

2.3 NATURAL GAS HYDRATE

Natural gas hydrates occur worldwide (Figure 2.6). They are a unique hydrocarbon trap, consisting of a solid ice lattice surrounding hydrocarbon molecules, which forms due to specific pressure and temperature conditions. Those conditions are influenced by water depth and bottom water temperature, heat flow from the Earth (geothermal gradient) and pressure from the overlying sediment load (overburden). The storage capacity of gas hydrates is high and a deposit can contain significant amounts of hydrocarbon gas, most commonly methane. For example, if methane gas molecules filled all the available spaces, a cubic metre of idealised methane hydrate contains more than 160 m^3 of methane at standard temperature pressure conditions (National Energy Technology Lab., 2011). The gas hydrate crystal lattice is stabilised primarily by pressure. A decrease in pressure can lead to hydrate dissociation and the subsequent release of free water and hydrocarbon gas, resulting in localised loss of sediment cohesion.

2.3.1 Natural Gas Hydrate Structure

Methane hydrate is non-stoichiometric in that the crystal structure of the gas hydrate can be established without all the methane lattice sites being occupied (Max and Lowrie, 1997). Some of the molecular sites available for methane in the gas hydrate lattice may be filled with another gas such as ethane. The gas hydrate crystal lattice is stabilized primarily by pressure. The water molecules which grow into lattices to trap gases can take three forms; structure I, structure II and structure H (Fig. 2.7). In general, large molecules such as methane, hydrogen sulphide and carbon dioxide will be found in structure I lattices (Fig. 2.7). Structure II lattices have a mix of small and large cages so methane, propane and butane will be found in conjunction with small molecules such as argon, krypton and nitrogen (Fig. 2.7). Methane can also be found

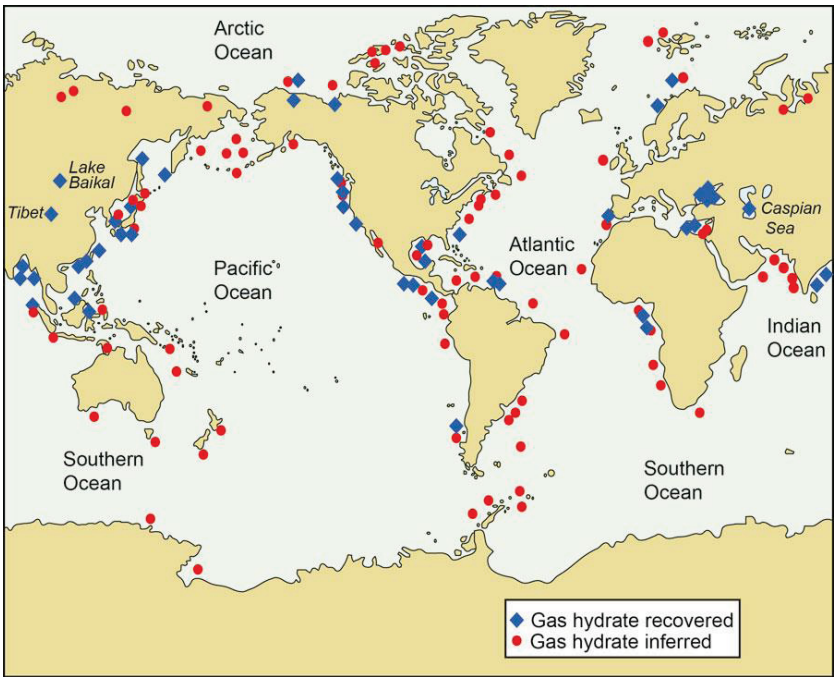

Figure 2.6 Global distribution of gas hydrates. Some locations have been confirmed by recovered gas hydrate samples. Other locations have gas hydrate inferred from the presence of BSRs or through advanced seismic attribute analysis. Figure from Ruppel and Noserale (2012).

as a stabilizing guest molecule in structure H lattices which house the largest gas molecules such as methylcyclohexane (Fig. 2.7). Structure H gas hydrates are rare (Mao et al., 2007).

Individual cage geometries form from the specific arrangement of water molecules, which in turn gives specific cavity geometries. Cavity radii range from 4 to 6 Angstroms (1Å = 10^{-8} cm) which allows a variety of gas molecules to be trapped inside the cages e.g. methane, ethane, propane, butane, nitrogen, carbon dioxide and hydrogen sulphide (Hardage et al., 2006). As the ice lattice forms, the size of available gas molecules determines the final structure. The fit of the gas molecules within the cages determines the pressure and temperature of optimum stability. The bulk density of pure hydrate is between 0.90 and 0.95 g/cm^3 (Hardage et al., 2006), which

results in the gas hydrate being buoyant in seawater. Therefore, any outcrop on the seafloor must be anchored in the sediments or have enough sediment in its structure to overcome buoyancy.

The most common gas hydrate formed in marine environments is Structure I. The source gas for Structure I methane hydrate is mainly biogenic, a product of organic matter decomposition and CO_2 reduction by micro-organisms in low temperature environments. Most marine sediments, however, have relatively low organic content suggesting that overall rates of biogenic gas production within the hydrate stability zone would also be low. Migration of fluid charged with thermogenic methane into the gas hydrate stability zone (GHSZ) is required to increase gas concentrations to sufficient levels within the GHSZ to allow formation of gas hydrate (Pecher et al., 2010; Pause, 2011).

2.3.2 Natural Gas Hydrate Stability

Max and Lowrie (1997) defined the oceanic gas hydrate stability zone (GHSZ) as "the nearly seafloor-parallel zone of thermodynamic equilibrium that extends downwards from the seafloor in water depths greater than about 400 m to a depth determined by the geothermal gradient". This zone is controlled by four factors: 1) geothermal and hydrothermal gradients; 2) seafloor temperature; 3) pressure (hydrostatic – related to the weight of the water, and lithostatic – related to the weight of the overlying rock); and 4) hydrocarbon gas type which controls the hydrate phase boundary (i.e. the change from hydrocarbon gas plus liquid to solid hydrate).

The geothermal gradient is the rate of increase in temperature in the sediments with depth and is measured in degrees Celsius per metre (°C/m). This gradient varies with location. The hydrothermal gradient is the decrease in temperature in the water column with depth and is measured in °C/m. This gradient also varies with location. In general, heat flows from warmer

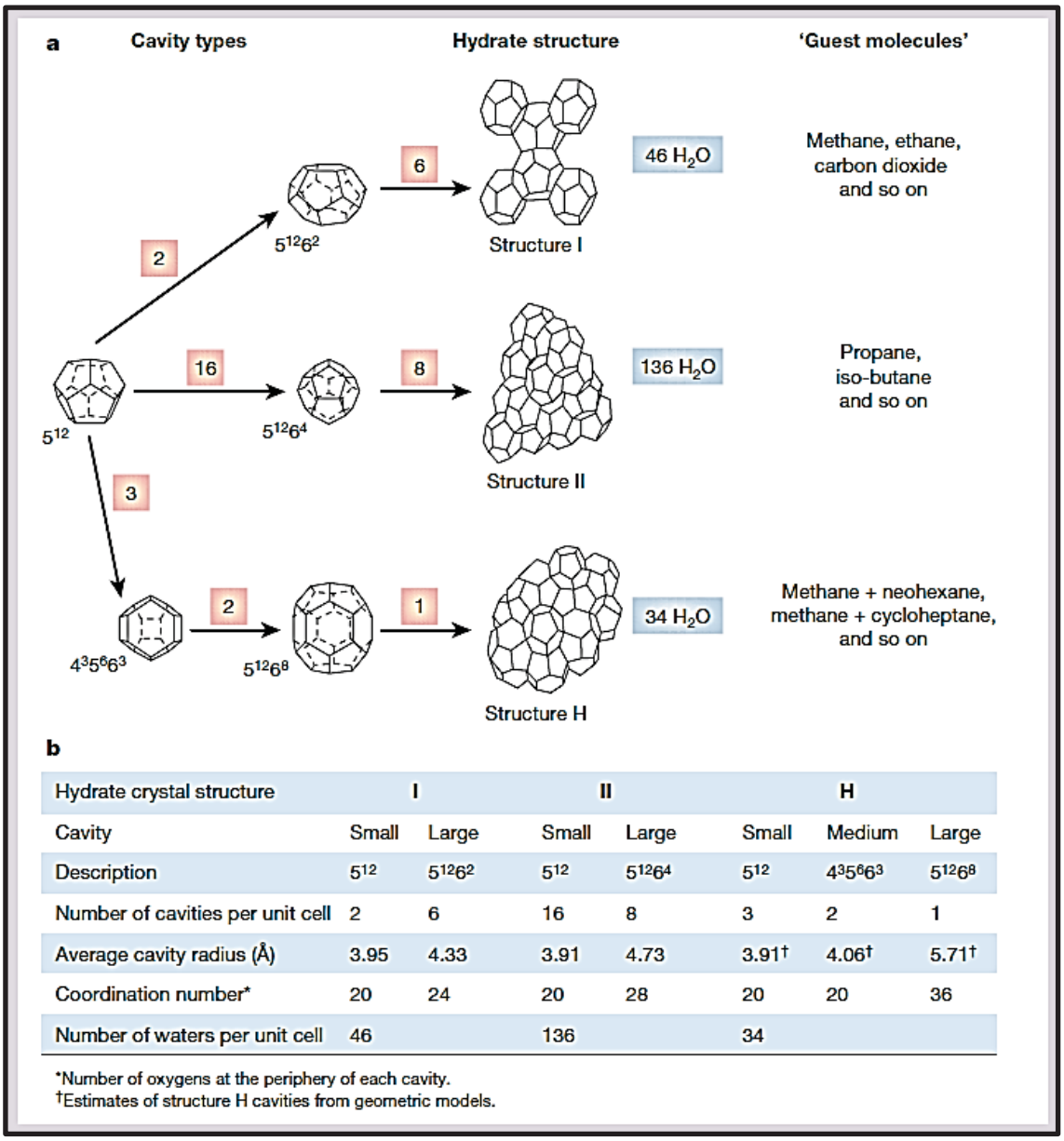

b

Hydrate crystal structure	I		II		H		
Cavity	Small	Large	Small	Large	Small	Medium	Large
Description	5^{12}	$5^{12}6^2$	5^{12}	$5^{12}6^4$	5^{12}	$4^35^66^3$	$5^{12}6^8$
Number of cavities per unit cell	2	6	16	8	3	2	1
Average cavity radius (Å)	3.95	4.33	3.91	4.73	3.91†	4.06†	5.71†
Coordination number*	20	24	20	28	20	20	36
Number of waters per unit cell	46		136		34		

*Number of oxygens at the periphery of each cavity.
†Estimates of structure H cavities from geometric models.

Figure 2.7 Three crystalline structures which gas hydrate can form. The cavity structure with twelve pentagonal faces (5^{12}) is found in all known gas hydrate structures. The pink boxes denote the number of small, medium and large 5^{12} cavities present in a gas hydrate structure. Structures I and II have small and large cavities. Structure H has three types of cavities in order to maintain stability. Figure from Sloan (2003).

marine sediments to the colder ocean waters. Seafloor temperature is determined by the bottom water temperature, which is influenced by the water mass at a particular geographical location, depth of the location of interest, and ocean currents. The seafloor temperature and geothermal gradient together control the GHSZ thickness. Hydrostatic pressure is the pressure at a given depth in a static liquid (the ocean is considered static as it is an open system) and is the result of the weight of the liquid acting on a unit area at a given depth plus any pressure acting on the surface of the liquid itself (Sheriff, 2002). Pressure is assumed to be hydrostatic to the base of the GHSZ but this requires 100 % permeability to the seafloor which is not always the case. Therefore, lithostatic pressure can be a contributive factor. In the calculation of a GHSZ, pressure is a function of depth below the seafloor. In general, the GHSZ tends to be thicker in deeper waters (>1500m) where pressures are higher and in areas where heat flow is low (Max and Lowrie, 1997). Wood and Jung (2008) modelled the global methane hydrate stability zone for water depths of 800 to 2000 m, assuming a constant geothermal gradient of 0.054 K/km. The estimated thickness of the methane hydrate stability zone offshore Nova Scotia using that method is 400 to 800 m (Fig. 1.1).

The main components of the GHSZ calculation are shown diagrammatically in Figure 2.8. For gas hydrate to form the amount of hydrocarbon gas, in this case methane, must exceed its solubility in water so that the gas can no longer dissolve in water at a specific temperature and pressure. The change in solubility is marked by the gas hydrate phase boundary (blue curve) in Figure 2.8. When conditions move to the left of the phase boundary, gas hydrate formation will occur. A move to the right of the phase boundary will lead to hydrate dissociation and the release of free water and methane gas. In general, a combination of high pressure and low temperature are required for gas hydrate formation. The base of the GHSZ is limited to the point at which the

hydrate phase boundary crosses the geothermal gradient (dark red line, Figure 2.8). Above this crossover point, solid gas hydrate will form in the sediments if pore space is available and the concentration of hydrocarbon gas is sufficiently high (orange hatched area, Figure 2.8). Below this point, free hydrocarbon gas can occur in the sediments. The theoretical GHSZ may extend above the seafloor into seawater but gas hydrate will not remain stable here as the water would be undersaturated in methane causing gas hydrate to dissociate. Gas hydrate dissociates when a change in the stability conditions is sufficient to move the gas hydrate out of the stability zone.

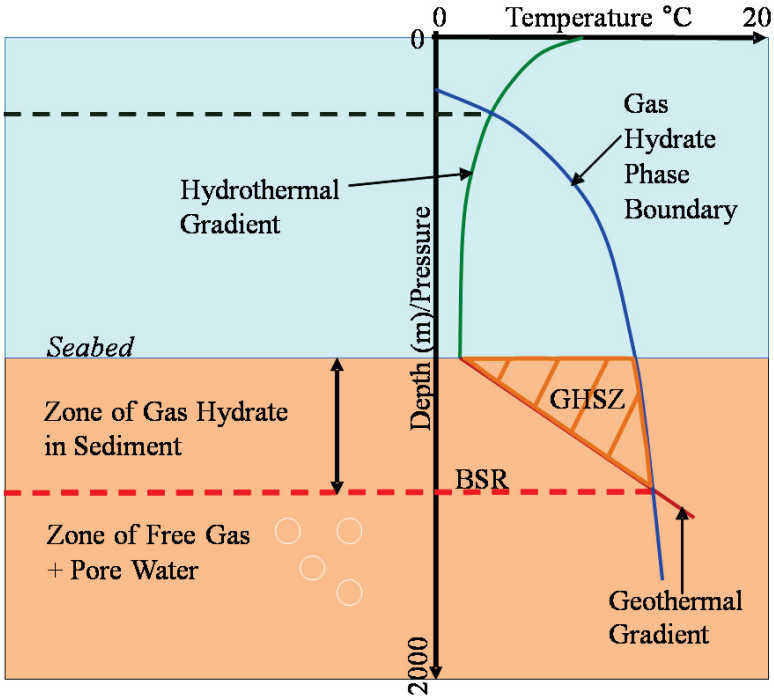

Figure 2.8 Phase diagram describing the conditions necessary for gas hydrate development in oceanic sediments. A water depth of 1200 m is assumed. Adapted from Tinivella and Giustiniani (2012).

2.3.3 Factors Affecting Gas Hydrate Formation

Gas hydrate can exist anywhere within the GHSZ (Hardage et al., 2006). However, a number of factors can influence gas hydrate formation, such as gas composition, gas concentration, sediment properties, and sulphate reduction.

The combination of gases such as carbon dioxide, hydrogen sulphide, ethane and propane with methane will shift the hydrate stability curve to the right in Figure 2.8. That would increase the pressure-temperature field within which the gas hydrate is stable and deepen the base of the GHSZ (Max and Lowrie, 1997). This is the basis behind the formation of structure II gas hydrate.

The formation of gas hydrate is also constrained by sediment properties such as available pore space. When gas hydrate fills sediment pore space, it reduces permeability and creates a gas trap. Trapping of free gas beneath gas hydrate may cause the formation of the most concentrated gas hydrate deposits, and form a reservoir of free gas below the gas hydrate zone. The free gas can continually migrate upwards through cracks or fractures to fill any open pore spaces. This process, in turn, causes the trap to become more effective, producing highly concentrated methane gas and methane hydrate reservoirs.

Sulphate-reducing bacteria area common in anaerobic environments where they break down large organic molecules, such as methane, for energy. Methane reduction can exceed methane formation in some locations, preventing the formation of gas hydrate in shallow parts of the sediment column.

2.3.4 Types of Gas Hydrate Accumulation

Milkov and Sassen (2002) described three types of gas hydrate accumulation based on the mode of fluid migration and gas hydrate concentration within the GHSZ: 1) Structural accumulations; 2) Stratigraphic accumulations; and 3) Combined accumulations (Figure 2.9).

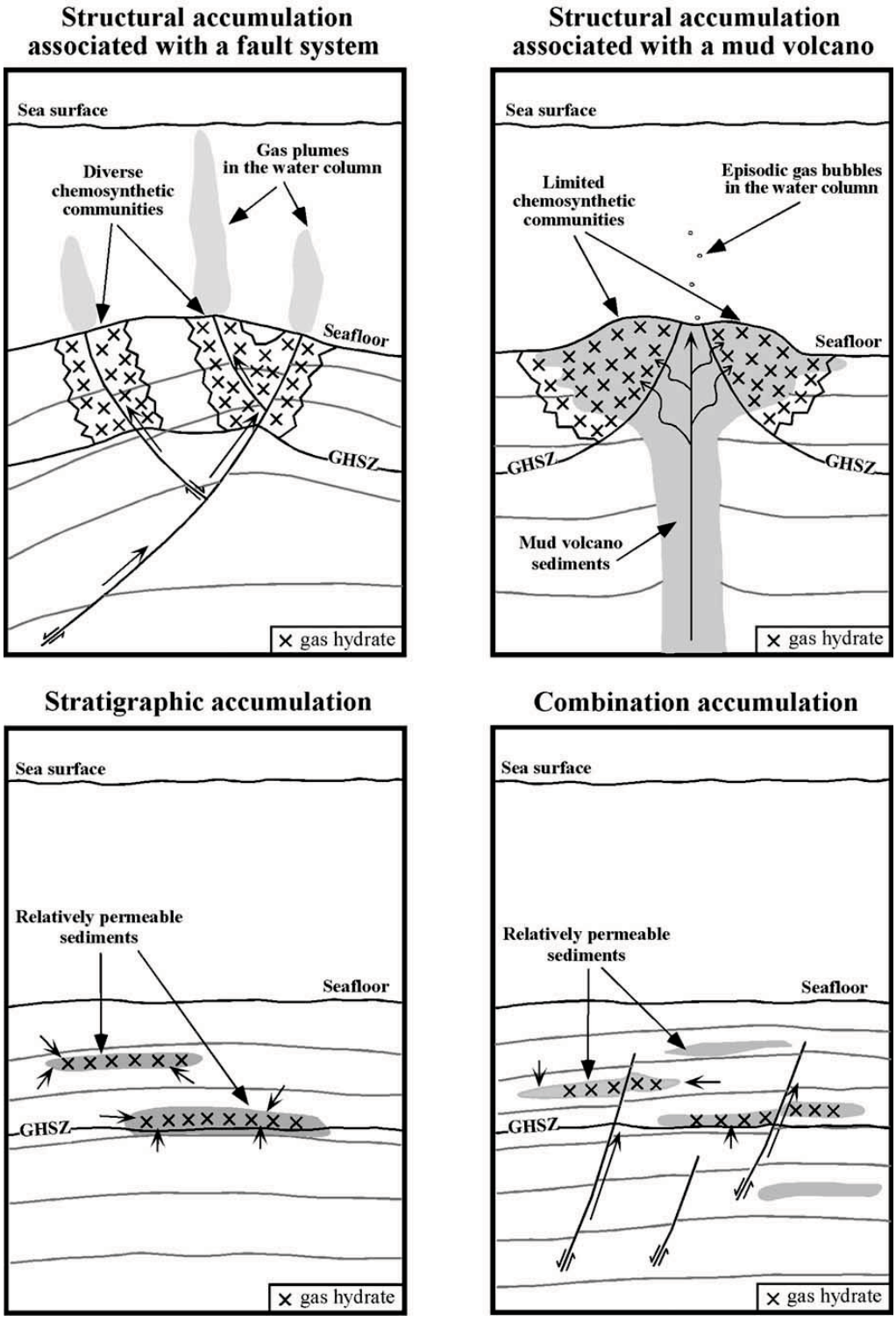

Figure 2.9 Three types of gas hydrate accumulations as described by Milkov and Sassen (2002). The arrows show fluid migration. The x's denote hydrate accumulation.

Structural accumulations form where geological structures such as mud volcanoes and fault systems facilitate rapid fluid flow from depth into the GHSZ such as Hydrate Ridge (Suess et al., 2000) and the Haakon Mosby mud volcano in the Norwegian Sea (Ginsburg et al., 1999). Gas hydrate concentration within the sediments is generally high while gas vents and chemosynthetic communities are common at the seafloor. Methane is the dominant gas in the hydrate lattice.

Stratigraphic accumulations form in relatively permeable strata where either bacterial gas is generated in situ or where gas slowly accumulates as it rises from great depths such as the Blake Ridge (Paull et al., 2000) and the Gulf of Mexico minibasins (Milkov and Sassen, 2002). In these accumulations, gas hydrate forms well below the seafloor, localised in coarse-grained sediments and in low concentrations throughout the GHSZ.

Combined accumulations have both structural and stratigraphic elements with varied ratios and are believed to occur in the Caspian Sea and Nankai Trough (Milkov and Sassen, 2002). In general, combined accumulations occur within relatively permeable strata but the gas is supplied from depth rather than generated in situ.

2.3.5 Bottom Simulating Reflection (BSR)

The acoustic impedance contrast between hydrate-bearing sediment and the underlying, gas-charged sediments produces a feature called a Bottom Simulating Reflection (BSR) on seismic sections (Shipley et al., 1979; Hyndman and Spence, 1992; MacKay et al., 1994). The presence of a BSR is currently the main indicator of gas hydrates in the marine environment. They were first identified at Blake Ridge by Tucholke et al. (1977) who discovered that: 1) the reflection largely parallels the seafloor and cuts across bedding planes; 2) the reflection is phase-reversed relative to the seafloor reflection; and 3) the depth of the BSR increases with increasing

seafloor depth and decreasing water-bottom temperature (Figure 2.10). The BSR can be obscured in areas where the stratigraphic reflections lie parallel to the seafloor or where strong seafloor multiples occur.

The BSR is interpreted to denote the base of the gas hydrate stability zone (BGHSZ) above which gas hydrate formation is possible. In marine environments, a free gas layer often forms beneath the gas hydrate as at ODP Site 889 (Westbrook et al., 1994; Singh and Minshull, 1994). A number of scientific boreholes drilled during the past 10 years have confirmed that the BSR is closely related to the BGHSZ (Tréhu et al., 2004; Riedel et al., 2006; Torres et al., 2008).

Tucholke et al. (1977) also discovered that the BSRs of Blake Outer Ridge and offshore New Jersey occur in a specific structural framework unlike the rest of the continental slope. At those locations, bedding planes containing the gas hydrates dip in a direction opposite to the dip of overlying beds, forming traps for gas accumulation and the formation of gas hydrate. Structural controls have also been discovered to play a role by Andreassen et al. (2003) at the Storegga Slide area on the mid-Norwegian continental slope. The authors discovered that gas hydrate and BSRs are confined to the Naust Formation and that the areal extent of the gas hydrate is constrained by regional faulting as well as local sediment characteristics (e.g. specific pore spacing, water content and sediment grain size).

Gas hydrates also occur in areas without a BSR such as Blake Ridge (ODP leg 164, Holbrook et al., 1996) and the Gulf of Mexico (Zhang et al., 2011). In the case of diagenetic BSRs formed by opal A to opal CT conversion, BSRs can also occur in areas without hydrate such as the mid-Norwegian margin (Berndt et al., 2004). Because of such occurrences, the use of the BSR as the primary gas hydrate indicator is undergoing reassessment. A recent report by Hydrate Energy International (HEI) calculated the volume of gas in-place in hydrate-bearing

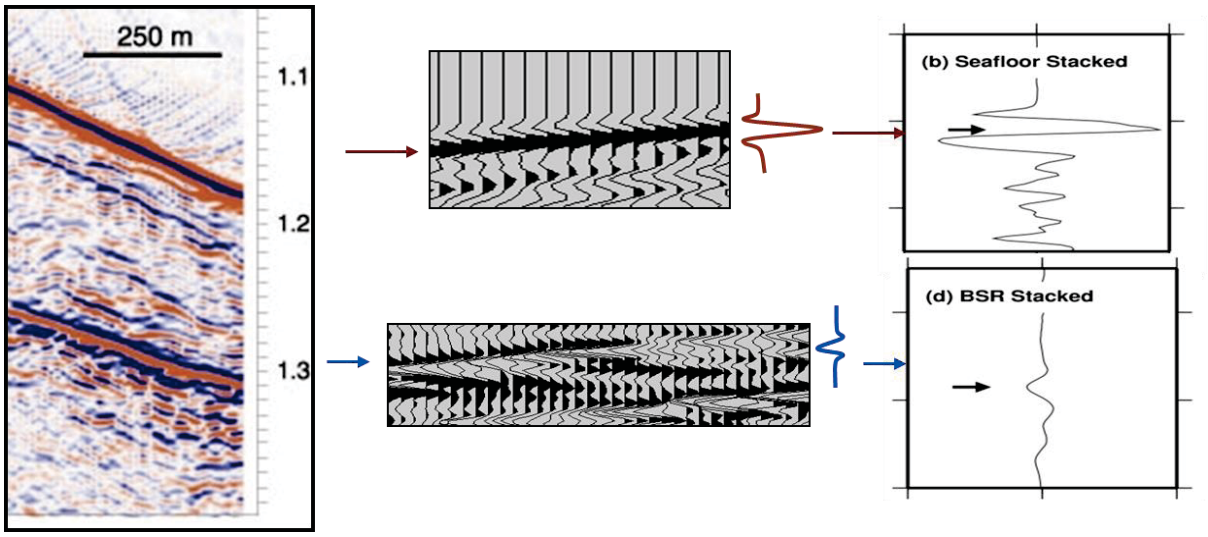

Figure 2.10 Properties of a bottom-simulating reflection (BSR). The BSR typically has phase-reversed reflection relative to the seafloor reflection, and runs parallel to the seafloor. The amplitude of the BSR is usually less than that of the seafloor reflection.

sands using a petroleum systems approach (Johnson, 2011). Johnson (2011) noted that "high grade gas hydrate deposits are best viewed as an extension of conventional petroleum system, and a petroleum systems approach is essential for a valid assessment of hydrate resource potential". This approach combined with advances in seismic data analysis may reduce the influence of the BSR in gas hydrate assessment in the future.

2.3.6 Acoustic Properties

The change from the gas phase to the gas hydrate phase causes changes in physical properties of the host sediment such as velocity and density. This results in an impedance increase and a corresponding strong reflection coefficient. In shallow unconsolidated sediments, the presence of gas hydrates increase the sediment P-wave velocity from the expected values of 1600-1800 m/s while the presence of free gas can significantly reduce the sediment P-wave

velocities. As little as 1-3 % free gas in sediments can reduce normal sediment velocity to as low as 1200 m/s, a value less than the average seismic velocity of seawater at ~1500 m/s (e.g. MacKay et al., 1994).

Studies involving the forward modelling and inversion of seismic reflection data have been carried out since the 1990's by researchers such as Hyndman and Spence (1992) and Yuan et al. (1996). Those papers and associated work used a combination of BSR reflection coefficients, waveform modelling, and amplitude versus offset (AVO) characteristics to determine velocity variations above and below BSRs. Sites drilled by the Ocean Drilling Program (ODP) contributed physical information on sediment types and their porosity values. Subsequent concurrent downhole logging and vertical seismic profiling (VSP) at ODP sites showed that in some cases there were low velocities immediately below the BSR which implied the presence of free gas.

Hyndman and Spence (1992) used porosity-depth models based on physical data which in turn increased the accuracy of their velocity models. They used multi-channel seismic (MCS) data to explore a BSR on the northern Cascadia subduction zone and determined a 10 - 30 m thick high-velocity layer with a maximum value of 2300 m/s occurred above the BSR. The authors did not find evidence for the presence of free gas below the BSR. Yuan et al. (1996) conducted detailed semblance velocity analysis and full waveform inversion of the MCS data over ODP Site 889/890 (offshore Vancouver Island) using a no-hydrate reference velocity-depth profile for accretionary prism sediments. Results showed an increase in velocity above the BSR to ~1900 m/s and a drop in velocity to ~1600 m/s immediately below the BSR. The reference velocity at the BSR depth was 1650 m/s ± 50 m/s.

The first confirmed seismic detection of gas hydrates using velocity analysis alone was reported by Hornbach et al. (2003). The authors used multi-channel seismic reflection data from the Blake Ridge area (Line R22 crossing ODP sites 994/995/997 on Leg 164) and performed detailed velocity picking of the data to delineate the areas of differing velocities along the seismic profiles. They discovered a lens with P-wave velocity significantly higher (1920 m/s) than that of the surrounding sediments (1820-1850 m/s). Individual bright spots, believed to be caused by the concentration of hydrates in one location, had P-wave velocities as high as 2100 m/s. The authors specifically stated that the accurate estimation of gas hydrates using seismic data depended on very detailed velocity information developed for that area.

LeBlanc et al. (2007) carried out similar work on the central Scotian margin. Detailed velocity analyses were carried out on three ocean-bottom seismometer (OBS) datasets (acquired in 2002) which contained both reflection and refraction information. A comparison with 2D single channel seismic data showed that the OBS data could identify the BSR as well as distinguish the high and low velocity zones typically present above and below the BSR respectively. LeBlanc et al. (2007) found a high velocity zone above the BSR with a velocity increase of 70 – 130 m/s and a low velocity zone below the BSR with a velocity decrease of 50 – 75 m/s on data on OBS I (Figure 2.11).

2.4 Previous Work in the Study Area

Concurrent work by other researchers provided results during the course of this study that were incorporated into the overall interpretations developed in this thesis. Figure 2.11 shows the locations of the contributing datasets.

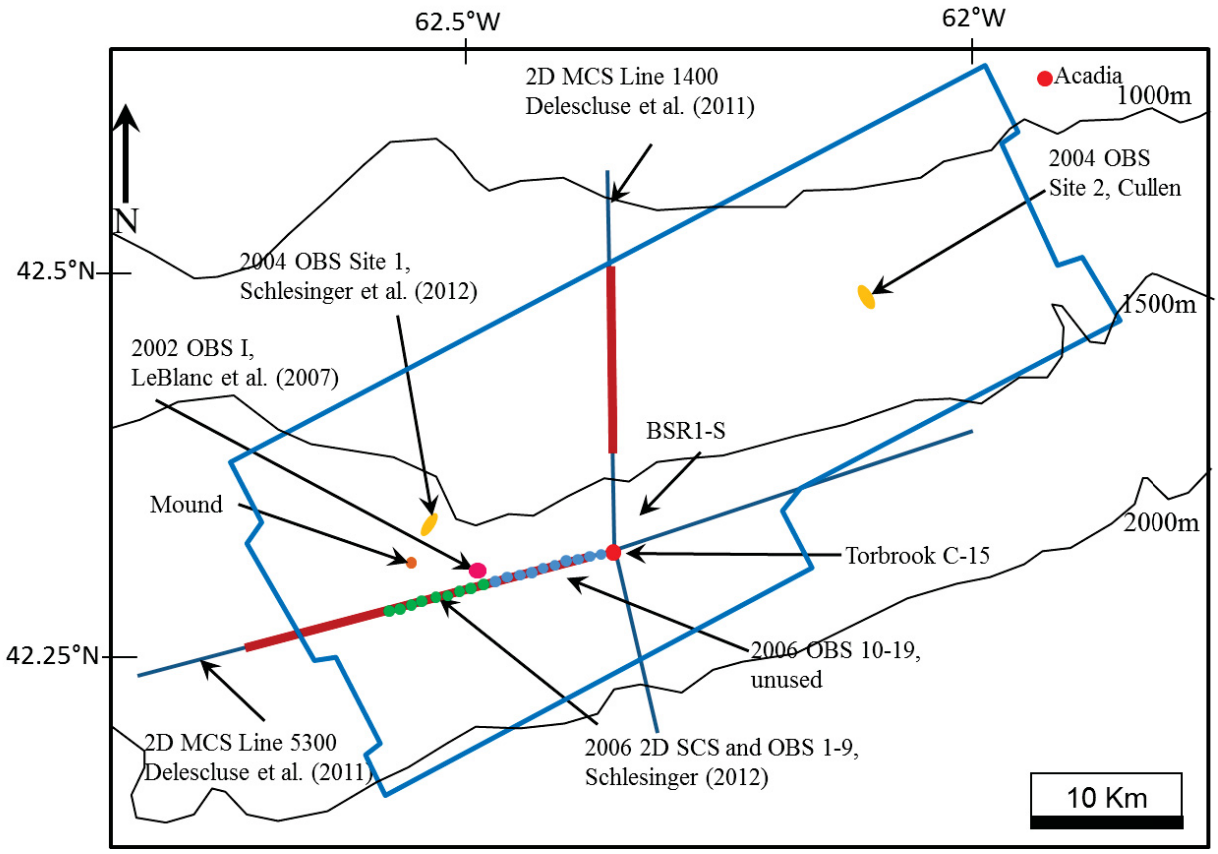

Figure 2.11 Locations of velocity models developed within the Torbrook study area (blue polygon). 2004 OBS Sites 1 and 2 from this study are marked by orange ovals. LeBlanc et al. (2007) OBS I is marked by a pink circle. Delescluse et al. (2011) completed frequency domain 2D waveform tomography on regional 2D MCS data (blue lines). The areas showing a velocity response interpreted as gas hydrates are marked on the regional lines in red. Schlesinger et al. (2012) completed simultaneous travel-time inversion of 2004 Site 1 and 2006 OBS data (green dots)., and 2D SCS data in the west of the study area. The blue dots on the regional line mark 10 OBS locations without velocity models. The Torbrook and Acadia wells are marked with red dots and the Torbrook seafloor mound is marked with an orange dot.

OBS data acquired in 2002 was sparsely distributed and located away from the area of the strongest BSR response later identified in 3D MCS data. The first velocity model in the Torbrook study area was constructed by LeBlanc et al. (2007) from the 2002 OBS data.

In 2004, a linear array of 10 OBS units with ~ 100 m spacing was dropped in two locations: Site 1 - over the area of the strongest BSR response to further examine the acoustic

properties of gas hydrates in the Mohican Channel area, and Site 2 - in an area without a BSR visible on available seismic datasets (Figure 2.11). The 2004 OBS data is the focus of this study.

In 2006, a set of 20 OBS units were dropped in a linear array, with ~ 1 km separation (Figure 2.11). That array began in the west of the study area, over the strong BSR response, and stretched eastwards, into an area without a strong BSR response, in an attempt to determine if the edge of the gas hydrate could be detected using velocity models from OBS datasets. Only 10 units (to the west) had useable data for the study, the remaining 10 units (to the east) proved too noisy to pick reflections and refractions for the velocity models. Schlesinger (2012) instead conducted simultaneous time travel inversion of 2004 and 2006 OBS data and 2D single-channel data, and addressed the question of whether the BSR is a good indicator of significant gas hydrate on the Scotian margin. New constraints on gas hydrate and free gas concentrations in the sediments were provided by that study (Schlesinger et al., 2012 in Appendix C).

Delescluse et al. (2011) conducted 2D waveform tomography on 2D regional long-streamer MCS data acquired over the study area on the Scotian Slope. The waveform velocity model revealed a high-velocity layer at ~ 300 m below the seafloor, interpreted as gas hydrates, imaged in areas where a BSR was not visible in the seismic reflection data. Line 5300, running EW, has a velocity drop of ~ 200 m/s that clearly corresponds to the visible BSR. Of particular interest is that this low-velocity zone continues eastwards, past the area of the visible BSR (Figure 2.12). Line 1400, running NS, crosses Line 5300 close to the Torbrook C-15 well. Line 1400, located in an area without a visible BSR on seismic reflection data, shows similar velocity variations as Line 5300 with the low velocity zone decreasing seawards (Figure 2.13). The study by Delescluse et al. (2012) provided new constraints on the location of gas hydrates within the study area.

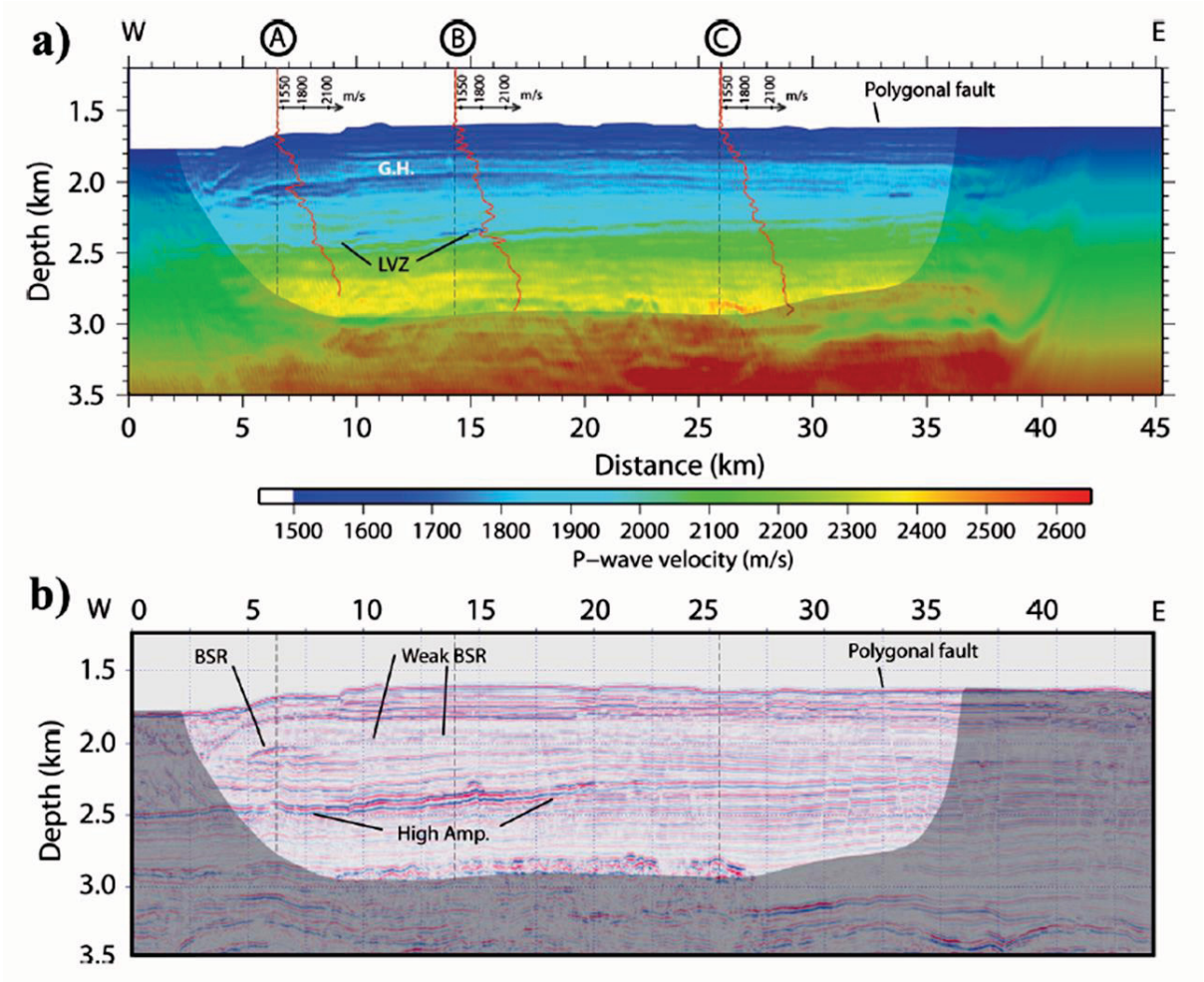

Figure 2.12 a) Waveform tomography velocity model for GXT line 5300. (b) The prestack depth-migrated reflection image for comparison. The BSR is visible at 2-km depth between distances of 5–8 km. Red curves on a) show velocity versus depth at three specific locations (A, B, and C). Position C is the crossing point with profile 1400 (Figure 2.13). Shaded areas are not covered by the refracted rays recorded on the 9-km-long streamer. G.H. indicates the gas-hydrates layer (high velocity) below which low-velocity free gas is trapped. Figure 10 from Delescluse et al. (2011).

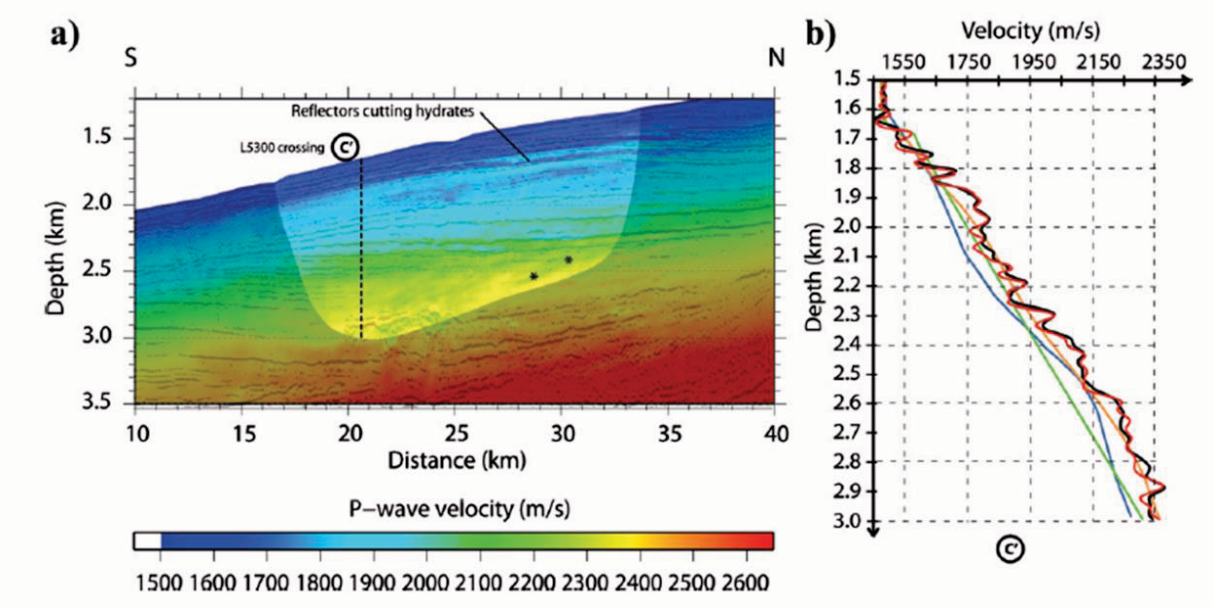

Figure 2.13 a) Waveform tomography velocity model for GXT line 1400 superimposed on the pre-stack depth-migrated reflection image. Shaded areas are not covered by the refracted rays recorded on the 9-km-long streamer. (b) Velocity at the crossing point C with line 5300. The NMO (blue), migration (green), traveltime tomography (orange), and waveform tomography velocities for lines 1400 (black) and 5300 (red) are displayed. Note the excellent agreement between the waveform inversion models at the crossing point. Figure 12 from Delescluse et al. (2011).

CHAPTER 3 DATA AND METHODS

Five datasets were available in the study area (Figure 3.1): 1) pre-stack time-migrated industry 3D multi-channel seismic (MCS) reflection data volume; 2) wide angle reflection and refraction data acquired with ocean bottom seismometers in 2004 (OBS); 3) GSC(A) single channel seismic reflection data; 4) GSC(A) piston cores; 5) multibeam bathymetry.

3.1 INDUSTRY 3D MCS DATA

The pre-stack time-migrated 3D seismic data volume from EnCana, known as the Torbrook survey, covers an area approximately 1,500 km^2 on the central Scotian Slope in water depths of 1,250 – 2,000 m. These data were acquired in June to August 2000 by the vessel Geco Prakla. The seismic system consisted of six 6 km-long multi-channel streamers with 25 m group intervals and 240 channels per streamer. Streamer separation was 100 m and streamer tow depth was 8 – 9 m. The airgun source consisted of an array of pneumatic guns with a total volume of 63.5 litres. Two arrays were towed at 6 m depth and fired in flip-flop mode with 50 m shot intervals. This configuration resulted in 60-fold data and a bin spacing of 12.5 x 25 m.

The received raw signals were filtered at 3 to 180 Hz before being digitally sampled at 2 ms. Pre-stack processing of the data cube by EnCana included spherical divergence compensation, FK filtering, spiking deconvolution, resampling to 4 ms, velocity analyses, multiple attenuation, binning to 12.5 x 12.5 m grid, and time migration.

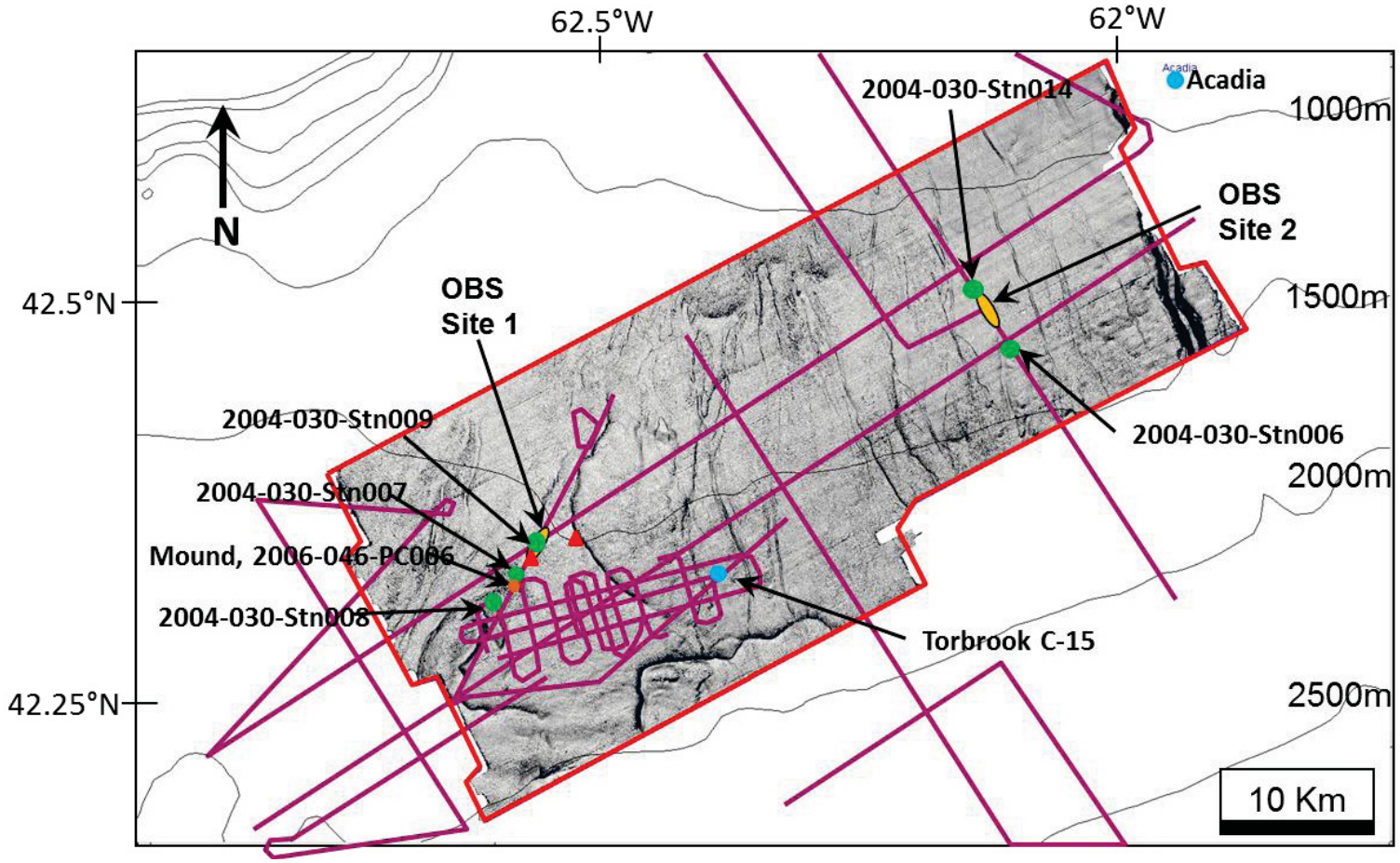

Figure 3.1 Dataset Locations. The red polygon marks the extent of the Torbrook 3D MCS dataset, the seafloor is shown inset. Seafloor bathymetry contours are labelled on the right. The two OBS sites are marked with golden ovals. Purple lines show the location of the GSC 2D single channel seismic reflection data used in this study. The green dots mark the core locations analysed in the east and west of the study area. The location of the seafloor mound is shown using an orange dot in the west. The Torbrook and Acadia wells are shown using blue dots. Red triangles mark the 2004 heat flow positions.

3.1.1 Horizon Picking

Horizons of interest were picked using the SMT Kingdom Suite™ software. Every 10th inline and crossline was manually picked through the 3D data volume to provide seed-picks for automatic picking. Horizon picking errors of +/- 4 ms are estimated based on the sampling rate of the data.

An automatic picking program called 3D Hunt filled the horizon between the seed picks. Due to small offsets in horizon characteristics caused by widespread faulting, small polygons were used to run the hunt systematically through the volume. The program used three rounds of intelligent iteration which began with the seed points and expanded outwards to fill gaps. The mean smoothing operator was 5 inlines x 5 crosslines in size. The hunt was allowed to continue over faults. The data were then gridded to fill gaps in the horizon and jumps between faults. Gridding was computed from the input data and unconstrained, that is it used only the parameters of the input horizon to make the new grid. The algorithm of choice was flex gridding as its solution causes the interpolated surface to pass through, or very close to, the source data (Figure 3.2). The final grid is output in Amplitudes (Time). Both grids and horizons were then examined in SMT Kingdom Suite™ 3D visualisation package (VuPak) as surface renders.

3.1.2 Attribute Analysis

Two main volume attributes were used to examine the 3D Torbrook Block MCS dataset:

1) Amplitude: Data amplitudes were examined using filters and by selectively displaying specific amplitude ranges. Such methods were useful for identifying features such as high negative and positive amplitude areas relative to the background amplitudes, which could indicate gas-charged sediments for example (Figure 3.3).

2) ‘Similarity’ and ‘Dip of Maximum Similarity’: The ‘similarity’ and ‘dip of maximum similarity’ volumes proved the most useful for identifying structural features in the 3D seismic dataset in close detail (Fig 3.4). The dip of maximum similarity volume was generated in conjunction with the similarity volume. The programme scanned adjacent traces with continuously running time windows and dip directions for each output trace, and then computed the similarity value in each direction. Smoothing was optional but the resulting attributes can contain smoothed information from adjacent traces.

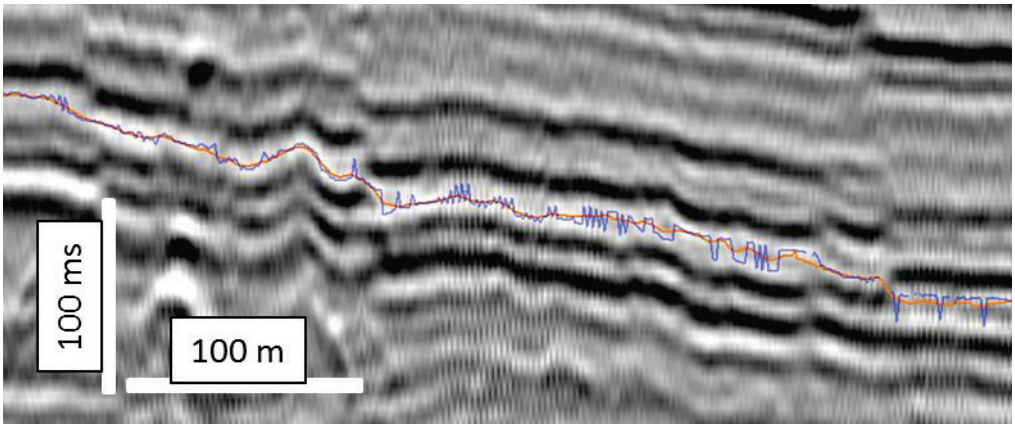

Figure 3.2 The result of automatic picking program 3D Hunt is shown in blue. The smoothed pick used for all attribute analyses is shown in orange.

3.1.3 Time – Depth Conversion of Horizons

A time - depth table was constructed from simplified OBS velocity models and the Torbrook C-15 checkshot data (Table 3.1). It was used to convert all picked horizons from time to depth and vice versa. The water velocity used for depth conversion of the seafloor pick came from a CTD profile, described in section 3.4.2.3.

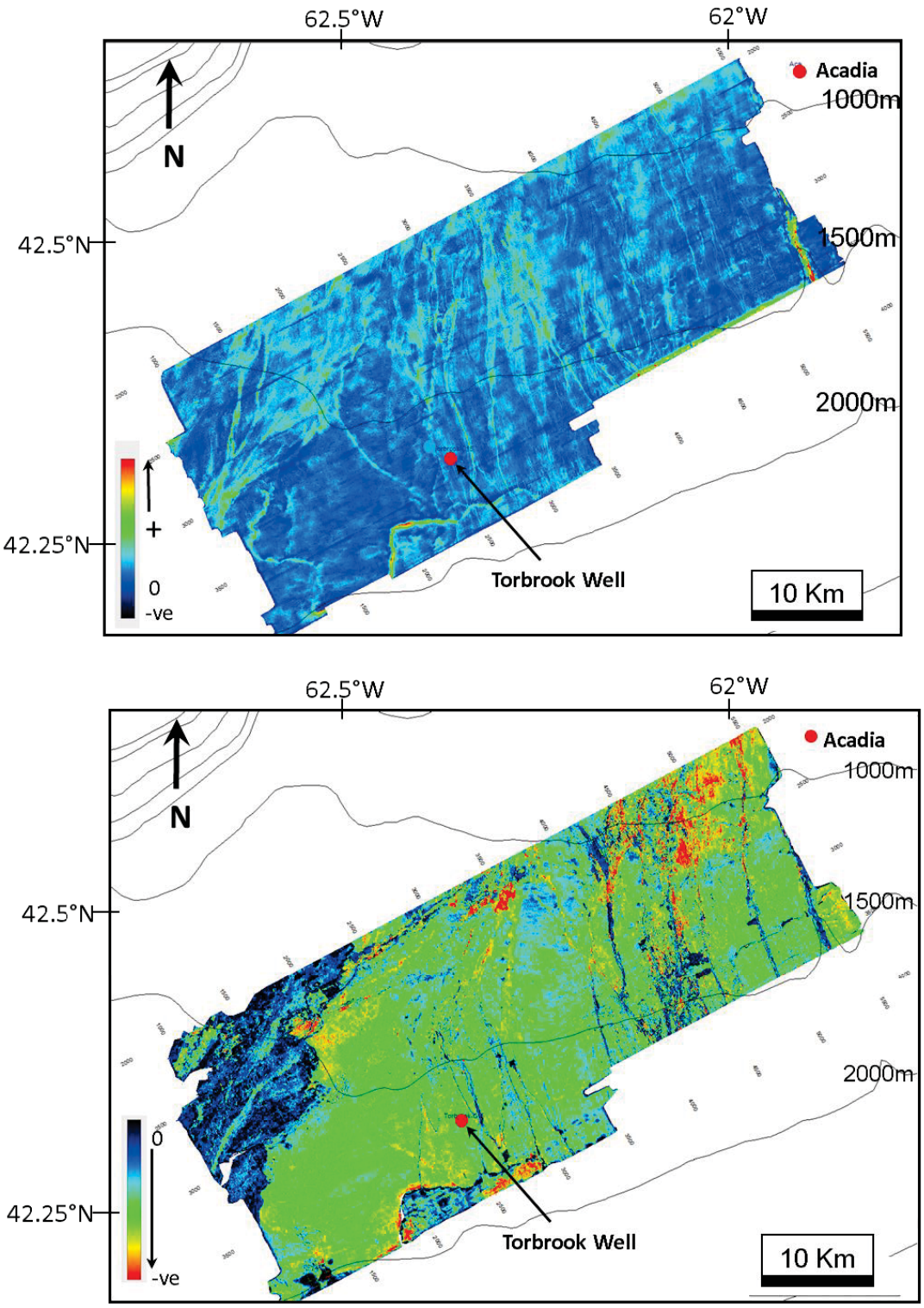

Figure 3.3 Amplitudes shown on picked horizons in the 3D MCS dataset. Top: Seafloor horizon showing the full range of amplitudes; Bottom: Horizon 2 showing negative amplitudes only. See chapter 5 for descriptions of these horizons. Seafloor contours are on both plots.

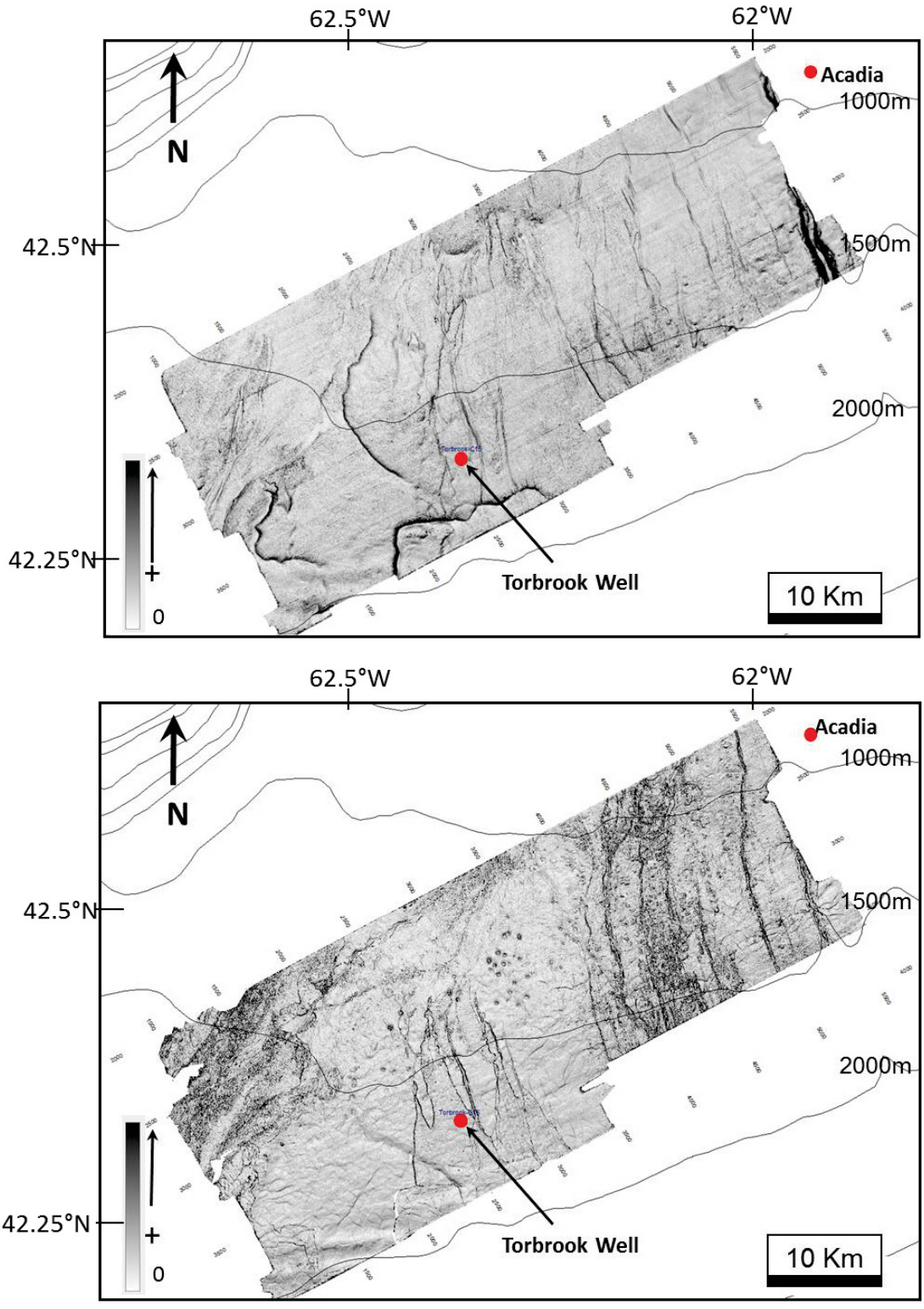

Figure 3.4 Dip of maximum similarity shown on picked horizons in the 3D MCS dataset. Top: Seafloor horizon; Bottom: Horizon 2. See chapter 5 for descriptions of these horizons. Seafloor contours are on both plots.

Depth below seafloor (m)	Travel time from the seafloor (ms)
380	450
810	1060
930	1185
1050	1300
1150	1400
1250	1485
1315	1562
1400	1650
1490	1690

Table 3.1 A simplified time-depth table used to convert all picked horizons.

3.1.4 Modeling the Base of the Gas Hydrate Stability Zone

The model for the base of the gas hydrate stability zone was developed using the method outlined in Leon et al. (2009). Geothermal gradients were derived from measurements taken during a 2004 cruise in the Mohican Channel area (CCGS Hudson cruise 2004 -030) (Figure 3.1). The bottom seawater temperature is assumed to be constant at 3.7 ° C and the geothermal gradient is assumed to be constant at 31.5 mK/m. A geothermal gradient of 37.6 mK/m was recorded adjacent to a large mound on the seafloor where warm fluids are believed to be moving through the chimney from depth (Figure 3.1). However, the lower value of 31.5 mK/m measured away from the mound is believed to be more applicable throughout the study area.

Functions I and IV from Leon et al. (2009) were rearranged and Newton's method used to calculate the depth of the base of the gas hydrate stability zone.

$$T_{BHSZ} = (\ln D_{BHSZ} - 5.2398) \,/\, 0.12061$$ (Function I, biogenic gas, Leon et al., 2009)

where D_{BHSZ} = Depth in metres of the base of the gas hydrate stability zone

and T_{BHSZ} = temperature in °C at the base of the gas hydrate stability zone.

$$T_{BHSZ} = T_{SEAFLOOR} + (D_{BHSZ} - D_{SEAFLOOR})\delta_g$$ (Function IV, Leon et al., 2009)

where $T_{SEAFLOOR}$= Temperature on the seafloor (constant for this model at 3.7°C), $D_{SEAFLOOR}$ = seafloor depth (from the seafloor horizon picked throughout the Torbrook block), and δ_g = geothermal gradient (constant for this model at 31.5 mK/m)

The equations above were rearranged to give:

$$T_{BHSZ} = (\ln D_{BHSZ} - 5.2398) / 0.12061 = T_{SEAFLOOR} + (D_{BHSZ} - D_{SEAFLOOR})\delta_g$$

$$T_{BHSZ} = (\ln D_{BHSZ} - 5.2398) / 0.12061 = T_{SEAFLOOR} + (\delta_g * D_{BHSZ}) - (\delta_g * D_{SEAFLOOR})$$

$$\left(\ln D_{BHSZ} - 5.2398\right) = 0.12061 * \left(T_{SEAFLOOR} + \left(\delta_g * D_{BHSZ}\right) - (\delta_g * D_{SEAFLOOR})\right)$$

$$(\ln D_{BHSZ} - 5.2398) = (0.12061 * T_{SEAFLOOR}) + \left(0.12061\left(\delta_g * D_{BHSZ}\right)\right) - \left(0.12061(\delta_g * D_{SEAFLOOR})\right)$$

The following values were substituted, $T_{SEAFLOOR}$ = 3.7°C, $\delta_g = 0.0315°C/m$, to give:

$$(\ln D_{BHSZ} - 5.2398) = (0.446) + (0.0038 * D_{BHSZ}) - (0.0038 * D_{SEAFLOOR})$$

$$\text{Function F(n)} = -\ln D_{BHSZ} + 5.2398 + (0.446) + (0.0038 * D_{BHSZ}) - (0.0038 * D_{SEAFLOOR})$$

$$\text{Function F(n)} = -ln\, D_{BHSZ} + (0.0038 * D_{BHSZ}) - (0.0038 * D_{SEAFLOOR}) + (0.446 + 5.2398)$$

$$\text{Function F(n)} = -ln\, D_{BHSZ} + (0.0038 * D_{BHSZ}) - (0.0038 * D_{SEAFLOOR}) + (5.686)$$

The derivative of a natural log = 1/number, therefore the derivative of the function F'(n) = $(1/D_{BHSZ}) + 0.0038$

Using Newtons Method Equations where:

D_0 = seafloor + 320 m (estimated depth of BHSZ below seafloor according to observations, and using time-depth conversion outlined in section 3.4.2.3)

Dn+1 = Dn - [F(Dn) / F'(Dn)]

The final function solves as:

$$D_1 = D_0 - \frac{\left((-\ln D_0) + (0.0038 * D_0) - \left(0.0038 * D_{seafloor}\right) + 5.686\right)}{((1/D_0) + 0.0038)}$$

This final function is run until the output value converges.

3.2 2D Single Channel Data

The Geological Survey of Canada (Atlantic) has acquired a large volume of 2D high-resolution single channel data for a variety of projects along the Canadian east coast margin over the past number of decades. The single channel data shot over the study site in 2004 (CCGS Hudson cruise 2004-030) used a 61 m streamer with six groups of 16 hydrophones (Figure 3.5). The signals from the active groups in the streamer were summed into a single channel. A GI gun array with two 3.4 L units operated in harmonic mode were used as the seismic source for both reflection lines and refraction (OBS) acquisition. Seismic gun firing rate was 6 - 8 s when firing on time and 16 – 20 m when firing on distance. The received signals were digitized with a maximum sample interval of 250 ms. Processing consisted of bandpass filtering, gain recovery and F-K time migration.

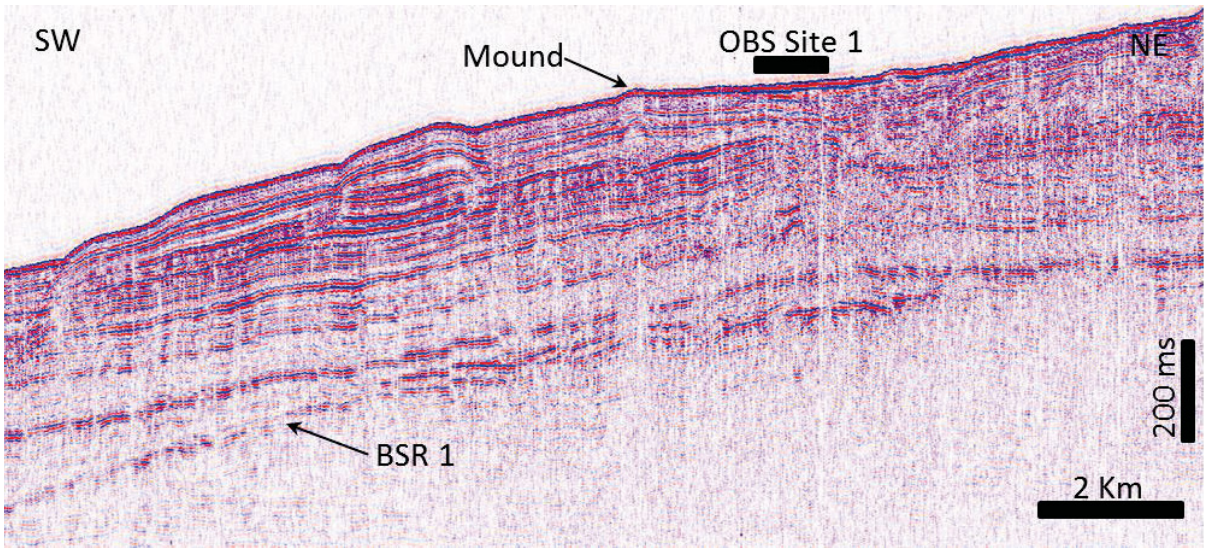

Figure 3.5 Example of the filtered 2D SCS reflection profile available in the study area.

3.3 Core Data

Six cores taken during two separate research cruises were analysed for this study. Five cores from CCGS Hudson cruise 2004-030 and one core from CCGS Hudson cruise 2006-046 provided information on gas composition in the east and west of the study area (Figure 3.6). One circular feature was identified on the seafloor in an area close to OBS Site 1 (Figure 3.1). Core Site 2006-046-PC006 sampled a seafloor mound approximately 10 m high which is found above one of the rare faults to reach the seafloor in the study area. The mound was cored to a depth of 10 m. Subsamples were taken from the piston cores as soon as the core samples were onboard and stored in a refrigerated container until interstitial gas concentration analyses could be completed. Head gas analysis was carried out by TDI Brooks International. The core expanded upon recovery to the surface due to gas expansion when the core was removed from its in-situ pressure condition. This expansion resulted in cracking of the sediment and liberation of free gas.

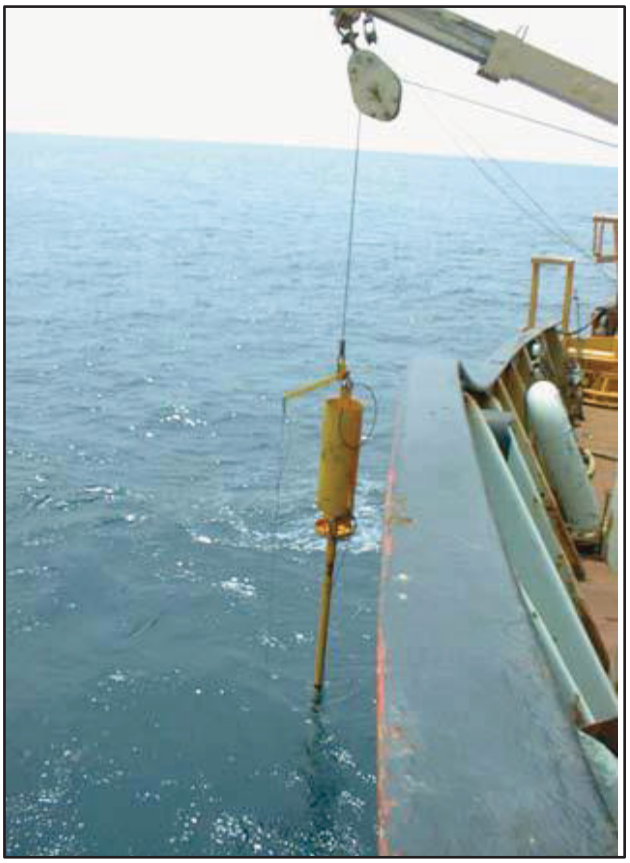

Figure 3.6 Piston Core unit ready for deployment on the CCGS Hudson 2004-030 cruise

3.4 Ocean Bottom Seismometer Data

Wide angle reflection and refraction data were recorded by a total of 20 ocean bottom seismometers (OBS) for this project. Two sets of 10 units with approximate spacing of 100 m were deployed over two specific sites in the study area during the Hudson 2004-030 cruise (Fig. 3.1). Both OBS drop sites are within the 3D Torbrook block and have similar stratigraphy, but Site 1 has a strong BSR response while Site 2 shows no BSR response in industry seismic reflection data.

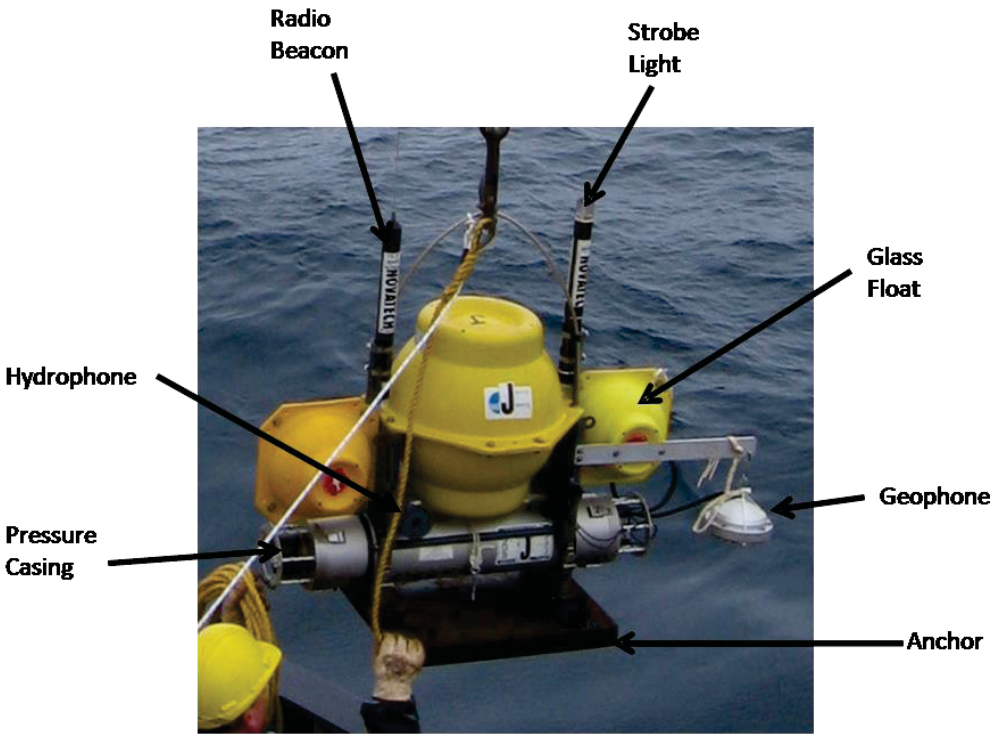

Figure 3.7 Modified Dalhousie University OBS with an externally mounted geophone used in the CCGS Hudson 2004-030 cruise.

3.4.1 OBS Description

The digital OBS units used in this study were a modified Dalhousie University model developed and supplied by Dalhousie University Dept. of Oceanography, and the GSC(A). Each OBS consists of an 82 kg platform carrying three pressurised floats as well as an external 4.5 Hz hydrophone, a pressure casing, strobe light, and radio beacon (Fig. 3.7). The modified OBS unit had the 3-component geophone moved from an internal position to an external position which isolated the geophone from ringing and other noise created by reverberations of the unit body and improved coupling with the seafloor. The pressure casing holds the battery pack which provides power for up to 30 days and a data logger with fixed length files stored on a 1 Gb hard drive. The

unit is attached to a 55 kg steel anchor which remains behind on the seafloor after the survey is complete.

Dalhousie OBS units are deployed by crane from a ship, released at the sea surface, and sink to rest on the seafloor to a maximum water depth of 6 km. Signals received on each OBS unit by a hydrophone and a 3-component geophone are digitized at a sample rate of 558 Hz and recorded to hard drive. The geophone package is mounted to an external arm by a corrodible release which drops the geophone onto the seafloor sediments approximately 10 minutes after settling into position. The geophone usually couples well with the seafloor sediment. A 12.5 kHz acoustic command sent to the OBS triggers its release from the anchor and it floats to the surface. A timed backup release command is in place should the acoustic command fail. Timing comes from a Seascan precision clock with a drift of less than one millisecond per day. An attached strobe light and radio beacon are used to locate the unit for retrieval. Upon retrieval, OBS data are downloaded to a PC and burned to DVDs for storage. The survey sound source consisted of a two 3.4L G.I. gun array at Site 1 and one 3.4L G.I. gun at Site 2. Shot times were triggered by GPS positioning to enable shooting on a 20 m distance interval. Firing times were logged by a GPS clock.

3.4.2 OBS Data Preparation

A number of steps are required to determine the final location of the instruments on the seafloor, which is necessary for accurate velocity model building. The data preparation steps are outlined in Figure 3.8.

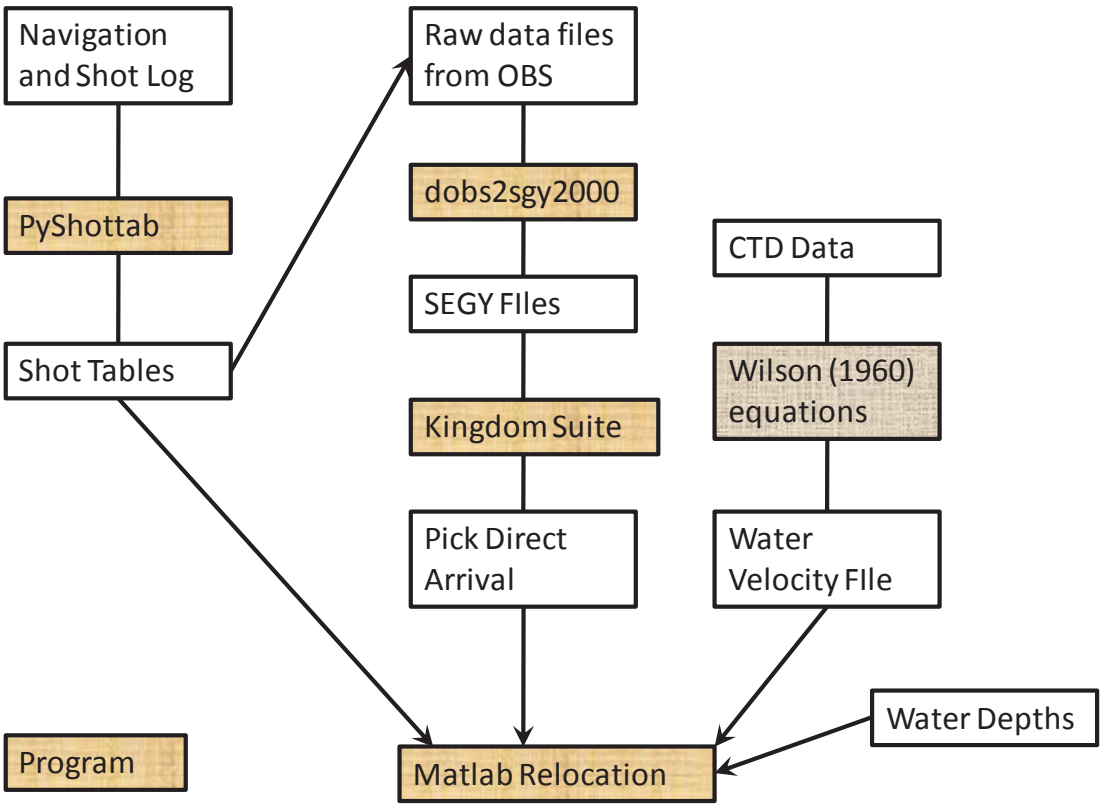

Figure 3.8 A flow chart showing the steps necessary to reach the stage of instrument relocation. Yellow rectangles denote programs used while the brown rectangle denotes a set of sound equations used to derive the water velocity file.

3.4.2.1 Shot Table and SEGY File Creation

The PyShottab program is a shot table creator written in Python and run in MS Windows. It was created by D. LeBlanc and C. LeBlanc at Dalhousie University in 2002 and used in this study to make shot tables for relocation of the OBS. The navigation data from differential GPS provide the shot positions. The shot logs were trimmed to restrict the shot range to within 12 km of the OBS as data beyond this range generally does not provide useful seismic data for this type of study. The trimmed shot logs and the ships navigation logs were then combined to provide a shot table with latitude and longitude positions.

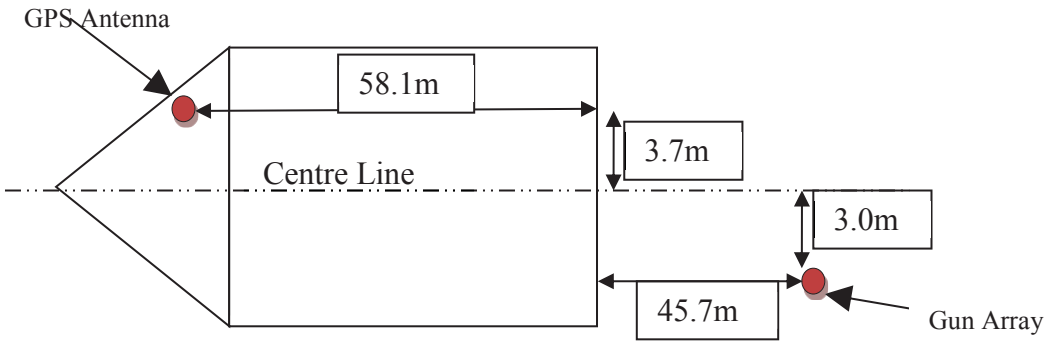

Figure 3.9 A schematic showing the physical positions of the GPS antenna and the seismic gun array relative to the center line of the CCGS Hudson.

The CCGS Hudson has a unique shooting system setup as the ships GPS antenna is set to the right (starboard) of the ships central line while the guns used in the survey were towed from the left (port) side, again off the ships central line (Fig. 3.9). Therefore the guns and the GPS antenna are on opposite sides of the ship. The program PyShottab provides the opportunity to account for this geometry and values shown in Figure 3.9 were used. In this case a total of (3.7 m + 3.0 m =) 6.7 m was used as the shot offset position to the right and (58.1 m + 45.7 m =) 103.8 m was used as the shot offset position to the rear.

On all lines, shot times were triggered by the ships GPS position in order to shoot by distance interval (every 20 m) and logged by the ships GPS clock in order to record exact firing times. Times logged in the shot table were taken from the clock time break (CTB) output of the Real Time Systems Long Shot™ seismic source controller. These times are the aim point shot times with a 50 ms delay following the trigger.

The program dobs2sgy2000 was used to convert the OBS raw data files to SEGY files for further processing. This program is run in MS Windows also and outputs SEGY files in Vista format (little endian (intel/amd), IEEE (ascii) encoded header, and (short) integer formatted data)

which can be read by the Claritas™ processing software. At least 8 seconds of data are required in order to include the refracted arrivals necessary for ray tracing in later steps.

3.4.2.2 Direct Arrival Picking

Once the SEGY files are created, the data are imported into SMT Kingdom Suite™ for direct arrival picking, which defines the actual travel times from the shot to the OBS. The SEGY files are debiased for display purposes. Picking is completed on the hydrophone data which is usually the clearest of the data types. Filtering is not used at this stage. Missing traces are infilled to prevent any processing problems at later stages. An example of a direct arrival pick is shown in Figure 3.10. The picks are exported from SMT Kingdom Suite™ as a Geoquest data file which is then converted to an xy file for input into the relocation program.

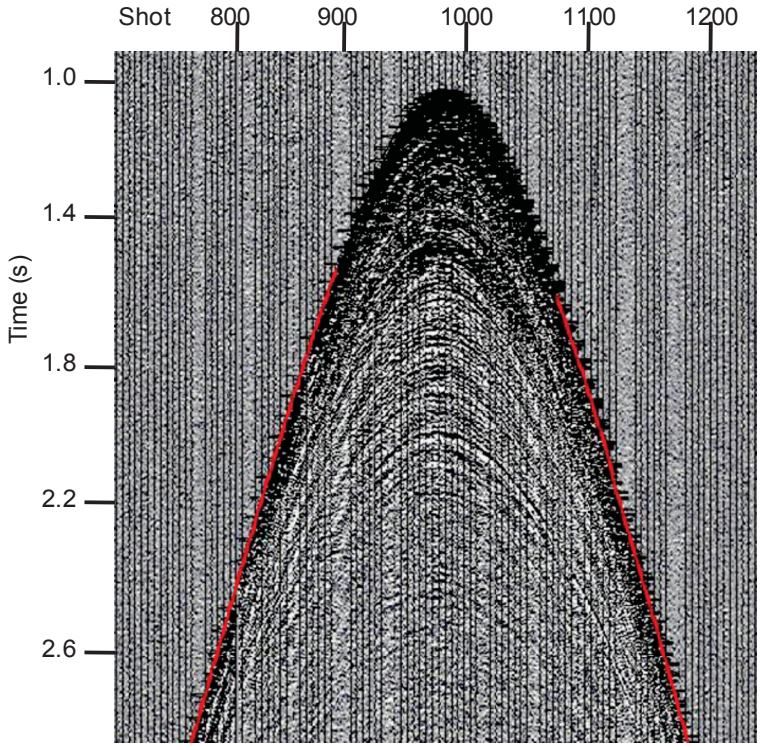

Figure 3.10 An example of direct arrival picking on debiased unfiltered hydrophone data. The manual pick is shown in red.

3.4.2.3 Water Velocity Profile

A Seabird 19 CTD (Conductivity, Temperature and Depth) instrument recorded data at OBS Site 1 during the CGGS Hudson 2004-030 cruise. The recorded bottom water temperature was 3.7 °C at water depths of 1,520 – 1,540 m. The CTD data were processed to derive a velocity profile of the water column in the study area which was used to convert the seafloor depth into seafloor travel times. CTD data conversion to sound velocity required the use of equations developed by Wilson (1960). Although alternative equations are available (DelGrosso, 1974; Medwin, 1975; MacKenzie, 1981; See Appendix E), testing showed that differences in output were negligible (<1%) for this project (Table 3.2), and so the method used by previous researchers in this area (LeBlanc et al., 2007) was retained.

Wilson (1960) initially measured the speed of sound in sea water by timing the duration required for a sound pulse to travel a known distance through a range of salinities and pressures (depth). About 99.5 % of all seawater falls in the temperature range of -4˚C<T<+30˚C, the pressure range 1.033 kg/cm^2<P<1000 kg/ cm^2, and the salinity range 0‰<S<37‰.

$$V = 1449.14 + \Delta V_T + \Delta V_P + \Delta V_S + \Delta V_{STP}$$

where T = temperature °C; P = hydrostatic pressure, kg/cm^2; S = salinity, parts per thousand.

$$\Delta V_T = 4.5721\,T - 4.4532\,x\,10^{-2}T^2 - 2.6045\,x\,10^{-4}T^3 + 7.9854\,x\,10^{-6}T^4$$

$$\Delta V_P = 1.60272 \text{ x } 10^{-1}\,P + 1.0268 \text{ x } 10^{-5}P^2 + 3.5216 \text{ x } 10^{-9}\,P^3 - 3.3603 \text{ x } 10^{-12}P^4$$

$$\Delta V_S = 1.39799\,(S - 35) - 1.69202 \text{ x } 10^{-3}\,(S - 35)^2$$

$$\begin{aligned}\Delta V_{STP} = (S - 35)(&-1.1244 \text{ x } 10^{-2}T + 7.7711 \text{ x } 10^{-7}T^2 + 7.7016 \text{ x } 10^{-5}P \\ &- 1.2943 \text{ x } 10^{-7}P^2 + 3.1580 \text{ x } 10^{-8}\,PT + 1.5790 \text{ x } 10^{-9}PT^2) \\ &+ P(-1.8607 \text{ x } 10^{-4}T + 7.4812 \text{ x } 10^{-6}T^2 + 4.5283 \text{ x } 10^{-8}T^3) \\ &+ P^2(-2.5294 \text{ x } 10^{-7}T + 1.8563 \text{ x } 10^{-9}T^2) - P^3 \text{x } 1.9646 \text{ x } 10^{-10}T\end{aligned}$$

These are the equations used to convert the CTD data into a water column velocity file for the study area as shown in Figure 3.11.

Depth m	Temp °C	Salinity PSU	Pressure bar	Pressure kPa	Pressure kg/cm2	Wilson 1960	DelGrosso 1974*	Medwin 1975	MacKenzie 1981
4.12	15.65	32.39	0.4146	41.46	0.42	1506.15	1505.75	1510.65	1505.71
47.04	6.10	36.64	4.7334	473.34	4.83	1478.27	1477.89	1477.28	1477.92
97.11	8.95	33.69	9.7719	977.19	9.96	1486.23	1485.94	1489.20	1485.93
147.17	11.49	35.02	14.8104	1481.04	15.10	1497.93	1497.50	1498.94	1497.51
194.56	9.63	35.29	19.579	1957.9	19.97	1492.37	1491.99	1493.09	1492.00
243.74	9.48	35.19	24.5275	2452.75	25.01	1492.48	1492.13	1493.33	1492.14
292.02	7.58	35.12	29.3861	2938.61	29.97	1486.01	1485.73	1487.04	1485.75
342.09	6.03	35.12	34.4245	3442.45	35.10	1480.70	1480.51	1481.81	1480.51
391.26	5.76	34.94	39.373	3937.3	40.15	1480.17	1480.00	1481.52	1480.01
439.54	5.38	34.93	44.2315	4423.15	45.10	1479.37	1479.25	1480.76	1479.25
512.85	4.93	34.91	51.6091	5160.91	52.63	1478.70	1478.60	1480.11	1478.61
559.34	4.81	34.97	56.2876	5628.76	57.40	1479.06	1478.94	1480.39	1478.99
607.62	4.67	35.00	61.146	6114.6	62.35	1479.31	1479.20	1480.58	1479.25
655.01	4.61	34.91	65.9144	6591.44	67.21	1479.69	1479.61	1481.09	1479.66
701.50	4.57	34.92	70.5929	7059.29	71.98	1480.27	1480.22	1481.65	1480.25
749.78	4.47	34.98	75.4512	7545.12	76.94	1480.72	1480.68	1482.02	1480.72
798.06	4.35	34.97	80.3096	8030.96	81.89	1480.98	1480.96	1482.29	1481.00
845.44	4.25	34.95	85.0779	8507.79	86.76	1481.31	1481.30	1482.64	1481.35
891.04	4.17	34.99	89.6663	8966.63	91.43	1481.82	1481.81	1483.06	1481.87
938.42	4.11	35.02	94.4347	9443.47	96.30	1482.35	1482.34	1483.56	1482.42
1007.26	4.04	34.96	101.3622	10136.22	103.36	1483.09	1483.10	1484.35	1483.18
1057.33	3.99	34.94	106.4004	10640.04	108.50	1483.69	1483.69	1484.97	1483.81
1102.03	3.97	34.92	110.8988	11089.88	113.09	1484.29	1484.32	1485.58	1484.42
1147.63	3.95	34.94	115.4871	11548.71	117.76	1484.99	1485.02	1486.25	1485.14
1195.01	3.93	34.94	120.2553	12025.53	122.63	1485.67	1485.72	1486.92	1485.84
1240.60	3.89	34.97	124.8436	12484.36	127.31	1486.28	1486.34	1487.47	1486.47
1309.44	3.85	34.95	131.771	13177.1	134.37	1487.19	1487.29	1488.39	1487.41
1356.83	3.82	34.92	136.5392	13653.92	139.23	1487.84	1487.91	1489.06	1488.07
1400.63	3.81	34.95	140.9475	14094.75	143.73	1488.51	1488.64	1489.67	1488.76
1442.65	3.78	34.91	145.1758	14517.58	148.04	1489.02	1489.16	1490.23	1489.30
1489.14	3.76	34.93	149.854	14985.4	152.81	1489.73	1489.87	1490.89	1490.02
1532.05	3.72	34.94	154.1723	15417.23	157.21	1490.27	1490.43	1491.41	1490.58

Table 3.2 A section of the dataset tested using a variety of sound velocity equations. The data points have approximately 50 m depth separation. All four equations in Appendix E produced similar results.

3.4.2.4 Water Depths

Water depths in the study area were extracted from the GSC(A) multibeam data. A short script extracts the water depth for given latitude and longitude for both the drop and retrieval coordinates (Table 3.3). Both the drop and retrieval location water depths are then used in the relocation program.

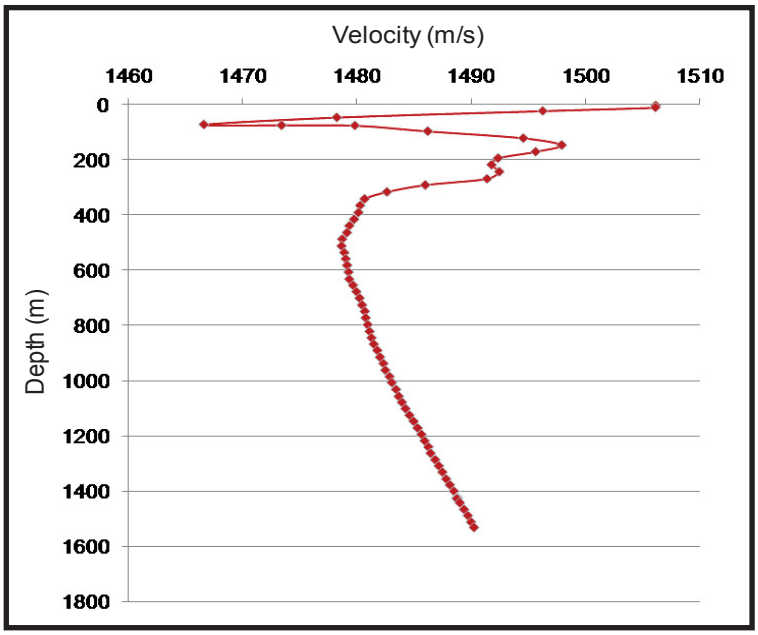

Figure 3.11 A graph of the water velocity profile for the Mohican Channel study area using data acquired during the CCGS Hudson 2004-030 cruise. Vertical sample spacing is ~ 25 m.

3.4.3 OBS Relocation

After the OBS are deployed at the sea surface, they sink to the seafloor. During sinking, they are subject to ocean currents which cause a lateral drift from their original deployment position. Knowing the actual positions of the instruments on the seafloor is fundamental to OBS wide angle reflection and refraction analyses. The ray tracing method used to develop velocity models depends on the position of each shot relative to the OBS. OBS relocation is affected by the position of the seismic guns on the sea surface as it is necessary to accurately detect the direct

SITE 1	drop latitude	drop longitude	drop water depth (m)	retrieval latitude	retrieval longitude	retrieval water depth (m)
OBS 1	42.579420	-62.449940	1544	42.580685	-62.454422	1546
OBS 2	42.580230	-62.449350	1544	42.581262	-62.453535	1545
OBS 3	42.581060	-62.448680	1543	42.582853	-62.451585	1544
OBS 4	42.581840	-62.448020	1542	42.584962	-62.451230	1543
OBS 5	42.582710	-62.447500	1541	42.588142	-62.447950	1540
OBS 6	42.583380	-62.446940	1541	42.590822	-62.448907	1536
OBS 7	42.584220	-62.446290	1540	42.585905	-62.448748	1542
OBS 8	42.584990	-62.445850	1539	42.591452	-62.450117	1537
OBS 9	42.585790	-62.445370	1539	42.589080	-62.447732	1540
OBS 10	42.586590	-62.444530	1538	42.584962	-62.450970	1543
SITE 2						
OBS 1	42.731443	-62.078895	1225	42.731200	-62.079782	1226
OBS 2	42.730750	-62.078335	1228	42.729847	-62.079212	1231
OBS 3	42.729938	-62.077717	1231	42.729415	-62.078162	1233
OBS 4	42.729090	-62.077185	1235	42.726310	-62.077522	1244
OBS 5	42.728437	-62.076548	1237	42.728507	-62.077340	1237
OBS 6	42.727540	-62.075948	1240	42.727735	-62.076203	1239
OBS 7	42.726702	-62.075275	1243	42.728440	-62.079377	1236
OBS 8	42.725922	-62.074680	1246	42.725535	-62.076505	1247
OBS 9	42.725260	-62.074025	1248	42.725053	-62.075823	1249
OBS 10	42.724418	-62.075708	1251	42.723738	-62.075708	1254

Table 3.3 OBS drop and retrieval locations and water depths extracted from a GSC(A) multibeam survey for those locations. The values were input to the relocation method.

arrival of shots from the seismic guns to the instruments from multiple shots and different directions. A MatLab™ relocation program (Wu, PhD Thesis, 2007) was used to determine these absolute positions of the OBS on the seafloor. The program helps minimise the discrepancy between the observed and calculated direct arrival travel times.

Two assumptions are made for repositioning the OBS. The first assumption is that the OBS clock is correct and functioned throughout the survey period. The second assumption is that the water depth is constant around the deployment position. Fortunately the study area is relatively flat and water depth does not vary significantly at the scale of positional uncertainty as shown in the multibeam data provided by GSC(A). Clock calibration calculations are described in Appendix D.

The actual travel times from the OBS to all shots are recorded in the OBS data as direct travel times, which were picked in SMT Kingdom Suite™ as described above (Figure 3.10). The detailed water velocity profile described above (Figure 3.11) was used to convert the seafloor depth into seafloor travel times. The relocation program searches for one point on the seabed where the travel times from that point to all the shots and the direct travel times have the smallest root mean square (RMS) residual i.e. smallest offset in ms between observed and calculated travel times. For a 2D survey, there may be two points with the smallest RMS error located on the seafloor. These will be conjugate points on either side of the shooting line and both locations can provide the correct distance for all seismic traces along the 2D survey line. In this case, it is up to the processor, using information such as the position of the OBS recovery, to choose which point is most likely. The program outputs a plot onscreen with all the relocation information.

Drift rate and direction were consistent at both sites. Average instrument drift at Site 1 was 54 m in a north-northwesterly direction with average RMS error of 39 ms. Average instrument drift at Site 2 was 91 m in a southwesterly direction with average RMS error of 23 ms. Table 3.4 shows the relocated positions and water depths for all 20 OBS in the survey area.

SITE 1	Relocated latitude	Relocated longitude	Relocated water depth (m)	Instrument Drift (m)	RMS error (ms)
OBS 1	42.5798	-62.4505	1547	67	37
OBS 2	42.5805	-62.4498	1535	47	40
OBS 3	42.5813	-62.4490	1543	42	43
OBS 4	42.5822	-62.4483	1542	47	42
OBS 5	42.5830	-62.4482	1542	63	33
OBS 6	42.5837	-62.4474	1541	53	41
OBS 7	42.5845	-62.4467	1540	42	41
OBS 8	42.5854	-62.4464	1540	67	37
OBS 9	42.5862	-62.4459	1539	60	40
OBS 10	42.5870	-62.4450	1538	53	36
		average	**1540**	**54**	**39**
SITE 2	**Relocated latitude**	**Relocated longitude**	**Relocated water depth (m)**	**Instrument Drift (m)**	**RMS error (ms)**
OBS 1	42.731046	-62.079878	1226	92	28
OBS 2	42.730395	-62.079012	1229	68	20
OBS 3	42.729496	-62.078762	1232	99	25
OBS 4	42.728649	-62.078291	1235	103	28
OBS 5	42.727905	-62.077533	1238	100	22
OBS 6	42.727007	-62.076872	1241	96	22
OBS 7	42.726482	-62.075950	1243	60	19
OBS 8	42.725658	-62.075478	1246	72	21
OBS 9	42.724638	-62.075072	1250	110	26
OBS 10	42.723751	-62.074494	1253	110	25
		average	**1239**	**91**	**23**

Table 3.4 Table showing relocated latitude, longitude and water depth for each OBS in the study area. Drift and error results are also included for each instrument.

3.4.4 OBS Travel Time Inversion

This section introduces the algorithm developed by Zelt and others (see below) which was used to complete seismic travel time inversion on the OBS geophone data. This method produces valuable subsurface velocity information relatively inexpensively.

3.4.4.1 Forward Modeling and Inversion

Ray path inversion techniques are used to calculate acoustic raypaths for a given velocity model (Zelt and Ellis, 1988; Zelt and Smith, 1992; Zelt, 1999). These raypaths can be compared with field results such as OBS data to confirm the seismic velocity model resulting from OBS analyses. The model is reiterated to derive a best fit and provide sensitivity analyses.

The program used was Rayinvr version 1.3 designed by C.A. Zelt of the Geological Survey of Canada and released in December 1993. Rayinvr traces rays in 1D and 2D models for rapid forward modelling and inversion of the travel times for reflected and refracted rays. Routines based on ray tracing are currently the most practical choice for interpreting OBS data (Zelt and Ellis, 1988; Zelt and Smith, 1992; Zelt, 1999).

Three types of ray families are used by the program (Figure 3.12): 1) turning or refracting rays within a layer; 2) reflections off the bottom of a layer; 3) head waves along the bottom of a layer. Ray take-off angles are computed for the specified ray groups based on the input source-receiver geometry and host medium velocities. The iterative search mode is based on determining the minimum and maximum take-off angles of ray groups so the traveltime associated with a specific receiver location is determined by linear interpolation across the endpoints of the two closest rays that bracket the point of interest. This approach means that the model needs to be extended slightly beyond the edges of the receiver array to ensure these points are bracketed by rays on either side.

The search mode for the turning rays looks for the take-off angles for the shallowest and deepest rays to turn in a layer. For the reflected rays, it looks for the smallest take-off angle, measured from the horizontal, which reflects off the bottom of a specific model layer. For head waves, it looks for the ray which intersects the bottom of the layer at a critical angle. The

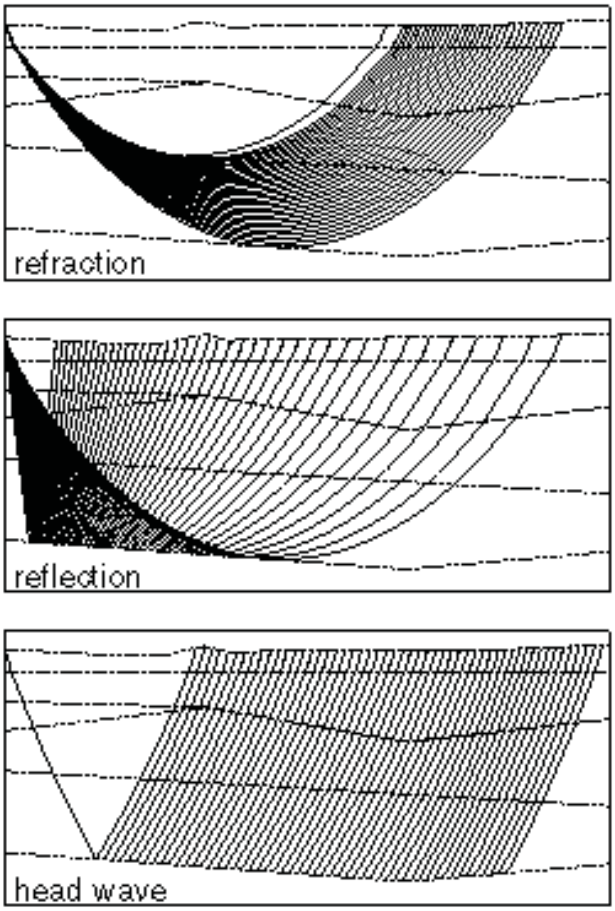

Figure 3.12 The three types of ray families traced by the Rayinvr Program.

maximum number of rays traced is specified by the user. Rays can also be traced upwards for shotpoints located below the model surface. A ray group is defined as a set of rays that have all turning and/or reflection points in the same layer or layers. The number of rays traced in search mode depends on the velocity model i.e. velocity gradients and lateral variation.

3.4.4.2 Data Filtering

The amplitude spectrum of the OBS geophone data showed a spike at 8 Hz on each unit (Figure 3.13). A bandpass filter of 10 – 240 Hz was applied to the data to reduce the influence of the spike and low frequency noise.

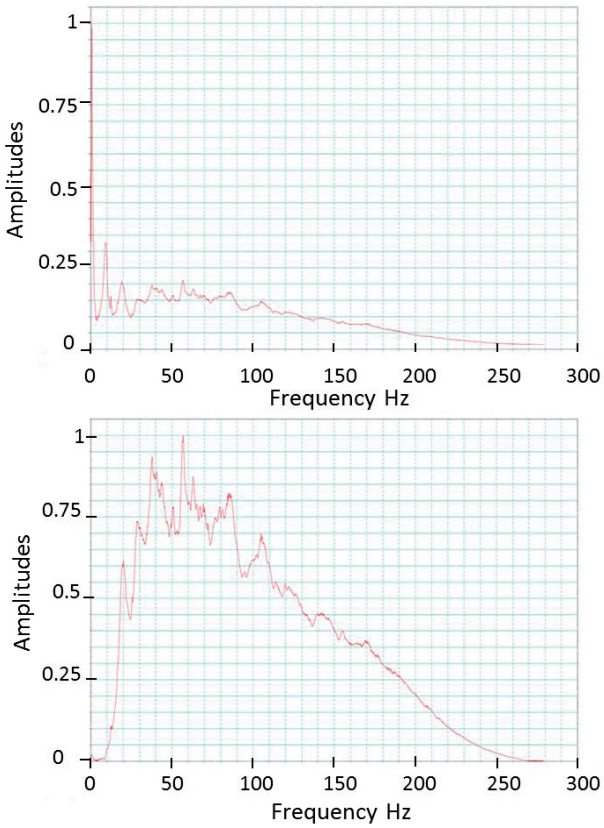

Figure 3.13 An example of the OBS data amplitude spectrum. The top graph shows the unfiltered data with a spike at 8 Hz. Bandpass filter of 10 – 240 Hz removed the low frequency noise (bottom graph).

3.4.4.3 Identification of Reflections and Refractions

Reflected phases were picked on the hydrophone data in SMT Kingdom Suite™ based on strong laterally-continuous reflections which could be traced through each unit and matched to the reflections visible in a seismic profile through the 3D dataset at the drop locations (Fig. 3.14)

Picking was enhanced by using a variety of normal moveout (NMO) water velocity (1500 m/s) / receiver depth pairs to flatten horizons of interest and increase the ease of identification of sub-seafloor reflections (Fig 3.15). Refracted phases were picked using a similar method except the NMO had a linear term (distance/reduction velocity) to flatten the arrivals. Profiles through the 3D dataset showed that deeper sedimentary layers followed the same overall slope as the seafloor and identified pinch-out and faulted layers which could be included in velocity models. It was possible to pick common reflections on all ten units at both sites. At Site 1 however, the visible BSR in the 3D MCS did not correspond to a negative-phase reflection in the OBS data. This picking was necessary for 2D modelling of the site. It was also necessary to have accurate reflected phase picks before modelling refracted phase picks, as the latter are associated with specific layers based on a comparison of velocities and depth. It proved impossible to pick refractions common to each set of OBS, which restricted refraction modelling. A damped least squares iterative inversion was used to design a pseudo-1D velocity model for each OBS that best fit the combined phase picks (Rayinvr software, Zelt 1993). Model adjustments were made using a layer stripping method which inverted one layer (velocity or depth) at a time from the top of the velocity model to the bottom. This method ensured similar lateral velocities and boundary depths were maintained throughout the models.

Model resolution and traveltime fits were constrained by traveltime RMS and normalized chi-squared (χ^2) values calculated for each run of the rayinvr program. Chi-squared (χ^2) is used to determine if the data are well described by a hypothesised function, in this case the velocity model An ideal normalised χ^2 value would be close to 1, its mean value for a “good fit”. A value less than 1 means that that fit was not required by the data or the data was overfit, while a value greater than 1 means that the model underfit the data.

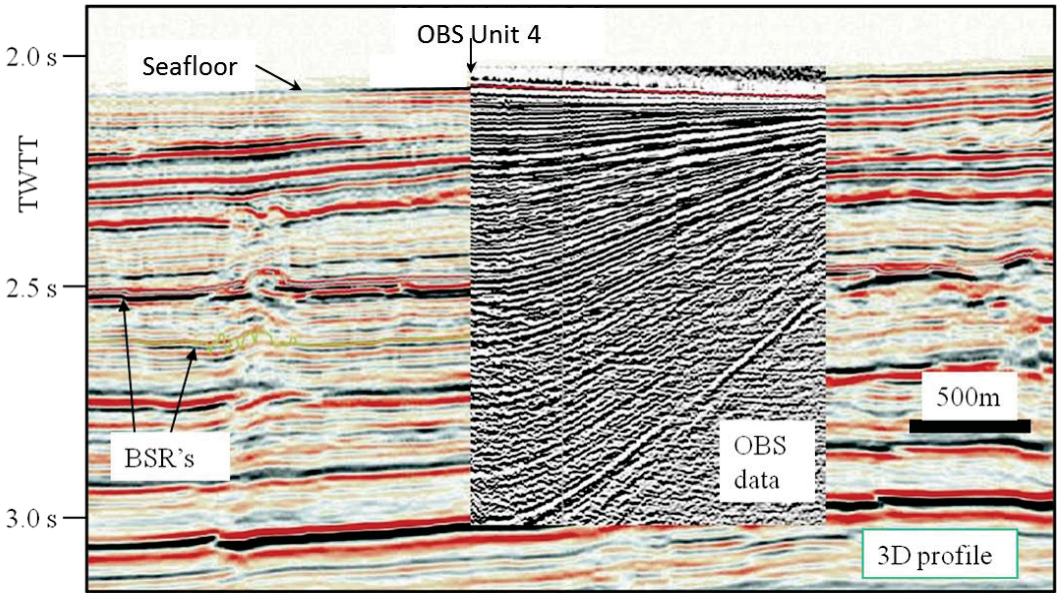

Figure 3.14 Example of data matching between OBS data (grey scale plot) and a 3D seismic reflection profile (coloured plot) at Site 1. The seafloor and a prominent reflection at ~3.0 s twtt are identifiable in both datasets and mark the top and base of useable reflections present in the Site 1 OBS data. The BSR in the 3D seismic reflection profile does not correspond to a strong negative-phase reflection in the OBS data.

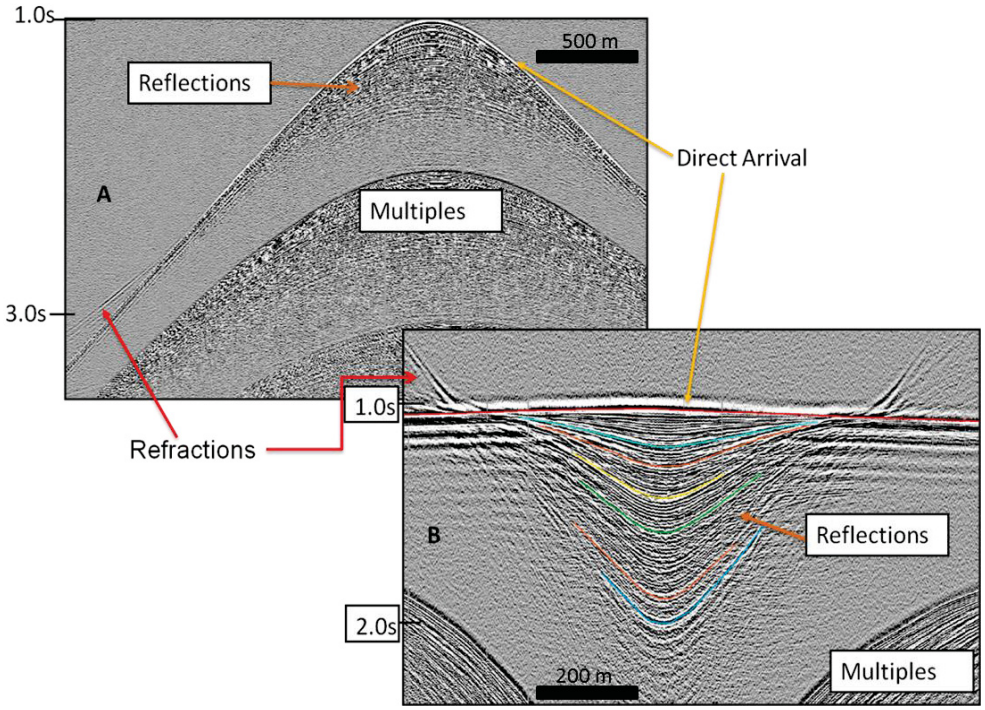

Figure 3.15 A: An example of OBS data ready for horizon picking. B: An example of OBS data flattening on the seafloor showing the direct arrival (red line) and a series of reflections (various colours). Strong multiples limit the depth of useful horizons.

CHAPTER 4 MODEL RESULTS

The chapter focuses on two modeling exercises completed: 1) 1D velocity models developed from the OBS datasets, and 2) modeling of the base of the gas hydrate stability zone using theoretical principles. This section also describes gas volume calculations made using results from both the 1D modeling and the area of the interpreted BSR in the Mohican Channel area.

4.1 1D Velocity Model Results from OBS Data

4.1.1 Introduction

This section describes the differences observed in the velocity models developed for OBS Site 1 with a visible BSR and OBS Site 2 without a visible BSR in the Torbrook area. Further analysis of OBS data available in the area was completed in conjunction with A. Schlesinger of the University of Victoria (2012) and published in 2012 in Marine and Petroleum Geology Journal v. 35, p. 105 – 115 (Appendix C).

A distinctive velocity response would be expected in the model if gas hydrate and free gas are present, that is, the gas hydrate would produce a high velocity zone (HVZ) above while free gas would produce a low velocity zone (LVZ) below. The schematic in Figure 4.1 shows an example of the expected response at OBS Site 1 where the units were dropped over an area with a strong BSR identified in industry seismic reflection data. This response is not expected at OBS Site 2 where no BSR was identified in industry seismic reflection data. In this study, velocity models were derived for all 20 OBS datasets. Data processing began simply by attempting to match one side of the reflections from a particular unit. The complexity of these models increased until processing reached the final stage of two linear arrays of ten velocity models.

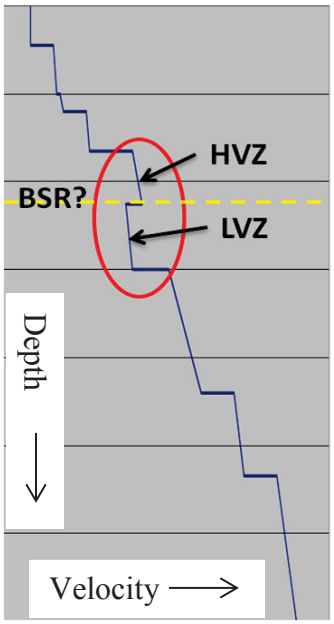

Figure 4.1 A schematic of the acoustic response expected in an area with gas hydrate present above free gas. The gas hydrate would produce a high velocity zone (HVZ) relative to the background velocity while the free gas would produce a low velocity zone (LVZ) relative to the background velocity. The change from HVZ to LVZ is believed to mark the location of the BSR or the base of the GHSZ (yellow dashed line).

4.1.2 Identification of Reflections and Refractions

The OBS data were compared to both the 2D SCS data and profiles extracted from the 3D MCS data for reflection matching. A hyperbolic moveout using the water velocity (1.48 km/s) was applied to "flatten" the seafloor and shallow reflections (Figure 4.2). At OBS Site 1, nine reflections, including the seafloor, were identified which could be picked on all ten OBS units (Figures 4.2 and 4.3). At OBS Site 2, ten reflections, including the seafloor, were identified which could be picked on all ten OBS units (Figures 4.2 and 4.4). Due to varying noise levels in the units, it was not always possible to match both sides of the data. The reflections associated with BSRs 1 and 2 at OBS Site 1 correspond to reflections 6 and 7 on the OBS data (Figure 4.3). No BSR is present at OBS Site 2 but reflection 6 on the OBS Site 2 data marks the correlative stratigraphic position of the BSR when followed from the west to the east (Figure 4.4). Refracted arrivals identified on the data came from 250 – 350 m below the seafloor. Despite the long shot profiles of the survey, no refractions were identified from deeper horizons.

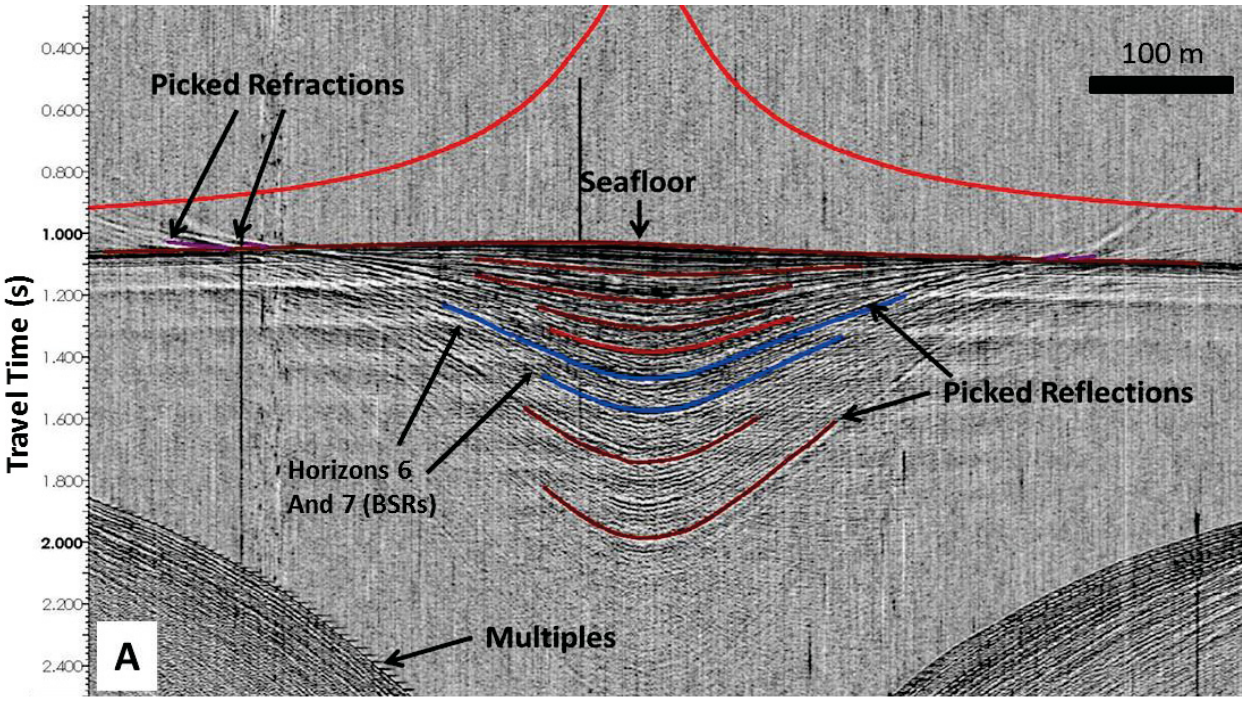

Figure 4.2 Picked reflections and refractions on hydrophone data at OBS Site 1 and Site 2. The data are flattened on the seafloor horizon. Refractions are in purple above the seafloor pick. Multiples are visible at the base of the records. (A) OBS 9 Site 1: The blue horizons (6 and 7) mark the positions of BSR 1 and 2 respectively as identified using 3D seismic profiles. B) OBS 5 Site 2: The yellow horizons (3 and 4) mark the top and base of an MTD, while blue horizon 6 marks the stratigraphic BSR.

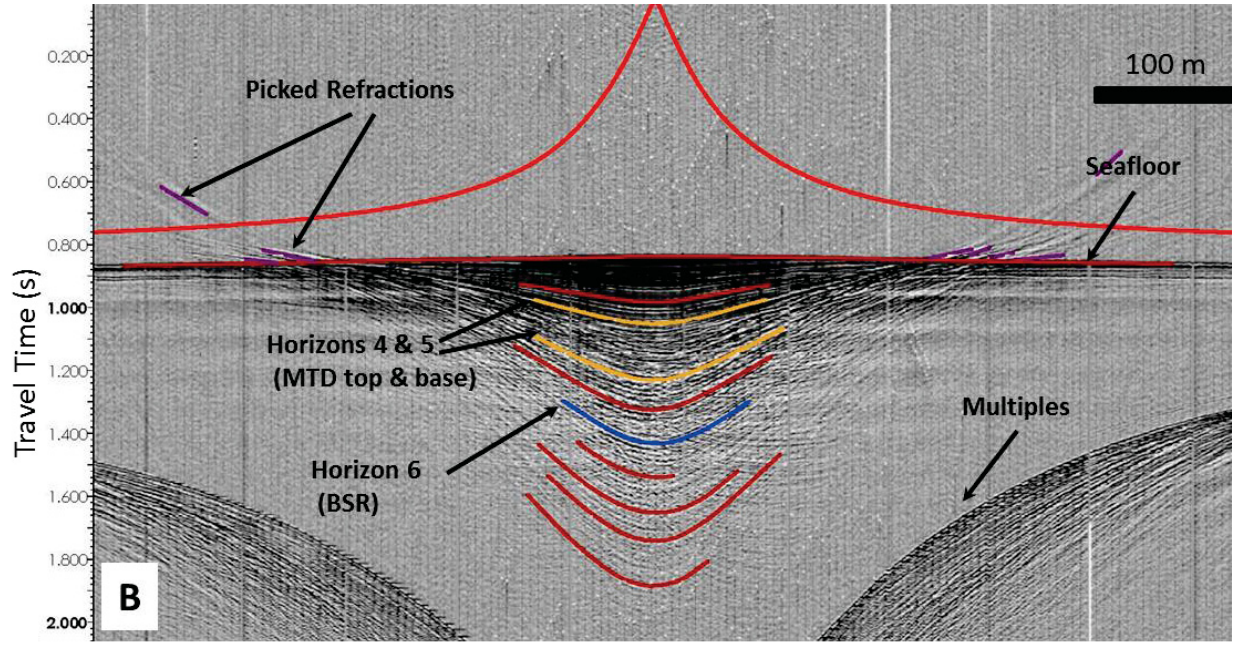

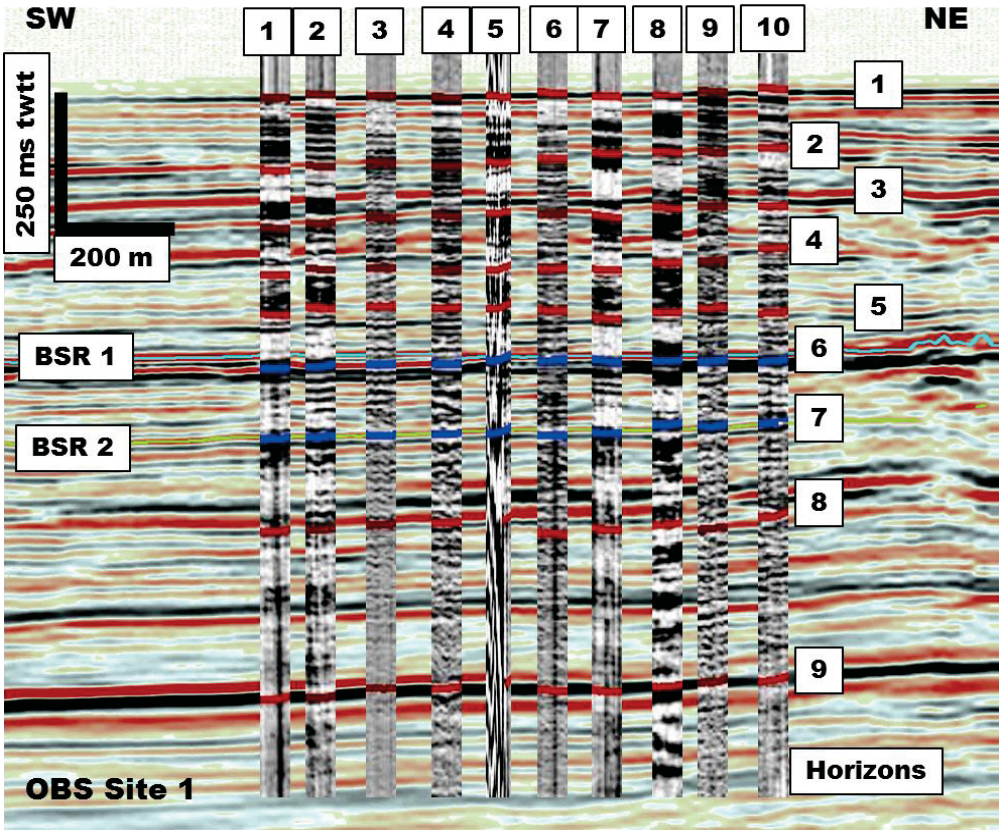

Figure 4.3 Reflections picked on OBS dataset matched to reflections visible in the 3D MCS dataset for OBS Site 1 in the west (see figure 3.1 for location). The blue horizons (6 and 7) on the OBS data mark the locations of BSR 1 and BSR 2 respectively as identified using the 3D seismic data. OBS units are numbered along the top. Horizons are numbered on the right side.

4.1.3 1D Velocity Model Results

Due to the sloping seafloor at both OBS sites and the tilted subsurface reflections underneath, modelling began on one side of the OBS and extended to the second side where possible. A series of reflections common to all ten OBS at each site were picked in SMT Kingdom Suite™ during the processing steps described in Chapter 3. Using the Rayinvr program, a model was developed for each OBS to fit the picked velocities and depths. An example of raytracing for a modelled horizon is shown in figure 4.5. The normalised chi-squared (χ^2) guided the fit as it was discovered that the high-resolution OBS data are sensitive to perturbations in

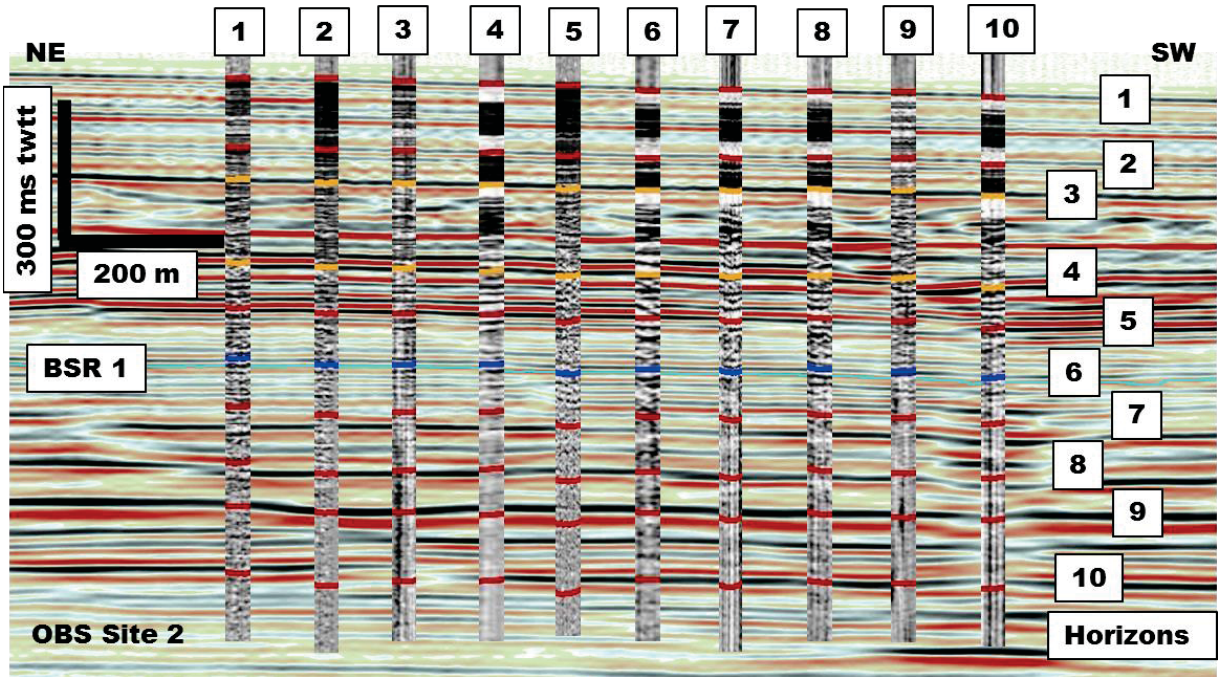

Figure 4.4 Reflections picked on OBS dataset matched to reflections visible in the 3D MCS dataset for OBS Site 2 in the east (see figure 3.1 for location). The yellow horizons (3 and 4) on the OBS data mark the top and base of an MTD respectively as identified using the 3D seismic data. The blue horizon 6 marks the location of the stratigraphic BSR in this area. OBS units are numbered along the top. Horizons are numbered on the right side.

the velocity/depth pairing. It was possible to get very close to a normalised χ^2 of 1 both for each picked layer when following the layer-stripping approach, and for the overall fit of a completed model (See Appendix F). In general, a χ^2 ranging between 0.9 and 1.1 was considered a "good" overall fit for each velocity model. The series of individual velocity models for OBS Site 1 and OBS Site 2 are shown in Figures 4.6 and 4.7 respectively.

The 1D velocity models for OBS Site 1 (over a strong BSR identified in industry seismic reflection data) show the distinctive combined high and low velocity zones indicative of gas hydrate overlying free gas on some units (Fig. 4.6). A velocity increase of 170 – 440 m/s occurs within a 120 m layer at a depth of 150 – 270 mbsf across the array profile. The velocity of the

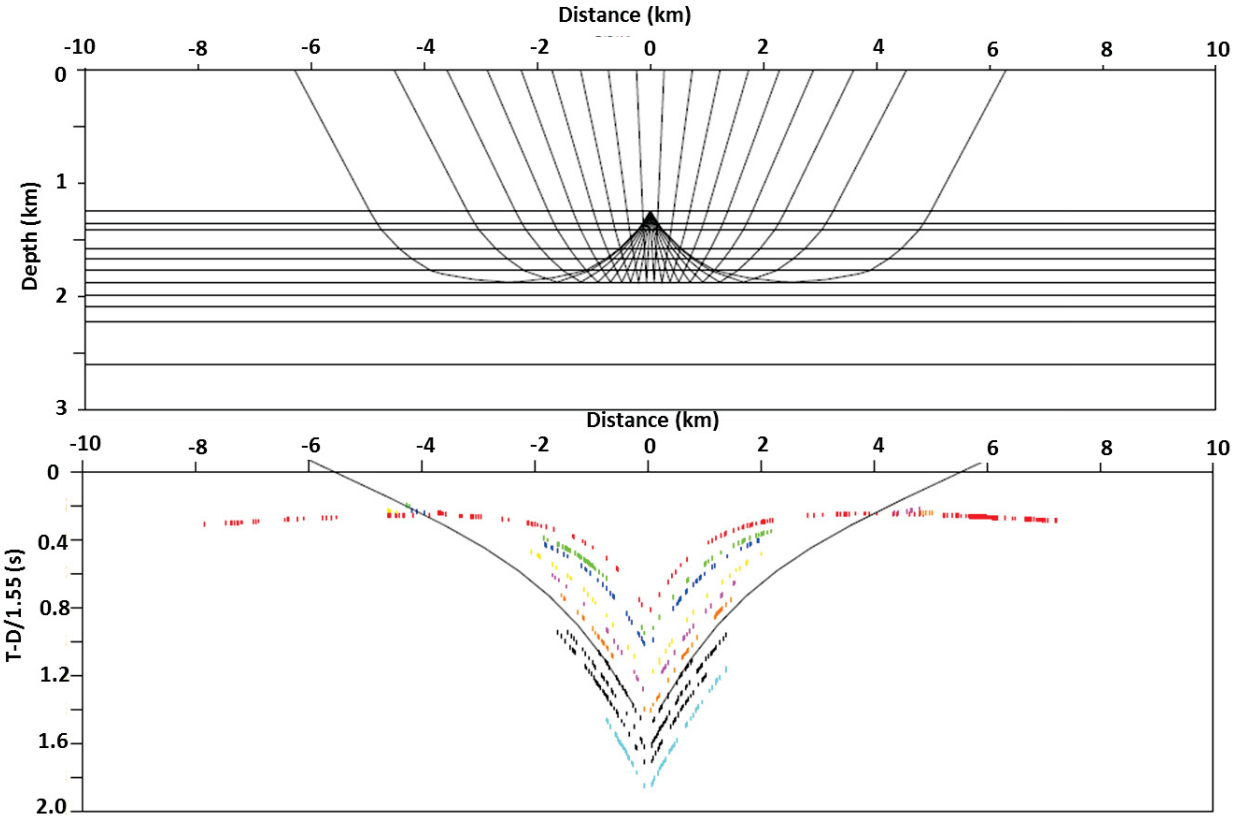

Figure 4.5 Top: Raytracing for horizon 7 of an OBS unit. The OBS is located at the 0km distance marker. Reflection points on a horizon are located over several kilometers around the OBS location. Bottom: the solid black line shows the model fit to the horizon picks (coloured dots).

HVZ ranges from 1.77 to 1.98 km/s and varies in depth from 1690 mbsl at OBS 6 to 1810 mbsl at OBS 9. The velocity profiles show a velocity decrease of 170 – 300 m/s within a 100 m layer at a depth of 220 – 360 mbsf across the profile. The velocity of the LVZ ranges from 1.44 to 1.68 km/s and varies in depth from 1760 mbsl at OBS 6 to 1900 mbsl at OBS 3, 4 and 9. The combined HVZ/LVZ is shallowest at OBS 6 and deepest at OBS 3, 4 and 9. The combined HVZ/LVZ is missing from OBS 5. OBS 7 does have a combined HVZ/LVZ but produces anomalous values at depths below 1980 mbsl. In that case, it proved impossible to model velocities for horizons 5 to 9. Modeling of OBS 7 horizon 5 gave a normalised χ^2 value of 6.5

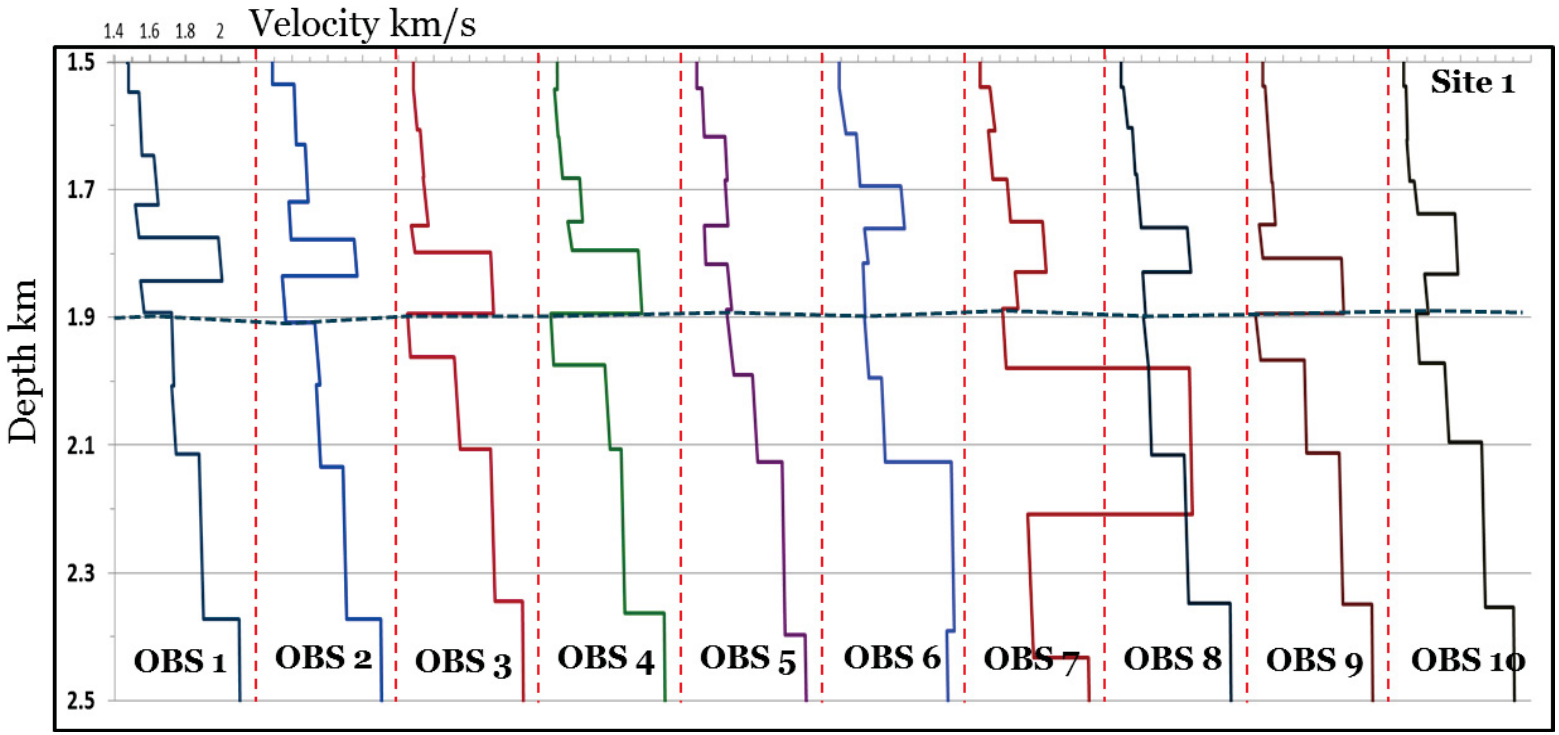

Figure 4.6 Plot of the individual 1D velocity models derived from Site 1 OBS data showing a strong BSR in industry seismic reflection data. The location of horizon 6 (BSR) is marked by the brown dotted line. There is strong lateral variation in response between the models. Note that the OBS are separated by approximately 100 m at this site. Reference velocity of 1.4 km/s is shown for each model as a dashed red line.

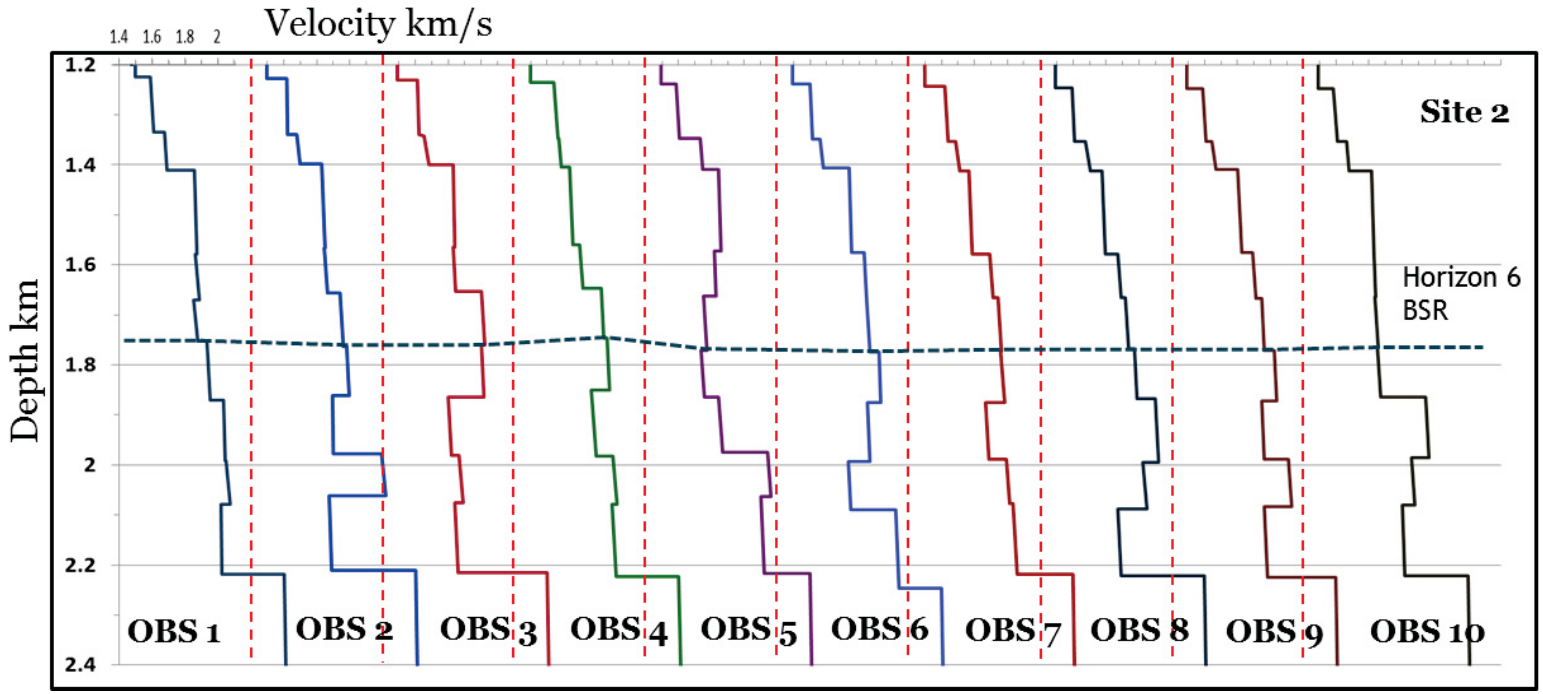

Figure 4.7 Plot of the individual 1D velocity models derived from Site 2 OBS data where a BSR is not present in industry seismic reflection data. Horizon 6 (BSR horizon continued from the Site 1) is shown as a brown dashed line. There is lateral variation in the response between the models but the model gradient appears consistent across the ten models. No HVZ and /or LVZ are visible in these models suggesting a lack of gas hydrate and/or free gas in the area. Note that the OBS are separated by approximately 100 m at this site. Reference velocity of 1.4 km/s is shown for each model as a dashed red line.

which is outside the acceptable range. High levels of noise are present on the data from OBS 7 but it is undetermined if this is the cause of the anomalous values.

Horizons 6 and 7 were picked along BSR 1 and BSR 2 (identified using 3D seismic profiles) for all the OBS units at OBS Site 1. None of the velocity models however shows a stacked combined HVZ/LVZ expected from the presence of two BSRs.

The velocity models for OBS Site 2 (over an area with no BSR identified in seismic reflection data) do not show the combined HVZ/LVZ seen at OBS Site 1 (Fig. 4.7). The velocity models appear consistent at the site for the first 600 m below the seafloor with velocities increasing linearly from 1.48 to 2.0 km/s. At depth however, lateral velocity variations are visible but not consistent across models. A small LVZ does occur from ~2070 mbsl on OBS 1 - 5 and 8 - 10 of the velocity models with an average velocity of 1.8 km/s. This LVZ however occurs deeper than the expected BHSZ for this location and is interpreted as caused by a deep gas-charged sand layer. It was not possible to pick refractions through all 10 OBS units at either site. One refracted arrival was identified on OBS 4, 5 and 7 with an apparent velocity of ~1.66 km/s. This matched the depth of horizon 4 at these locations.

4.1.4 OBS Site 1, Unit 5

The velocity model for OBS unit 5 at OBS Site 1 lacks the expected combined HVZ/LVZ when compared to the surrounding units (Figure 4.6). As the raypaths for each OBS unit overlap by several kilometers, it is not possible to determine what has caused the differences in models, particularly at OBS 5. However there are a number of theories as to the cause.

A seismic profile through the area shows subsurface features which may affect raytracing in the area (Figure 4.8). First is the effect of a shallow MTD. The cross-cutting layers are difficult to model in 1D and it is possible that the parameters are not adequate to capture the raypaths.

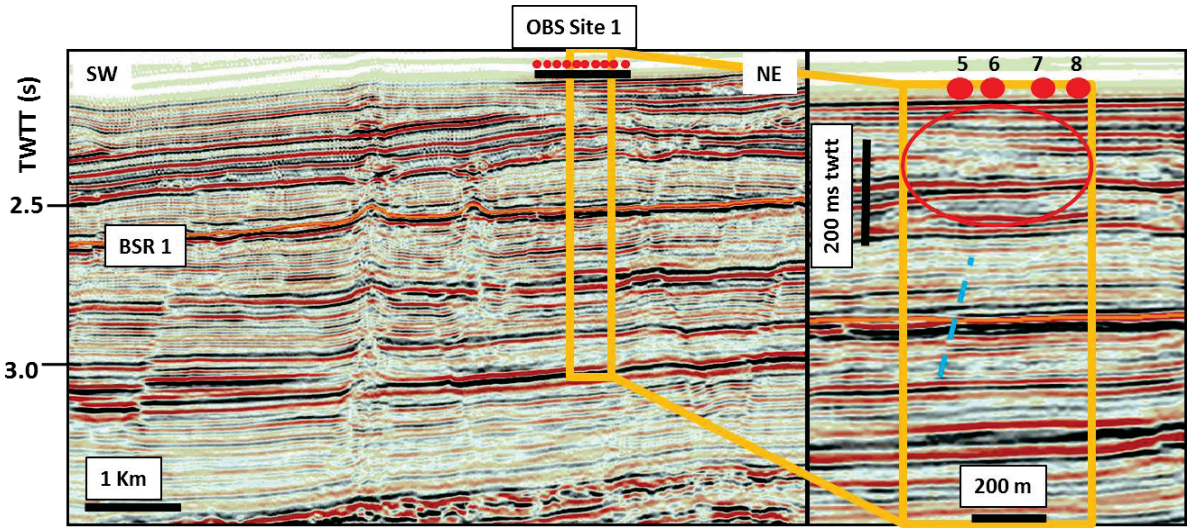

Figure 4.8 Left: A seismic profile through OBS Site 1 showing the change in character of BSR 1 (OBS horizon 6). The OBS units are marked by red dots. Right: zoom-in of the profile outlined in the yellow box. A red oval marks the shallow MTD in the area. A possible fault at the level of the BSR is marked by the blue dashed line.

Second, there is a noticeable change in character of the BSR reflection across the central unit locations. That variation may be caused by lithological changes such as decreased sand or increased mud content in this layer, which in turn could influence the concentration of gas hydrate and/or free gas. Horizon 7 (BSR 2 fades) out in this central section of the array at OBS Site 1. Third, there may be a fault present directly under OBS 5 and 6 that is not fully resolved in the seismic data, providing a path for gas-charged fluid to move up through the sedimentary section, perhaps causing a localized change in the gas hydrate stability zone.

The modeling parameters used may also be influential in this case. The 2D models by Schlesinger et al. (2012) show some variability in gradients but not to the extent seen in the 1D models (Figure 4.9). First, certain assumptions made in the modeling may not be entirely valid, such as the use of sharp gradients. It is known that the top of gas hydrate, for example, is a diffusive boundary. Also lateral changes in layers cannot be modelled along a gradient in 1D

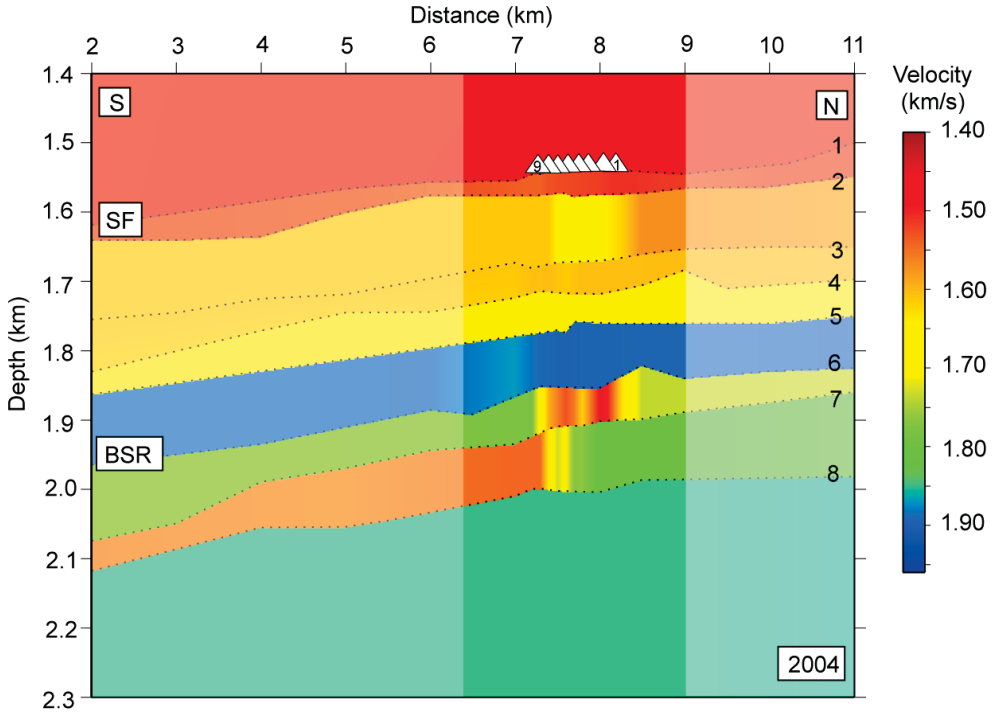

Figure 4.9 2004 2 -D velocity model from travel-time tomography using arrivals from the nine OBS stations (triangles) and the corresponding 2D SCS vertical incidence profile. The BSR marks the transition to a layer of reduced velocity (1590 m/s) below a high velocity zone (average 1900 m/s). The numbers indicate the eight reflections used in the travel-time inversion modelling. The velocity model shows a 4 km long section of the whole 12 km long profile that indicates the region of full ray-coverage where the travel-time arrivals provide control on velocities. Figure from Schlesinger et al. (2012).

models. Second, only reflections were used in the 1D models for this study as it was not possible to pick refractions consistently through the OBS datasets. Reflections provide good boundary depth control but provide poor velocity control compared to refractions. Third, the overall χ^2 for OBS 5 was 0.5 which is overfit, possibly due to the high noise level and subsequent low number of picks available for the horizon modeling compared to other OBS data.

4.1.5 Discussion

Each model is slightly different from the next. The cause of this variation is undetermined as the geometry of the raypaths for each model overlap, and variability in a model is not due only to the area directly underneath that unit. The 2D models of Schlesinger et al. (2012) do show some variability over a longer array length of 9 km (Figure 4.9) but in general there is less variability along the profile, possibly due to smoothing used. Therefore 1D models from OBS data are not suitable for determining gas hydrate variability.

The reason for the lack of distinction between the two BSRs is also undetermined but may be due to several factors. The visible BSR 2 occurs 40 – 70 m (or 80 - 100 ms) below BSR 1 at OBS Site 1 in the 3D MCS dataset. However, horizon 7 (BSR 2) was picked at 100 – 120 ms below horizon 6 (BSR 1) in the OBS data, as this was the closest consistent horizon that could be picked on all 10 OBS units. Therefore horizon 7 (BSR 2) may not represent the strongest BSR 2 response at OBS Site 1. Delescluse et al. (2011) carried out 2D waveform tomography on 2D MCS lines running through the Torbrook study area. They also did not detect the presence of BSR 2. This could be due to two reasons: 1) BSR 2 is mis-identified as a response due to gas hydrate and instead could be due to another substance such as trapped water; or 2) the 2D tomography is not of high enough resolution to pick-up the more subtle feature underneath the BSR. Delescluse et al. (2011) decimated the shot spacing to 94 m to avoid aliasing. That spacing is similar to the 2004 OBS data spacing which does not distinguish between BSR 1 and BSR 2.

4.2 Model of the Base of the Gas Hydrate Stability Zone

4.2.1 Introduction

Modeling the base of the gas hydrate stability zone (BGHSZ) from theoretical principles is useful to determine if the observed BSR falls within the calculated gas hydrate stability zone using modern pressure and temperature parameters.

4.2.2 Modeling Results

Using the equations derived from Leon et al. (2009) and described in section 3.1.4, calculations were made to compare the calculated BGHSZ to the position of the observed BSR. Figure 4.10 shows the key finding in this exercise. BSR 1 directly adjacent to the Mohican Channel is observed 1,820 – 2,300 mbsl in water depths of 1,500 – 1,920 m. However, the calculated BGHSZ using water depths extracted from the seafloor horizon picked in SMT Kingdom Suite ™, modern bottom water temperatures (constant at 3.7 °C) and the modern geothermal gradient (constant at 31.5 mW/m) plots considerably deeper at 2,000 – 2,480 mbsl (red horizon in Figure 4.10). The depth of the observed BSR (320 – 380 mbsf) is therefore less than the calculated BGHSZ depth (500 – 560 mbsf) by approximately 200 m. This difference was explored by individually varying bottom water temperature, water depth and geothermal gradient in the model calculations.

An increase in bottom water temperature to 9 °C, while the geothermal gradient and water depths remained constant at modern values, resulted in the calculated BGHSZ moving upwards to the location of the observed BSR 1.

A decrease in water depth of 200 m, while the bottom water temperature and geothermal gradient remained constant at modern values, also resulted in the calculated BGHSZ moving up to the location of the observed BSR 1.

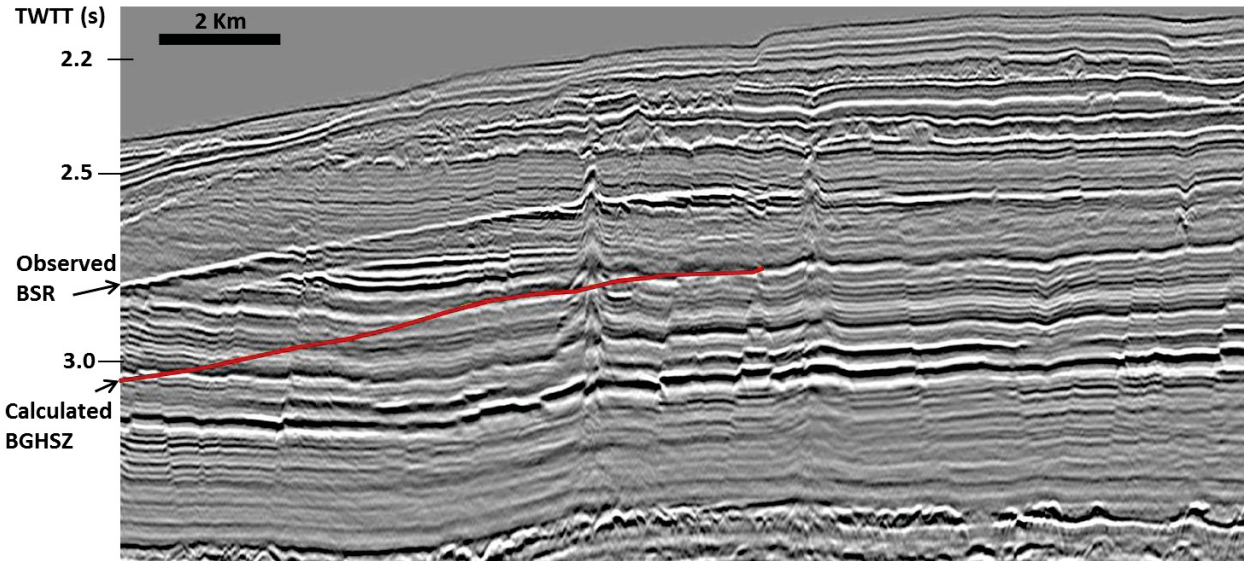

Figure 4.10 A seismic reflection profile through the Mohican Channel BSR showing the position of the calculated base of the gas hydrate stability zone (red line) using model equations of Leon et al. (2009). The model result was calculated using modern water depths from the depth-converted seafloor horizon, bottom water temperature (3.7°C) and geothermal gradient (31.5 mK/m).

An increase in geothermal gradient to 48 mK/m, while the bottom water temperature and water depths remained constant at modern values, also resulted in the calculated BGHSZ moving up to the location of the observed BSR 1.

The BGHSZ was also calculated for a thermogenic gas source using Function II described by Leon et al. (2009). For this area however, the calculated BGHSZ for thermogenic methane is located considerably deeper (a further 100 m in depth) than the observed BSR at 600 - 700 mbsf. The adjustments in bottom water temperature, water depth or geothermal gradient required to move the calculated thermogenic BGHSZ upwards to the position of the observed BSR were considered unrealistic for this area. A 100 % thermogenic gas source was therefore discounted as the methane source for the Mohican Channel area gas hydrate.

4.2.3 Discussion

The ~ 200 m difference between the observed BSR depth and the calculated BGHSZ is an interesting puzzle. The model parameter changes of bottom water temperature (increased to 9°C) and water depth (decreased by 200 m) were considered implausible for this location on the Scotian margin. There is no evidence that sea level dropped to that degree nor that bottom water temperatures rose by 5°C. This leaves the geothermal gradient or other as yet unidentified processes. The heat flow measurements available to date in or near the study area have proven inconsistent. There were considerable differences between measurements taken on the CCGS Hudson 2004-030 cruise and subsequent measurements on for example the CCGS Hudson 2009 cruise. Measurements taken through the Torbrook area were 10 – 15 mW/m^2 lower than predicted by models (Negulic et al., 2011). Temperature measurements in nearby boreholes such as Acadia K-62 and Torbrook C-15 were taken at the bottom of the well, below the level of the BSR, and could not be used in this model. Straight-line extrapolation of temperature from the seafloor temperature to the bottom of wells did not prove useful in this case. The geothermal gradient value of 48 mK/m would be consistent with predicted models by Negulic et al. (2011) but a suite of high-quality heat flow measurements are required adjacent to the Mohican Channel area to confirm this theory.

4.3 Gas Volume Calculations

4.3.1 Introduction

A recent report by Hydrate Energy International (HEI) calculated the global volume of gas in-place in hydrate-bearing sands using a petroleum systems approach (Johnson, 2011. Collett et al. (2009) noted that “high grade gas hydrate deposits are best viewed as an extension

of conventional petroleum system and a petroleum systems approach is essential for a valid assessment of hydrate resource potential". The evaluation by HEI supports the probability of a large volume of hydrate being present in sand reservoirs in polar and deepwater sediments, with 10's of thousands tcf (trillion cubic feet) present in marine sands. The calculated volumes for the Canadian continental margin and Arctic sediments have a median value of 2,228 tcf or 63.1 tcm (trillion (10^{12}) cubic metres) (Johnson, 2011).

The hydrate stability zone of the eastern Canadian continental margin from Georges Bank to southern Baffin Island covers an area of approximately 2,200,000 km^2 (Mosher, 2011). The calculated gas hydrate stability zone lies in water depths greater than 350 m given current bottom water temperatures of 2 to 4°C. The Scotian Slope area, from the 350 – 3,500 m isobath, is approximately 124,000 km^2 (Mosher, 2011). Using an inferred mean hydrate thickness of 79 m and hydrate saturation of the sediments of 2 - 6% (Majorowicz and Osadetz, 2003), the methane hydrate volume estimate for the Scotian Slope is approximately 0.2 - 0.6 x 10^{12} m^3 (tcm).

More recently, Schlesinger et al. (2012) provided new constraints on the gas hydrate and free gas concentrations in the Mohican Channel area using 2D velocity models. When converted to gas hydrate concentrations using effective medium theory; the 2D velocity models showed a gas hydrate layer approximately 100 m thick above the identified BSR and average gas hydrate concentrations of 4 – 13 %. Schlesinger et al. (2012) also showed a reduction in gas hydrate concentration with horizontal distance from the Mohican Channel BSR over the extent of the array (approximately 10 km in length). The authors theorised that this change was due to higher mud concentration in the sediments away from the channel, resulting in lower overall sediment porosity at the depth of the BSR. Free gas concentrations remained at 1-2 % of the sediment pore space, similar to concentrations determined by LeBlanc et al. (2007).

4.3.2 Gas Hydrate Volume Calculations

Gas hydrate may well be present in areas without a BSR, but for the scope of this study gas hydrate volumes were calculated where the BSR was confidently observed within the 3D MCS data (Figures 4.11 and 4.12). Calculations for hydrate volumes are presented in Table 4.1. BSR 1 is inferred to be present over 330.4 km^2 adjacent to the Mohican Channel. The total sediment volume containing gas hydrate was calculated using three values: 1) the 79 m bulk thickness calculated by Majorowicz and Osadetz (2001), 2) the 100 m bulk thickness determined adjacent to the Mohican Channel by Schlesinger et al. (2012), and 3) an estimated 55 m for thickness of BSR 2. Schlesinger et al. (2012) also found that gas hydrate concentrations decreased moving eastwards out of the area adjacent to the Mohican Channel resulting in a larger range of estimated saturations. Hydrate volume is calculated in this study at 2 - 6 % bulk gas hydrate as estimated by LeBlanc et al. (2007) and at 4 - 13 % as estimated by Schlesinger et al. (2012). Total hydrate volume for the observed BSR1 ranges from 5.21 x 10^8 m^3 at the lowest saturation and thickness, to 42.96 x 10^8 m^3 at the highest saturation and thickness (Table 4.1). Assuming a gas volume expansion of 164 times at STP, this suggests that total methane gas in formation ranges from 0.85 – 7.05 x 10^{11} m^3.

BSR 2 was interpreted to lie 40 – 70 m below BSR 1 over an area 61.5 km^2 (Figure 4.12). A mean value of 55 m was used for the thickness of possible gas hydrate in the area of BSR 2. Total hydrate volume for the observed BSR 2 ranges from 1.36 – 4.41 x 10^8 m^3 (Table 4.1). Assuming a gas volume expansion of 164 times at STP, this suggests that total methane gas in formation in the area of BSR 2 ranges from 0.22 – 0.72 x 10^{11} m^3.

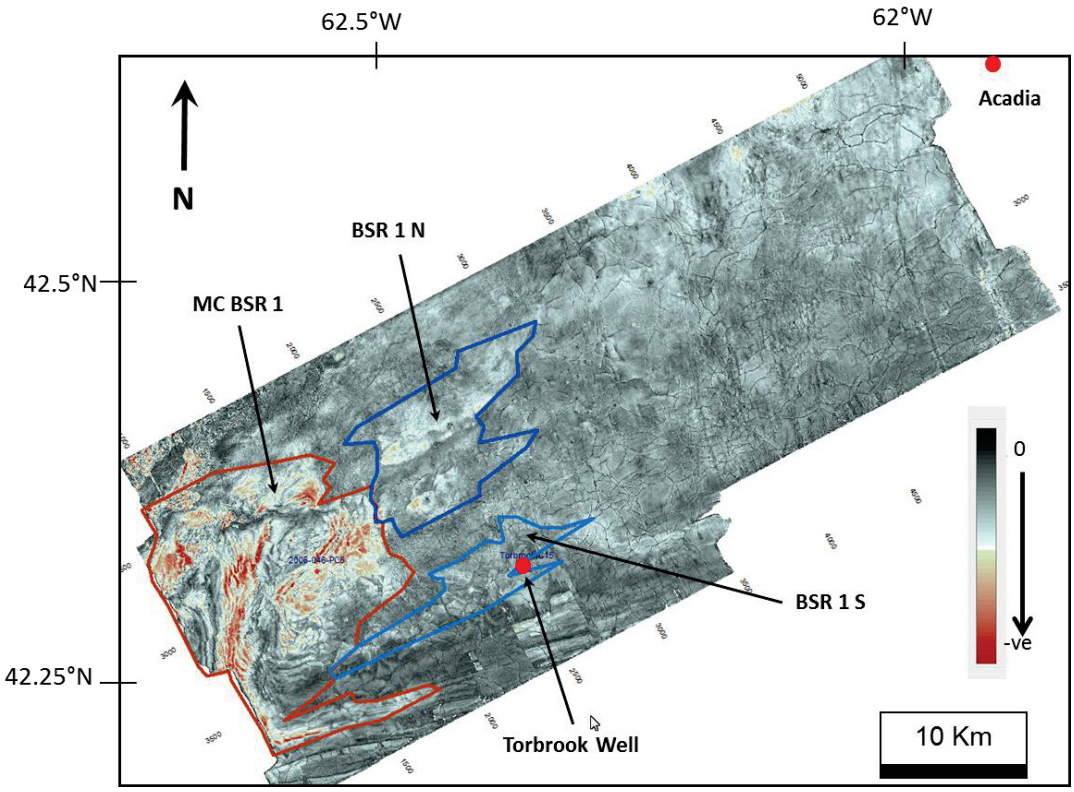

Figure 4.11 Extent of the interpreted BSR 1 through the Torbrook 3D MCS dataset. The figure shows the picked BSR horizon plotted with negative amplitudes. The classic negative phase, cross-cutting BSR occurs adjacent to the Mohican Channel in the brown polygon (MC BSR 1). Areas of enhanced coincident reflections, interpreted as a BSR, are outlined by the two blue polygons (BSR 1 N and BSR 1 S). This interpretation is described in detail in Chapter 5 of this thesis.

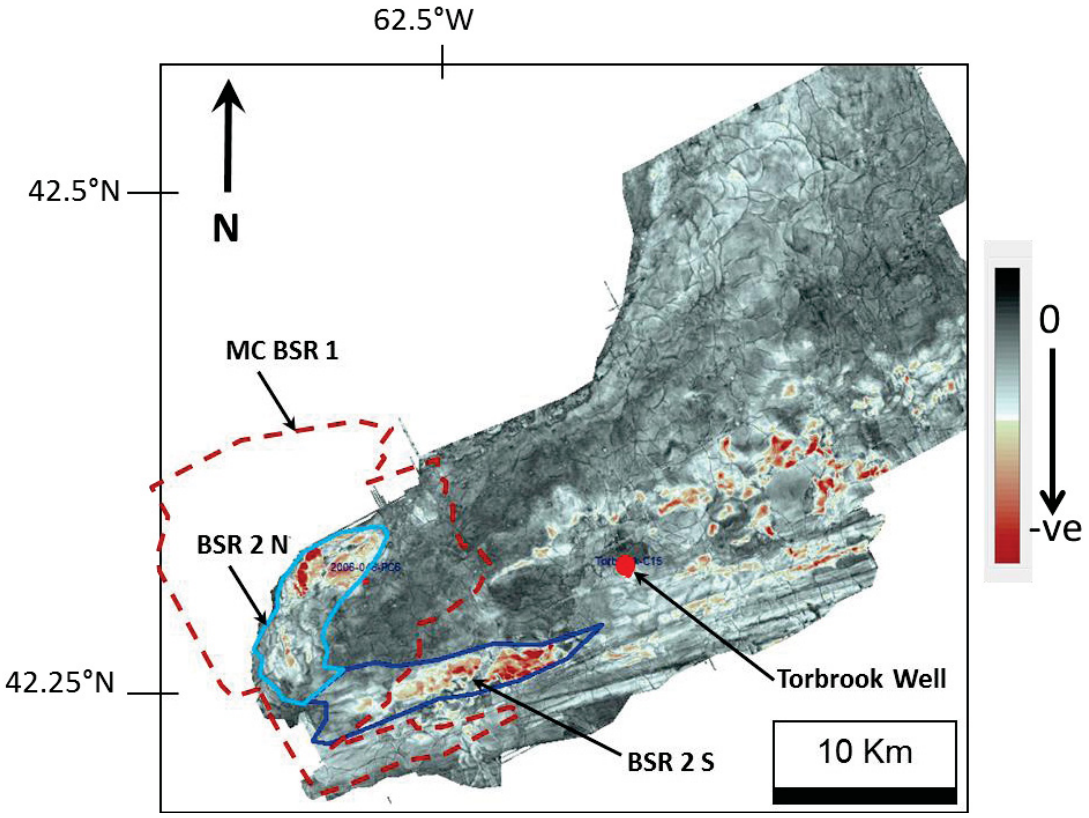

Figure 4.12 Extent of the interpreted BSR 2 through the Torbrook 3D MCS dataset. The figure shows the picked BSR 2 horizon plotted with negative amplitudes. The classic negative phase, cross-cutting BSR 2 occurs adjacent to the Mohican Channel in the light blue polygon (BSR 2 N). The area of enhanced parallel reflections, interpreted as a BSR, is outlined by the dark blue polygon (BSR 2 S). The brown dashed polygon marks the location of the interpreted MC BSR 1 for reference. This interpretation is described in detail in Chapter 5 of this thesis.

Mohican Channel BSR Area (km^2)		Bulk volume assuming 55m thickness (km^3)	Hydrate volume assuming 4-13 % saturation ($x10^8$ m^3)	Bulk volume assuming 79m thickness (km^3)	Hydrate volume assuming 2-6 % saturation ($x10^8$ m^3)	Bulk volume assuming 100m thickness (km^3)	Hydrate volume assuming 4-13 % saturation ($x10^8$ m^3)
MC BSR1	210.7			16.65	3.33-9.99	21.07	8.43-27.4
BSR1-N	79.3			6.27	1.25-3.76	7.93	3.17-10.31
BSR1-S	40.4			3.16	0.63-1.9	4.04	1.62-5.25
Total BSR1 Area	330.4			26.08	5.21-15.65	33.04	13.22-42.96
BSR2-N	30.1	1.66	0.66-2.16				
BSR2-S	31.4	1.73	0.70-2.25				
Total BSR2 Area	61.5	3.39	1.36-4.41				

Table 4.1 Gas volume calculations for the Mohican Channel BSR. The combined BSR 1 is interpreted to cover an area of 330.4 km^2. BSR 2 is interpreted over 61.5 km^2. Majorowicz et al. (2001) originally calculated an average bulk gas hydrate thickness of 79 m along the eastern Canadian continental margin. LeBlanc et al. (2007) calculated gas hydrate concentration of 2 – 6 % adjacent to the Mohican Channel. Schlesinger et al. (2012) determined an overall bulk gas hydrate thickness of ~100 m above the identified BSR 1. Schlesinger et al. (2012) also found that gas hydrate concentrations were greatest adjacent to the Mohican Channel itself and reduced going eastwards into the central section of the study area, resulting in a range of saturation calculations greater than those estimated previously of 4 – 13 %. BSR 2 lies 40 – 70 m below BSR 1 with a mean value of 55 m, used to estimate gas hydrate thickness for BSR 2.

CHAPTER 5 FLUID FLOW FEATURES IN THE MOHICAN CHANNEL AREA, SCOTIAN SLOPE, EASTERN CANADA

This chapter is written as a stand-alone manuscript for submission to a peer-reviewed journal.

5.1 Introduction

Fluid flow indicators in marine sediments are gaining attention when applied to the investigation of slope stability and gas hydrate formation. Fluid expulsion through marine sediments and at the seafloor is believed to play an important role in identifying potential geohazards and slope instabilities (Sun et al., 2012; Ostanin et al., 2012, 2013) while focussed fluid flow appears to be a key factor for the formation of gas hydrates in marine sediments (Plaza-Faverola et al., 2012). However, low-resolution or sparse sub-seafloor imaging can hinder understanding of the plumbing systems involved. The Canadian eastern continental margin has an extensive geophysical database gained through over 40 years of hydrocarbon exploration. A recent paper by Mosher (2011) described a gas hydrate assessment using bottom simulating reflections (BSRs) along Canada's Atlantic margin. Hydrocarbon transport by fluid flow systems is widespread on continental margins and sedimentary basins and the expelled fluids can provide clues regarding the underlying petroleum system. The study of fluid flow features is crucial for understanding the dynamics of gas hydrate accumulation, distribution and stability.

The objectives of this study are to analyse fluid pathways on a local scale in an area adjacent to the Mohican Channel (Figure 5.1) and determine the role of pathways in influencing local and potentially regional perturbations of gas hydrate distribution. This study examines the Mohican Channel BSR (first described by Mosher et al., 2005) using industry 3D seismic data and shallow sediment cores to determine if specific fluid flow pathways such as faults or pipes exist in the area. Such pathways may control the heterogeneous distribution of gas hydrates

within the area and could provide clues to the underlying petroleum system present in this section of the eastern Canadian continental margin.

5.2 Regional Setting and Background

5.2.1 Regional Setting

The eastern Canadian continental margin is a passive margin formed during mid-Triassic rifting approximately 220 Ma between the African and North American tectonic plates (Jansa and Wade, 1975; Wade and MacLean, 1990). The creation of the North Atlantic Ocean during the Mesozoic and Cenozoic caused several periods of subsidence and deposition which formed the thickest sedimentary basins on the outer shelf and slope (Jansa and Wade, 1975). The Scotian Basin consists of a series of inter-connected sedimentary subbasins which have thick accumulations of evaporites, carbonates and marine siliciclastic sediments 15-20 km in depth (Wade and MacLean, 1990). Along much of the southern margin, late Triassic to early Jurassic evaporites are overlain by Jurassic carbonates and middle and late Jurassic marine siliciclastic sediments (Wade and MacLean, 1990). A variably thick wedge of Cenozoic prodeltaic deep water clastics, predominately mudstones and chalk, is distributed over the slope (Piper, 2005).

Numerous sediment mass-failure events affected much of the margin during the Neogene period (Piper, 2001; Piper and Ingram, 2003; Campbell, 2011). Glaciations dominated slope processes during the Plio-Pleistocene and strongly influenced the modern margin morphology, depositing thick sequences of glacial sediment outwash and deepening pre-existing Tertiary canyons (Mosher et al., 2004; Piper, 2005). Slope sediment mass failure events and regional unconformities are common within the succession (Mosher et al., 2004; Campbell et al., 2004; Campbell and Mosher, 2010). Campbell (2011) and Campbell and Deptuck (2012) determined

that the Late Miocene to Late Pliocene was dominated by bottom current deposition resulting in large contourite drifts along the lower slope and stacked sequences of giant sediment waves. Gravity flows were dominant from the Late Pliocene to present with most deposition at the lower slope and beyond (Campbell, 2011). Holocene processes have covered most of the seafloor in a thin 1-2 m drape of hemipelagic muds (Piper and Campbell, 2003; Jenner et al., 2007).

The study area is located on the central Scotian Slope approximately 350 km southeast of Halifax (Figure 5.1). The area lies in water depths of 900 - 2000 m and has a regional gradient of approximately 3°. It is bounded by the Mohican Channel to the east and the Acadia Valley system to the west. The Scotian Salt Province to the south comprises numerous salt diapirs with up to 8 km of structural relief (Shimeld, 2004), some of which subtly influence bathymetric contours at the southern limits of the study area. Large failure escarpments up to 80 m high are visible in water depths of 1500 - 2500 m on a regional 3D seismic dataset.

The Play Fairway Anlaysis Report (OERA, 2011) on the hydrocarbon potential of the western Scotian Slope concluded that three main source rock intervals were present in the area and that approximately 2/3 of generated hydrocarbons were in place. This confirms the presence of an active slope hydrocarbon system which could provide the hydrocarbon gas necessary for gas hydrate formation.

5.2.2 Gas Hydrates – Distribution and Stability

The gas hydrate stability zone for the eastern Canadian Atlantic margin runs the entire length of the continental margin from northern Labrador to the southern tip of Nova Scotia (Majorowicz and Osadetz, 2001). It lies beneath the continental slope in water depths of about 350 – 3,500 m and covers an area of approximately 715,000 km^2 (Mosher, 2011). Wood and Jung (2008) modelled the extent and thickness of the global methane hydrate stability zone and

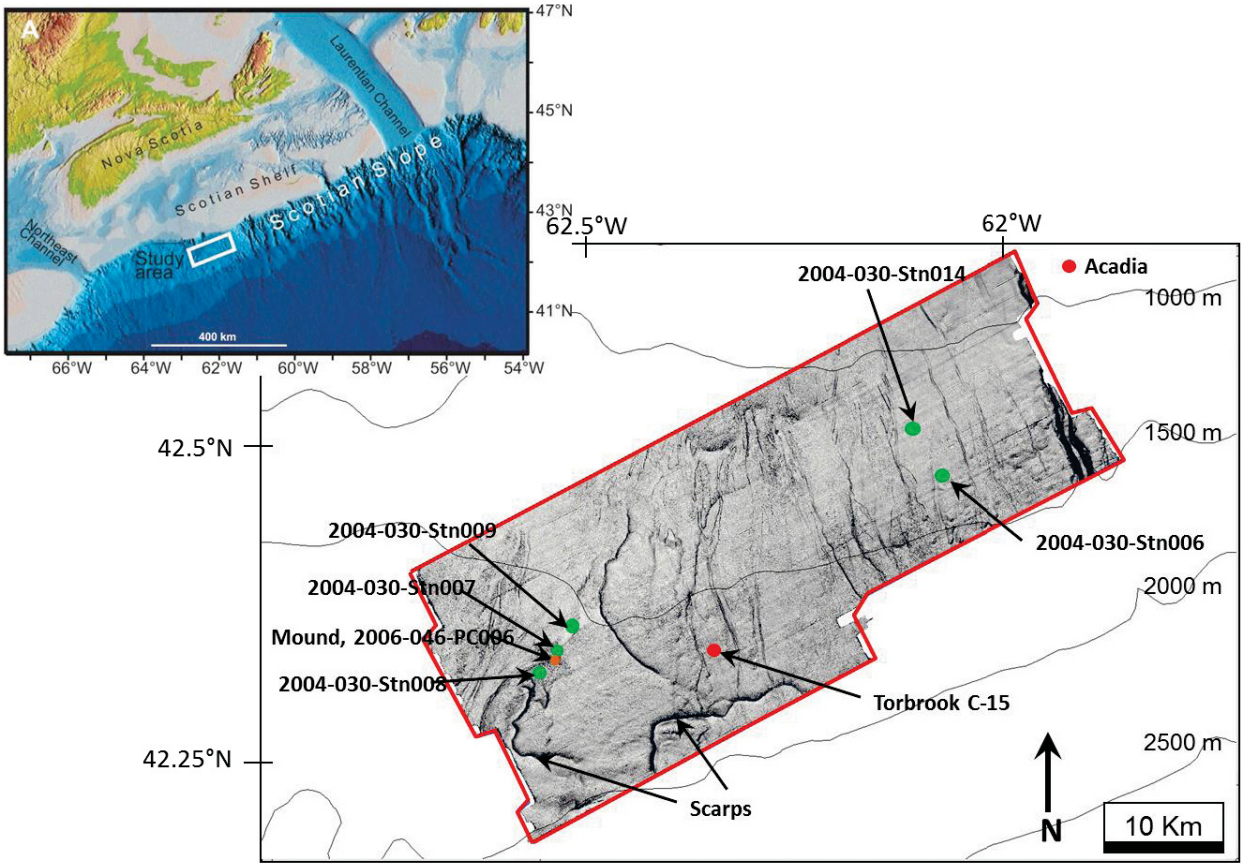

Figure 5.1 Study area location map. A) shows the study area location on the modern continental margin off Nova Scotia. B) Map showing the data available for this study. Cores are marked by green dots. The modern seafloor mound is marked with an orange dot. Wells in the area are marked by red dots. Torbrook C-15 is within the area of the 3D dataset. The red polygon marks the extent of the Torbrook 3D datasets with seafloor plotted inside. Large scarps are visible on the seafloor.

estimated a 500 m thick stability zone over much of offshore Nova Scotia. The size of the stability zone is only one factor in determining the presence of gas hydrate, however. Like any petroleum system, there needs to be a source of hydrocarbon, a reservoir and pathways for the hydrocarbon to reach the reservoir. This latter point is why it is important to understand the fluid pathways in formation.

5.2.3 Bottom Simulating Reflection (BSR)

BSRs attributed to gas hydrates were first identified at Blake Ridge by Tucholke et al. (1977) and described as a phase-reversed reflection event which runs broadly parallel to the seafloor and can cut across bedding planes. The first formal recognition of a BSR on the eastern Canadian continental margin was published by Mosher et al. (2004) and the first description of the Mohican Channel site was published in 2005 (Mosher et al., 2005).

The acoustic impedance contrast between hydrate-bearing sediment and the underlying, free gas in sediments frequently produces a Bottom Simulating Reflection (BSR) on seismic sections (Shipley et al., 1979; Hyndman and Spence, 1992). BSRs visible in seismic datasets are currently used as the main indicator of the presence of gas hydrates in marine sediments. The BSR is interpreted to denote the base of the gas hydrate stability zone (BGHSZ) above which gas hydrate formation is possible. A number of scientific boreholes drilled during the past 10 years in locations such as the northern Cascadia margin and Hydrate Ridge have confirmed that the BSR is closely related to the BGHSZ (Tréhu et al., 2004; Torres et al., 2008; Riedel et al., 2006).

5.2.4 Fluid Flow Pathways and Features

Recognition of active or paleo-fluid flow pathways and expulsion features can indicate the status of the hydrocarbon system in a location of interest. Vertical fluid flow through marine sediments is a globally widespread dynamic process on passive and active continental margins. However, the role of focussed fluid flow in gas hydrate formation remains under examination worldwide (Crutchley et al., 2011; Plaza-Faverola et al., 2012; Vadakkepuliyambatta et al., 2013).

A special class of normal, non-tectonic, non-gravitational faults has been described over the past two decades in basin slope and floor sediments (Cartwright and Dewhurst, 1998;

Dewhurst et al., 1999). These are termed polygonal faults (PF) due to their distinctive honeycomb structure in map view (Cartwright et al., 1994; Lonergan et al., 1998). Polygonal faulting was first described by Cartwright et al. (1994) and has since been found in sedimentary basins worldwide (Hansen et al., 2004; Sun et al., 2009; Cartwright, 2011). PF systems could potentially act as fluid flow pathways from deeper to shallower reservoirs so understanding their nature and distribution within a basin may enhance understanding of the local or regional hydrocarbon potential of shallow plays (Stuevold et al., 2003). This type of faulting develops in passive margin basins within fine to very fine grained sedimentary sequences with high clay content as well as carbonate chalks (Cartwright and Lonergan, 1996; Dewhurst et al., 1999; Hansen et al., 2004). To date, a number of mechanisms have been proposed such as 1) syneresis, volumetric contraction and liquid expulsion (Cartwright and Lonergan, 1996; Dewhurst et al., 1999), 2) low coefficients of residual friction (Goulty, 2008), 3) density inversion related to overpressured pore water (Henriet et al., 1989; Plaza-Faverola et al., 2012) and 4) thermal and chemical contraction due to the opal A to opal CT conversion (Davies et al., 2009; Cartwright, 2011). Gay et al. (2006a/b and 2007a/b) related polygonal faulting to fluid transport and dewatering structures such as pockmarks identified on the seafloor of the Lower Congo Basin. Berndt et al. (2003) and Bunz et al. (2005) determined that PFs played an important role in focussing fluid flow into a gas hydrate stability zone on the mid-Norwegian margin. Hansen et al. (2004) described a major PF system in the Upper Cretaceous chalk and Cenzoic mudrocks of the Sable Subbasin, north of the study area, and attributed their formation to syneresis and the distribution to distinct lithological changes.

The migration of pressurised fluids in stratified sediments produces features such as pipes. Subsequent expulsion of overpressured fluids onto the seafloor results in pockmarks or mounds.

Pockmarks are defined as concave, crater-like depressions ranging in diameter from a few metres to several hundred metres, and were first described on the Scotian Shelf by King and MacLean (1970). In general, most seafloor pockmarks appear dormant when surveyed suggesting their fluid flow activity may be episodic, implying multiple phases of fluid flow, although the timing is generally unknown. Mounds can reach considerable height above the seafloor, with relief of several tens of metres (Gay et al., 2007; Matsumoto et al., 2011). Active seeps frequently attract diverse benthic and chemosynthetic communities (Judd and Hoveland, 2007; Herbozo et al., 2013).

Ascending gas and fluid can leave traces in seismic datasets in the form of amplitude anomalies or disturbed zones in the subsurface due to the effect of different fluid content on seismic velocity. Stacked or columnar acoustic disturbances are termed seismic pipes and are understood to represent vertical gas and fluid pathways (Cartwright, 2007; Loseth et al., 2011, Andresen et al., 2012). They are circular to sub-circular in map view and can have vertical to sub-vertical lengths of over 1 km (Cartwright, 2007). Seismic pipes may terminate in pockmarks on the seafloor depending on their pressure regime (Cartwright, 2007). They are distinct from seismic processing artifacts because their development shows both structural and stratigraphic control such as formation above structural traps or faults (Cartwright, 2007; Huuse et al., 2010, Andresen et al., 2012). The presence of traceable reflections indicates the sediments are not reworked unlike mud volcanoes which carry reworked sediments through conduits to the seafloor (Matsumoto et al., 2011).

5.3 DATA AND METHODS

Datasets available for use in this study included processed 3D industry seismic data provided by EnCana Corp., and high-resolution seismic reflection data, multibeam bathymetry, and piston cores provided by the GSC(A) (Figure 5.1).

5.3.1 Processed Industry 3D Seismic Volume

The time-migrated 3D seismic data volume from EnCana, known as the Torbrook survey, covers an area of 1,550 km^2 on the central Scotian Slope in water depths of 1,500 – 2,000 m (Figure 5.1). These data were acquired in June to August 2000 by the vessel Geco Prakla. The seismic system consisted of six 6 km-long multi-channel streamers with 25 m group intervals and 240 channels per streamer. Streamer separation was 100 m and streamer tow depth was 8 – 9 m. The airgun source consisted of an array of pneumatic guns with a total volume of 63.5 L. Two arrays were towed at 6 m depth and fired in flip-flop mode with 50 m shot intervals. This gun-streamer configuration resulted in 60 fold data with a bin spacing of 12.5 x 25 m.

The received raw signals were filtered at 3 to 180 Hz before being digitally sampled at 2 ms. Processing of the data cube by EnCana included spherical divergence compensation, FK filtering, spiking deconvolution, resampling to 4 ms, velocity analyses, multiple attenuation, interpolation to 12.5 x 12.5 m bin spacing, and post- stack time migration. The frequency of the processed data ranges from 5 to 70 Hz, and has a peak frequency of 12 Hz. Using average sediment velocity of 1600 m/s and the highest frequency of 70 Hz, vertical resolution ($\lambda/4$ where $\lambda = V/F$) of the data is approximately 5 - 6 m.

5.3.2 Cores

The GSC(A) carried out an extensive coring program over the past few decades around the study area. The majority of these were piston cores had an average depth of penetration of 10 - 12m. Subsamples were taken from the some of the cores and stored in a refrigerated container for interstitial gas concentration analyses. Three cores were examined in the study area, with gas analysis carried out on one core from site 2006-046-PC006 (Figure 5.1).

5.3.3 Seismic Attribute Analysis

Seismic reflections were mapped within the 3D seismic dataset to determine the distribution and vertical extent of fluid flow features. Four of these horizons are used to demonstrate features for discussion and interpretation. The mapped surfaces included horizon 1 the seafloor, horizon 2 above the visible BSR, horizon 3 along the visible BSR, and horizon 4 below the visible BSR (Figure 5.2).

Every 10^{th} inline and crossline was manually picked in SMT Kingdom Suite™ software to provide seed-picks for the automatic picking program. Horizon picking errors of 4 ms are estimated from the data sampling interval. Using a series of small polygons, an automatic picking program within SMT Kingdom Suite ™ software filled the horizon between the seed picks. Horizons were then gridded and manually adjusted to fill gaps around faults and other features.

Volume attributes such as similarity and instantaneous frequency were calculated on the entire 3D seismic dataset. These attributes were used to examine fault distribution within the study area as well as possible fluid flow features and possible lithology indicators.

5.3.4 Time-Depth Conversion

A time-depth table was constructed from refraction analysis (Schlesinger et al., 2012) and Torbrook C-15 checkshots and used to convert all picked horizons including the seafloor (horizon 1), from time to depth and vice versa.

Depth below seafloor (m)	Travel time from the seafloor (ms)
380	450
810	1060
930	1185
1050	1300
1150	1400
1250	1485
1315	1562
1400	1650
1490	1690

Table 5.1 A simplified time-depth table

5.4 OBSERVATIONS

5.4.1 Age Estimation

The Mohican Channel BSR occurs within the thickest section of the Shubenacadie Drift, identified by Campbell (2011), and formed between horizons of estimated Pliocene age (horizons N50 – early Pliocene and N60 – late Pliocene of Campbell, 2011) (Figures 2.3A and 5.2). Campbell (2011) determined that the Shubenacadie Drift exceeds 1,500 m thickness near the Torbrook C-15 well and covers a total area of 9,500 km^2. The Torbrook 3D seismic dataset lies completely within the Shubenacadie Drift area. Horizon 4 in the Torbrook study area, below the visible BSR, is equivalent to horizon N50 of early Pliocene (Zanclean) age while horizon 2, above the visible BSR, is equivalent to horizon N60 of late Pliocene age (Figure 5.2). Over much

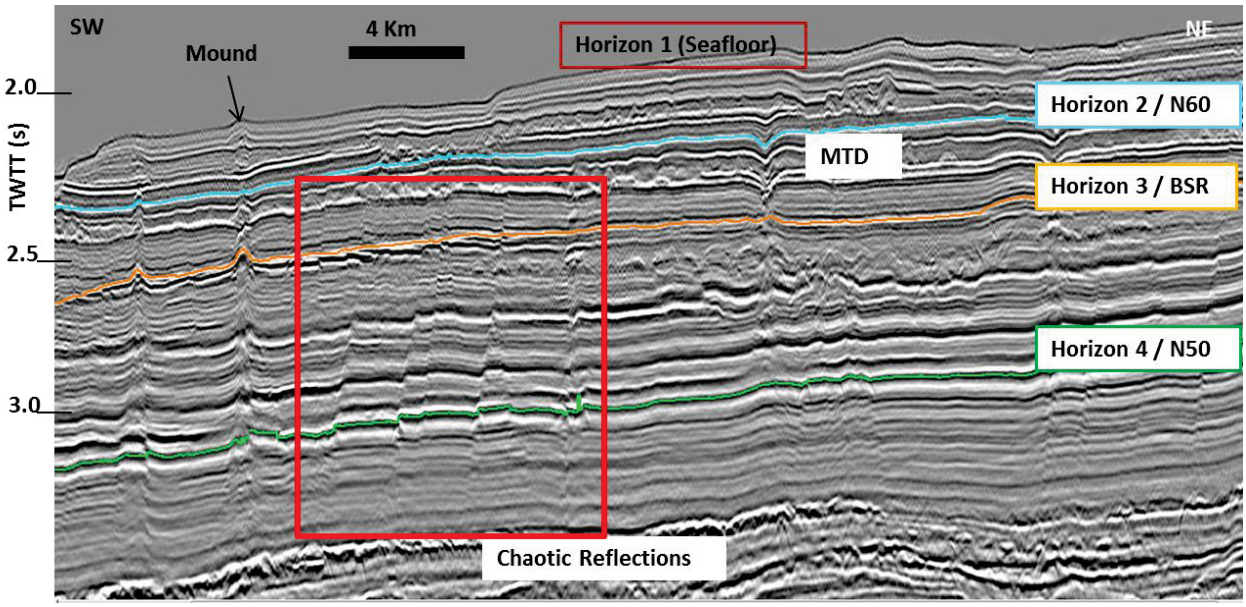

Figure 5.2 A profile through the 3D MCS dataset showing age estimation in the area of the Mohican Channel. Horizon 2 is equivalent to the Late Pliocene N60 horizon interpreted by Campbell (2011). Horizon 4 is equivalent to the Early Pliocene N50 horizon interpreted by Campbell (2011). Horizon 1 is the seafloor pick while horizon 3 is picked along the visible BSR in the Mohican Channel area. The red rectangle marks the zone of faulting.

of the Shubenacadie Drift, the N50 horizon occurs as a gently undulating erosional surface, a feature associated with winnowed and abraded surfaces in contourite systems (Campbell, 2011). Sediment sample control in the area is sparse and points to mainly mud-based lithology. Campbell (2011) theorised that muddy turbidities and hemipelagic sediments were the sediment source for the Drift. Alongslope currents have moved and moulded sediments possibly sorting the sediments sufficiently to provide the pore space necessary for gas hydrate formation in parts of the Drift.

5.4.2 Mapped BSR

The Mohican Channel BSR (MC BSR 1) lies at depths of 300 - 480 m below the seafloor in modern water depths of 1,285 – 1,920 m immediately adjacent to and underlying the Mohican

Channel (Figure 5.3). The attribute map of this reflection event (horizon 3) displayed in Figure 5.3 shows a high negative amplitude response in the area adjacent to the Mohican Channel when compared to the general amplitude response of this reflection elsewhere. The Mohican Channel BSR 1 is visible on survey inlines running parallel to the slope over distances of 20 - 30 km and on survey crosslines running perpendicular to the slope over distances up to 20 km, and maps out to a total area of 210.7 km^2 (Figure 5.3, brown polygon).

The MC BSR 1 distinctly cuts across other reflections that are presumably related to depositional bedding planes (Figure 5.3). Moving eastwards out of the area adjacent to the Mohican Channel and into the central portion of the study area, the seismic stratigraphy runs mostly parallel to the flat-lying seafloor and so a cross-cutting reflection is not present in the seismic data. Instead enhanced parallel seismic reflections are visible (Figure 5.3) and are mapped in two sections (BSR1-N and BSR1-S) throughout the seismic dataset over an area of 119.7 km^2, resulting in a total BSR 1 area of 330.4 km^2.

The Mohican Channel area is distinctive in that a second BSR is identified underneath the main MC BSR 1 but over a smaller area (Figure 5.4). The deeper BSR occurs in water depths of 1,550 – 1,820 m at 350 – 400 m below the seafloor forming a series of brightened seismic reflections referred to as “segmented” (Shedd et al., 2009 and 2012). The second BSR is visible both as a segmented response and as enhanced parallel reflections in two sections (BSR2-N and BSR2-S) and covers a total area of 61.4 km^2. BSR 2 occurs approximately 40 – 70 m below MC BSR 1, with a mean value of 55 m.

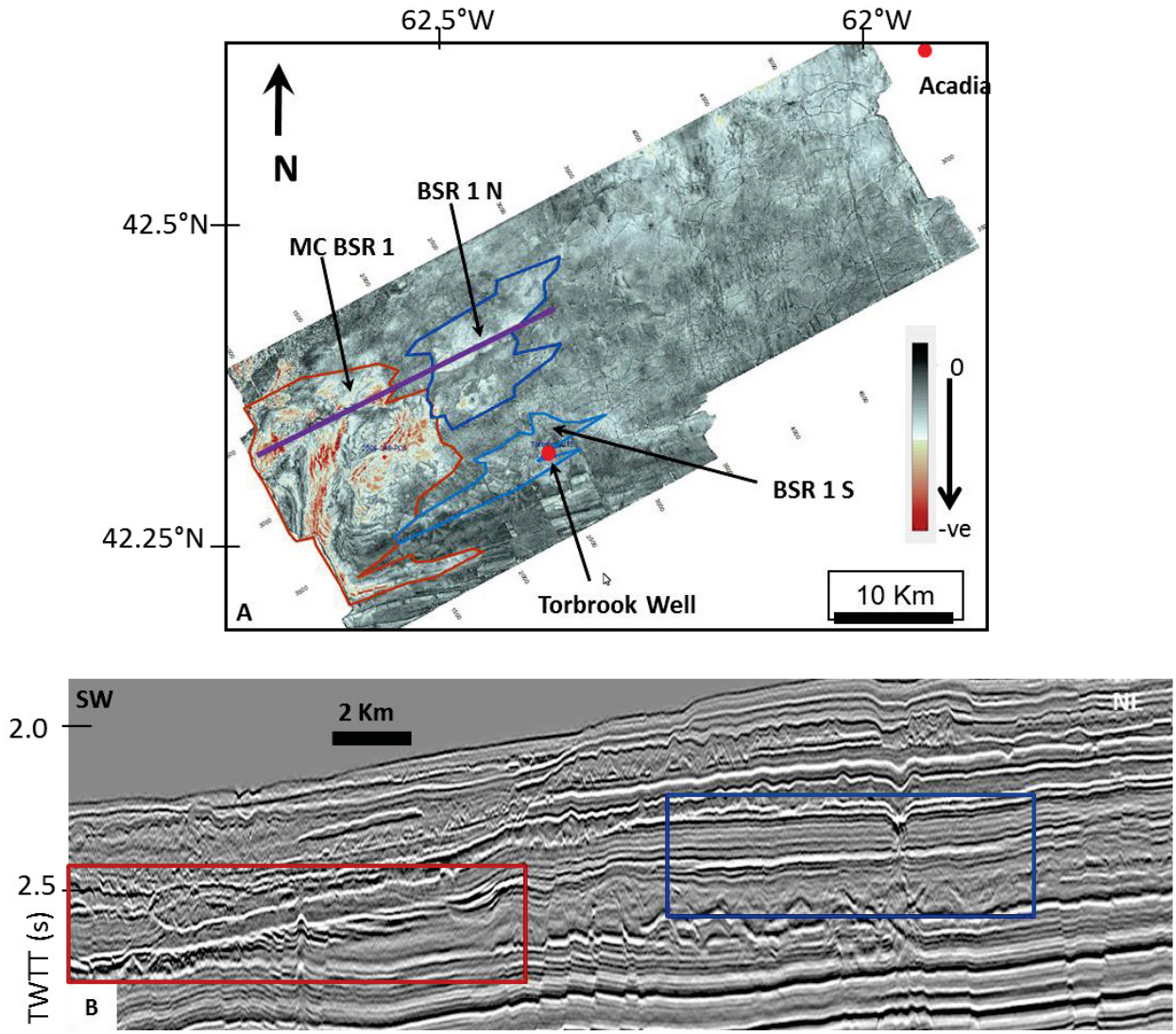

Figure 5.3 Seismic character of BSR 1 in the Mohican Channel area. A) A map showing negative amplitude plotted on horizon 3 (BSR 1), highest negative amplitudes are in red. The brown polygon outlines the area in which the MC BSR 1 visibly cuts across seismic reflections (brown rectangle in seismic profile above). Area = 210.7 km^2. The blue polygons outline areas in which enhanced parallel reflections are visible (blue rectangle on seismic profile above). Total area = 119.7 km^2 (79.3 and 40.4 km^2 respectively). B) Seismic reflection profile at the location marked by a purple line on the map showing the changing character of BSR 1 from west to east.

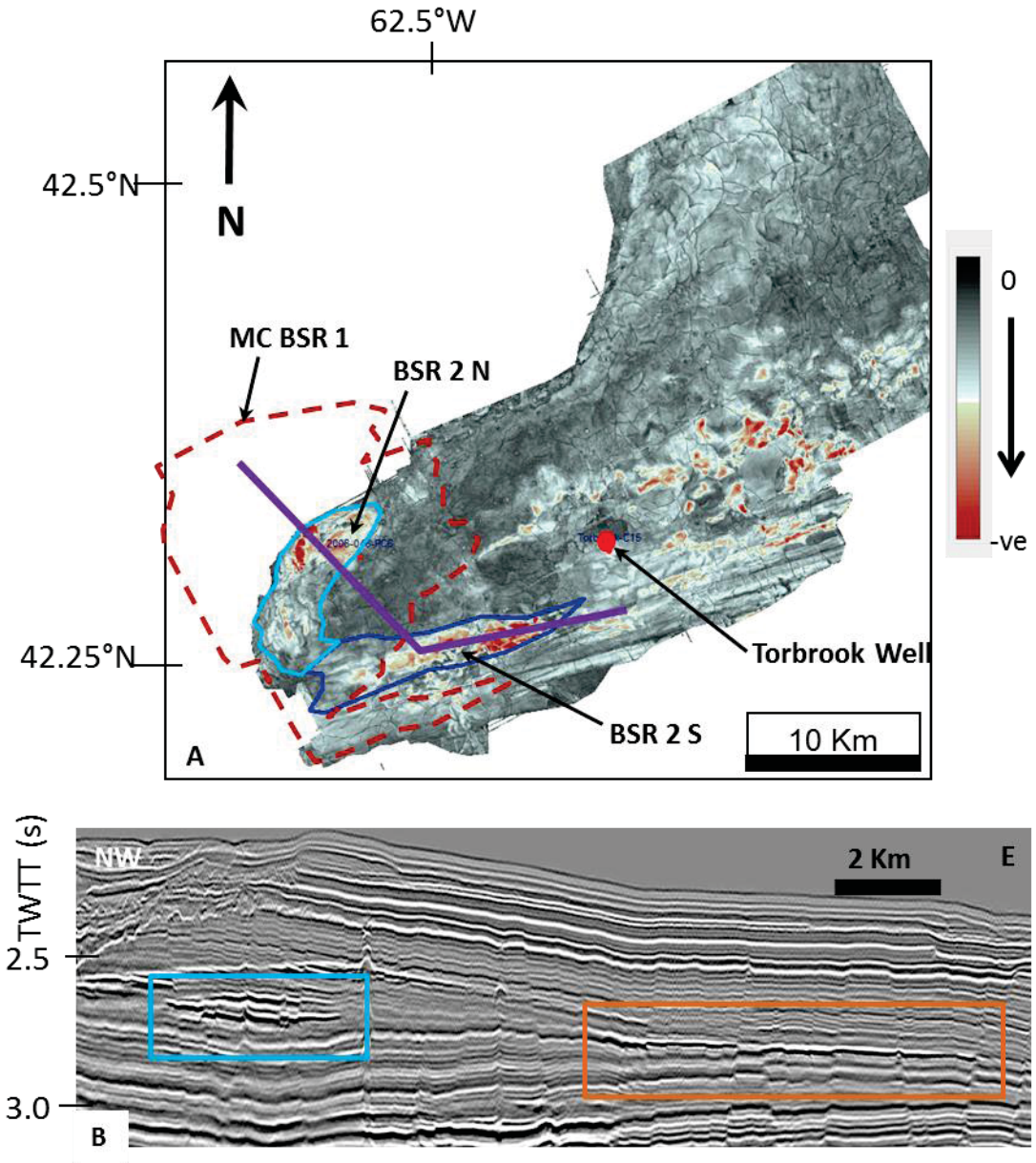

Figure 5.4 Seismic character of BSR 2 in the Mohican Channel area. A) The map shows negative amplitude plotted on BSR 2 picked in the 3D seismic dataset; highest negative amplitudes are in red. The light blue polygon outlines the area in which BSR 2 presents as a "segmented" BSR (light blue rectangle in seismic profile below). Area = 30 km^2. The dark blue polygon outlines an area in which enhanced parallel reflections are visible (dark blue rectangle on seismic profile below). Area = 31.4 km^2. B) Seismic reflection profile at the location marked by a purple line on the map showing the changing character of BSR 2 from north to east.

5.4.3 Fault System

A fault system is visible throughout the Torbrook 3D seismic dataset. Inline and crossline profiles show that the majority of faults are confined to a specific zone with an upper boundary at ~2.3 s twtt and a lower boundary at ~3.5 s twtt (Figure 5.5). The faulted interval is described as layer-bound as the reflections above and below this section are highly continuous with few disruptions (Cartwright and Dewhurst, 1998). A small number of faults, however, do extend towards the seafloor above the upper boundary, possibly due to reactivation in recent times (Figure 5.5). The faults appear rooted in chaotic reflections at ~ 3.5 s twtt. Numerous MTDs are present in the shallow section above the upper fault boundary at 2.3 s twtt. The faulted interval has an average thickness of 1200 ms as seen on profiles throughout the 3D seismic reflection dataset. The majority of faults are normal faults with throws ranging from 15-30 ms, with an average throw of 20 ms at velocities in this interval, corresponding to offsets of 12 - 25 m.

The seismic attribute "Dip of Maximum Similarity" on mapped horizons shows a distinctive fault pattern emerging with depth in the section (Figures 5.6 to 5.8). The faults are spaced 500 – 1,000 m apart with an average spacing of 650 m. Fault trace lengths range from 150 – 600 m although the high degree of connectivity in the fault system makes it difficult to determine precise fault lengths throughout the area. The fault trace pattern is mostly curved on the upslope side with straight fault traces on the downslope side. On horizon 2, the fault pattern is not distinct as this horizon occurs close to the top of the faulted zone (Figures 5.2 and 5.6). The pattern visible on horizon 3 (the BSR horizon) is influenced in the western area by the BSR cross-cutting seismic reflections, and produces a pattern of lens-shaped faults in the area with the dipping BSR (Figure 5.7). Away from the Mohican Channel, horizon 3 displays the classic polygonal faulting pattern. At greater depth in the section (horizon 4) the faults are clustered

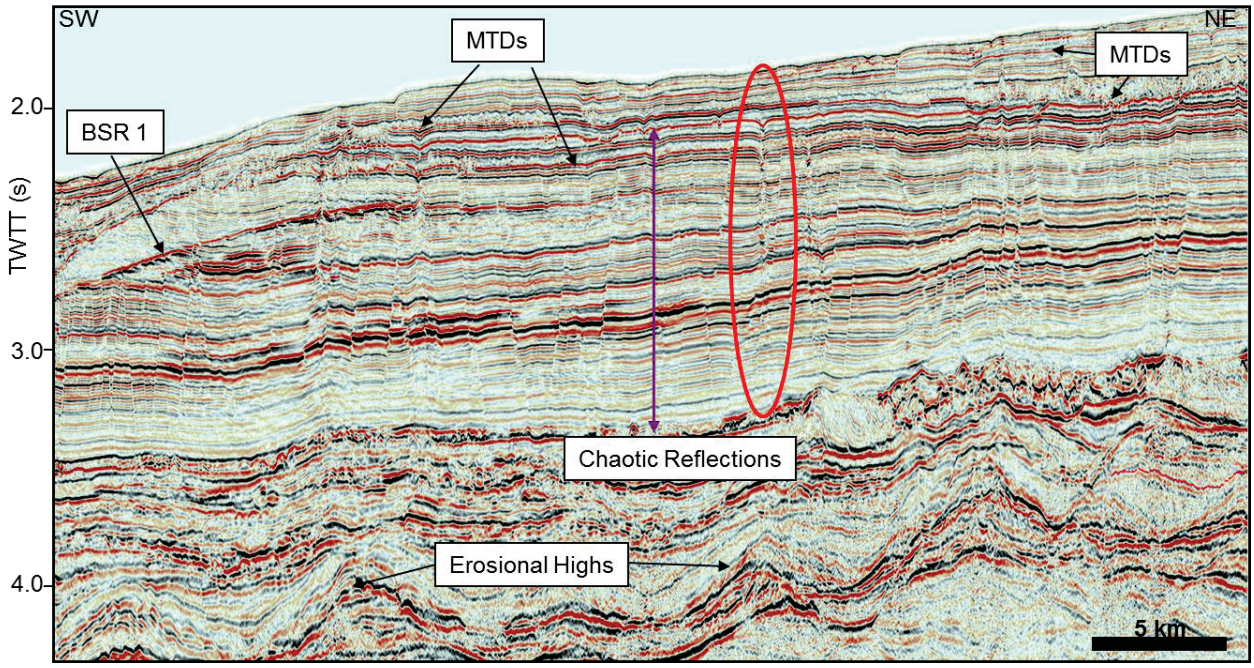

Figure 5.5 A seismic reflection profile showing the fault system in the study area. Faults appear confined to a zone from 2.3 to 3.5 s twtt (purple arrow), and appear rooted in chaotic reflections at ~ 3.5 twtt. MTDs are common in the shallow section. Paleo-pockmarks appear to occur at the top of faults (red oval). Erosional highs are visible at ~4.0 s twtt.

around the tops of deep erosional highs (Figure 5.8). Fault distribution throughout the Torbrook 3D dataset does not appear to be specifically related to the areas of high negative amplitude visible on the mapped BSR horizon, nor to the visible BSR in the seismic dataset.

5.4.4 Seafloor Pockmarks and Mounds

The seafloor in the study area shows a small number of pockmarks and mounds in water depths 1500 – 2000 m. Four pockmarks were identified west of Torbrook C-15 well, each with diameter of 300 – 350 m (Figure 5.9). A seismic line through the area shows disturbed shallow reflections directly underneath the pockmarks and above a distinctive mass transport deposit (Figure 5.9). Instantaneous frequency shows a change within these shallow reflections which may

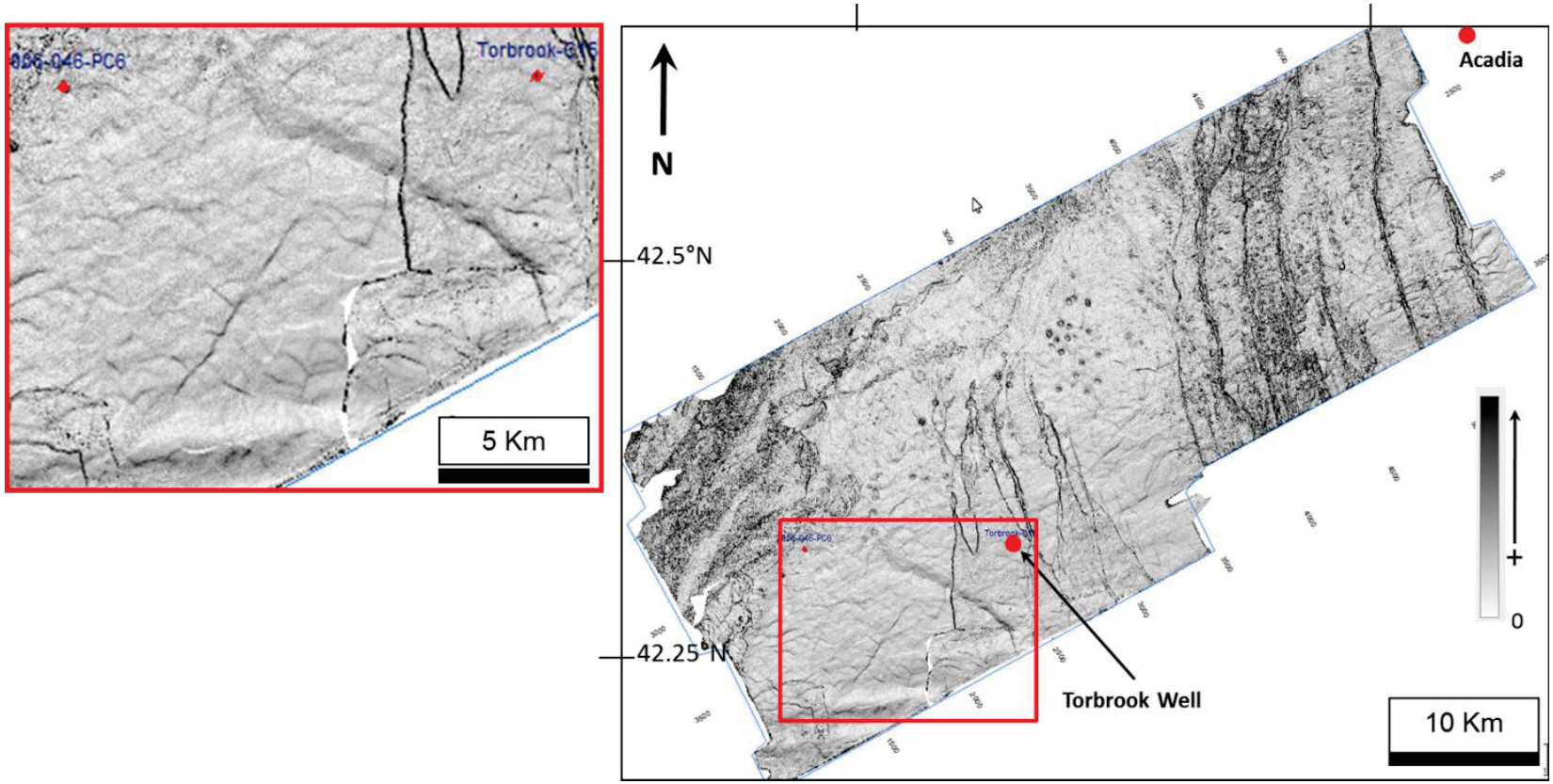

Figure 5.6 Map of the dip of maximum similarity on horizon 2 (Figure 5.2). Shallow features such as channels are visible on the mapped surface. Inset shows that the fault pattern is not distinct on this horizon as it lies just above the top of the faulted zone.

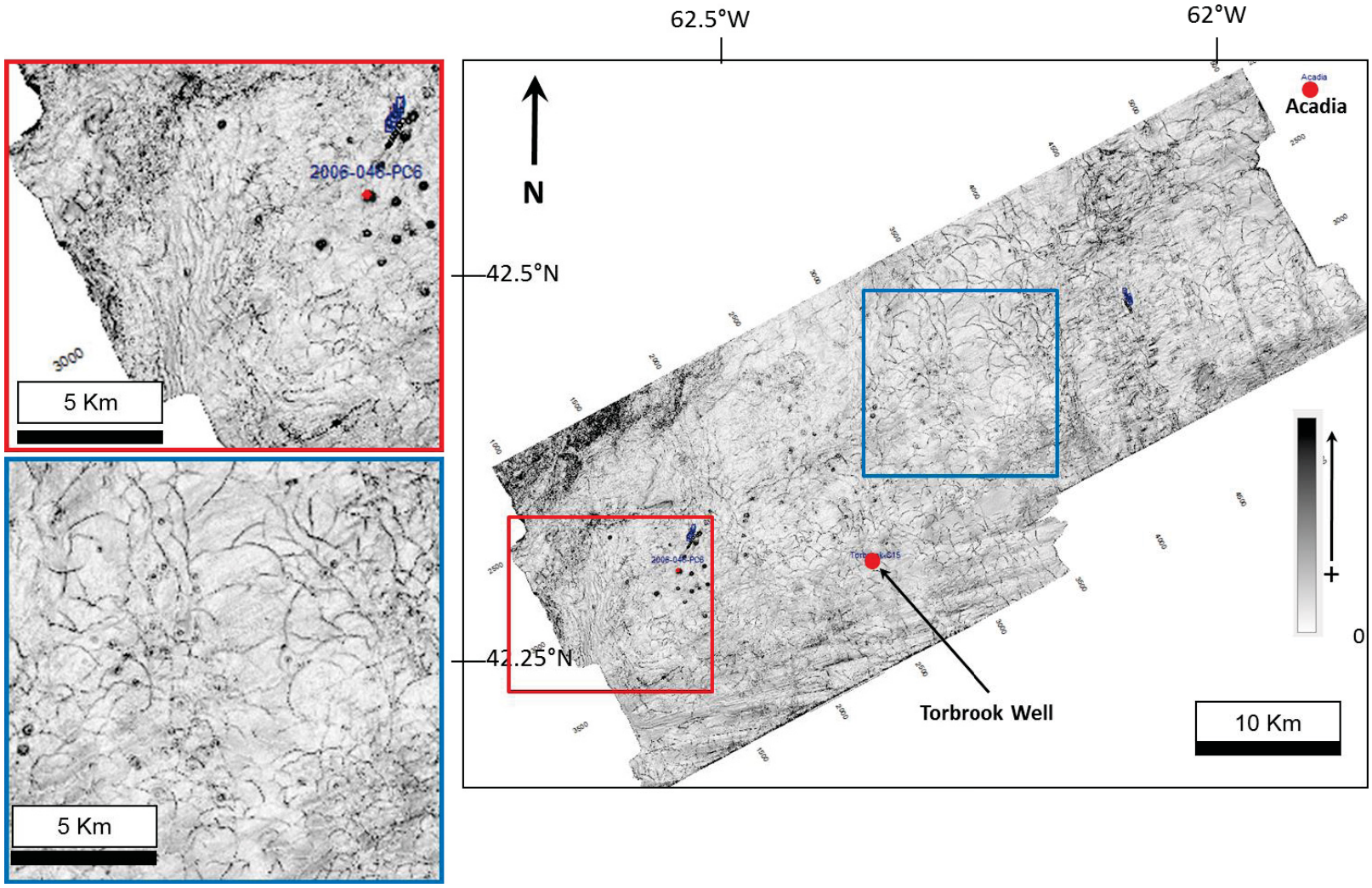

Figure 5.7 Map of the dip of maximum similarity on horizon 3 (BSR 1, Figure 5.2). The classic polygonal fault pattern is visible in the area (blue box). Inset shows the pattern in more detail. A distinct fault pattern is visible in the west due to the curve of the BSR cross-cutting seismic stratigraphy, causing the faults to appear lens-shaped (inset red box).

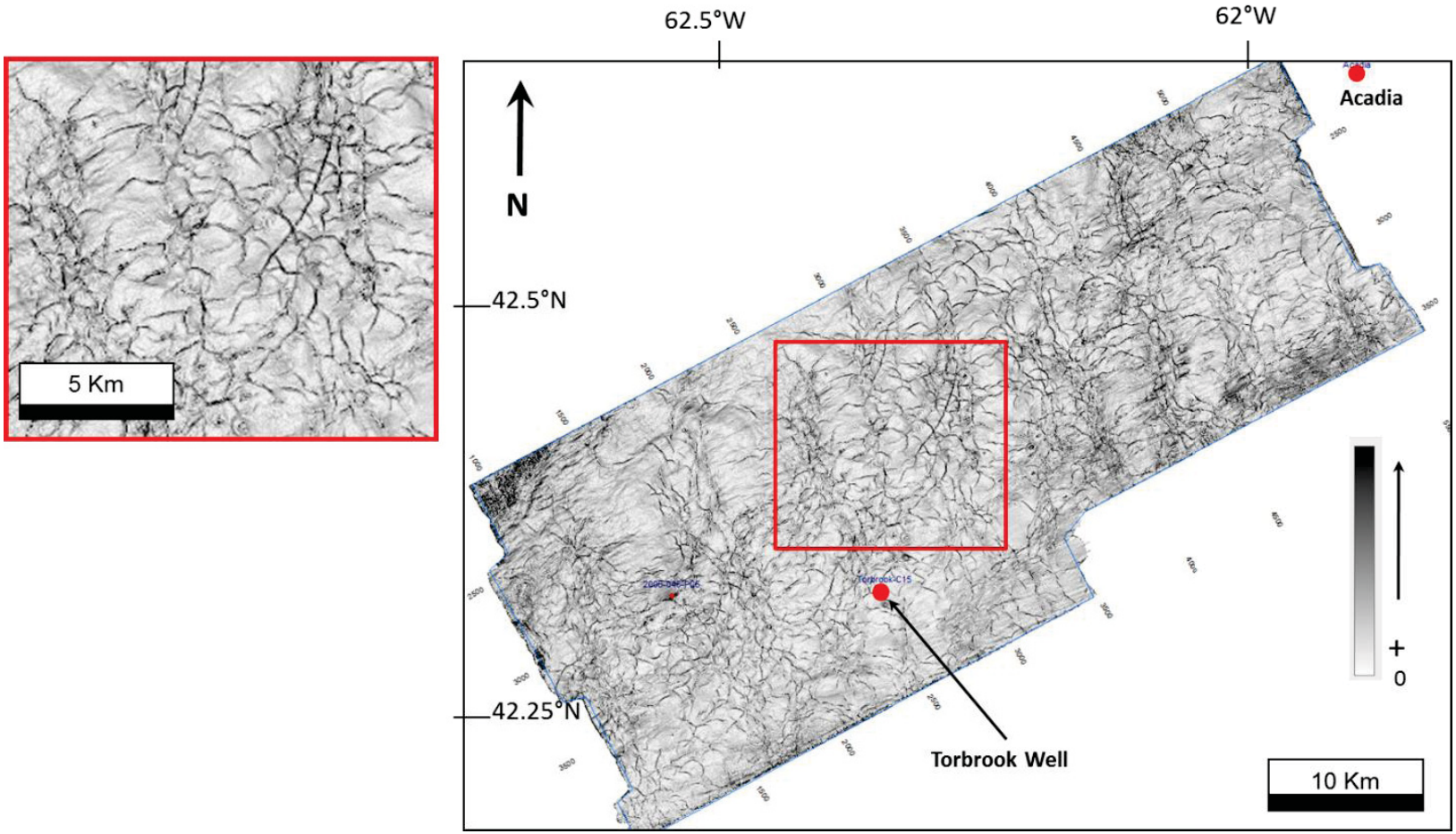

Figure 5.8 Map of the dip of maximum similarity on horizon 4 (Figure 5.2). A distinct fault pattern is visible due to the faults clustering on erosional highs. Inset shows the pattern in more detail.

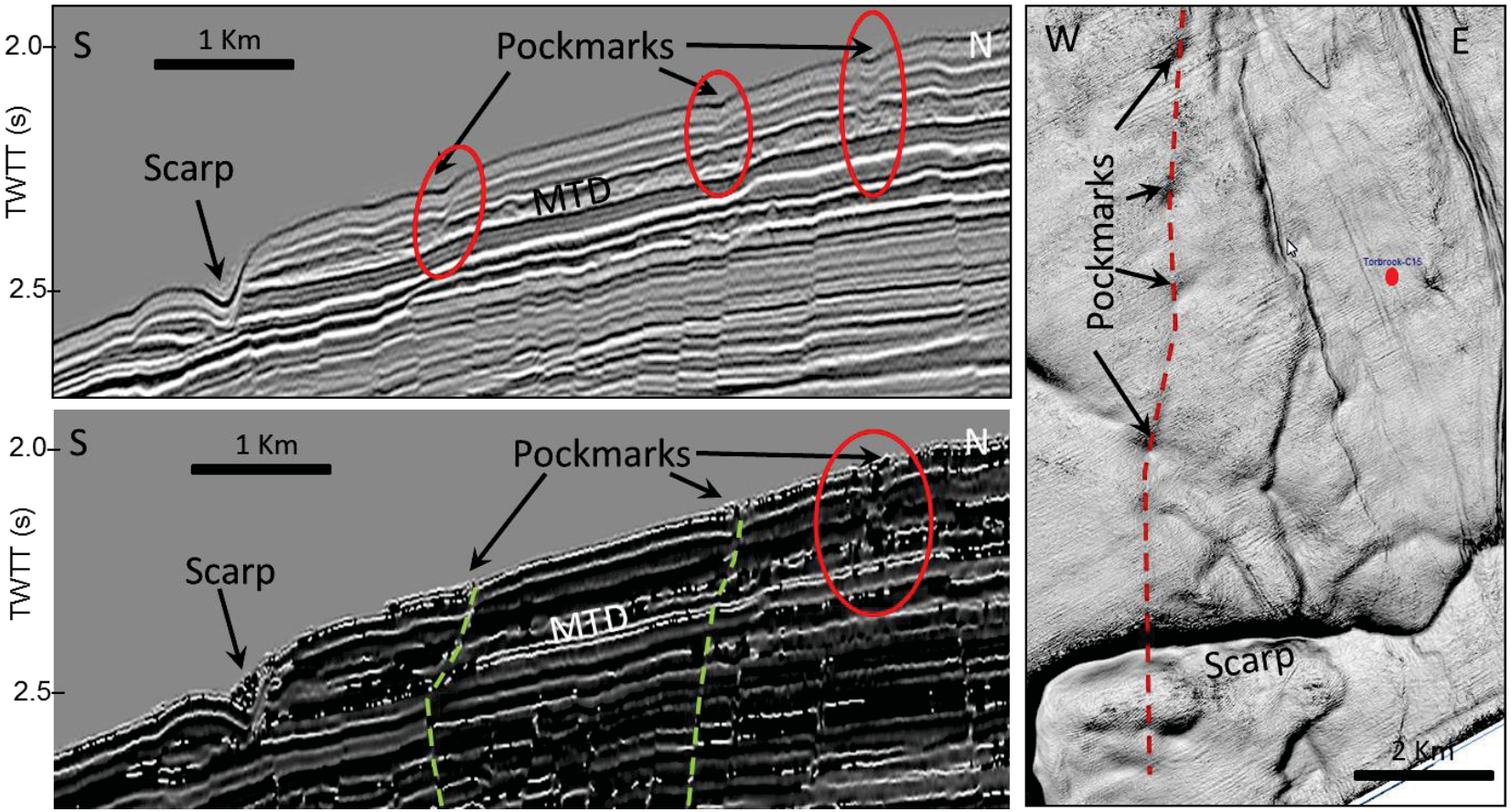

Figure 5.9 Pockmarks on the seafloor. Top Left: Seismic profile through the series of pockmarks on the seafloor (brown dashed line on the map to the right). Bottom Left: Instantaneous frequency attribute shows shallow changes in the seismic reflections. Two of the pockmarks shown appear to lie above faults (green dashed lines) which may have been reactivated. The rightmost pockmark appears confined to the shallow sediments suggesting it may be due to dewatering of the shallow MTD. Right: Location of the seismic profile on the seafloor. The red dot denotes the Torbrook C-15 well.

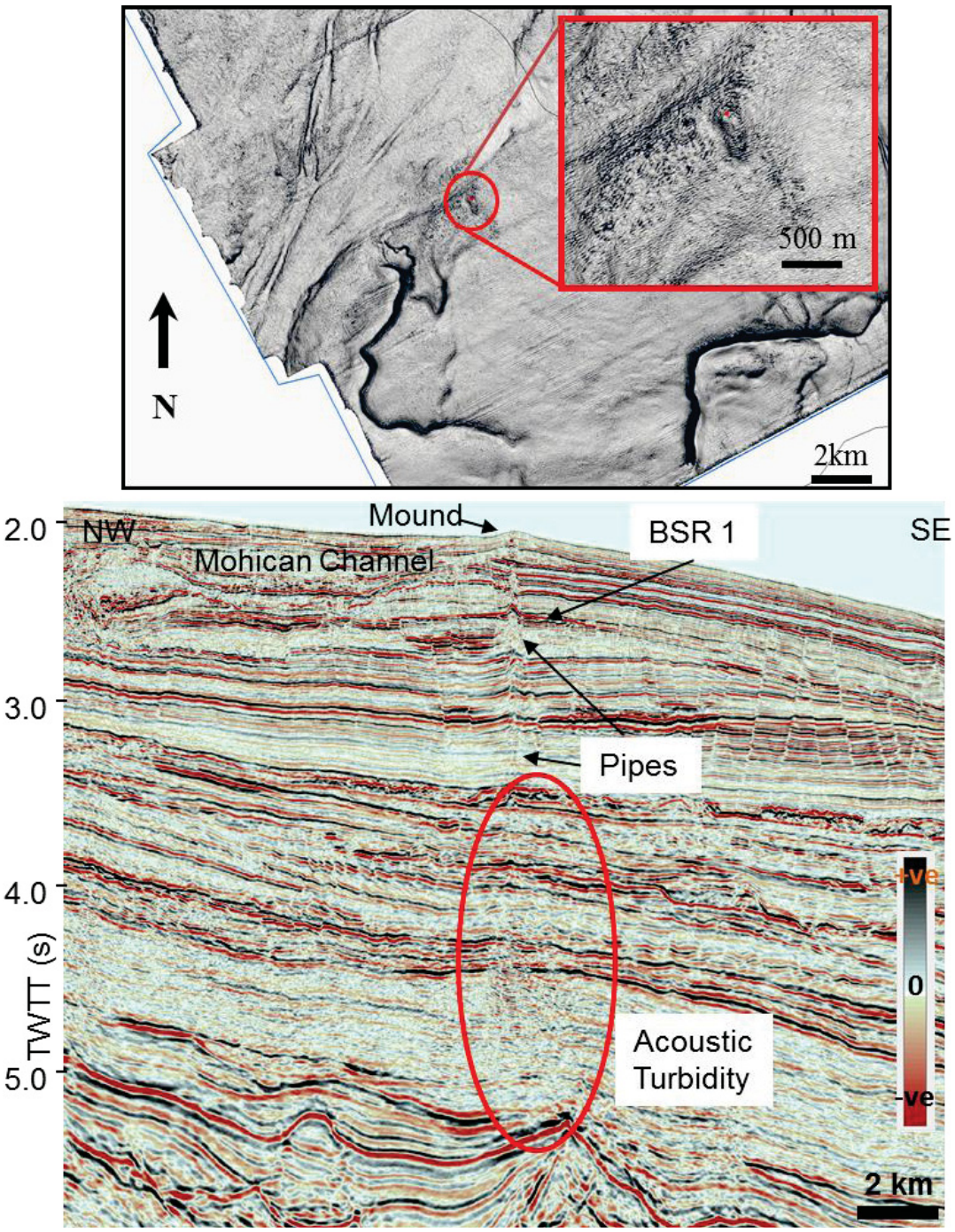

Figure 5.10 Seismic reflection profile showing characteristics of the Torbrook seafloor mound. Top: Dip of maximum similarity map for the seafloor showing the location of the mound, sampled by piston core 2006-046-006. Bottom: Seismic reflection profile through the seafloor mound. Pipes are visible from 2.0 to ~4.0 s twtt. Acoustic turbidity is visible deeper, below 4.0 s twtt and appears to originate from the deep structural high at ~ 5.2 s twtt.

be due to the presence of fluid or gas (Figure 5.9). Three pockmarks are located at the tops of faults that reach the seafloor. A fault cannot be identified at pockmark 4. A seismic reflection profile through the feature suggests it may instead be due to dewatering of a shallow MTD.

Two mounds are present on the seafloor west of the Torbrook C-15 well and east of the Mohican Channel. The largest mound rises approximately 10 m off the seafloor as measured on multibeam data, and has a diameter of ~ 250 m. Figure 5.10 shows a seismic profile through the feature which displays stacked acoustic disturbances matching the description of a seismic pipe (Cartwright et al., 2007, Huuse et al., 2010, Andresen et al., 2012). Pipes are visible between 2.0 and ~4.0 s twtt. An area of acoustic turbidity is visible below 4.0 s twtt and appears to originate from the deep structural high at ~ 5.2 s twtt. The Torbrook seafloor mound is located in the section of the study area with the strongest BSR amplitude response. Piston cores samples were taken in the area on CCGS Hudson cruises in 2004 and 2006 (Figure 5.1).

5.4.5 Paleo-Pockmarks and Mounds

Deeper in the stratigraphic section, paleo-pockmarks and mounds are considerably more common than modern seafloor features. Figures 5.11 and 5.12 show features on two of the horizons mapped within the Torbrook 3D seismic dataset (horizons 2 and 4, Figure 5.2).

The features present on horizon 2 are mainly pockmarks except for two distinct areas, one to the west associated with the modern seafloor mound and one to the east (Figure 5.11). Seismic profiles through both areas show that fluid flow features all root in deeper chaotic reflections at approximately 3.5 s twtt (Figure 5.5). Faults are associated with mounds in both locations and fault density appears similar.

The western mounds average 400 m in diameter while the eastern mounds are smaller with an average diameter of 250 - 300 m. In the central portion of the study area , pockmark

diameter ranges from 400 - 600 m. Seismic profiles show that most pockmarks occur at the top of faults which root in the deeper chaotic reflections approximately 3.5s twtt below the seafloor (Figure 5.5). Some seismic disturbances along the faults suggest that fluid or gas used these faults as pathways in the past, and there may be some gas-charged fluid remaining in situ after initial flow ceased. MTDs are visible throughout the shallow seismic section. The presence of pockmarks above these features suggests that overpressured fluid could have escaped from the MTDs during faulting, providing a pathway for fluid flow.

Horizon 4 features are a scattered combination of pockmarks and mounds (Figure 5.12). Most of the mounds occur in the west of the study area and average 400 m in diameter. Pockmarks are distributed over the entire study area and occur in two shapes: 1) circular with diameters of 200 – 600 m, and one particularly large pockmark in the west has a diameter of 740 m; and 2) oval or elongate features with a long axis of 200 - 450 m and a short axis of 100 - 200 m. The elongate pockmarks are preferentially oriented SW-NE and are found in the western portion of the study area

Seismic profiles through the area show disturbances along faults suggesting the presence of fluid flow pathways (Figure 5.5 and 5.10). The majority of the pathways go through horizon 3 (orange horizon - the BSR) but cease at or close to horizon 2 (blue horizon) suggesting that fluid flow was more prevalent in the recent past. The fault system present in the area is not as clearly defined on the seismic section below horizon 4 (green horizon) possibly due to lower contrast between stratigraphic reflections.

Pockmarks and mounds identified on horizons through the 3D seismic dataset all show seismic reflections truncating against the feature (Figures 5.11 and 5.12). This distinguishes the features from simple fill where the sediment drapes over the hole or mound already present. In

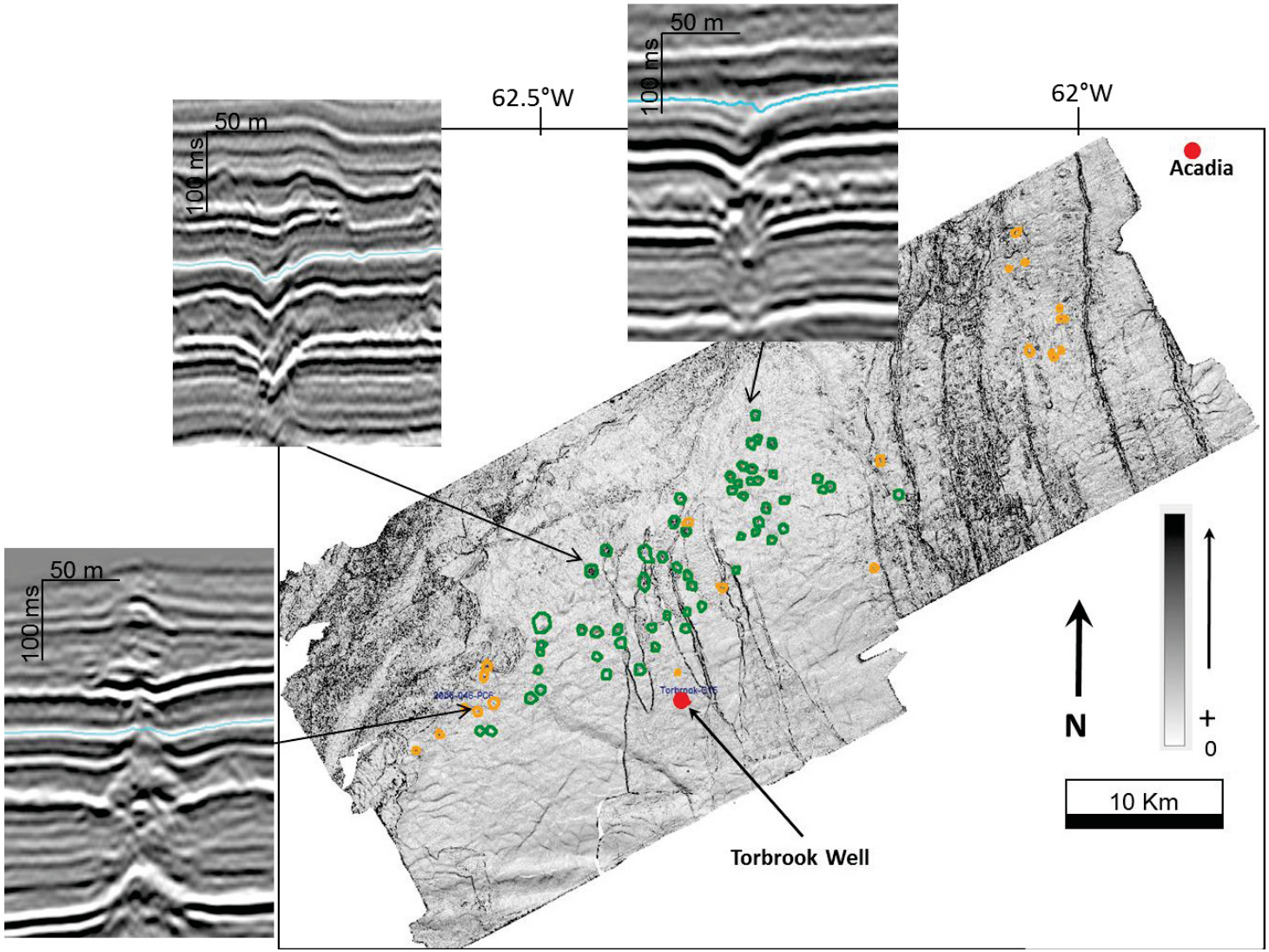

Figure 5.11 Map showing paleo-features on horizon 2. Pockmarks are marked with green polygons and mounds are marked with orange polygons. Zoom windows show pockmarks and mounds in detail. The blue line marks the location of horizon 2.

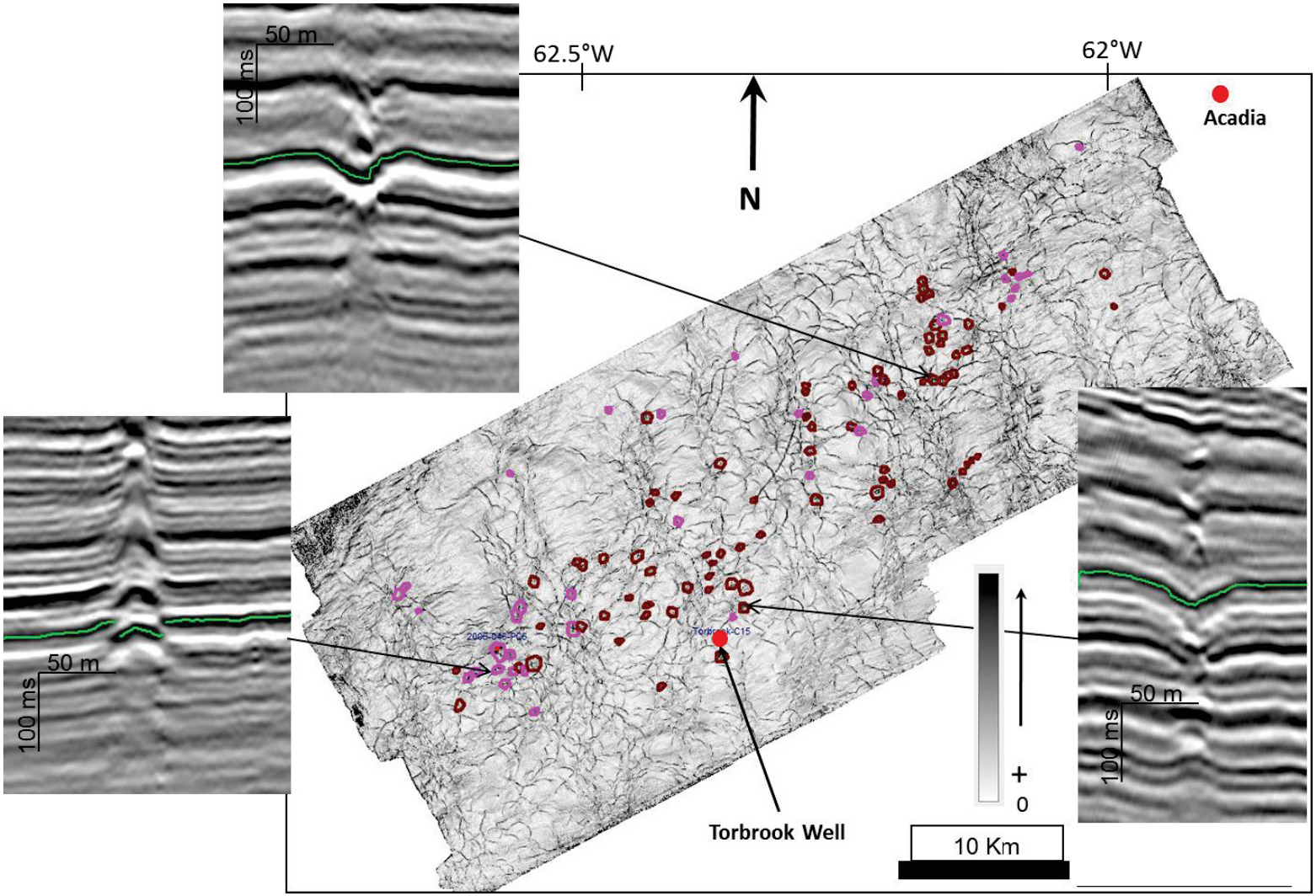

Figure 5.12 Map showing paleo-features on horizon 4. Pockmarks are marked with brown polygons and mounds are marked with pink polygons. Zoom windows show pockmarks and mounds in detail. The green line marks the locations of horizon 4.

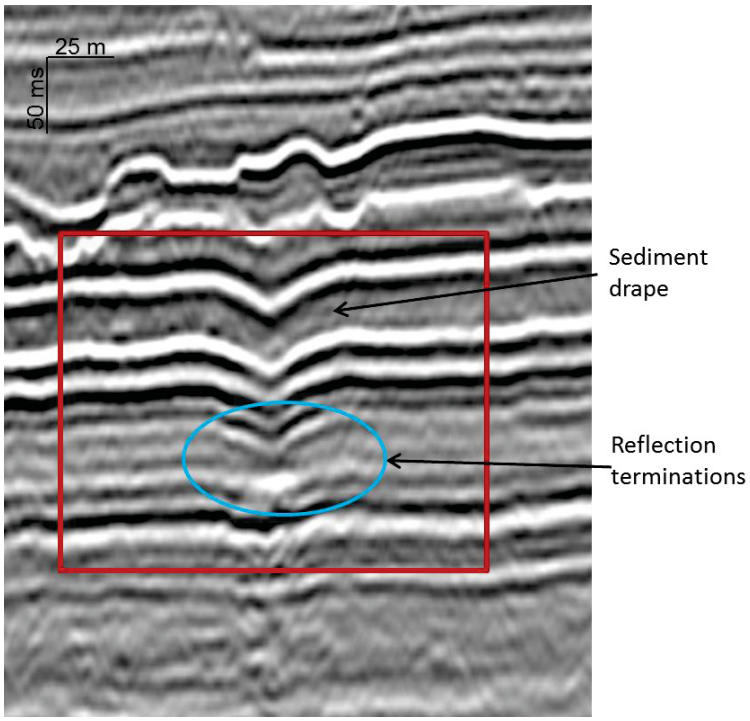

Figure 5.13 An example of pockmark versus fill. The blue oval marks the location of a pockmark on the paleo-seafloor identified by the presence of terminating reflections directly underneath the feature. The upper arrow identifies subsequent sediment fill which drapes along the pockmark. The sediment drape presents as an unbroken reflection with consistent thickness. Above this non-related chaotic reflections are visible. The pockmark was likely active in the section outlined by the red square.

that case, the seismic reflection is continuous across the pockmark and exhibits consistent thickness (Figure 5.13).

5.4.6 Gas Analyses

A series of cores, including a10 m core taken adjacent to the Torbrook seafloor mound, were collected on CCGS Hudson cruises 2004-030 and 2006-046 (Figure 5.1). Subsamples were taken from the piston cores as soon as the core samples were onboard and stored in a refrigerated container until interstitial gas concentration analyses could be completed.

Sample analysis at core site 2006-046-PC006 (adjacent to the Torbrook seafloor mound) confirms 99.95% methane gas exiting at the seafloor mound (Table 5.2). The core expanded upon recovery to the surface due to gas expansion when the core was removed from its in-situ pressure condition. This expansion resulted in the development of cracks in the sediment and liberation of free gas.

Gas origin was determined by plotting $\delta^{13}C$ of methane against the ethane to ethene ratio (Bernard et al., 2001). Results derived from Site 2006-046-PC006 (Table 5.2) plotted within the mixed zone tending towards the biogenic side suggesting that the source of the methane is microbial or biogenic rather than thermogenic (Figure 5.14).

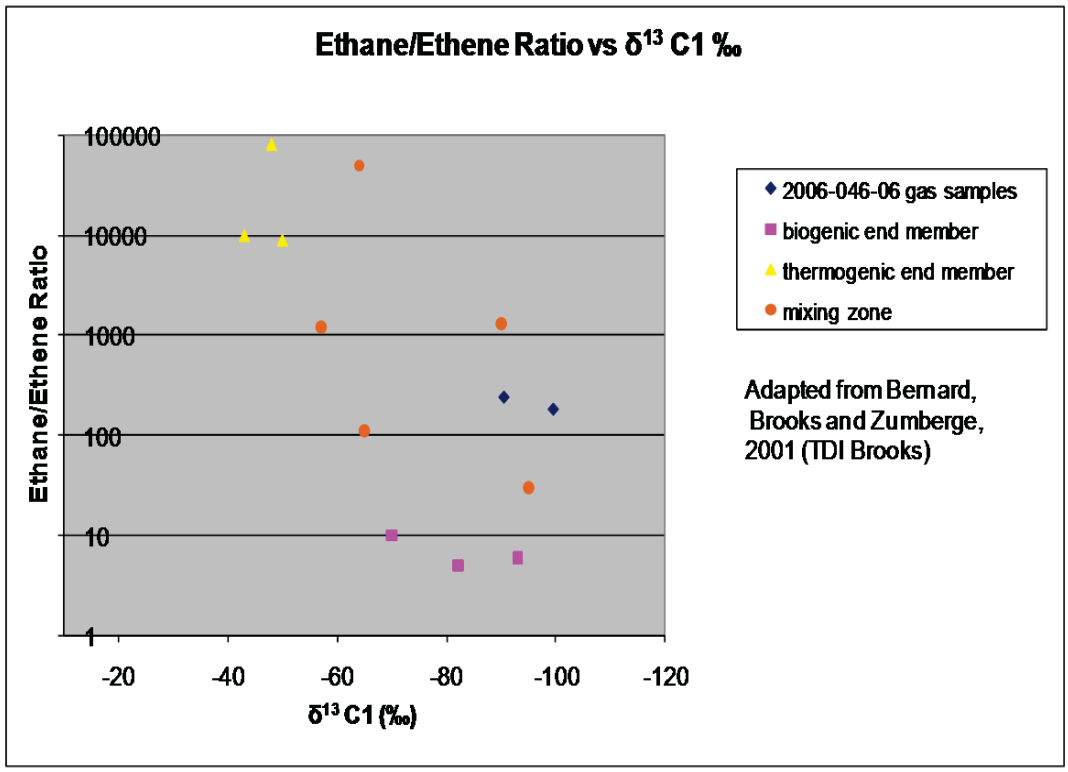

Figure 5.14 The two samples analysed for site 2006-046-PC006 (blue diamonds) are plotted on the right side of the graph in the mixed zone (orange dots) and tending towards the biogenic end member (pink squares) rather than the thermogenic end member (yellow triangles).

COMPOSITIONAL ANALYSES (PPM)							STABLE CARBON ISOTOPES			ETHANE /ETHENE RATIO	% METHANE
CORE SECTIONS		METHANE	ETHENE	ETHANE	PROPENE	PROPANE	C1	C2	C3		
2006-046-PC006	B/B	88,185.50	0.17	41.32	0.04	6.57	-90.6	-56.2	-23.5	243.06	99.95
2006-046-PC006	D/D	63,051.10	0.15	27.71	0.04	3.42	-99.5	-55.0	-23.3	184.73	99.95
2004-030-PC006	A/A	7,040.9	0.06	0.75	0.03	0.27				12.72	99.98
2004-030-PC006	C/C	3.2	0.08	0.11	0.03	0.10				1.43	84.82
2004-030-PC006	E/E	6.6	0.42	0.30	0.22	0.22				0.71	78.18
2004-030-PC006	G/G	2.0	0.14	0.14	0.05	0.11				0.99	71.63
2004-030-PC007	A/A	100,104.7	0.06	40.73	0.01	5.08				670.81	99.95
2004-030-PC007	C/C	88,527.2	0.09	44.75	0.02	6.74				520.37	99.94
2004-030-PC007	E/E	48,813.5	0.12	21.17	0.03	2.33				174.41	99.95
2004-030-PC008	A/A	31.7	0.12	0.27	0.06	0.14				2.22	95.57
2004-030-PC008	C/C	79.8	0.11	0.50	0.04	0.21				4.75	97.89
2004-030-PC008	E/E	14.9	0.11	0.32	0.08	0.18				2.89	92.92
2004-030-PC009	A/A	33,347.8	0.05	14.08	0.03	1.30				256.31	99.95
2004-030-PC009	C/C	26,958.9	0.10	15.90	0.04	1.82				161.29	99.93
2004-030-PC009	E/E	5,454.8	0.06	5.07	0.03	1.05				85.45	99.88
2004-030-PC014	A/A	5.9	0.10	0.18	0.03	0.09				1.71	88.27
2004-030-PC014	C/C	8.2	0.17	0.20	0.06	0.13				1.14	89.74
2004-030-PC014	E/E	6.9	0.17	0.20	0.08	0.12				1.18	77.57

Table 5.2 Results from cores for site 2006-046-PC006 and for cores from Hudson cruise 2004-030 showing the main compositional gases found; the percentage of gas which is methane; stable carbon isotope analyses for 2006-046-PC006; and the Ethane/Ethene ratio for each core sample. Stable carbon isotopes C1, C2 and C3 refer to Methane, Ethane and Propane respectively.

Other cores taken in the Mohican Channel area during Hudson cruise 2004-030 also showed high methane gas content and the cores themselves contain well over 90% methane gas (Table 5.2). As stable carbon isotope analyses were unavailable for any other cores, their source could not be determined using the method of Bernard et al. (2001). Calculation of the Ethane to Ethene ratios for each core sample, however, shows a peak ratio of 670.81 with an average value of approximately 200. Although still within the mixed zone, this result tends strongly towards the biogenic end member.

5.5 Discussion

Fluid flow appears focussed throughout the Torbrook dataset or was in the past when it travelled more-or-less vertically along fault planes. Polygonal faulting is present through the Torbrook 3D MCS dataset providing ample pathways for fluid migration. Formation of paleo-pockmarks and mounds dramatically declines around the late Pliocene – early Pleistocene which points to a relatively recent change in the hydrate stability regime. Paleo-pockmark and mound distribution through the Torbrook area suggests methane gas could have been transferred from depths into the gas hydrate stability zone over a wider area in the past. Delescluse et al. (2011) carried out 2D waveform tomography on 2D MCS lines running through the Torbrook study area. They discovered a high velocity response interpreted as gas hydrate in areas without a visible BSR suggesting that gas hydrate is present in at least 50 % of the study area. The enhanced parallel reflections found in the Torbrook 3D MCS dataset increase the area of the observed BSR to be more in line with that suggested by the work of Delescluse et al. (2011) (Figure 5.15). This would tie in with the acoustic disturbances and fluid flow features present throughout the Torbrook dataset rather than confined to the western area around the MC BSR 1. Delescluse et al. (2011) did not detect the presence of BSR 2 however. This could be due to two reasons: 1) BSR 2

is mis-identified as a response due to gas hydrate and instead could be due to another substance such as trapped water; or 2) the 2D tomography is not of high enough resolution to pick-up the more subtle feature underneath the BSR 1 as Delescluse et al. (2011) decimated the shot spacing to 94 m to avoid aliasing.

Acoustic disturbances visible on seismic profiles, such as through the Torbrook seafloor mound, indicate that the gas-charged fluids may be coming from deep within the stratigraphic section. The majority of fluid flow pathways in the area appear to come off the top of the chaotic reflections interpreted as widely distributed mass transport deposits (MTDs). The head gas analysis of samples from cores at site 2006-046-PC006 suggests a mixed origin for the gas tending towards a biogenic or microbial source rather than a thermogenic source. This suggests that thermogenic gas moved upwards from a deeper source and was reworked by in-situ bacteria, causing a mixed biogenic signature.

Pockmarks occur throughout the sedimentary section, although pipes and faults appear to bring gas and fluids from deeper within the section > 500 mbsf. Dewatering of buried MTD's (the chaotic reflections) appear to be the source of the fluids which travel along the faults up to what was the seafloor in the late Pliocene. There does not appear to be a water depth or hydrostatic control on pockmark or mound formation when compared to today's seafloor bathymetry.

Numerous MTD's through the area suggest that the sediment load may have changed since the Pliocene. Large scarps occur within the area of the observed BSR (Figure 5.1) and appear to occur at the edges of BSR 2 formation suggesting either slope failure changed the local stability regime or ongoing remobilisation of gas-charged fluids facilitated sediment failure.

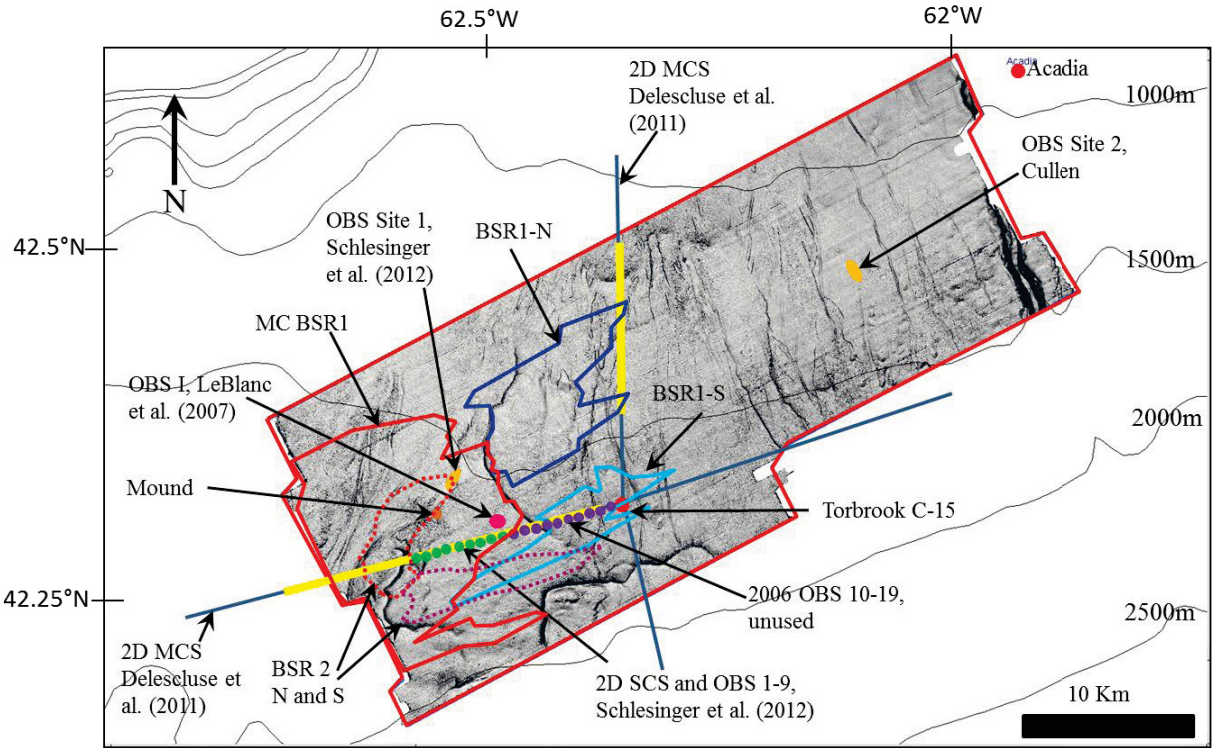

Figure 5.15 Locations of velocity models developed within the Torbrook area. OBS Sites 1 and 2 from this study are marked by orange ovals. LeBlanc et al. (2007) OBS I is marked by a pink circle. Delescluse et al. (2011) completed frequency domain 2D waveform tomography on regional 2D MCS data (blue lines). The areas showing a velocity response interpreted as gas hydrates are marked on the regional lines in yellow. Schlesinger et al. (2012) completed simultaneous travel-time inversion of 2D SCS and 9 OBS units in the west of the study area (green dots). The purple dots on the regional line mark 10 OBS locations without 2D inversion. The Torbrook and Acadia wells are marked with red dots and the Torbrook seafloor mound is marked with an orange dot. Three areas of visible BSR 1 are identified in the Torbrook 3D MCS dataset – classic cross-cutting reflections in the red polygon, enhanced parallel reflections in the dark blue and light blue polygons. Two areas of visible BSR 2 are interpreted also – classic cross-cutting reflections in the red dotted polygon and enhanced parallel reflections in the purple dotted polygon.

5.6 Conclusions

The Mohican Channel BSR is interpreted to occur over an area of 330.4 km^2. Enhanced parallel reflections identified in the seismic data are interpreted as a response due to gas hydrate formed within gently-dipping stratigraphic layers. This interpretation extends the area of the BSR

out to the locations identified by Delescluse et al. (2011) using 2D MCS tomography on regional lines as having a distinctive velocity response normally associated with the presence of gas hydrate.

Fluid flow features and polygonal faults are present throughout the study area not just in the area of the identified BSR. Numerous pockmarks and mounds occur throughout the study area on buried surfaces suggesting that fluid flow was active through the area until the late Pliocene, and then declined. Paleo-pockmarks frequently occur above the buried polygonal faults suggesting fluid moved along these faults from depth in the past. In contrast, only two mounds occur on the modern seafloor in the west of the study area indicating that active fluid flow has retreated westwards in area. Head gas analysis of samples from 2006-046-PC006 shows that almost 100% methane gas is carried through the pathways at this location. Examination of the seismic data shows that pipes transporting the gas-charged fluid at that site are visible from 2.0 – 4.0 s twtt while acoustic turbidity visible below 4.0 s twtt to come off a structural high at ~ 5.2 s twtt. These observations suggest that gas is carried from hydrocarbon-bearing sources at depth into the shallow gas hydrate stability zone.

Although pathways potentially move gas charged fluids from sources at depth over the entire study area, and gas appears widespread throughout the study area, BSRs are identified only in the western half of the study area. This suggests that the formation of gas hydrate is limited to the western half of the study area possibly due to the influence of lithology, trapping mechanisms or factors other than the presence of adequate fluid flow pathways.

CHAPTER 6 DISCUSSION

6.1 INTRODUCTION

The four objectives described in chapter 1 resulted in 1) an improved understanding of the extent of gas hydrate occurrence in the Torbrook area, 2) a description of fluid flow features which occur throughout the study area not just in the Mohican Channel area where a BSR is visible, 3) confirmation that wide-angle refraction and reflection studies can assist in detection of gas hydrates 4) new constraints on the volume of gas hydrate and free gas calculated in the Mohican Channel area. This chapter discusses the key findings of the study.

6.2 KEY RESULTS

6.2.1 Extent of Gas Hydrate in the Torbrook Area

The presence of gas hydrate is interpreted beyond the location of the visible BSR with reasonable confidence. A combination of advanced processing methods completed by Delescluse et al. (2011) and Schlesinger et al. (2012) show responses within velocity models consistent with the presence of gas hydrate and free gas. A seismic profile through the Torbrook area (Figure 6.1) shows an example of an enhanced parallel reflection with well-defined ends which continues eastwards from the cross-cut reflections, suggesting a solid gas hydrate is present here.

Identification of enhanced parallel reflections extending eastwards from the classic cross-cutting phase-reversed BSR coincided with the location of a high velocity zone identified on 2D MCS dataset by Delescluse et al. (2011). Equally important, the velocity models derived from OBS Site 2 indicate that gas hydrate is not present at that location in detectable quantities (Figure 5.15). Schlesinger (Ph.D. Thesis, 2012) examined a total of 19 OBS units (2006 survey) and determined that clear velocity signatures could be identified in the data from OBS 1 to 9 (green

dots in figure 5.15). The remaining 10 OBS (purple dots in figure 5.15) were of poor data quality and analysis showed that key refractions from below the low velocity zone were not identifiable. 2006 OBS units 10-19 are located directly outside the polygon marking the visible cross-cutting BSR and partly inside the area of enhanced parallel reflections (BSR1-S in figure 5.15). The enhanced parallel reflections cannot therefore be confirmed as a gas hydrate response using OBS data available to date.

6.2.2 Observed Fluid Flow Features

Fluid flow features are present throughout the Torbrook study area identified as acoustic disturbances along faults and by the presence of pockmarks or mounds at the tops of the faults. Seismic attribute analysis shows that paleo-pockmarks and mounds are scattered throughout the study area. In comparison the modern seafloor has a total of four identified pockmarks and two visible mounds.

The seafloor pockmarks to the west of the Torbrook C-15 well appear to have formed due to dewatering of the mass transport deposits several hundred metres below the seafloor. These modern pockmarks occur at the tops of faults which extend through the base of the MTD and reach the seafloor, indicating recent activity. The pockmarks do form a linear feature however, possibly the site of a future mass sediment failure (Figure 5.9).

The large mound reaching the seafloor in the west of the study area shows a distinctive pipe in profile with stacked acoustic disturbances and seismic pull-ups. Acoustic turbidity occurs at the interpreted base of the structure suggesting that the fluid is coming off a structural high about 5.2 s twtt below the seafloor (Figure 5.10). The presence of identifiable stratigraphic reflections along the pipe path suggests that fluid flow was not explosive or of volume high enough to rework the sediments.

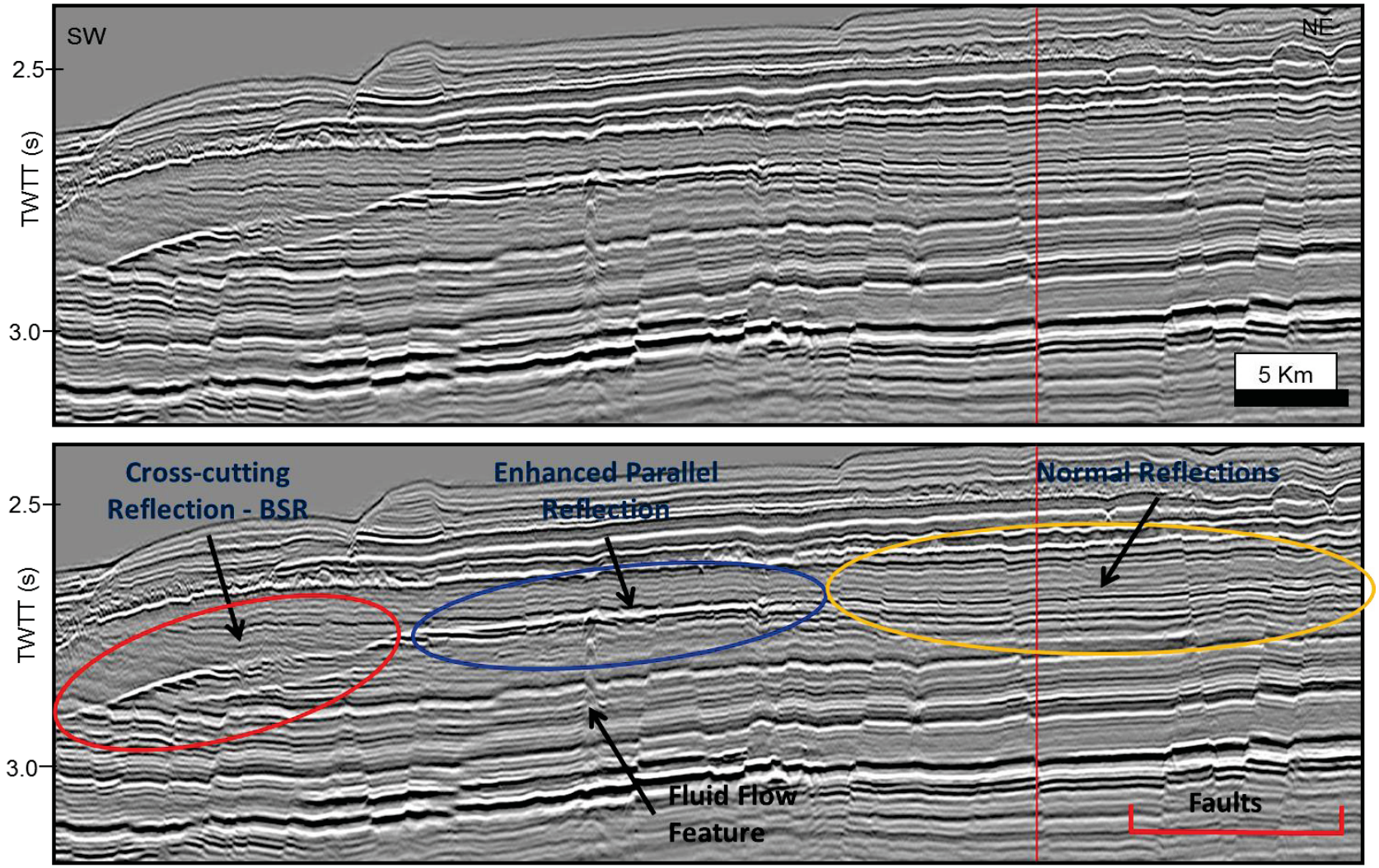

Figure 6.1 A seismic profile showing the change of reflection across the Torbrook area from west to east. The classic cross-cutting BSR is clearly identified in the west. An enhanced parallel reflection continues eastward from the BSR in the central section.

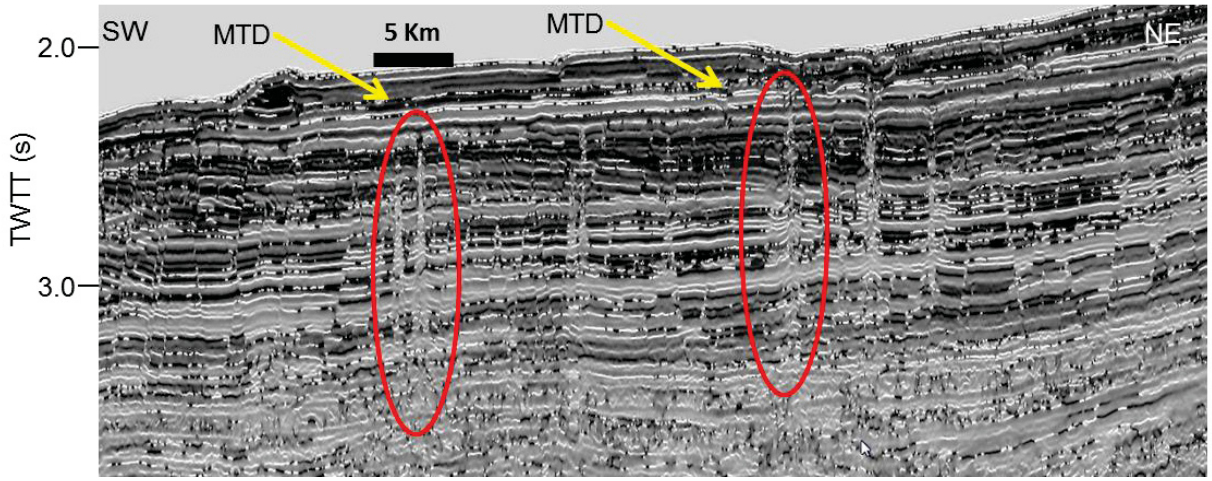

Figure 6.2 Instantaneous frequency plotted on a seismic reflection profile through the 3D seismic dataset. Fluid flow pathways are clearly visible in the profiles (red ovals). Few features reach the seafloor except along the scarps and channel edges.

Instantaneous frequency profiles show changes along faults east and west (Figures 5.9 and 6.2). Most changes appear to cease below a large regional Pliocene MTD. Some faults do extend to the seafloor in the areas of the seafloor scarps and along channel edges.

Pockmark size, density and structure vary around the globe. In general the shape of a pockmark is dictated by local conditions and processes. Seismic reflections at the depth of the BSR show relatively flat stratigraphy running essentially parallel to the seafloor. Large MTD's do occur through the stratigraphic section and above the Shubenacadie Drift. Dewatering is expected to occur as faults continue through the MTDs in some places suggesting reactivation or continuous activity. A small number of pockmarks are present on the seafloor suggesting that internal pressures have built to critical level in isolated areas. Preferred lateral migration at shallow depths would likely occur beneath the MTD until an exit such as a fault is encountered. Fluid from depths appears to come off the top of the erosional highs ~ 2 km below the seafloor (Figure 5.10).

Three types of hydrate accumulations are possible (as described by Milkov, 2002), each with specific fluid flow regime. The gas hydrate deposit in the Torbrook area is classified as a combination accumulation. The structural component is provided by the faulting present throughout the area. The stratigraphic component is provided by the favourable sedimentary conditions in the Shubenacadie Drift within which the gas hydrate stability zone occurs.

Marcon et al. (2014) found that mussel growth occurs is areas of high intensity fluid flow. Marcon et al. (2014) also found that clams occurred in areas of transient and low fluid flow activity. Recent seafloor video (2012) around the seafloor mound shows that brittle stars and cnidarians (radicipes spp) are visible throughout the area on a muddy substrate, but chemosynthetic communities and algal mats appear absent. The lack of chemosynthetic fauna suggests that the flow rate through the mound is too low to sustain chemosynthetic life on the seafloor. There is also no evidence of shallow or outcropping hydrates in the area.

6.2.3 Wide Angle Reflection and Refraction Studies, and Improved Volume Assessments

The variability apparent across the 2D velocity models from OBS Site 1 is consistent with variability discovered through drilling at locations such as Blake Ridge and Cascadia ODP Sites. The character of a BSR in seismic data and the physical character of gas hydrate in sediments are not necessarily consistent due to differences in scale or resolution. Less variability is seen on lower frequency seismic data than on very high frequency seismic data. It is unlikely that the 1D velocity models from the OBS data are able to completely resolve gas hydrate variability due to overlapping reflection points in the models.

The 2004 OBS Site 1 velocity models show a velocity increase of 150 - 270 m/s in a high velocity layer about 120 m thick and a decrease of 170-300 m/s in a low velocity layer ~100 m

thick. The 2006 OBS units 1 – 9 velocity models show a velocity increase of 140 m/s in a high velocity layer ~120 m thick and a decrease of 50-80 m/s in the low velocity layer (Schlesinger et al., 2012).

Schlesinger (2012) conducted volume assessments using the effective medium theory of Helgerud et al. (1999) based on the rock physics model of Dvorkin et al. (1999). The 2004 OBS Site 1 velocity models yielded a gas hydrate concentration of 8 – 18 % while the 2006 OBS units 1 – 9 velocity models resulted in a gas hydrate concentration of 2 – 11 % (see figure 5.15 for locations). The variations are due to a number of factors. The modelled velocities for 2004 OBS Site 1 are higher than those found at the 2006 OBS units 1 – 9 corresponding to a higher gas hydrate concentration calculation. In contrast the free gas calculations for the two locations resulted in concentrations below 1% in the sediments at 310 – 320 mbsf. The 2004 array is a 1km long array located close to the Mohican Channel while the 2006 array stretched 9 km from the channel edge to the SE.

The results from the suite of velocity models available for the study area indicate lateral variation of gas hydrate concentrations. The models suggest a reduction of gas hydrate concentrations away from the Mohican Channel most likely due to variations in sediment composition at the depth of the BSR such as increased mud content, which would reduce pore space available for gas hydrate formation (Figure 6.3). The overall amount of gas hydrate present in the area is much less than the predicted potential of the Nova Scotian margin. Overall low gas hydrate concentrations and variable distribution suggest that global estimates of gas hydrate along passive margins are likely exaggerated.

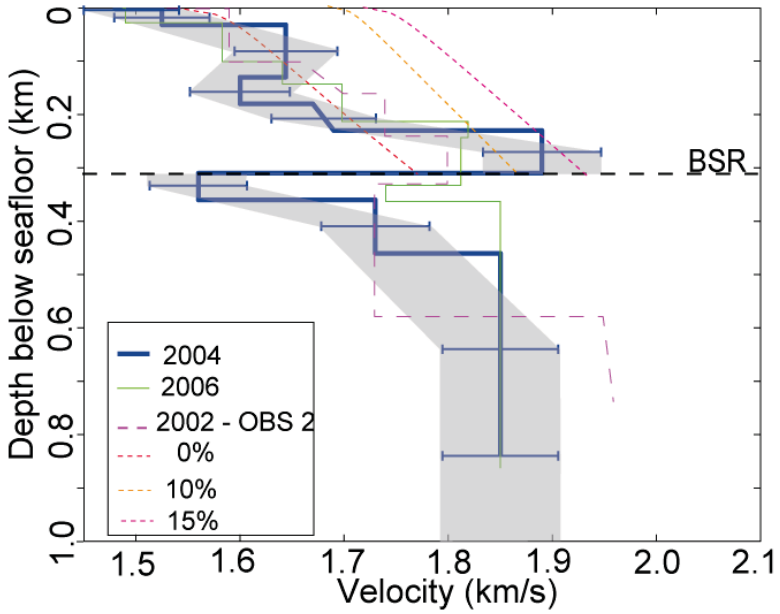

Figure 6.3 Velocity-depth profiles for 2002, 2004 and 2006 OBS data. Top: 1-D velocity-depth profile (thick blue line) obtained by averaging the 2004 2-D velocity model at constant depth below the seafloor, with approximate error estimates (grey shaded area) and error bars for the interval velocities based on the sensitivity analysis in figure 8 of Schlesinger et al. 2012. The high velocity region is more prominent for the 2004 model than for the 2006 model (thin green line) or for the model of Leblanc et al. (2007) based on a 2002 OBS survey (purple dashed line); OBS2 from this survey was located 2 km south of the 2004 array. The velocity drop of ~300 m/s at a depth of ~310 m below seafloor indicates the base of the gas hydrate stability zone (BGHSZ). The red-dashed line is the reference velocity profile calculated with the parameters of Table 1 in Schlesinger et al. (2012) and standard rock-physics modelling (Dvorkin et al., 1999; Helgerud et al., 1999) assuming no gas hydrate and free gas in the pore space of the sediments. The orange dashed line is a reference velocity profile with the same physical parameters including 10% gas hydrate in the sediment. However, results of the 2004 model suggest even higher values, about 13 ± 5% (pink dashed line). (From Schlesinger et al. 2012).

6.2.4 Differences between Modelled BGHSZ and Observed BSR

Calculations used to determine the expected BGHSZ have consistently placed the calculated BGHSZ depth for the Mohican Channel area at ~ 510 m below the seafloor using current pressure-temperature conditions. This is considerably deeper than the observed BSR (at ~

320 m) which is understood to mark the velocity contrast between high velocity gas hydrate and low velocity free gas in sediments (Figure 4.10). BSRs mark the pressure-temperature conditions of the BGHSZ at the time of formation. It is generally assumed, until further evidence arises, that the gas hydrate in a location formed under recent pressure-temperature conditions. However, in a situation such as this where the observed BSR is shallower than the calculated BGHSZ, further examination of the modeling parameters is necessary.

Perturbation of the modeling parameters (using the method described by Leon et al. (2009)) show that this difference in depth between the calculated BGHSZ and the observed BSR can possibly be caused by three factors: 1) a change in water depth or sediment thickness; 2) higher local geothermal gradient, or 3) higher bottom water temperature.

Modelling shows that if water depth were to decrease then the BGHSZ would move upwards. Although sea level has dropped during glacial periods in the past along the Scotian margin, there is no evidence of a 200 m fall. Therefore sea level decrease would not be a practical explanation for the difference between the observed BSR and the calculated BGHSZ in the Mohican Channel area.

This model is unable to account for lithostatic pressures and/or overpressures. Hydrostatic pressure is not practical in fine-grained sediments as there has to be some lithological influence. Model complexity would need to increase to account for sediment density and composition.

If the geothermal gradient increased in the model, then the BGHSZ would move upwards. The Scotian margin is a passive one and has an overall lower geothermal gradient than an active margin. A small suite of heat flow measurements are available from cruises completed in 2004 and 2009 on the Scotian margin. The heat flow measurements varied more than expected over the five year gap indicating that bottom temperatures may be unstable in the region. Temperatures

may vary non-linearly within the sediment. A series of deeper heat flow measurements are needed on the Scotian margin to define the sediment temperatures and provide high-confidence geothermal gradient parameters for BGHSZ models.

It is possible that bottom water temperatures may have increased in the interglacial periods e.g. the Mid-Pliocene warm period from 3.29-2.97 Ma, ~300,000 years. Evidence for a bottom water temperature increase of 5 °C on the Scotian Shelf is however lacking and so an increase in bottom water temperature is considered an impractical solution.

A combination of high-quality sediment temperature measurements and increased model complexity, to include lithostatic pressures and sediment composition, must first be explored to determine if the discrepancy between the modelled BGHSZ and observed BSR can be explained without requiring more extreme possibilities.

CHAPTER 7 CONCLUSIONS

7.1 SUMMARY

Gas hydrate is interpreted to occur adjacent to the Mohican Channel over an area approximately 330 km^2. Velocity models show that gas hydrate concentration varies laterally with the greatest concentrations appearing to occur near the Mohican Channel edge and reducing eastwards. This lateral variation is believed due to changes in lithology and pore space at the depth of the BSR within the Shubenacadie Drift which covers the study area. The Drift formed due to reworking and winnowing of sediments which removed mud and increased pore spacing in places allowing gas hydrate to form. Free gas concentrations below the BSR remain low at <1%. The velocity models from OBS Site 2 in the east of the study area show that gas hydrate and free gas are not present in detectable quantities in this area. Gas hydrate concentrations vary over the area from 2 to 18%. Highest concentrations, estimated from velocity analyses, appear parallel with the strongest observed BSR response in the west of the study area. Overall low gas hydrate concentrations, variable distribution and poor fit of the observed vs modelled stability field suggest that global estimates of gas hydrate along passive margins are likely exaggerated.

Fluid flow features are present throughout the Torbrook area. Deep hydrocarbon sources are known to occur along the Scotian margin (OERA PFA, 2011) and the presence of near-vertical faults would enable gas-charged fluids to move directly from depth into the gas hydrate stability zone. Paleo-pockmarks and mounds suggest that fluid flow was active in the region until the late-Pliocene to early-Pleistocene when a regional change occurred and fluid flow was dramatically reduced.

Modelling of the base of the gas hydrate stability zone adjacent to the Mohican Channel produces a 200 m difference between the observed BSR (~320 mbsf) and the calculated base of the gas hydrate stability zone (~510 mbsf). Model parameter testing suggests that the difference is due to geothermal gradient values. A suite of deep temperature readings are required in the study area to determine if the model result is due to inaccurate geothermal gradient values, or to the possibility that the geothermal gradient was higher at the time of gas hydrate formation.

7.2 Recommendations for Future Work

1. A series of high-quality heat flow measurements across the Scotian margin would improve model parameters;
2. An increase in the complexity of the gas hydrate stability zone modelling to include lithostatic parameters;
3. Sediment composition parameters could possibly be improved by tying in wells which were logged from seafloor to bottom of the well.

REFERENCES

Andreassen, K., Berteussen, K.A., Sognnes, H., Henneberg, K., Langhammer, J., Mienert, J., 2003. Multicomponent ocean bottom cable data in gas hydrate investigation offshore of Norway. Journal of Geophysical Research, v. 108, no. B8, pp. 11.

Andresen, K.J., 2012. Fluid flow features in hydrocarbon plumbing systems: What do they tell us about the basin evolution. Marine Geology, v. 332-334, p. 89-108.

Bernard, B.B., Brooks, J.M., and Zumberge, J., 2001. Determining the origin of gases in near-surface sediments. AAPG Hedberg Conference "Near-Surface Hydrocarbon Migration: Mechanisms and Seepage Rates", September 2001, Vancouver, B.C., Canada.

Berndt, C., Buenz, S., and Mienert, J., 2003. Polygonal fault systems on the mid-Norwegian margin; a long-term source for fluid flow. Geological Society Special Publications, v.216, 283-290.

Berndt, C., Bunz, S., Clayton, T., Mienert, J., and Saunders, M., 2004, Seismic character of bottom simulating reflectors: examples from the mid-Norwegian margin. Marine and Petroleum Geology, v. 21, p. 723-733.

Berndt, C., 2005. Focused fluid flow in passive continental margins. Phil. Trans. R. Soc. A, v.363, p. 2855-2871.

Birchwood, R., Dai, J., Shelander, D., Boswell, R., Collett, T., Cook, A., Dallimore, S., Fujii, K., Imasato, Y., Fukuhara, M., Kusaka, K., Murray, D., Saeki, T., 2010. Developments in Gas Hydrates. Oilfield Review 22:1, p. 18-33.

Bunz, S., Mienert, J., Vanneste, M., Andresen, K.J., 2005. Case History: Gas hydrates at the Storegga Slide : Constraints from an anlaysis of multicomponent, wide-angle seismic data. Geophysics 70, B19-B34.

Campbell, D.C., Shimeld, J.W., Mosher, D.C., Piper, D.J.W., 2004. Relationships between sediment mass-failure modes and magnitudes in the evolution of the Scotian Slope, offshore Nova Scotia. Offshore Technology Conference, pp.14.

Campbell, D.C., Mosher, D.C., 2010. Middle to late Miocene slope failure and the generation of a regional unconformity beneath the western Scotian Slope, eastern Canada., in *Submarine Mass Movements and their Consequences IV*, Vol. 28. Advances in Natural and Technological Hazards Research. Springer Science + Business Media B.V. 2010, pp. 645-656.

Campbell, D.C., 2011. The Late Cretaceous and Cenozoic Geological History of the Outer Continental Margin off Nova Scotia, Canada: Insights into Margin Evolution from a Mature Passive Margin, Ph.D. Thesis, Dept. of Earth Sciences, Dalhousie University, Halifax, Nova Scotia, Canada.

Campbell, D.C., Deptuck, M.E., 2012. Alternating bottom-current-dominated and gravity-flow-dominated deposition in a lower slope and rise setting - insights from the seismic geomorphology of the western Scotian margin, eastern Canada, in *Application of the Principles of Seismic Geomorphology to Continental-Slope and Base-of-Slope Systems: Case Studies from Seafloor and Near-Seafloor Analogues*, SEPM Special Publication No. 99 ed. SEPM (Society for Sedimentary Geology), pp. 329-346.

Cartwright, J. A., 1994. Episodic basin-wide hydrofracturing of overpressured early Cenozoic mudrock sequences in the North Sea basin. Marine and Petroleum Geology, 11(5), p. 587-607.

Cartwright, J. A., 1996. Polygonal fault systems; a new type of fault structure revealed by 3-D seismic data from the North Sea basin. AAPG Studies in Geology, 42, p. 225-230.

Cartwright, J. A., and Lonergan, L., 1996. Volumetric contraction during the compaction of mudrocks; a mechanism for the development of regional-scale polygonal fault systems. Basin Research, 8(2), p. 183-193.

Cartwright, J. A., and Dewhurst, D. A., 1998. Layer-bound compaction faults in fine-grained sediments. GSA Bulletin, v. 110, p. 1242-1257.

Cartwright, J.A., 2007. The impact of 3D seismic data on the understanding of compaction, fluid flow and diagenesis in sedimentary basins. Journal of the Geological Society of London, 164(5), p. 881-893.

Cartwright, J.A., 2011. Diagenetically induced shear failure of fine-grained sediments and the development of polygonal fault systems. Marine and Petroleum Geology, 28(9), p. 1593-1610.

Collett, T.S., Riedel, M., Boswell, R., Cochran, J.R., Kumar, P., Sethi, A.K., Sathe, A.V., NGHP Expedition-01 Scientific Party, 2006. International team completes landmark gas hydrate expedition in the offshore of India. Fire in the Ice Newsletter, v.6, i. 3, p. 1-4.

Collett, T. S., Johnson, A. H., Knapp, C. C., Boswell, R., 2009. Natural gas hydrates; a review. AAPG Memoir 89, 1-4, p. 146-219.

Crutchley, G.J., Gorman, A.R., Pecher, I.A., Toulmin, S., Henry, S.A., 2011. Geological controls on focused fluid flow through the gas hydrate stability zone on the southern Hikurangi Margin of New Zealand, evidenced from multi-channel seismic data. Marine and Petroleum Geology, v. 28, i. 10, p. 1915 – 1931.

Dallimore, S.R., Collett, T.S., 2005. Scientific results from the Mallik 2002 gas hydrate production research well program, MacKenzie Delta, Northwest Territories, Canada. Bulletin 585, Geological Survey of Canada.

Dash, R., Spence, G., 2011. P-wave and S-wave velocity of northern Cascadia margin gas hydrates. Geophy. J. Int., vol. 187, p. 1363 – 1377.

Davies, R. J., Ireland, M. T., and Cartwright, J. A., 2009. Differential compaction due to the irregular topology of a diagenetic reaction boundary; a new mechanism for the formation of polygonal faults. Basin Research, 21(3), p. 354-359.

Del Grosso, V. A., 1974. New equation for the speed of sound in natural waters (with comparisons to other equations). The Journal of the Acoustical Society of America, v. 56(4), p. 1084-1091.

Delescluse, M., Nedimovic, M.R., Louden, K.E., 2011. Case History: 2D waveform tomography applied to long-streamer MCS data from the Scotian Slope. Geophysics 76, B151-B163.

Deptuck, M.E., 2011. Proximal to distal postrift structural provinces on the western Scotian Margin, offshore Eastern Canada: Geological context and parcel prospectivity for Call-for-Bids NS11-1. Geoscience Open File Report 2011-001MF, Canada – Nova Scotia Offshore Petroleum Board, Halifax, Nova Scotia, pp. 181.

Dewhurst, D.N., Cartwright, J.A., Lonergan, L., 1999. The development of polygonal fault systems by syneresis of colloidal sediments. Marine and Petroleum Geology, v.16(8), p. 793-810.

Gay, A., Lopez, M., Cochonat, P., 2004. Polygonal faults-furrows system related to early stages of compaction – upper Miocene to recent sediments of the Lower Congo Basin. Basin Research 16, p. 101-116.

Gay, A., Lopez, M., Cochonat, P., Levache, D., Sermondadaz, G., and Seranne, M., 2006a. Evidences of early to late fluid migration from an upper Miocene turbiditic channel revealed by 3D seismic coupled to geochemical sampling within seafloor pockmarks, Lower Congo Basin: Marine and Petroleum Geology, v. 23, p. 387-399.

Gay, A., Lopez, M., Cochonat, P., Seranne, M., Levache, D., and Sermondadaz, G., 2006b. Isolated seafloor pockmarks linked to BSRs, fluid chimneys, polygonal faults and stacked Oligocene-Miocene turbiditic palaeochannels in the Lower Congo Basin: Marine Geology, v. 226, p. 25-40.

Gay, A., Berndt, C., 2007a. Cessation/reactivation of polygonal faulting and effects on fluid flow in the Voring Basin, Norwegian Margin. Journal of the Geological Society 164, p. 129-141.

Gay, A., Lopez, M., Berndt, C., Seranne, M., 2007b. Geological controls of focused fluid flow associated with seafloor seeps in the Lower Congo Basin. Marine Geology 244, p. 68-92.

Ginsburg, G.D., Milkov, A.V., Soloviev, V.A., Egorov, A.V., Cherkashev, G.A., Vogt, P.R., Crane, K., Lorenson, T.D., Khutorskoy, M.D., 1999. Gas hydrate accumulation at the Haakon Mosby mud volcano. Geo-Marine Letters, v. 19, p. 57 – 67.

Goulty, N. R., 2008. Geomechanics of polygonal fault systems; a review. Petroleum Geoscience, v. 14, i. 4, p. 389-397.

Hansen, D.M., Shimeld, J.W., Williamson, M.A., Lykke-Andersen, H., 2004. Development of a major polygonal fault system in Upper Cretaceous chalk and Cenozoic mudrocks of the Sable Subbasin, Canadian Atlantic margin. Marine and Petroleum Geology 21, p. 1205-1219.

Hardage, B. A., Roberts, H. H., & Herron, D., 2006. Gas hydrate in the Gulf of Mexico; what and where is the seismic target? Leading Edge, 25(5), p. 566-571.

Helgerud, M. B., Dvorkin, J., Nur, A., Sakai, A., and Collett, T. S., 1999. Elastic-wave velocity in marine sediments with gas hydrates; effective medium modeling. Geophysical Research Letters, 26(13), p. 2021-2024.

Herbozo, G., Hubscher, C., Kaul, N., Wagner, M., Pecher, I.A., Kukowski, N., 2013. Influence of recent depositional and tectonic controls on marine gas hydrates in Trujillo Basin, Peru Margin. Marine Geology 340, p. 30-48.

Holbrook, W. S., Hoskins, H., Wood, W. T., Stephen, R. A., and Lizarralde, D., 1996. Methane hydrate and free gas on the Blake Ridge from vertical seismic profiling. Science, 273(5283), p. 1840-1843.

Hornbach, M.J., Holbrook, W.S., Gorman, A.R., Hackwith, K.L., Lizarralde, D., Pecher, I., 2003. Direct seismic detection of methane hydrate on the Blake Ridge. Geophysics, v. 68, no. 1, p. 92-100.

Hustoft, S., Mienert, J., Bunz, S., Nouze, H., 2007. High-resoultion 3D-seismic data indicate focussed fluid migration pathways above polygonal fault systems of the mid-Norwegian margin. Marine Geology 245, p. 89-106.

Huuse, M., Jackson, C. L., Van Rensbergen, P., Davies, R. J., Flemings, P. B., and Dixon, R. J., 2010. Subsurface sediment remobilization and fluid flow in sedimentary basins: an overview. Basin Research, 22(4), p. 342-360.

Hyndman, R.D., Spence, G.D., 1992. A seismic study of methane hydrate marine bottom simulating reflectors. Journal of Geophysical Research 97, p. 6683-6698.

Hyndman, R.D., Yuan, T., Moran, K., 1999. The concentration of deep sea gas hydrates from downhole electrical resistivity logs and laboratory data. Earth and Planetary Science Letters 172, p. 167-177.

Hyndman, R. D., Spence, G. D., Chapman, R., Riedel, M., and Edwards, R. N., 2001, Geophysical Studies of marine gas hydrate in Northern Cascadia, in *Natural Gas Hydrates: Occurrence, Distribution and Detection*, Geophysical Monograph, 124, p. 273-295, American Geophysical Union.

Jansa, L. F., and Wade, J. A., 1975. Geology of the continental margin off Nova Scotia and Newfoundland, Offshore Geology of Eastern Canada, Paper 74-30, Geological Survey of Canada, p. 51-105.

Jenner, K. A., Piper, D. J., Campbell, D. C., and Mosher, D., 2007, Lithofacies and origin of late Quaternary mass transport deposits in submarine canyons, central Scotian Slope, Canada. Sedimentology, v. 54, p. 19-38.

Johnson, A.H. 2011. Global resource potential of gas hydrate – a new calculation. Proceedings of the 7th International Conference on Gas Hydrates (ICGH 2011), Edinburgh, Scotland, U.K.

King, L.H., MacLean, B., 1970. Pockmarks on the Scotian Shelf. Geological Society of America Bulletin 81, p. 3141-3148.

Laurent, D., Gay, A., Baudon, C., Berndt, C., Soliva, R., Planke, S., Mourgues, R., Lacaze, S., Pauget, F., Mangue, M., Lopez, M., 2012. High-resolution architecture of a polygonal fault interval inferred from geomodel applied to 3D seismic data from the Gjallar Ridge, Voering Basin, Offshore Norway. Marine Geology, 332-334, p. 134-151.

LeBlanc, C., Louden, K., Mosher, D., 2007. Gas hydrates off Eastern Canada: Velocity models from wide-angle seismic profiles on the Scotian Slope. Marine and Petroleum Geology, 24, p. 321-335.

Lee, S., UBGH2 Science Party, 2011. 2nd Ulleung Basin Gas Hydrate Expedition (UBGH2): Findings and Implications. Fire in the Ice Newsletter, v. 11, p. 6-9.

Leon, R., Somoza, L., Gimenez-Moreno,C.J., Dabrio, C. J., Ercilla, G., Praeg, D., Diaz-del-Rio, V., Gomez-Delgado, M., 2009. A predictive numerical model for potential mapping of the gas hydrate stability zone in the Gulf of Cadiz. Marine and Petroleum Geology, 26(8), p. 1564-1579.

Loseth, H., Gading, M., and Wensaas, L., 2009. Hydrocarbon leakage interpreted on seismic data. Marine and Petroleum Geology, 26(7), p. 1304-1319.

Loseth, H., Wensaas, L., Arntsen, B., Hanken, N., Basire, C., and Graue, K., 2011. 1000 m long gas blow-out pipes. Marine and Petroleum Geology, 28(5), p. 1047-1060.

Lonergan, L., Cartwright, J. A., and Jolly, R., 1998. The geometry of polygonal fault systems in Tertiary mudrocks of the North Sea. Journal of Structural Geology, v. 20, p. 529-548.

MacKay, M.E., Jarrad, R.D., Westbrook, G.K., Hyndman, R.D., Shipboard Scientific Party of Ocean Drilling Program Leg 146, 1994. Origin of bottom simulating reflectors: Geophysical evidence from the Cascadia accretionary prism. Geology, v. 22, p. 459-462.

Mackenzie, K. V., 1981. Nine-term equation for sound speed in the oceans. The Journal of the Acoustical Society of America, 70(3), p. 807-812.

Majorowicz, J.A., Osadetz, K.G., 2001. Gas hydrate distribution and volume in Canada. AAPG Bulletin, v. 85, p. 1211-1230.

Majorowicz, J.A., Osadetz, K.G., 2003. Natural gas hydrate stability in the east coast offshore – Canada. Natural Resources Research, v. 12, no. 2, p. 93-104.

Majorowicz, J.A., Osadetz, K.G., Safanda, J., 2013. Methane gas hydrate stability models on continental shelves in response to glacio-eustatic sea level variations: examples from Canadian oceanic margins. Energies 6, p. 5575-5806.

Mao, W.L., Koh, C.A., Sloan, E.D. 2007. Clathrate hydrates under pressure. Physics Today, October 2007, p. 42-47.

Marcon, Y., Ondreas, H., Sahling, H., Bohrmann, G., Olu, K. 2014. Fluid flow regimes and growth of a giant pockmark. Geology, v. 42, no. 1, p. 63-66.

Matsumoto, R., Hiromatsu, M., Sato, M., YK10-08 Shipboard Scientists, 2011. Fluid flow and evolution of gas hydrate mounds of Joetsu Basin, eastern margin of Japan Sea: Constraints from high-resolution geophysical survey by AUV. Proceedings of the 7th International Conference on Gas Hydrates (ICGH 2011), Edinburgh, Scotland, U.K. pp. 11.

Max, M.D., Lowrie, A. 1997. Oceanic methane hydrate development: Reservoir character and extraction. Offshore Technology Conference, Houston, Texas, U.S.A. OTC 8300, p. 235-240.

Medwin, H., 1975. Speed of sound in water: A simple equation for realistic parameters. The Journal of the Acoustical Society of America, 58(6), p. 1318-1319.

Milkov, A.V., Sassen, R., 2002. Economic geology of offshore gas hydrate accumulations and provinces. Marine and Petroleum Geology, 19, p. 1-11.

Milkov, A.V., 2004. Global estimates of hydrate-bound gas in marine sediments: how much is really out there? Earth Science Reviews 66, p. 183-197.

Mosher, D., Piper, D. J., Campbell, D. C., and Jenner, K. A., 2004. Near-surface geology and sediment-failure geohazards of the central Scotian Slope. AAPG Bulletin, v. 88, p. 703-723.

Mosher, D. C., Louden., K., LeBlanc, C., Shimeld, J. W., and Ozadetz, K., 2005. Gs Hydrates Offshore Eastern Canada: Fuel for the Future. Offshore Technology Conference, Houston, Texas, U.S.A. OTC 17588, pp. 9.

Mosher, D.C. 2011. A margin-wide BSR gas hydrate assessment: Canada's Atlantic margin. Marine and Petroleum Geology, 28, p. 1540-1553.

National Energy Technology Laboratory, 2011. Energy Resource Potential of Methane Hydrate: An Introduction to the Science and Energy Potential of a Unique Resource. U.S. Department of Energy.

Negulic, E., Louden, K.E., Wielens, H., Mukhopadhyah, P., Nedimovic, M., 2011. Thermal modelling of the central Scotian Slope, offshore Eastern Canada: Seafloor heat flow data, hydrocarbon maturation potential and the effects of salt on heat flow. Central and North Atlantic Conjugate Margins Conference, Lisbon, Spain. Vol. IV, p. 207 – 210.

Offshore Energy Research Association of Nova Scotia, 2011. Play Fairway Analysis Atlas. Last accessed September 2014 at http://www.oera.ca/offshore-energy-research/geoscience.

Ostanin, I., Anka, Z., di Primio, R., Bernal, A., 2012. Identification of a large Upper Cretaceous polygonal fault network in the Hammerfest basin: Implications on the reactivation of regional faulting and gas leakage dynamics, SW Barents Sea. Marine Geology, 332-334, p. 109-125.

Ostanin, I., Anka, Z., di Primio, R., Bernal, A., 2013. Hydrocarbon plumbing systems above the Snohvit gas field: Structural control and implications for thermogenic methane leakage in the Hammerfest Basin, SW Barents Sea. Marine and Petroleum Geology, 43, p. 127-146.

Paull, C.K., Matsumoto, R., 2000. Leg 164 Overview in *Proceedings of the Ocean Drilling Program, Scientific Results,* Vol. 164, p. 3 – 10, College Station, Tx.

Pause, P.H., 2011. Fire from ice: Methane hydrate petroleum systems and resources. AAPG Search and Discovery Article #80193. Last accessed August 2014, http://www.searchanddiscovery.com/documents/2011/80193pause/ndx_pause.pdf.

Pecher, I.A., Henrys, S.A., Wood, W.T., Kukowski, N., Crutchley, G.J., Fohrmann, M., Kilner, J., Senger, K., Gormann, A.R., Coffin, R.B., Greinert, J., Faure, K., 2010. Focussed fluid flow on the Hikurangi Margin, New Zealand – Evidence from possible local upwarping of the base of gas hydrate stability. Marine Geology, 272, p. 99-113.

Piper, D. J., 2001. The Geological Framework of Sediment Instability on the Scotian Slope: Studies to 1999. Geological Survey of Canada Open File 3920.

Piper, D. J., and Campbell, D. C., 2002. Surficial geology of the Scotian Slope, eastern Canada. Geological Survey of Canada Report 2002-E15, pp.12.

Piper, D. J., and Ingram, S., 2003. Major Quaternary sediment failures on the east Scotian Rise, eastern Canada. Current Research 2003-D1, Geological Survey of Canada.

Piper, D. J., 2005. Late Cenozoic evolution of the continental margin of eastern Canada. Norwegian Journal of Geology, v. 85, p. 305-318.

Plaza-Faverola, A., Bunz, S., Mienert, J., 2012. The free gas zone beneath gas hydrate bearing sediments and its link to fluid flow: 3-D seismic imaging offshore mid-Norway. Marine Geology 291-294, 211-226.

Ramaswamy, V., Boucher, O., Haigh, J., Hauglustaine, D., Haywood, J., Myhre, G., Nakajima, T., Shi, G.Y., Solomon, S., 2001. Chapter 6: Radiative Forcing of Climate Change, in *Climate Change 2001: The Scientific Basis. Contribution of Working Group I to the Third Assessment Report of the Intergovernmental Panel on Climate Change*. Cambridge University Press, Cambridge, U.K. and New York, U.S.A., p. 351-416.

Riedel, M., Novosel, I., Spence, G.D., Hyndman, R.D., Chapman, R.N., Solem, R.C., Lewis, T., 2006. Geophysical and geochemical signatures associated with gas hydrate-related venting in the northern Cascadia margin. GSA Bulletin 118, p. 23-38.

Ruppel, C.D., 2011a. Methane Hydrates and Contemporary Climate Change. Last accessed August 2014 at http://www.nature.com/scitable/knowledge/library/methane-hydrates-and-contemporary-climate-change-24314790.

Ruppel, C.D., 2011b. MITEI Natural Gas Report, Supplementary Paper 4 on Methane Hydrates: Methane hydrates and the Future of Natural Gas. Last accessed August 2014 at http://mitei.mit.edu/system/files/Supplementary_Paper_SP_2_4_Hydrates.pdf.

Ruppel, C., Noserale, D., 2012. Gas hydrates and climate warming – Why a methane catastrophe is unlikely. Last accessed September 2014 at http://soundwaves.usgs.gov/2012/06/.

Schlesinger., A., 2012. A study of gas hydrates with ocean-bottom-seismometer data on the east coast of Canada. Ph.D. Thesis, Dept. of Earth and Ocean Sciences, University of Victoria, B.C., Canada.

Schlesinger, A., Cullen, J., Spence, G., Hyndman, R., Louden, K., Mosher, D., 2012. Seismic velocities on the Nova Scotian margin to estimate gas hydrate and free gas concentrations. Marine and Petroleum Geology, 35, p. 105-115.

Shankar, U., Riedel, M., 2013. Heat flow and gas hydrate saturation estimates from Andaman Sea, India. Marine and Petroleum Geology 43, p. 434-449.

Shedd, W., Frye, M., Boswell, R., Hutchinson, D. R., and Godfriaux, P., 2009. Variety of seismic expression of the base of gas hydrate stability in the Gulf of Mexico, USA. Abstracts: Annual Meeting - American Association of Petroleum Geologists.

Shedd, W., Boswell, R., Frye, M., Godfriaux, P., Kramer, K., 2012. Occurrence and nature of "bottom simulating reflectors" in the northern Gulf of Mexico. Marine and Petroleum Geology, v. 34, i. 1, p. 31-40.

Sheriff, R. 2002. Encyclopedic dictionary of Applied Geophysics, 4th Edition. Published by Society of Exploration Geophysicists.

Shimeld, J., 2004. A comparison of salt tectonic subprovinces beneath the Scotian Slope and Laurentian Fan. 24th Annual GCSSEPM Research Conference "Salt-Sediment Interactions and Hydrocarbon Prospectivity: Concepts, Applications and Case Studies for the 21st Century", Houston, Tx..

Shipley, T. H., Houston, M. H., Buffler, R. T., Shaub, F. J., McMillen, K. J., Ladd, J. W., and Worzel, J. L., 1979. Seismic evidence for widespread possible gas hydrate horizons on continental slopes and rises. AAPG Bulletin, 63(12), p. 2204-2213.

Singh, S.C., Minshull, T.A., 1994. Velocity structure of a gas hydrate reflector at Ocean Drilling Program site 889 from a global seismic waveform inversion. Journal of Geophysical Research, v. 99, no. B12, p. 24221-24233.

Skarke, A., Ruppel, C., Kodis, M., Brothers, D., Lobecker, E., 2014. Widespread methane leakage from the sea floor on the northern US Atlantic margin. Nature Geoscience, v. 7, i. 9, p. 657 – 661.

Sloan, E.D., 2003. Fundamental Principles and Applications of Natural Gas Hydrates. Nature 426, p. 353-363.

Smith, S.L. and Judge A.S. 1993. Gas hydrate database for Canadian Arctic and selected east coast wells. Geological Survey of Canada Open File 2746, pp.54.

Stuevold, L. M., Faerseth, R. B., Arnesen, L., Cartwright, J., and Moller, N., 2003. Polygonal faults in the Ormen Lange field, More Basin, Offshore mid-Norway. Geological Society Special Publications, 216, p. 263-281.

Suess, E., Bohmann, G., Greinert, J., and Lausch, E., 1999, Flammable Ice: Scientific American, v. 281, p. 76-83.

Suess, E., Torres, M. E., Bohrmann, G., Collier, R. W., Rickert, D., Goldfinger, C., Linke, P., Heuser, A., Sahling, H., Heeschen, K., Jung, C., Nakamura, K., Greinert, J., Pfannkuche, O., Trehu, A., Klinkhammer, G., Whiticar, M.J., Eisenhauer, A., Teichert, B., Elvert, M., 2000. Sea floor methane hydrates at Hydrate Ridge, Cascadia margin in *Natural Gas Hydrates: Occurrence, Distribution and Detection*, Geophysical Monograph 124, p. 87-98, American Geophysical Union.

Sun, Y., Wu, S., Dong, D., Ludmann, T., Gong, Y., 2012. Gas hydrates associated with gas chimneys in fine-grained sediments of the northern South China Sea. Marine Geology 311-314, p. 32-40.

Tinivella, U., Giustiniani, M. 2012. An overview of Mud Volcanoes associated to Gas Hydrate System. Ch. 6 in *Updates in Volcanology – New Advances in Understanding Volcanic Systems,* p. 225 - 267.

Torres, M.E., Trehu, A.M., Cespedes, N., Kastner, M., Wortmann, U.G., Kim, J., Long, P., Malinverno, A., Pohlman, J.W., Riedel, M., Collett, T., 2008. Methane hydrate formation in turbidite sediments of northern Cascadia, IODP Expedition 311. Earth and Planetary Science Letters 271, p. 170-180.

Trehu, A.M., Long, P.E., Torres, M.E., Bohrmann, G., Rack, F.R., Collett, T.S., Goldberg, D.S., Milkov, A.V., Riedel, M., Schultheiss, P., Bangs, N.L., Barr, S.R., Borowski, W.S., Claypool, G.E., Delwichs, M.E., Dickens, G.R., Gracia, E., Guerin, G., Holland, M., Johnson, J.E., Lee, Y-J., Liu, C-S., Su, X., Teichert, B., Tomaru, H., Vanneste, M., Watanabe, M., Weinberger, J.L., 2004. Three-dimensional distribution of gas hydrate beneath southern Hydrate Ridge: constraints from ODP Leg 204. Earth and Planetary Science Letters, v. 222, p. 845-862.

Tucholke, B.E., Bryan, G.M., Ewing, J.I., 1977. Gas-hydrate horizons detected in seismic-profiler data from the Western North Atlantic. AAPG Bulletin, v. 61, no. 5, p. 698-707.

Vadakkepuliyambatta, S., Bunz, S., Mienert, J., Chand, S., 2013. Distribution of sub-surface fluid flow systems in the SW Barents Sea. Marine and Petroleum Geology, v. 43, p. 208 – 221.

Wade, J. A., and MacLean, B. C., 1990. Chapter 5 The geology of the southeastern margin of Canada: Aspects of the geology of the Scotian Basin from recent seismic and well data, in *Geology of the Continental margin of Eastern Canada No. 2: The Geology of North America/Geology of Canada*, p. 190-238.

Westbrook, G. K., Carson, B., Shipboard Scientific Party, 1994. Summary of Cascadia drilling results. Proceedings of the Ocean Drilling Program, Part A: Initial Reports, 146, Part 1, p. 389-396.

Weston, J.F., MacRae, A.R., Ascoli, P., Cooper, K.E., Fensome, R.A., Shaw, D., Williams, G., 2012. A revised biostratigraphic and well-log sequence-stratigraphic framework for the Scotian Margin, offshore eastern Canada. Canadian Journal of Earth Sciences Special Issue: Mesozoic-Cenozoic Geology of the Scotian Basin, v. 49, p. 1417-1462.

Wilson, W. D., 1960. Equation for the speed of sound in sea water. The Journal of the Acoustical Society of America, 32(10), p. 1357-1357.

Winguth, A.M., Thomas, E., Winguth, C., 2012. G lobal decline in ocean ventilation, oxygenation, and productivity during the Paleocene-Eocene Thermal Maximum: Implications for the benthic extinction. Geology, v. 40, no. 3, p. 263 – 266.

Wong, G. S., Zhu, S. M., 1995. Speed of sound in seawater as a function of salinity, temperature, and pressure. The Journal of the Acoustical Society of America, 97(3), p. 1732-1736.

Wood, W.T., and Ruppel, C., et al. 2000. Seismic and thermal investigations of the Blake Ridge gas hydrate area: a synthesis. in *Proceedings of the ODP, Scientific Results, 164*. College Station, TX (Ocean Drilling Program), p. 253–264.

Wood, W., Jung, W., 2008. Modeling the extent of Earth's marine methane hydrate cryosphere, Proceedings of the 6th International Conference on Gas Hydrates (ICGH 2008), July 6-10, 2008, Vancouver, British Columbia, Canada, pp. 8.

Wu, Y. 2007. Crustal structure of the central Nova Scotia margin and the transition from volcanic to non-volcanic rifting off eastern Canada. Ph.D. Thesis, Dalhousie University, Halifax, Canada.

Yuan, T., Hyndman, R. D., Spence, G. D., and Desmons, B., 1996. Seismic velocity increase and deep-sea gas hydrate concentration above a bottom-simulating reflector on the northern Cascadia continental slope. Journal of Geophysical Research, v. 101, p. 13655-13671.

Yuan, T., Spence, G. D., Hyndman, R. D., Minshull, T. A., and Singh, S. C., 1999. Seismic velocity studies of a gas hydrate bottom-simulating reflector on the northern Cascadia continental margin: Amplitude modeling and full waveform inversion. Journal of Geophysical Research, v. 104, p. 1179-1191.

Zhang, Z., Han, D., and Yao, Q., 2011. Quantitative interpretation for gas hydrate accumulation in the eastern Green Canyon area, Gulf of Mexico using seismic inversion and rock physics transform. Geophysics, 76(4), B139-B150.

Zelt, C. A., and Ellis, R. M., 1988. Practical and efficient ray tracing in two-dimensional media for rapid traveltime and amplitude forward modelling. Journal of the Canadian Society of Exploration Geophysicists, 24(1), p. 16-31.

Zelt, C. A., and Smith, R. B., 1992. Seismic traveltime inversion for 2-D crustal velocity structure. Geophysical Journal International, 108(1), p. 16-34.

Zelt, C. A., 1999. Modelling strategies and model assessment for wide-angle seismic traveltime data. Geophysical Journal International, 139(1), p. 183-204.

APPENDIX A STUDENT CONTRIBUTION TO MANUSCRIPT

MANUSCRIPT AUTHORS:	Angela Schlesinger, Janette Cullen, George Spence, Roy Hyndman, Keith Louden, David Mosher
MANUSCRIPT TITLE:	Seismic velocities of the Nova Scotian margin to estimate gas hydrate and free gas concentrations
JOURNAL:	Marine and Petroleum Geology
DOI:	10.1016/j.marpetgeo.2012.03.008
STUDENT CONTRIBUTION:	Provided ten 1D velocity models for the paper; provided information on processing and modeling methods used; reviewed drafts; discussed background, results and conclusions.

APPENDIX B COPYRIGHT PERMISSION FOR SCHLESINGER ET AL. (2012) IN APPENDIX C.

Copyright Clearance Center RightsLink®

Home | Account Info | Help

Title: Seismic velocities on the Nova Scotian margin to estimate gas hydrate and free gas concentrations

Author: Angela Schlesinger,Janette Cullen,George Spence,Roy Hyndman,Keith Louden,David Mosher

Publication: Marine and Petroleum Geology

Publisher: Elsevier

Date: August 2012

Logged in as: Janette Cullen

LOGOUT

Order Completed

Thank you very much for your order.

This is a License Agreement between Janette Cullen ("You") and Elsevier ("Elsevier"). The license consists of your order details, the terms and conditions provided by Elsevier, and the payment terms and conditions.

Get the printable license.

License Number	3411911327249
License date	Jun 18, 2014
Licensed content publisher	Elsevier
Licensed content publication	Marine and Petroleum Geology
Licensed content title	Seismic velocities on the Nova Scotian margin to estimate gas hydrate and free gas concentrations
Licensed content author	Angela Schlesinger,Janette Cullen,George Spence,Roy Hyndman,Keith Louden,David Mosher
Licensed content date	August 2012
Licensed content volume number	35
Licensed content issue number	1
Number of pages	11
Type of Use	reuse in a thesis/dissertation
Portion	full article
Format	both print and electronic
Are you the author of this Elsevier article?	Yes
Will you be translating?	No
Title of your thesis/dissertation	Geophysical Character of the Mohican Channel Gas Hydrate, Nova Scotia, Eastern Canada
Expected completion date	Sep 2014
Estimated size (number of pages)	200
Elsevier VAT number	GB 494 6272 12
Permissions price	0.00 USD
VAT/Local Sales Tax	0.00 USD / 0.00 GBP
Total	0.00 USD

5 August 2014

Journal of Marine and Petroleum Geology,
Elsevier Inc., 1600 John F. Kennedy Boulevard Suite 1800,
Philadelphia PA 19103-2879 USA

I am preparing my M.Sc. thesis for submission to the Faculty of Graduate Studies at Dalhousie University, Halifax, Nova Scotia, Canada. I am seeking your permission to include a manuscript version of the following paper in an Appendix of the thesis:
Title: Seismic velocities on the Nova Scotian margin to estimate gas hydrate and free gas concentrations
Authors: Angela Schlesinger, Janette Cullen, George Spence, Roy Hyndman, Keith Louden, David Mosher
Journal: Marine and Petroleum Geology, Vol. 35, Iss. 1, August 2012, p. 105-115
DOI: 10.1016/j.marpetgeo.2012.03.008

Canadian graduate theses are reproduced by the Library and Archives of Canada (formerly National Library of Canada) through a non-exclusive, world-wide license to reproduce, loan, distribute, or sell theses. I am also seeking your permission for the material described above to be reproduced and distributed by the LAC(NLC). Further details about the LAC(NLC) thesis program are available on the LAC(NLC) website (www.nlc-bnc.ca).

Full publication details and a copy of this permission letter will be included in the thesis.

Yours sincerely,
Janette Cullen

Permission is granted for:

a. the inclusion of the material described above in your thesis.
b. for the material described above to be included in the copy of your thesis that is sent to the Library and Archives of Canada (formerly National Library of Canada) for reproduction and distribution.

From: Permissions Helpdesk [mailto:permissionshelpdesk@elsevier.com]
Subject: RE: request to include manuscript in thesis Appendix

Dear Janette,
Permission is covered by the rights you retain as an Elsevier journal author as outlined at http://www.elsevier.com/journal-authors/author-rights-and-responsibilities, which include Inclusion in a thesis or dissertation, provided that proper acknowledgement is given to the original source of publication. Should you require any further clarification, please let me know.
Thank you,
Permissions Helpdesk Associate
Elsevier
1600 John F. Kennedy Boulevard
Suite 1800
Philadelphia, PA 19103-2899
Questions about obtaining permission: whom to contact? What rights to request?
When is permission required? Contact the Permissions Helpdesk at:
+1-800-523-4069 x 3808 *permissionshelpdesk@elsevier.com*

APPENDIX C SCHLESINGER ET AL., 2012. SEISMIC VELOCITIES ON THE NOVA SCOTIAN MARGIN TO ESTIMATE GAS HYDRATE AND FREE GAS CONCENTRATIONS

Authors: Angela Schlesinger, Janette Cullen, George Spence, Roy Hyndman, Keith Louden, David Mosher

Abstract:

This article provides new constraints on gas hydrate and free gas concentrations in the sediments at the margin off Nova Scotia. Two-dimensional (2-D) velocity models were constructed through simultaneous travel-time inversion of ocean-bottom seismometer (OBS) data and 2-D single-channel seismic (SCS) data acquired in two surveys, in 2004 and 2006. The surveys, separated by ~5 km, were carried out in regions where the bottom-simulating reflection (BSR) was identified in seismic reflection datasets from earlier studies and address the question of whether the BSR is a good indicator of significant gas hydrate on the Scotian margin. For both datasets, velocity increases by 200 to 300 m/s at a depth of approximately 220 m below seafloor (mbsf), but the results of the 2006 survey show a smaller velocity decrease (50 to 80 m/s) at the base of this high velocity layer (310 - 330 mbsf) than the results of the 2004 survey (130 m/s). When converted to gas hydrate concentrations using effective medium theory, the 2-D velocity models for both datasets show a gas hydrate layer of ~100 m thickness above the identified BSR. Gas hydrate concentrations are estimated at approximately 2 – 10% for the 2006 data and 8 – 18% for the 2004 survey. The reduction in gas hydrate concentration relative to the distance from the Mohican Channel structure is most likely related to the low porosity within the mud-dominant sediment at the depth of the BSR. Free gas concentrations were calculated to be 1 to 2% of the sediment pore space for both datasets.

Keywords

ocean-bottom seismometers; wide-angle reflections; travel-time tomography; 2-D velocity models; Nova Scotia; gas hydrate concentrations; free gas concentration; BSR

1. Introduction

Gas hydrates contain significant amounts of hydrocarbon gas, and so the identification and mapping of gas hydrate occurrences are important to define a potential massive energy resource. Bottom simulating reflections (BSR's), first identified in seismic reflection data at the Blake Ridge (Tucholke and Bryan, 1977), have been used as an indirect indicator for the presence of gas hydrate and underlying free gas. Ruppel et al. (2011) conclude that the presence of a BSR usually indicates that some gas hydrate, most commonly at low saturation, occurs near the base of the gas hydrate stability zone (GHSZ). BSRs are common in the accretionary sedimentary prisms of active margins but are less common for passive margins. An important question is whether this difference represents much less hydrate on passive margins or only less prominent BSRs.

A few areas may host gas hydrate without a visible BSR, such as portions of the Blake Ridge (Holbrook et al., 1996) and the Gulf of Mexico (Dai et al., 2004; GOM 2009). Studies by Xu and Ruppel (1999) show that a missing BSR in a gas hydrate-prone area might be due to low methane flux into GHSZ. Other possibilities include local perturbations in temperature, salinity and/or methane flux (Ruppel et al., 2011). However, Haacke et al. (2007) argue that passive margins without an observable BSR are unlikely to contain significant

quantities of gas hydrate. We therefore have focused on areas with a clear BSR with some data extending to where the BSR is not clear.

The passive margin off eastern Canada was widely mapped during the past 40 years by the hydrocarbon exploration industry. In 1998/9 the Geological Survey of Canada (GSC) collected a total of 34,000 km of two-dimensional (2-D) multi-channel seismic (MCS) data on the Scotian Slope. Therefore, an extensive database of seismic reflection lines exists for the east coast of Canada. The data were recently used by Mosher (2011) to estimate the distribution of gas hydrate based on the area where a BSR can be identified confidently. However, estimates of gas hydrate concentration are poorly constrained – no gas hydrate has been recovered on the Canadian Atlantic margin, and there has been limited interpretation of hydrate occurrence based on geophysical downhole logs (Thurber Consultants Ltd.; Neave, 1990) that has not been confirmed or calibrated by analysis of recovered hydrate.

Important constraints on gas hydrate concentrations are derived from seismic velocities determined from recordings of wide-angle reflections and refractions on ocean-bottom seismometers (OBS) and long-offset MCS streamer systems. Recent one-dimensional (1-D) velocity-depth profiles were obtained from waveform tomography on a 45 km long MCS profile (Delescluse et al., 2011). Mosher (2011) reported velocity results from four OBS surveys on the Atlantic margin, based on 1-D interpretations of individual OBSs. However, in only one survey (LeBlanc et al., 2007) were seismic velocities converted to gas hydrate and free gas concentrations, using an effective medium model (Dvorkin et al., 1999) to obtain estimates of 2 – 6% bulk gas hydrate and less than 1% free gas in the pore space

In this paper, we provide improved constraints on gas hydrate and free gas concentrations and volumes on the Atlantic margin of Canada, through careful determination of

seismic velocities in the region of the Mohican Channel (Figure 1) where a prominent BSR was identified. For two surveys, in 2004 and 2006, we constructed 2-D models of velocity through simultaneous inversion of travel-times from arrays of OBSs and from 2-D single-channel seismic (SCS) profiles.

2. Seismic data acquisition and processing

2.1 Ocean bottom seismometer and single-channel seismic data

In July 2004, an OBS array of nine instruments was deployed on the Scotian slope in approximately 1550 m water depth in the vicinity of the Mohican Channel (**Figure 1**), in a region where the BSR was identified in 2-D MCS reflection data (Mosher et al., 2004). Additional 2-D single-channel seismic reflection (SCS) data and high resolution Huntec DTS sparker data were acquired in the same survey to provide information about the shallow seismic stratigraphy (Mosher, 2004). The research vessel CCGS Hudson towed an array of two generator-injector (GI)-guns (Seismic System Inc.; 1.7 L generator volume; 1.7 L injector volume) at a depth of approximately 2 m. The shots were fired by distance at an interval of 20 m; the average ship speed was 4.5 knots. The OBS instruments were aligned in a 2-D profile with a horizontal separation of approximately 100 m. Shots were fired to offsets of 4.5 km to the south and 6. 3 km to the north. A SCS reflection line was collected simultaneously for a total length of ~12 km (**Figure 1)**.

In August 2006, a second OBS survey was carried out in an area ~5 km south of the 2004 survey on the Scotian Slope in the vicinity of the Mohican Channel. A total of 19 instruments were deployed in two independent arrays in an approximate water depth of 1650 m,

with nine stations in a western profile and ten stations in an eastern profile. The arrays extended from an area in the west, near the south-eastern side-wall of the Mohican Channel where the BSR was identified in the 2-D MCS reflection data (Cullen et al., 2008), to an adjacent area in the east where no BSR is apparent. Within this survey the same OBS instruments and GI-gun array as for the 2004 survey were used. However, the shot interval was 15 m and the spatial OBS separation averaged 900 m. The length of the shot line and the coincident 2-D SCS reflection line above the western OBS array was 12 km from west to east. The shot line was repeated for the eastern OBS array. However, only the data from the western OBS array were analysed in this paper.

The OBS data of both surveys (2004 and 2006) were sampled at an interval of 1 ms up to 200 Hz with a dominant frequency of 45 Hz. However, prominent low-frequency noise of unknown origin was present at 8 Hz in both datasets. Thus, a simple bandpass filter from 10 to 200 Hz was applied to improve the data quality.

2.2 Relocation of the OBS instruments

The OBS positions, clock drifts and the shot locations need to be known precisely in order to get a good velocity model. Although the OBS deployment and retrieval positions could be determined accurately with the ship's Global Positioning System (GPS), the instruments could drift by several hundred meters from the point of deployment while sinking to the seafloor. Therefore, the actual seafloor position of an instrument depends on the local water depth and the current speed. Since the internal clocks also drift, an approximate clock drift measurement is made when the OBS is recovered by comparing the OBS clock time to an accurate satellite time. The shot positions recorded from the ship also have an uncertainty of the order of tens of meters (e.g. Zykov, 2006).

The OBS and shot relocation is an inverse problem in which the objective is to find the seafloor location of the OBS, the shot positions, and a time correction that minimizes the error between the observed and calculated travel-times of the seismic signal through the water column. For this study the source-receiver localization (SRL) scheme of Zykov (2006) was used. It provides a solution for the shot and receiver positions and solves for the GPS clock drift. The SRL is ill-conditioned, because of the small area where the OBS instruments are located in comparison to the shot geometry (Zykov, 2006). The azimuths from far offset shots to the OBSs are concentrated in a narrow region and this causes instability in the solution. Thus, the method uses a regularized inversion approach, by incorporating *a priori* estimates of shot and receiver positions and their uncertainties into the solution (Zykov, 2006).

Direct arrival seismic travel-times were used for the source-receiver localization for both OBS arrays (2004 and 2006). After four iterations, the root-mean-square (RMS) travel-time residual misfit for the 2004 OBS instruments was between 2 and 4 ms, close to the sampling interval. Misfit results for the 2006 OBS instruments were generally less than 2 ms, comparable to the direct arrival travel-time picking uncertainties. The average horizontal drifts during the instrument drop to the seafloor were between 50 and 100 m to the south for the 2004 OBS stations, and 100 to 200 m to the west for the 2006 OBSs.

3. Data characteristics

3.1 Seismic reflection data

Within the 2004 2-D SCS reflection and OBS data, reflected arrivals were identified to 800 ms below the seafloor/direct arrival. The sub-seafloor structure is fairly uniform with reflections that are mostly continuous across the section. A strong amplitude reflection identified on the 2-D SCS reflection data, at ~370 ms below the seafloor (bsf) (**Figure 2a**), is recognized as the BSR, consistent with the conclusions of Mosher et al. (2004). However, the expected phase reversal of the BSR, relative to the seafloor reflection, is difficult to identify.

The 2006 2-D SCS reflection data (**Figure 2b**) shows a similar set of main reflections as the 2004 2-D SCS reflection data, including the BSR at ~370 ms below the seafloor reflection. The phase of the BSR is still ambiguous in the 2006 2-D SCS reflection data, but at some locations a phase reversal can be tentatively identified.

A 3-D multichannel seismic data set acquired and processed by EnCana Ltd. (not shown in this paper) was examined to confirm that the most significant reflections in the 2-D SCS datasets were also identified in the MCS data (Cullen et al., 2008).

3.2 OBS wide-angle reflections and refractions

On some of the 2004 OBS data, refracted arrivals emerging from the direct arrivals were identified over the offset range from approximately 4.5 km to 5.1 km (**Figure 3a**). In the 2006 OBS data, two first-arrival refracted phases were identified. On almost all OBS instruments, one phase extended over an offset range from ~4 km to nearly 6 km (**Figure 3b**); a second phase, identified on only four OBSs, extended an additional distance of ~750 m (**Figure 3b**), and its amplitude decreased with distance. Despite the long shot profiles in both surveys

(2004 – 12 km, 2006 – 10.5 km), shot-receiver offsets were still not long enough to record refracted arrivals from deeper horizons.

For both the 2004 and 2006 OBS data, near-offset reflections were compared to reflections selected in the 2-D SCS data, to identify the most prominent reflections that are consistent between the two datasets (**Figure 3**). The reflected arrivals typically converged and emerged from the direct arrival at an offset of ~4 km, arriving shortly after the first-arrival refractions. Most reflections could be picked confidently only for offsets less than ~3 km.

4. Modelling of refraction and reflection travel-times for P-wave velocities

We utilized the seismic travel-time inversion algorithm of Zelt and Smith (1992), which has been widely applied in gas hydrate-related studies (e.g. LeBlanc et al., 2007; Jaiswal et al., 2006; Lopez et al., 2010; Chabert et al., 2011). The algorithm uses ray-tracing for forward modelling followed by damped-least-squares inversion. Within the inversion step, the model parameters (velocity and depth) are modified to minimize the difference (misfit) between the observed and the predicted travel-times.

To obtain an appropriate starting model for the 2-D travel-time inversion using all nine OBSs in the 2004 survey, 1-D velocity profiles were obtained for each OBS individually (**Figure 4**). Starting with the water layer, layer-stripping was used in which the top layer was modelled first and then held fixed. Forward modelling and inversion were iteratively repeated until the solution converged with a χ^2 value less than or equal to 1, i.e., the root-mean-square (RMS) travel-time misfit fell to 10 ms which is comparable to the pick uncertainty.

The 1-D vertical profiles were used to form a starting model for a 2-D analysis. Seismic travel-times from the SCS vertical-incidence reflections and from wide angle-reflections

and refractions identified on the OBS data were all modelled simultaneously, using the tomographic inversion scheme of Zelt and Smith (1992). The wide-angle reflections and refractions control the velocities of the model, while reflections from the vertical incidence data provide additional control on the interface depths and detailed subsurface structure.

Similar to the 2004 data analysis, wide-angle reflections and refractions of the OBS data from the 2006 survey were modelled simultaneously with the SCS travel-time data.

The ray-coverage for the shallower layers (<100 mbsf) is much sparser for the 2006 data (**Figure 5**), which means that the shallow velocities are essentially 1-D profiles. This is because the instrument spacing was much wider in 2006 than in 2004 (900 m vs 100 m). The actual length of the profile that could be modelled with the 2006 data is also much greater than the 2004 modelled profile (8 km vs 2 km). Since the ray-coverage and path lengths over which velocities are calculated increase with depth, the constraints on average velocity for the deeper region are also improved.

The final 2-D velocity model based on the OBS and SCS data is shown in **Figure 6** for the 2004 survey and in **Figure 7** for the 2006 survey. The velocity contrast modelled with the 2004 OBS data appears to be larger than that modelled with the 2006 data, even though the ray-coverage is highest for the deeper layers (layer 7 - **Figure 5**). The velocity contrasts likely represent real structural differences between the two regions that are only ~5 km apart.

5. Results

5.1 2004 OBS data: 1-D velocity models

Since the seismic reflection data show that the sediment structure is relatively uniform laterally with near-horizontal layering, the 1-D velocity models for the nine OBSs of the 2004 survey provide meaningful information on the vertical velocity structure. However, all 1-D models are independent and treat noise and local structure complexity individually. The velocity profiles show a velocity increase of 210 – 450 m/s at a depth of 200 – 250 mbsf at most locations, with the exception of OBSs 4 and 5 which have smaller velocity contrasts (**Figure 4**), probably related to the local structure underneath. Velocity decreases by about the same amount at depths of 310 to 360 mbsf (corresponding to reflection 6 – **Figures 2, 6**) at the expected depth of the BSR (**Figure 4**- dashed line). At greater depths, modelled velocities generally increase uniformly.

5.2 2004 OBS and SCS data : 2-D models

Wide-angle reflection and refraction travel-times from all nine OBS stations of the 2004 data, plus travel-times from the 2-D SCS reflection data, were modelled simultaneously to create a 2-D velocity model (**Figure 6**). In comparison to the 1-D profiles, the 2-D velocity structure has less variability along the profile. As well, rays travelling from the shots to the receivers constrain the velocity structure over a total profile length of ~2.5 km, much wider than the 900 m length of the OBS array where the 1-D velocity profiles are located. The 2-D velocity model is smoothed over a range of 200 to 400 m; therefore, locally occurring, complex structures and noise are smoothed as well.

In the 2-D velocity model shown in Figure 6, the most prominent feature is a high-velocity layer between interfaces 5 and 6, with a thickness of ~110 m and an average velocity of 1900 m/s. Refractions produced at the top of this layer are observed on almost all OBSs. The velocity of the layer is significantly higher than the average velocity (1600 m/s) between the

seafloor and the top of this layer (~220 mbsf). The base of this high velocity layer, at 310 - 320 mbsf, corresponds to the BSR identified on the SCS reflections sections (**Figure 2a** - reflection 6) and the 2-D MSC reflection data (Mosher et al., 2004).

Below interface 6, a velocity decrease of ~130 m/s was modelled for a layer that has almost the same thickness as the layer above (~100 m) (**Figure 6**). The results are similar to those obtained from the 1-D velocity models (**Figure 4**), except that the 1-D velocities are less consistent laterally since each OBS was modelled independently. The velocity contrast at the BSR depth, achieved in the 1-D velocity models, is larger (~300 m/s) than the contrast modelled in the 2-D approach with the same data (~130 m/s).

Below interface 7, the velocity slowly increases to 1800 m/s for layer 8 at a depth of 400 mbsf. With deep reflections on some of the OBSs, layer 9 was modelled with a velocity of 1900 m/s and a base at ~850 mbsf. No vertical incidence data are available to provide additional constraints on the depth of this layer.

5.3 2006 OBS and SCS data: 2D models

The final 2-D velocity model of the 2006 data simultaneously incorporated seismic travel-time arrivals from the nine OBSs and the 2-D SCS vertical incidence profile (**Figure 7**). The velocity increases gradually, from 1490 m/s near the seafloor to 1650 m/s at ~210 mbsf. At that depth, the modelled rays refract at the top of a layer in which the velocity increases sharply to 1820 m/s in the central part of the profile, with indications of higher velocities (>1900 m/s) at the western and eastern ends. This layer has a thickness of only 30 to 40 m, so its velocity is poorly constrained. However, beneath that interval a thicker (100 m) layer was modelled with similar velocities (1810 to 1840 m/s), so the transition to higher velocities

over this depth range is well-established. The high-velocity layer extends downward to interface 7 at a depth of ~330 mbsf, corresponding to the BSR as identified in the 2-D SCS and 2-D MCS sections (Mosher et al.,2004) (**Figure 2b**). Below interface 7, the velocity model shows a small velocity decrease of 50 to 70 m/s that contrasts with the larger velocity decrease modelled in the 2004 data.

5.4 Sensitivity analysis for layers above and below BSRs

An analysis of sensitivity of the results to perturbations in selected velocity model parameters was performed for the 2004 and 2006 data using the method of Katzman et al. (1994). LeBlanc et al. (2007) used the same method to constrain their error estimates. Velocities are perturbed for a single layer of the final model and then they are held fixed while inverting for the corresponding depth values. The perturbations are made larger until the travel-time residual values increase significantly above the value of the starting model.

For the higher velocity zone above the BSR (**Figure 8a**), sensitivity results show that velocities can vary by ±3 - 5% (±60 - 100 m/s) for the 2004, but only ±3% (±60 m/s) for the 2006 data. For the low-velocity region below the BSR, the results (**Figure 8b**) show that velocities may vary by up to ±3 – 6% (±50 – 100 m/s) for the 2006 model, but only up to ±3% (±50 m/s) in the 2004 model.

6. Discussion:

6.1 Identification of reflected and refracted arrivals

The most significant reflected arrival is identified at the top of the high velocity region, where the first-arrival refracted waves occur (reflection 5 -2004, reflection 6 – 2006, **Figure 3**). Although this reflection occurred on all the OBS instruments, it was only picked over a limited offset range of 1 – 1.5 km from the OBS position, since we followed a conservative picking approach to reduce the picked time-error.

The almost non-reflective nature of the area of the high-velocity region, between the top reflection and the BSR (reflection 6 -2004, reflection 7 -2006, **Figure 3**), could indicate that gas hydrate cements the sediments and makes them more uniform, as suggested by Katzmann et al. (1994) on the Blake Ridge. However, our amplitude decrease above the BSR (**Figure 2**) is not as strong as on the Blake Ridge, where there is probably a higher degree of gas hydrate cementation. Large mass-transport deposits were also identified in areas adjacent to the study locations (Campbell et al., 2010) and can possibly be linked to the lower reflectivity of these sediment packages.

6.2 Velocity features: high- and low-velocity layers

A prominent feature in the final 2-D models for the 2004 and 2006 surveys is a high-velocity layer in which the velocity increases by 200 – 300 m/s (**Figures 9 and 10**). With a thickness of approximately 90 to 110 m, the top of the layer occurs at 220 mbsf, and the base at 310 – 330 mbsf. Beneath this layer, the velocity decreases by 130 m/s in the 2004 model, but only by 80 m/s in the 2006 model. The velocity decrease occurs at the interface identified as the BSR on 2-D seismic reflection sections (**Figure 2**). Thus, we interpret the high-velocity layer as a region of increased gas hydrate concentration. The low-velocity layer beneath the inferred hydrate zone is interpreted to correspond to a zone in which free gas is present.

To compare the final 2-D model results from the 2004 and 2006 data with the results from LeBlanc et al. (2007) and Delescluse et al. (2011), velocities for each interface were averaged with a constant spatial sampling of 100 m across the 2-D velocity profiles **(Figures 9 and 10**). Error estimates on the velocities obtained from the sensitivity analysis (**Figure 8**) are shown with error bars for each layer. The grey shaded area represents the confidence intervals for the velocities determined by the sensitivity analysis. The averaged 1-D velocity profiles (2004 and 2006) are comparable to results from two OBS stations (OBS1 and 2) from the 2002 data of LeBlanc et al. (2007), although there are some distinct differences.

The velocity model of OBS2 (2002) (**Figure 9** – purple line), which is closest (2 km to the south) to the 2004 OBS array, shows an increase in P-wave velocity of 70 m/s at 230 mbsf. This velocity increase is significantly lower than the one modelled with the 2004 data (300 m/s) for the high velocity zone above the BSR. However, the 100 m thickness of this high velocity zone is comparable to the thickness modelled with the 2004 data. Below the BSR, a velocity decrease was modelled with both datasets (2002 and 2004). However, the thickness and velocity values for this layer are significantly different in the two models. The P-wave velocity decreases to 1730 m/s in the 2002 model and the thickness of this layer is about 260 m (LeBlanc et al., 2007). The layer thickness modelled with the 2004 data is only approximately 100 m, and the velocity drop is larger (~130 m/s) than for the 2002 data (~75 m/s).

The velocities modelled for OBS 1 of the 2002 data (**Figure 10** – purple dashed line), which is closest to the 2006 OBS array (1 km north of OBSs 3 and 4), show similar results to OBS 2 of the 2002 survey. The velocity increases by an average of 150 m/s at a depth of 230 mbsf, but drops only by 50 m/s at approximately 360 mbsf. This is comparable to the final model of the 2006 OBSs, where the velocity increases by 130 m/s and decreases by only 50 to 80 m/s

below the high velocity layer. Hence, the thickness of the high velocity zone is approximately 120 m for the 2002 data and 2006 data. However, the thickness of the low velocity zone is much greater for the 2002 OBS 1 (150 m) than for the 2006 data (30 m).

The vertical velocity profile GXT-5300-B (**Figure 10** -green line), which is located approximately in the middle of the 2006 OBS array, was obtained from Delescluse et al. (2011) and is generally consistent with the velocity profile of the 2006 OBS survey. The velocity increases by an average of 130 m/s at 230 mbsf, and drops by only ~70 m/s at a depth of 350 mbsf.

Overall, the velocity contrasts for the 2002 models, for the inferred gas hydrate (high velocity zone) and free gas layers (low velocity zone), are closer to the results achieved with the 2006 data and smaller than the velocity contrasts from the 2004 data.

6.3 Gas hydrate concentrations

6.3.1 Calculations and errors.

To convert the P-wave velocity to hydrate concentration, the simplest methods basically use just the porosity at a given depth, and require an empirical estimate of the velocity for non-hydrate-bearing sediments (e.g. Lee et al., 1993; Hyndman et al., 1993, Jarrard et al., 1995). The resulting concentrations are directly dependent on the no-hydrate velocity for which the uncertainty is difficult to evaluate.

For the velocity models presented in this study, we used the effective medium theory of Helgerud et al. (1999) to calculate the P-wave velocity for a given gas hydrate concentration. Chand et al. (2004) evaluated a number of different effective medium theories, in

which they calculated sediment physical properties from estimates of the porosity, clay-content and quartz-content. The models predicted similar variations of P-wave velocity with hydrate concentration, but the most consistent values for the no-hydrate velocity were found using the theories of Helgerud et al. (1999) and Jakobsen et al. (2000). The calculations were validated by comparisons with velocities determined from drill holes using independent methods. The geological environments tested included both sand-rich sediments (Mackenzie Delta) and clay-rich sediments (Blake Ridge, where sediment compositions are similar to those on the Nova Scotia margin). In our calculations on the Scotia margin, the sediment parameters were taken from LeBlanc et al. (2007) (**Table 1**). Using effective medium theory, we calculated a reference velocity profile corresponding to no gas hydrate or free gas in the pore space (**Figures 9 and 10-** fine red dashed line), plus two other profiles in which the bulk gas hydrate concentration is 10% and 15% (**Figures 9 and 10**).

The calculated gas hydrate concentrations for the 2006 modelled velocities are approximately 2 - 11 % of the pore space. These values are slightly larger than the 2 – 6 % concentrations of bulk gas hydrate estimated from the nearby OBS1 in the study of LeBlanc et al. (2007). However, the modelled velocities for the 2004 data are higher, corresponding to a greater gas hydrate concentration of approximately 8 – 18 % in the pore space. This is our best estimate of the concentration range for the 2004 data, corresponding to an approximate velocity uncertainty of ±75 m/s; however, a larger range cannot be excluded since our sensitivity analysis provides only a rough velocity uncertainty of ±50-100 m/s.

The reference profile for no-gas hydrate is not explicitly included in the error estimate above, which deals with just velocity uncertainties. The concentration is also dependent on specific physical parameters of the sediments, such as the seafloor porosity and the

compaction factor, which defines the rate of the depth-dependent porosity decrease (**Table 1**). For example, if the seafloor porosity is decreased by 3%, the calculated reference velocity profile for no-gas hydrate increases by ~50 m/s, so it is near the upper bound of our confidence limit for the no-hydrate region above 220 mbsf. Hence, the calculated gas hydrate concentrations would show a decrease of 2% compared to the ranges calculated above. In contrast, increasing the seafloor porosity by 3% decreases the average reference velocities by 30 m/s, but the calculated values for gas hydrate concentration increase by ~10%. Therefore, we feel that our selected seafloor porosity of 60%, based on LeBlanc et al. (2007), represents a conservative estimate for gas hydrate concentrations.

6.3.2 Lateral variation in hydrate concentration.

The OBS sites of this study are located near the eastern sidewall of the Mohican Channel (**Figure 1**). The 2004 OBS array, oriented north to south, is parallel and very close to the channel wall, whereas the 2006 OBS array is oriented west to east, perpendicular to the channel wall and extending away from it. In the final 2-D velocity models, velocity values and calculated gas hydrate concentrations for the layer above the BSR are significantly higher for the 2004 data than for the 2006 data. That is, gas hydrate concentrations generally appear to decrease with distance from the Mohican Channel. This pattern is consistent with the 2 – 6% gas hydrate concentrations derived for the 2002 data for OBS1, located east of the channel (LeBlanc et al., 2007). Here, the decreasing gas hydrate concentrations with increasing distance from the channel is explained as an effect of lower porosity within the mud-dominant sediment at the depth of the BSR.

A similar pattern was observed in the 2-D reflection seismic datasets, for which BSRs occur in patches distributed over the Scotian margin, and are mainly located where channel structures appear (Cullen et al., 2008; Mosher, 2011). Although most of the Scotian margin sediments are fine-grained, glacially-derived, marine sediments with a high percentage of clay (Mosher et al., 2008), coarser grained deposits were probably transported in the outwash channels (e.g. Mohican Channel) and deposited over the sidewalls and foot of the channel.

Mosher (2011) stated that most of the recognized BSRs are within large sedimentary drift deposits that were transported during the Miocene and Pliocene (Campbell et al., 2010). Recent studies show that the Pleistocene-to-recent Mohican Channel cuts through these deposits, exhibiting various episodes of cut-and-fill during this period (Campbell et al., 2010; Mosher, 2011). The occurrence of gas hydrate is likely linked to grain-sorting and porosity changes that establish potential reservoir rocks along the Mohican Channel.

Recent studies from the Svalbard margin by Chabert et al. (2011) show similar results, where the formation of gas hydrate is controlled by lithology, which varies downslope from glacial-marine sediments to finer hemipelagic sediments. According to Chabert et al. (2011), gas hydrate concentrations in glacial-marine sediments are too small to produce a prominent increase in P-wave velocity. Estimated gas hydrate concentrations within the sediment frame, modelled using effective medium modelling (Helgerud et al., 1999) amongst others, range between 5% and 12% (Chabert et al., 2011). Another study from the mid-Norwegian margin by Bünz et al. (2005) shows a discontinuous BSR along the margin at the Storegga slide. Gas hydrate estimates are within a range of 3 to 6% of the pore space assuming hydrate as a component of the sediment frame using effective medium modelling (Bünz et al., 2005).

A key feature of the gas hydrate distribution on the passive Scotian margin, based on the seismic velocity analyses, is that the hydrate is distributed in the ~100 m thick region just above the BSR, with no indications of gas hydrate occurring between the seafloor and the top of that layer (~220 mbsf). Malinverno et al. (2008) presented modeling results from the Cascadia margin to show that this could be produced, either by low sedimentation rates or by low rates of diffusive upward fluid flow. On the passive Scotian margin, the low fluid flux rates are likely the dominant factor in restricting gas hydrate to the layer above the BSR.

6.4 Free gas concentrations

Laboratory studies (e.g. Lee, 2004) show that very small concentrations of free gas in the pore space can have a large velocity effect. Concentrations as small as 1% can reduce the P-wave velocity by more than 5%, or approximately 90 m/s (LeBlanc et al., 2007). Those free gas concentrations were calculated based on the rock physics models presented by Helgerud et al. (1999) and Dvorkin et al. (1999). Similar velocity decreases of 50 to 80 m/s, as modelled with the 2006 dataset, and 130 m/s, modelled with the 2004 dataset, correspond to concentrations of 1 to 2% gas in the sediments at depths of 310 – 330 mbsf. The modelled thickness for this low velocity layer beneath the BSR is approximately 30 to 150 m.

Our results for gas zone thickness are consistent with Xu and Ruppel (1999) and Haacke et al. (2008), who argue that a thick free gas zone is associated with passive margins with low rates of methane flux (< few tenths mm/yr, Haacke et al., 2007) and slower seafloor uplift, in contrast to active margins where a thin free gas zone (~10 – 30 m) is produced with high rates of

upward directed fluid flux (> few tenths of mm/yr, Haacke et al., 2007) and high rates of seafloor uplift (e.g., accretionary wedges).

The 1-D vertical velocity profiles obtained by Delescluse et al. (2011) show smaller contrasts between the two velocity zones at the BSR depth with increasing distance from the Mohican Channel. In addition to the velocity profile GXT-5300-B (**Figure 10**), Delescluse et al. (2011) modelled another vertical velocity profile that is located several kilometers to the west of the 2006 OBS array, at the edge of the Mohican Channel. The results show a velocity decrease of 200 m/s below the BSR depth. The lower velocity is most likely a result of higher gas concentrations within the sediments that are closer to the Mohican Channel.

6.5 OBS surveys

As the final velocity models of both surveys (2004 and 2006) show, the geometry for OBS surveys is crucial to the obtained results. Choosing the appropriate instrument spacing (< 500 m) is essential for modeling the velocity contrasts produced by even small amounts of gas hydrate in the pore-space of shallow sediments. Large shot offsets (> 5km) to both sides of the instruments are also necessary to detect refracted and wide-angle reflected arrivals from below the BSR that constrain the velocities in these deep regions.

7. Conclusions

The velocity structure beneath the Scotian margin off eastern Canada was modelled in a travel-time inversion approach using ocean-bottom seismometer and single-channel seismic data. Careful analysis and modelling permitted the small velocity anomalies

associated with low concentrations of gas hydrate and free gas to be resolved. A high velocity zone, occurring over the depth range of ~220 - 330 mbsf with a modelled velocity increase of 200 to 300 m/s, is interpreted as a gas hydrate layer. Depending on the chosen rock-physics model and a depth-dependent no-gas hydrate background velocity model, the modelled velocity increase implies gas hydrate concentrations of 4 – 13% of the pore-space. The presumed gas hydrate is located just above the identified bottom-simulating reflection. The region between the seafloor and the top of the gas hydrate layer (~220 mbsf) shows no indications of gas hydrate, which may be explained by the low diffusive fluid flux rates common for passive margins (e.g. Haacke et al., 2007). Based on results from three seismic surveys between 2002 and 2006, gas hydrate concentrations generally decrease with relative distance from the Mohican channel structure. The decreasing velocity contrast at the BSR depth with relative distance from the Mohican Channel, as concluded by Delescluse et al. (2011), strengthens this argument.

Beneath the bottom-simulating reflection, the velocity decreases by approximately 130 m/s, which corresponds to free gas concentrations of 1 - 2% of the sediment pore space. The thickness of the free gas layer is 30 to 150 m, which is significantly greater than for most active continental margins (10 to 30 m). The low concentrations and thicker layer for this passive margin are probably a consequence of the low upward directed fluid flux rates.

Acknowledgements

The authors thank the crew and staff of CCGS Hudson for their dedication in acquiring the seismic data used in this study. The work was supported by grants from the Natural Science and Engineering Research Council to K. Louden, D. Mosher, R. Hyndman and G. Spence, and from the Climate Change Technology and Innovation (CCTI) program to R. Hyndman. Natural

Resources Canada, Earth Science Sector, Gas Hydrate: Fuel for the Future program funded the research expeditions to acquire the data used in this study. The Climate Change Technology and Innovation Research and Development Initiative, Natural Resources Canada, partially funded development of the ocean bottom seismometers (OBS).

Further thanks go to Christan Berndt, Michael Riedel and an anonymous reviewer for their helpful ideas and criticism.

References

Bünz, S., Mienert, J., Vanneste, M., Andreassen, K., 2005. Case Study. Gas hydrates at the Storegga Slide: Constraints from an analysis of multicomponent, wide-angle seismic data. Geophysics, 70, 5, B19 – B34.

Campbell, C.D., Mosher, D.C., Shimeld, J.W., 2010. Erosional unconformities, megaslumps and giant mud waves: Insights into passive margin evolution from the continental slope off Nova Scotia. Central and North American conjugate margins conference: Re-discovering the Atlantic, New winds from an old sea, Lisbon 2010. Vol.IV, 37-41.

Chabert, A. , Minshull, T.A., Westbrook, G.K., Berndt, C., Thatcher, K.E., Sarkar, S., 2011. Characterization of a stratigraphically constrained gas hydrate system along the western continental margin of Svalbard from ocean bottom seismometer data. Journal of Geophysical Research, 116, 16 pp.

Claypool, G.E., 1996. Influence of water solubility, phase equilibrium, and capillary pressure on methane occurrence in sediments. American Association of Petroleum Geology Bulletin 13, 27 pp.

Cullen, J., Mosher, D.C., Louden, K.E. , 2008. The Mohican channel gas hydrate zone, Scotian Slope, Geophysical structure. Proceedings of the 6th International Conference on Gas Hydrates (ICGH2008).

Dai, J., Xu, H., Snyder, F., Dutta, N., 2004. Detection and estimation of gas hydrates using rock physics and seismic inversion: Examples from the northern deepwater Gulf of Mexico. The Leading Edge, 23,1; 60-66.

Delescluse M., Nedimovic, M.R., Louden, K.E., 2011. Case History - 2D waveform tomography applied to long-streamer MCS data from the Scotian Slope. Geophysics, 76, 4, B151 – B163.

Dvorkin,J., Prasad, M., Sakai, A., Lavoie, D., 1999. Elasticity of marine sediments: Rock physics modelling. Geophysical Research Letters, 26, 12, 1781-1784.

Haacke, R.R., Westbrook, G., Hyndman, R., 2007, Gas hydrate, fluid flow and free gas: Formation of the bottom-simulating reflector. Earth and Planetary Science Letters, 261, 407- 420, 17 pp.

Haacke, R.R., Westbrook, G., Riley, M., 2008, Controls on the formation and stability of gas hydrate related bottom-simulating reflectors (BSRs): A case study from the west Svalbard continental slope, Journal of Geophysical Research, 113.

Helgerud, M.B., Dvorkin, J., Nur, A., Sakai, A., Collett, T., 1999. Elastic-wave velocity in marine sediments with gas hydrates: Effective medium modelling Geophysical Research Letters, 26, 13, 2021-2024.

Holbrook, W.S., Hoskins, H., Wood, W.T., Stephen, R.A., Lizarrade D., 1996. Methane hydrate, bottom-simulating reflectors, and gas bubbles: Results of vertical seismic profiles on the Blake Ridge. Science, 273, 1840-1843.

Hyndman, R.D., Moore, G.F., Moran, K., 1993. Velocity, porosity, and pore-fluid loss from the Nankai subduction zone accretionary prism. in Hill, I.A., Taira, A., Firth, J.V., et al.,

Proceedings of the Ocean Drilling Program, Scientific Results, Vol. 131: College Station, TX , 211-220.

Jacobsen M., Hudson J.A., Minshull T.A., Singh S.C., 2000.Elastic properties of hydrate-bearing sediments using effective medium theory. Journal of Geophysical Research, 105, 561-577.

Jaiswal, P., Zelt. C.A., Pecher, I.A., 2006. Seismic characterization of a gas hydrate system in the Gulf of Mexico using wide-aperture data. Geophysical Journal International, 165, 108-120.

Jarrard, R.D., MacKay, M.E., Westbrook, G.K., and Screaton, E.J., 1995. Log-based porosity of ODP sites on the Cascadia accretionary prism. in Carson, B., Westbrook, G.K., Musgrave, R.J., and Suess, E., Proceedings of the Ocean Drilling Program, Scientific Results, 146 (Part 1): College Station, TX , 313-335.

Katzman, R., Holbrook, W.S., Paull, C. K., 1994. Combined vertical-incidence and wide-angle seismic study of a gas hydrate zone, Blake Ridge. Journal of Geophysical Research, 99, 17,975-17,995.

LeBlanc, C., Louden, K., Mosher, D., 2007. Gas hydrates off Eastern Canada: Velocity models from wide-angle seismic profiles on the Scotian Slope. Marine and Petroleum Geology, 24, 321 – 335.

Lee, M.W., Hutchinson, D.R., Dillon, W.P., Miller, J.J., Agena, W.F., and Swift, B.A., 1993. Method of estimating the amount of in-situ gas hydrates in deep marine sediments. Marine and Petroleum Geology, 10(5), 493–506.

Lee, M.W., 2004. Elastic velocities of partially gas-saturated unconsolidated sediments. Marine and Petroleum Geology, 21, 641 – 650.

Lopez, C., Spence, G., Hyndman, R., Kelley, D., 2010. Frontal ridge slope failure at the northern Cascadia margin: Margin-normal fault and gas hydrate control. Geology, 38, 11, doi:10.1130/G31136.1.

Malinverno, A, Kastner, M, Torres, M.E., Wortmann, U.E., 2008. Gas hydrate occurrence from pore water chlorinity and downhole logs in transect across the northern Cascadia margin (Integrated Ocean Drilling Program Expedition). Journal of Geophysical Research, vol. 113, B08103.

Mosher, D.C, Piper, D.J., Campbell, D.C., Jenner, K.A., 2004. Near surface geology and sediment-failure geohazards of the central Scotian Slope. AAPG, 88, 703-723.

Mosher, D., 2004.Hudson 2004-030 Cruise Report: July 10-20, 2004. Geological Survey of Canada (Atlantic), Open File, 72 p.

Mosher, D., 2008. Bottom simulating reflectors on Canada's east coast margin: Evidence for gas hydrate, Proceedings of the 6th International Conference on Gas Hydrates (ICGH 2008).

Mosher, D., 2011. A margin-wide BSR gas hydrate assessment: Canada's Atlantic margin, Marine and Petroleum Geology, 28 (8), 1540-1553.

Neave, K.G., 1990. Shallow seismic velocities on the eastern Grand Banks and Flemish Pass. Unpublished report Prepared for Alan Judge of the Terrain Sciences Division, Geological Survey of Canada, p. 19.

Ruppel, C., Collett, T., Boswell, R., Lorenson, T., Buczkowski, B., Waite, W., 2011. A new global gas hydrate drilling map based on reservoir type. Fire in the Ice, DOE NETL newsletter, 11(1), 13- 17.

Tucholke, B.E., Bryan, G.M., Ewing, J.I., 1977. Gas hydrate horizons detected in seismic-profiler data from the western North Atlantic. American Association of Petroleum Geologists Bulletin 61, 689-707.

Xu, W., Ruppel, C., 1999. Predicting the occurrence, distribution, and evolution of methane gas hydrate in porous marine sediments from analytical models. Journal of Geophysical Research, 104, 5081-5096.

Yuan, T., Spence, G., Hyndman, R., Minshull, T., Singh, S.C., 1999. Seismic velocity studies of a gas hydrate bottom simulating reflector on the northern Cascadia continental margin: amplitude modelling and full-waveform inversion. Journal of Geophysical Research, 104, 1179- 1191.

Zelt, C.A., Smith, R.B., 1992,.Seismic travel-time inversion for 2-D crustal velocity structure. Geophysical Journal International, 108, 16-34.

Zykov, M., 2006, 3-D travel time tomography of the gas hydrate area offshore Vancouver Island based on OBS data. PhD Thesis with the University of Victoria, BC, Canada.

Figures

Figure 1: *Location of the study area (box within the smaller map) on the Scotian margin in the vicinity of the Mohican Channel. The three different deployments from 2002 (circles), 2004 (triangles), and 2006 (squares and stars) are shown. The 2-D single-channel seismic (SCS) data and OBS data from 2004 and 2006 (diamonds only) are modelled and discussed in this paper.*

Figure 2: *(a) 2-D SCS reflection profile (2004) shows the positions of the nine OBS stations (triangles) with ~100 m instrument separation. Travel-times for the eight identified reflections were inverted simultaneously with travel-times for reflections and refractions from the OBSs. The BSR (reflection 6) was identified at approximately 350 ms two-way-travel-time (TWT) below the seafloor. (b) 2-D SCS reflection profile (2006) shows the positions of the nine OBS stations*

(diamonds) used in this study with an instrument separation of approximately 900 m. The eight identified horizons on the 2-D SCS profile were used for the seismic travel-time tomography simultaneously with the travel-times for reflections and refractions from the nine OBSs. The BSR (reflection 7) is identified at approximately 350 ms TWT below the seafloor.

***Figure 3**: (a) Example of the 2004 data (OBS 8) with a hyperbolic move-out correction to flatten the seafloor using 1480 m/s. The first-arrival refraction (enhanced box - left) and the eight main reflections including the BSR were used for the seismic travel-time tomography in the 1-D and 2-D modelling schemes. (b) Example the 2006 data (OBS 6) with a hyperbolic move-out correction to flatten the seafloor using 1480 m/s. The first-arrival refractions (enhanced box - left) and the eight main reflections including the BSR were used for the seismic travel-time inversion. The second refraction was only identified on four OBSs and was not further used for the seismic travel-time modelling. (Solid lines for both datasets show the picked reflected and refracted arrivals.)*

***Figure 4**: The 1-D velocity-depth models for the nine OBSs from 2004 are shown, where the red dashed lines are positioned at the spatial distances along the OBS line, and represent the origin (1400 m/s) of each velocity profile. The black dashed line indicates the depth of the expected BSR from the 2-D reflection data (**Figure 2a**). The velocity increase of 210 to 450 m/s at ~ 200 - 250 mbsf was modelled on all stations except OBSs 4 and 5, where a smaller velocity contrast occurs (see text for details).*

Figure 5**:** *Comparison of ray-tracing and travel-time inversion models for reflections from interface 3 at a depth of approximately 150 mbsf for the 2004 data (a) and 2006 data (b). Ray coverage for the 2006 OBS data is sparser than for the 2004 data due to the acquisition geometry. Plots show seismic travel-time inversion results (model- black dots) versus seismic travel-time picks (data - red bars) of the OBSs. Both modelled and original data are displayed with a reduced velocity of 1820 m/s. Reflections from interface 7 are shown for the 2004 data (c) and 2006 data (d). Plots show seismic travel-time inversion results (model - black dots) versus the seismic travel-time picks (data - red bars). Both modelled and original data are displayed with a reduced velocity of 1820 m/s.*

Figure 6: *2004 2 -D velocity model from travel-time tomography using arrivals from the nine OBS stations (triangles) and the corresponding 2-D SCS vertical incidence profile (**Figure 2a**) . The BSR marks the transition to a layer of reduced velocity (1590 m/s) below a high velocity zone (average 1900 m/s). The numbers indicate the eight reflections used in the travel-time inversion modelling. The velocity model shows a 4 km long section of the whole 12 km long profile that indicates the region of full ray-coverage where the travel-time arrivals provide control on velocities.*

Figure 7: *2006 2 -D velocity model from travel-time tomography using arrivals from the nine OBS stations (diamonds) of 2006 and the corresponding 2-D SCS vertical incidence profile. The travel-time inversion results show a small velocity contrast at the BSR depth. Refractions are produced below interface 5 at 210 – 220 mbsf, where the velocity increases by 200 m/s. The*

unshaded area indicates the region of ray-coverage, where the travel-time arrivals provide control on velocities.

***Figure 8**: (a) Results of the sensitivity analysis of the 2004 (dashed line) and 2006 (solid line) OBS data for the velocity perturbation of the high-velocity layer above the identified BSR. An approximate estimate of the confidence range for both OBS datasets is indicated by the shaded box. (b) Results of the sensitivity analysis of the 2004 (dashed line) and 2006 (solid line) OBS data for the velocity perturbation of the low-velocity layer below the identified BSR depth. Allowed velocity perturbations are ± 3% for the 2004 data (shaded box), but much greater (>± 5%) for the 2006 data.*

***Figure 9**: 1-D velocity-depth profile (thick blue line) obtained by averaging the 2004 2-D velocity model at constant depth below the seafloor, with approximate error estimates (grey shaded area) and error bars for the interval velocities based on the sensitivity analysis (**Figure 8**). The high velocity region is more prominent for the 2004 model than for the 2006 model (thin green line) or for the model of Leblanc et al. (2007) based on a 2002 OBS survey (purple dashed line); OBS2 from this survey was located 2 km south of the 2004 array. The velocity drop of ~300 m/s at a depth of ~310 m below seafloor indicates the base of the gas hydrate stability zone (GHSZ). The red-dashed line is the reference velocity profile calculated with the parameters of Table 1 (Mosher et al., 2008) and standard rock-physics modelling (Dvorkin et al., 1999; Helgerud et al., 1999) assuming no gas hydrate and free gas in the pore space of the sediments. The orange dashed line is a reference velocity profile with the same physical parameters*

including 10% gas hydrate in the sediment. However, results of the 2004 model suggest even higher values, about 13 ± 5% (pink dashed line).

Figure 10: *1-D vertical velocity-depth profile obtained by averaging the 2006 2-D velocity model at constant depth below the seafloor (thick blue line) with approximate error estimates (grey shaded area) and error bars for the interval velocities are shown. The profile is compared with the vertical velocity-depth profile of OBS1 from the 2002 survey (purple dashed line, LeBlanc et al., 2007) and one vertical velocity-depth profile of Delescluse et al. (2011) that is close to the middle section of the 2006 OBS array (thin green line). Velocities from the region above the recognized BSR are within the 10% bound (orange dashed line) of gas hydrate in the sediment. The velocity contrasts of the 2002 and 2006 model are similar to those achieved by Delescluse et al. (2011); however, the contrasts are smaller than those achieved with the 2004 data (**Figure 9**). The red-dashed line is the reference velocity profile calculated with the parameters of Table 1 and standard rock-physics modelling (Dvorkin et al., 1999; Helgerud et al., 1999) assuming no gas hydrate and free gas in the sediments.*

Porosity at seafloor (%)	60
Compaction factor lambda (m)	1000
Composition of Quartz (%),Clay (%)	15, 85

Table 1: Sediment parameters for the Nova Scotian margin environment modified from Mosher et al., 2008.

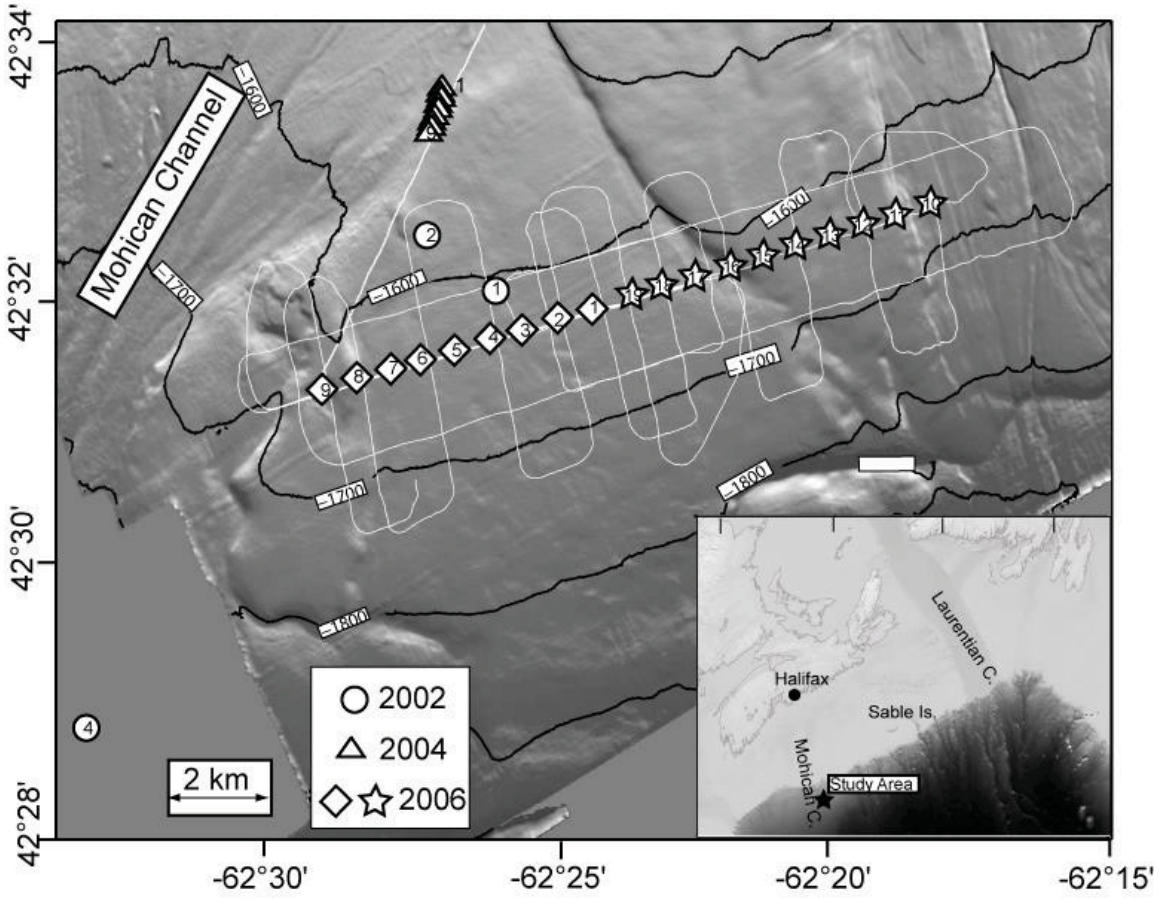
42°34'
42°32'
42°30'
42°28'
-62°30'
-62°25'
-62°20'
-62°15'
Mohican Channel
-1600
-1700
-1800
2 km
2002
2004
2006
Halifax
Sable Is.
Laurentian C.
Mohican C.
Study Area

Figure 1:

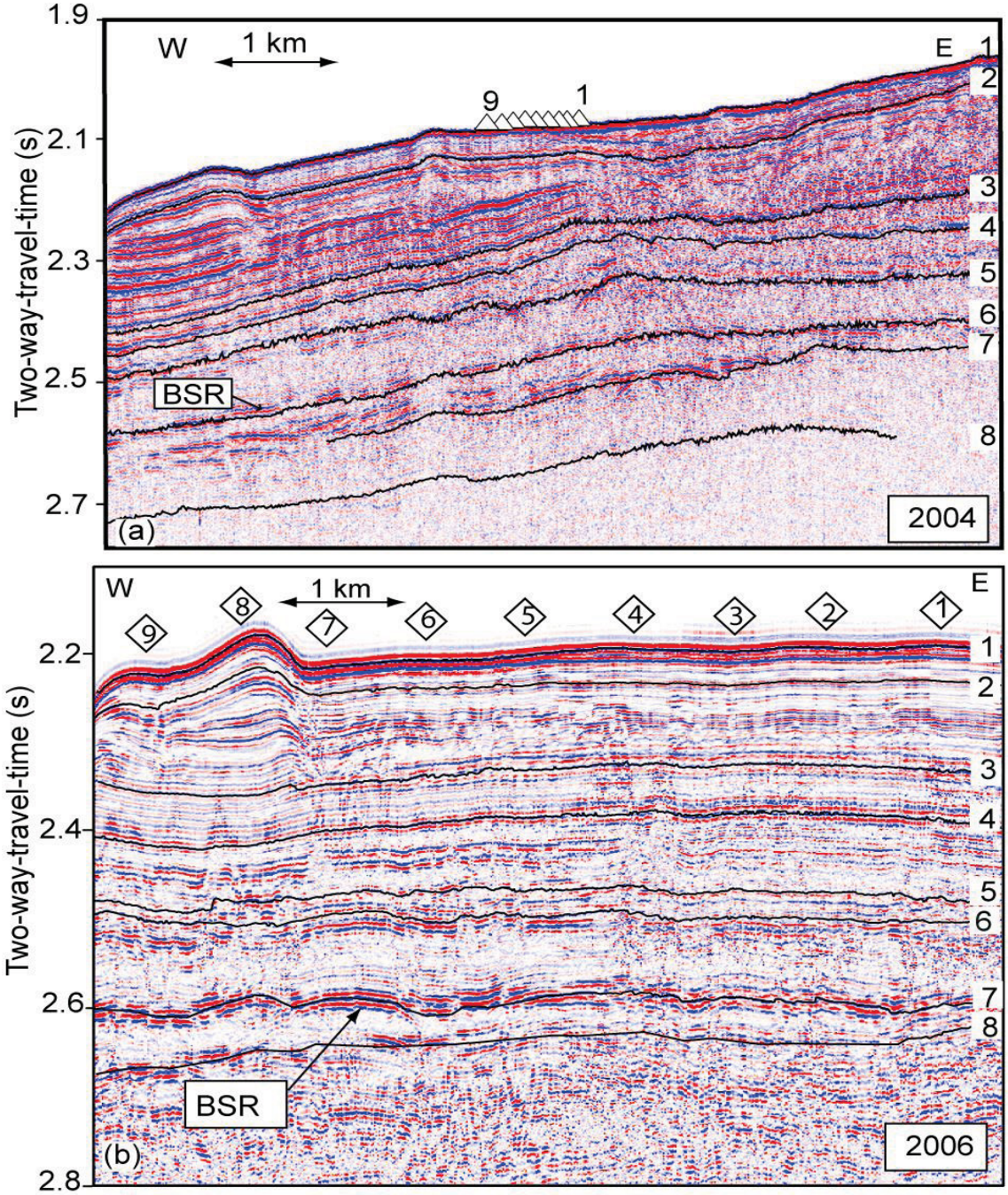
1.9
2.1
2.3
2.5
2.7
Two-way-travel-time (s)
W
1 km
E
9
1
2
3
4
5
6
7
8
BSR
(a)
2004
W
1 km
E
9
8
7
6
5
4
3
2
1
2.2
2.4
2.6
2.8
Two-way-travel-time (s)
BSR
(b)
2006

Figure 2:

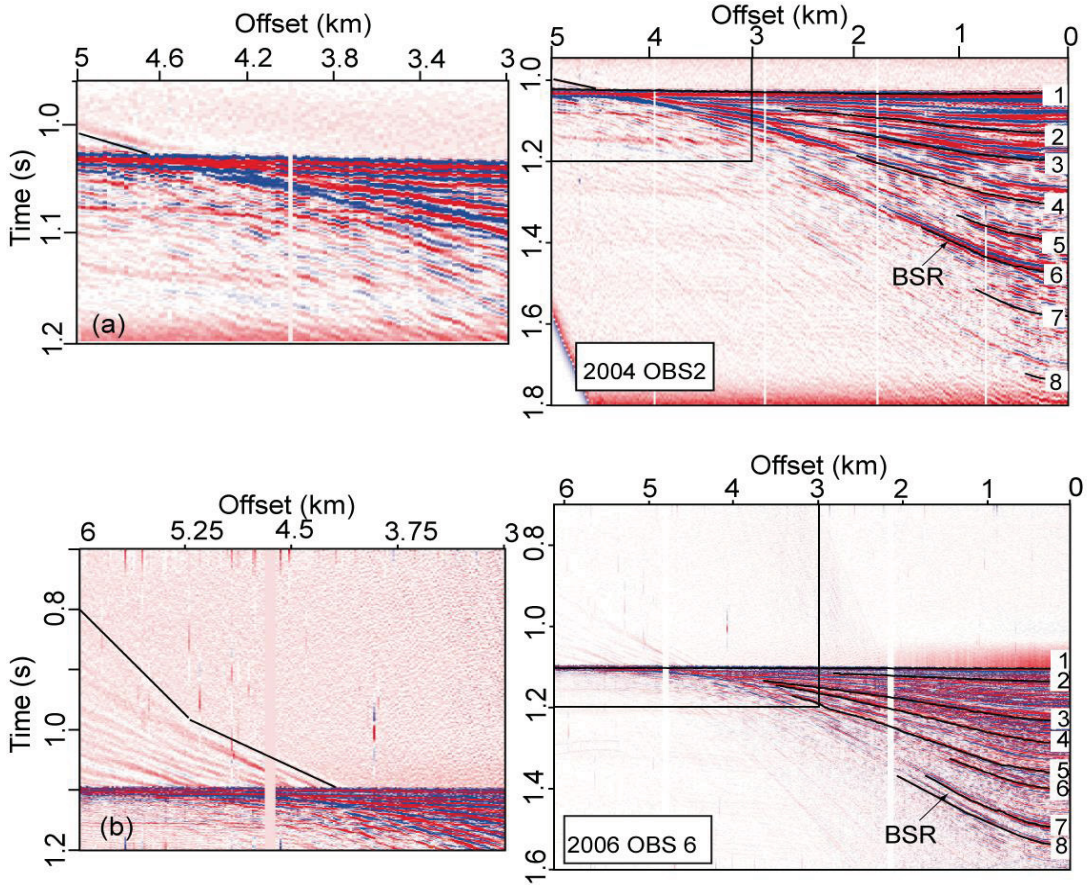
Offset (km)
5
4.6
4.2
3.8
3.4
3
Time (s)
1.0
1.1
1.2
(a)
Offset (km)
5
4
3
2
1
0
1.0
1.2
1.4
1.6
1.8
1
2
3
4
5
6
7
8
BSR
2004 OBS2
Offset (km)
6
5.25
4.5
3.75
3
Time (s)
0.8
1.0
1.2
(b)
Offset (km)
6
5
4
3
2
1
0
0.8
1.0
1.2
1.4
1.6
1
2
3
4
5
6
7
8
BSR
2006 OBS 6

Figure 3:

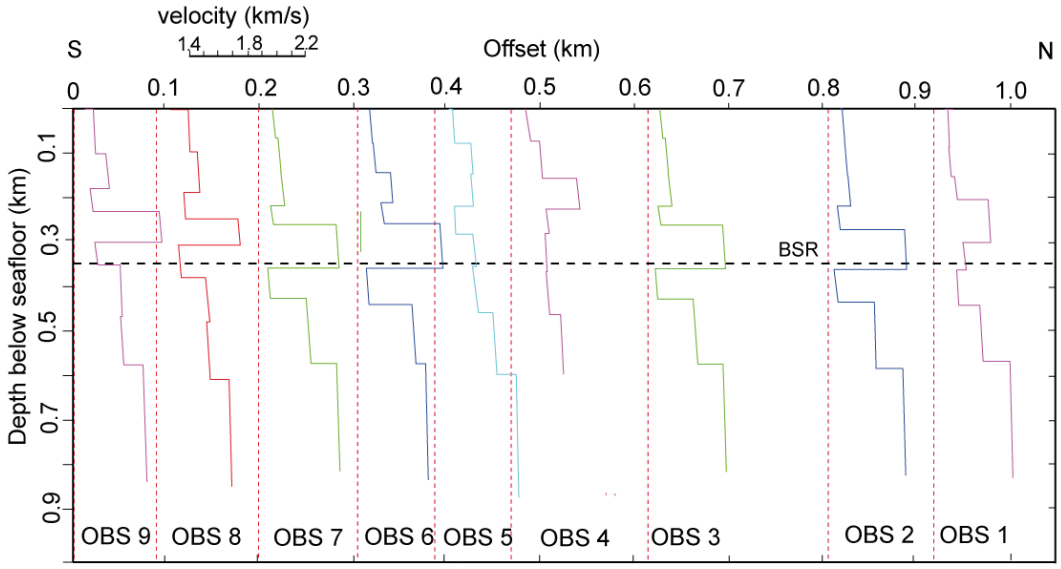
velocity (km/s)
1.4
1.8
2.2
S
Offset (km)
N
0
0.1
0.2
0.3
0.4
0.5
0.6
0.7
0.8
0.9
1.0
Depth below seafloor (km)
0.1
0.3
0.5
0.7
0.9
BSR
OBS 9
OBS 8
OBS 7
OBS 6
OBS 5
OBS 4
OBS 3
OBS 2
OBS 1

Figure 4:

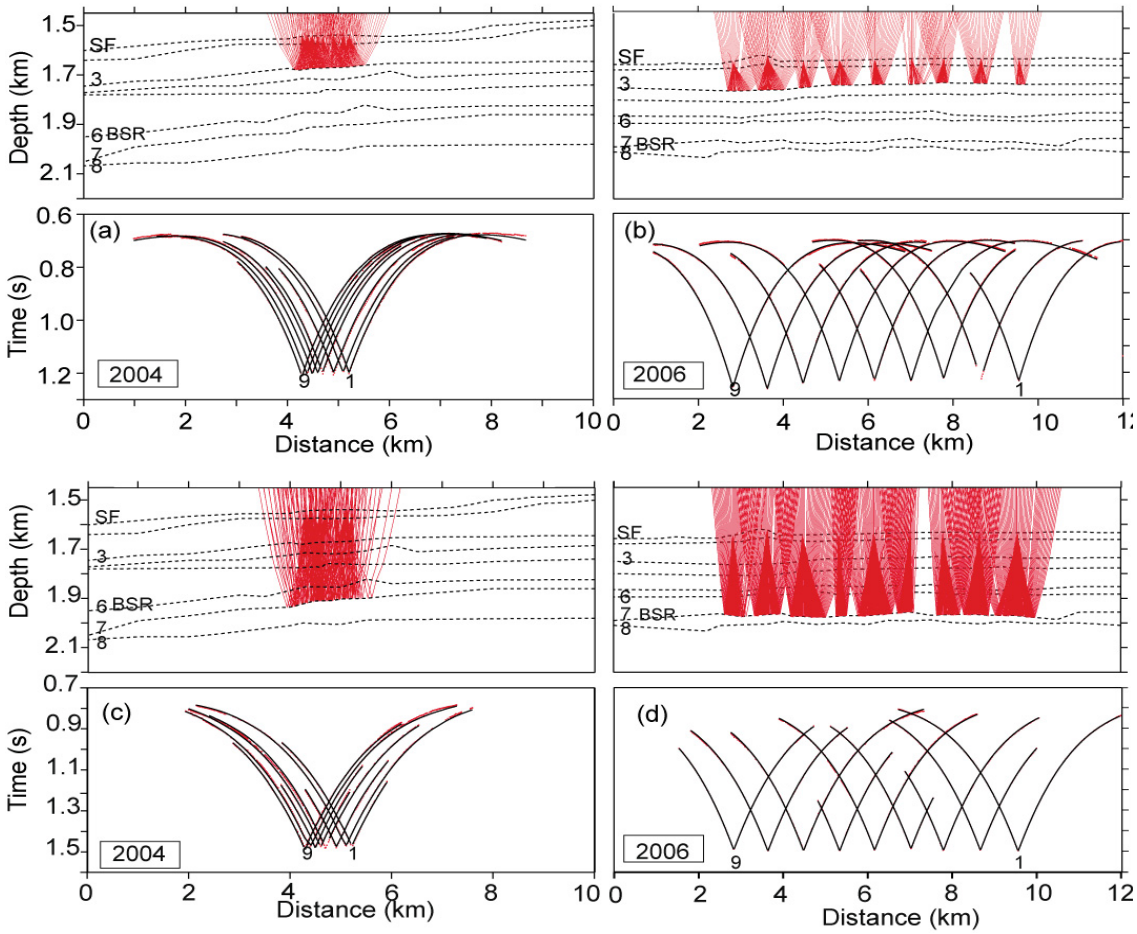

Figure 5:

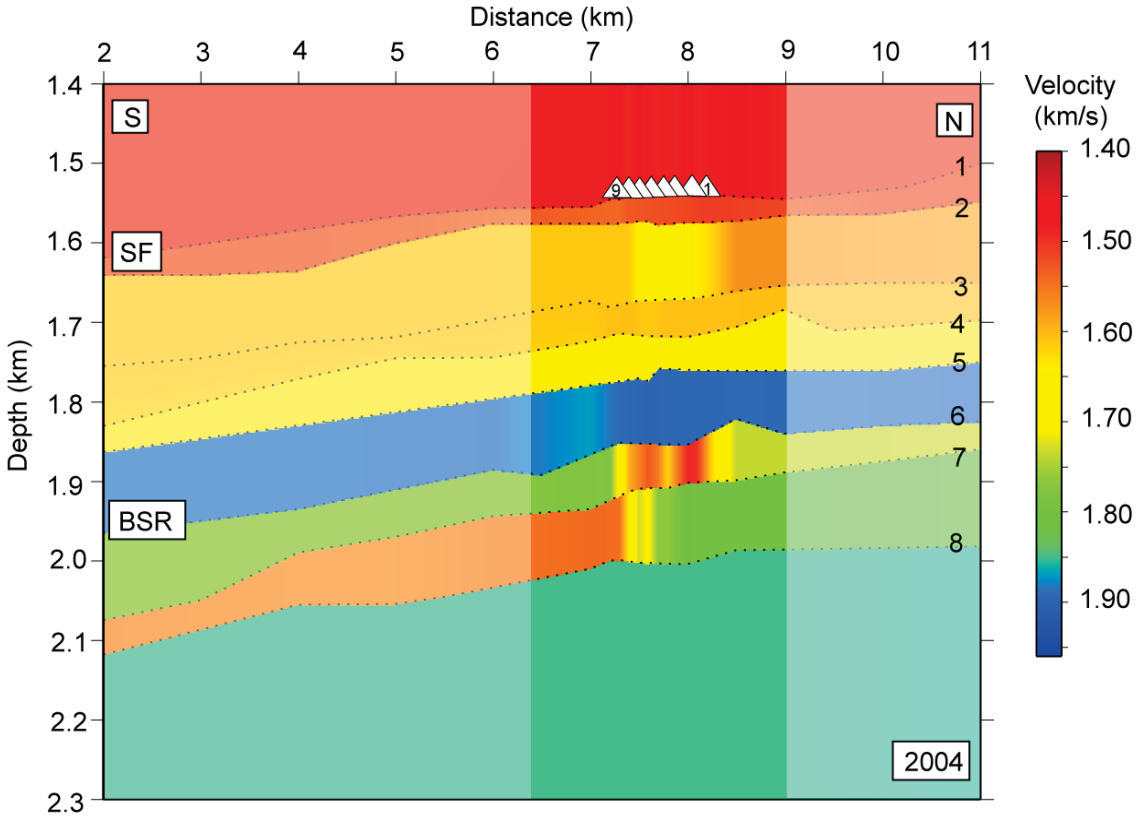
Distance (km)
2
3
4
5
6
7
8
9
10
11
Depth (km)
1.4
1.5
1.6
1.7
1.8
1.9
2.0
2.1
2.2
2.3
S
N
SF
BSR
2004
1
2
3
4
5
6
7
8
9
1
Velocity
(km/s)
1.40
1.50
1.60
1.70
1.80
1.90

Figure 6:

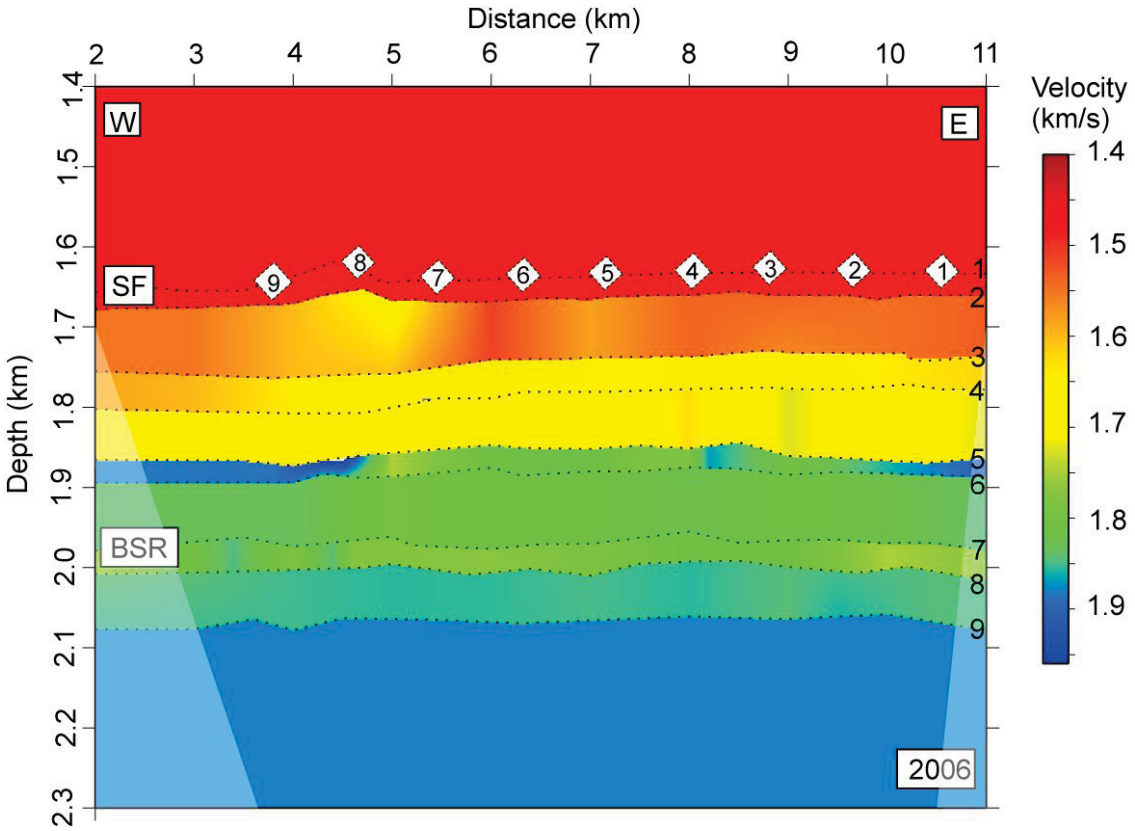
Distance (km)
2
3
4
5
6
7
8
9
10
11
Depth (km)
1.4
1.5
1.6
1.7
1.8
1.9
2.0
2.1
2.2
2.3
W
E
SF
BSR
2006
1
2
3
4
5
6
7
8
9
Velocity
(km/s)
1.4
1.5
1.6
1.7
1.8
1.9

Figure 7:

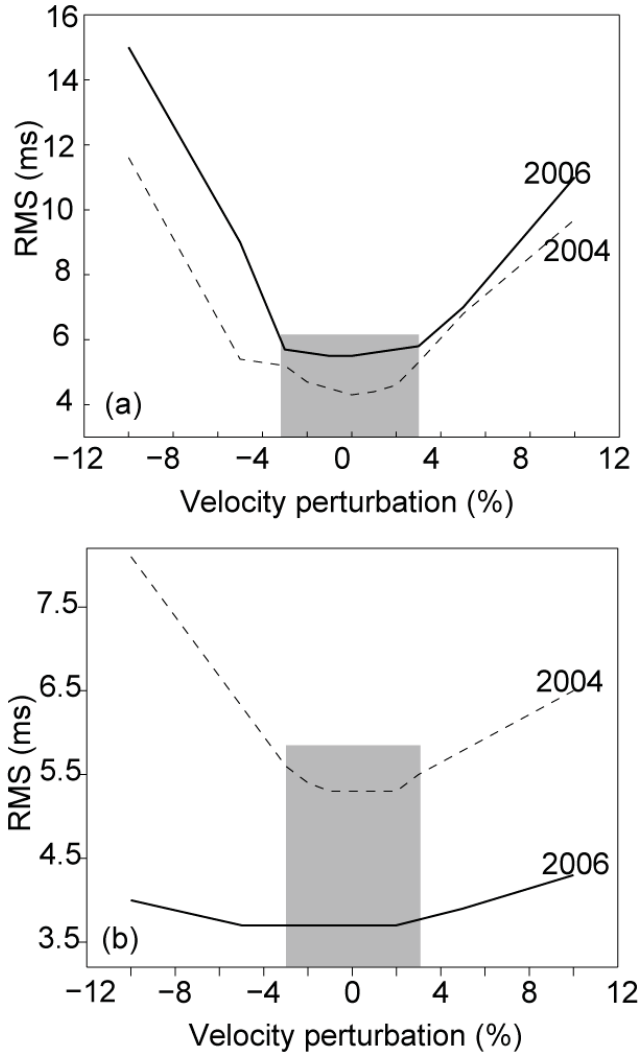
16
14
12
10
8
6
4
RMS (ms)
2006
2004
(a)
−12
−8
−4
0
4
8
12
Velocity perturbation (%)
7.5
6.5
5.5
4.5
3.5
RMS (ms)
2004
2006
(b)
−12
−8
−4
0
4
8
12
Velocity perturbation (%)

Figure 8:

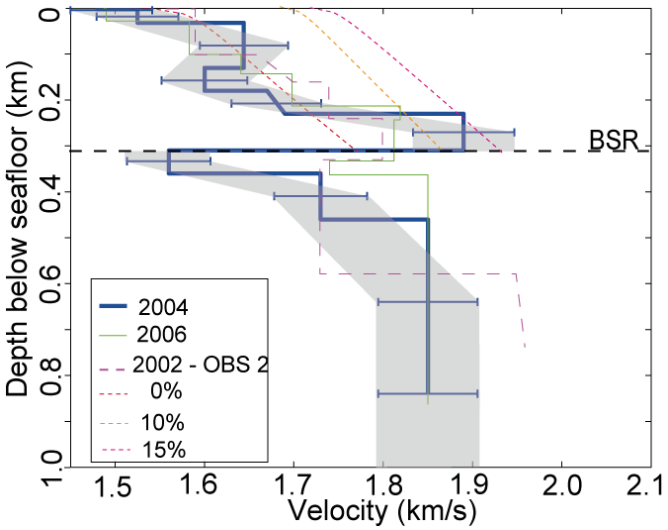

Figure 9:

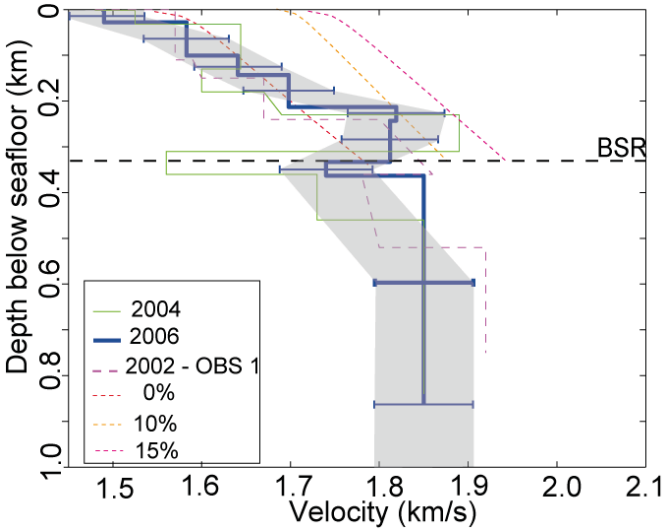

Figure 10:

APPENDIX D CLOCK CALIBRATION FOR OBS RELOCATION

	Time of Initial Calibration (JD)	Initial GPS Clock Value (s)	Initial GPS Offset (s)	Time of Final Calibration (JD)	Final GPS Clock Value (s)	Final GPS Offset (s)	Total Clock Drift (s)	Total Clock Drift (ms)
SITE 1								
OBS 1	195/2040	0.998050	0.001950	197/1237	0.995760	0.004240	0.002290	2.2900
OBS 2	195/2313	0.999840	0.000160	197/1241	0.999400	0.000600	0.000440	0.4400
OBS 3	195/2336	0.996180	0.003820	197/1337	0.996940	0.003060	-0.000760	-0.7600
OBS 4	196/1230	0.996710	0.003290	197/1448	0.998430	0.001570	-0.001720	-1.7200
OBS 5	195/2358	0.995450	0.004550	197/1705	1.000840	-0.000840	-0.005390	-5.3900
OBS 6	196/1144	0.995840	0.004160	197/1458	0.991200	0.008800	0.004640	4.6400
OBS 7	196/0044	0.994967	0.005033	197/1341	0.992020	0.007980	0.002947	2.9470
OBS 8	196/1320	0.994930	0.005070	197/1631	0.995510	0.004490	-0.000580	-0.5800
OBS 9	196/1257	1.001410	-0.001410	197/1610	1.000820	-0.000820	0.000590	0.5900
OBS 10	196/0019	0.999450	0.000550	197/1540	0.994718	0.005282	0.004732	4.7320
SITE 2								
OBS 2	198/1352	0.995611	0.004389	199/1430	0.996230	0.003770	-0.000619	-0.6190
OBS 1	198/1328	1.000210	-0.000210	199/1444	0.999800	0.000200	0.000410	0.4100
OBS 3	198/1235	1.001174	-0.001174	199/1630	0.997930	0.002070	0.003244	3.2437
OBS 4	198/1408	0.999730	0.000270	199/1932	1.003590	-0.003590	-0.003860	-3.8600
OBS 5	198/1224	0.995538	0.004462	199/1725	0.990870	0.009130	0.004668	4.6680
OBS 6	198/1202	0.997355	0.002645	199/1716	0.999299	0.000701	-0.001944	-1.9440
OBS 7	198/1145	0.998150	0.001850	199/1927	0.995440	0.004560	0.002710	2.7100
OBS 8	198/1109	0.994520	0.005480	199/1920	0.994360	0.005640	0.000160	0.1600
OBS 9	198/1135	0.999973	0.000027	199/1821	1.000638	-0.000638	-0.000665	-0.6650
OBS 10	198/1643	1.000998	-0.000998	199/1830	0.999340	0.000660	0.001658	1.6580

Table A.1 Clock readings at deployment and retrieval of the OBS during CCGS Hudson cruise 2004-030.

The calibration between the OBS clock and the ships GPS clock at the times of both deployment and recovery is entered into the PyShottab program. The ships GPS clock is fed into the onboard odetics box which times the shots taken in seconds. The notation for ships GPS clock calibration is as follows:

1.0000 s = no actual offset

0.9000 s = + 0.1 s actual offset

1.1000 s = - 0.1 s actual offset.

For example if the pre-deployment and post-deployment calibrations from the odetics box are given as 0.995450 s and 1.000840 s respectively for Site 1 OBS 5 (see Table A.1) then the corresponding offsets are:

1 - 0.995450 = +0.00455 s actual offset

1 - 1.000840 = -0.00084 s actual offset

The total clock drift for Site 1 OBS 5 therefore is the difference between the two offset values which is:

(+0.00455) - (-0.00084) = -0.005390 s or -5.39 ms.

APPENDIX E SOUND VELOCITY EQUATIONS

The equations tested are detailed below where T = Temperature (°C), S = salinity (PSU or practical salinity units), D = depth (m), P = Pressure (1 bar = 100 kPa = 1.019716 kg/cm^2) and V = velocity (m/s):

MacKenzie 1981

$$V = 1448.96 + 4.591T - 5.304\text{x}10^{-2}T^2 + 2.374 \text{ x } 10^{-4}\ T^2 + 1.34\ (S\text{-}35) + 1.63\text{x}10^{-2}D + 1.675\text{x}10^{-7}D^2 - 1.025\text{x}10^{-2}T(S\text{-}35) - 7.139\text{x}10^{-12}TD^2$$

Medwin 1975

$$V = 1.4492 + 4.6T - 5.5\text{x}10^{-2}T^2 + 2.9\text{x}10^{-4}T^3 + 1.34 - (0.01T)(S\text{-}35) + 1.6\text{x}10^{-2}D$$

DelGrosso 1975 required additional calculation whereby:

$$V = 1402.392 + V_T + V_S + V_P + V_{STP}$$

Where: $V_T = 5.012285T - 5.51184\text{x}10^{-2}T^2 + 2.21649\text{x}10^{-4}T^2$

$$V_P = 0.1560592P + 2.449993\text{x}10^{-5}P^2 - 8.833959\text{x}10^{-9}T^3$$

$$V_S = 1.329530S + 1.288598\text{x}10^{-4}S^2$$

$$V_{STP} = \text{-}0.01275936TS + 0.6353509\text{x}10^{-2}TP + 0.2656174\text{x}10\text{-}7T^2P^2 - 0.01593895\text{x}10^{-5}TP^3 + 0.5222483\text{x}10^{-9}TP^3 - 0.4383615\text{x}10^{-6}T^3P - 0.1616745 \text{ x } 10^{-8}\ S^2P^2 + 0.968841\text{x}10^{-4}T^2S + 0.4857614\text{x}10^{-5}TS$$

APPENDIX F MISFIT TABLES FOR OBS 1D MODELS

Horizon	Site 1	OBS 1			OBS 2			OBS 3	
	Npts	Trms (ms)	χ^2	Npts	Trms (ms)	χ^2	Npts	Trms (ms)	χ^2
1	59	9.9	1.00	479	9.82	0.97	59	9.93	1.00
2	25	9.8	1.00	169	9.94	0.99	27	9.81	1.00
3	26	9.8	1.00	95	9.95	1.00	7	9.25	1.00
4	19	9.7	1.00	85	9.94	1.00	22	9.79	1.00
5	36	9.9	1.00	45	9.89	1.00	36	9.86	1.00
6	103	10.0	1.00	11	9.52	1.00	112	9.96	1.00
7	68	10.0	1.01	22	9.77	1.00	80	9.95	1.00
8	17	9.7	1.01	41	9.87	1.00	17	9.68	1.00
9	30	9.8	1.00	118	9.96	1.00	32	9.84	1.00
Overall	383	9.8	1.00	1065	9.85	1.00	392	9.79	1.00

Horizon	Site 1	OBS 4			OBS 5			OBS 6	
	Npts	Trms (ms)	χ^2	Npts	Trms (ms)	χ^2	Npts	Trms (ms)	χ^2
1	47	10.3	1.09	71	3.35	0.11	65	10.38	1.09
2	36	9.9	1.00	18	2.69	0.08	21	9.76	1.00
3	30	9.8	1.00	10	7.08	0.56	5	8.93	1.00
4	27	9.8	1.00	19	7.31	0.56	29	9.84	1.00
5	24	9.8	1.00	16	6.08	0.39	21	9.77	1.00
6	136	9.9	0.98	19	8.64	0.79	131	9.98	1.00
7	91	9.9	1.00	17	7.63	0.62	107	9.96	1.00
8	23	9.8	1.00	21	7.09	0.53	37	9.86	1.00
9	25	9.8	1.00	26	11	1.26	35	10.47	1.13
Overall	439	9.9	1.01	368	6.76	0.54	451	9.88	1.03

Horizon	Site 1	OBS 7			OBS 8			OBS 9	
	Npts	Trms (ms)	χ^2	Npts	Trms (ms)	χ^2	Npts	Trms (ms)	χ^2
1	80	13.1	1.75	54	10.34	1.09	339	9.65	0.93
2	28	10.7	1.19	7	9.27	1.00	122	9.94	1.00
3	19	10.3	1.11	21	9.76	1.00	64	9.93	1.00
4	17	10.3	1.12	18	9.71	1.00	60	9.93	1.00
5	31	25.1	6.52	6	9.13	1.00	81	9.95	1.00
6	22	15.4	2.48	119	9.98	1.00	25	9.79	1.00
7	16	8.9	0.85	55	9.91	1.00	31	9.85	1.00
8	16	13.3	1.88	28	9.84	1.00	51	9.91	1.00
9	22	17.0	3.03	27	9.85	1.01	102	9.94	1.00
Overall	251	13.8	2.21	335	9.75	1.01	875	9.88	0.99

Horizon	Site 1	OBS 10	
	Npts	Trms (ms)	χ^2
1	363	9.9	0.98
2	131	10.0	1.00
3	77	9.9	1.00
4	85	10.0	1.00
5	57	9.9	1.00
6	10	9.5	1.00
7	16	9.7	1.00
8	30	9.8	1.00
9	96	10.0	1.01
Overall	865	9.9	1.00

Table E.1 Misfit tables for 1D velocity models derived from Site 1 OBS data.

Horizon	Site 2	OBS 1			OBS 2			OBS 3	
	Npts	Trms (ms)	χ^2	Npts	Trms (ms)	χ^2	Npts	Trms (ms)	χ^2
1	601	10.0	1.00	114	10.0	1.01	527	10.1	1.03
2	212	10.0	1.00	40	9.9	1.01	236	10.0	1.00
3	196	10.0	1.00	31	9.8	1.00	187	10.0	1.00
4	158	10.0	1.00	32	9.9	1.00	109	10.0	1.00
5	156	10.0	1.00	50	9.9	1.00	160	10.0	1.00
6	91	9.9	1.00	25	9.8	1.00	141	10.0	1.00
7	64	10.0	0.97	54	9.9	1.00	65	9.9	1.00
8	83	9.9	1.00	36	9.9	1.00	102	10.6	1.14
9	76	9.9	1.00	47	9.9	1.00	94	10.0	1.00
10	43	9.9	1.00	32	9.8	1.00	60	9.9	1.00
Overall	1680	10.0	1.00	461	9.9	1.00	1681	10.0	1.02

Horizon	Site 2	OBS 4			OBS 5			OBS 6	
	Npts	Trms (ms)	χ^2	Npts	Trms (ms)	χ^2	Npts	Trms (ms)	χ^2
1	44	10.2	1.07	629	10.0	1.00	677	10.0	1.00
2	14	10.0	1.08	133	9.9	1.00	94	9.9	1.00
3	30	10.2	1.07	131	10.0	1.00	139	10.0	1.00
4	13	9.9	1.06	74	11.4	1.31	94	10.0	1.01
5	29	10.1	1.07	99	10.0	1.00	106	10.0	1.00
6	25	10.1	1.06	79	9.9	1.00	53	9.9	1.00
7	28	10.1	1.06	24	9.8	1.00	54	9.9	1.00
8	38	9.6	0.94	45	9.9	1.00	71	10.0	1.00
9	14	9.4	0.94	83	9.9	1.00	179	10.0	1.00
10	22	9.5	0.95	51	9.9	1.00	45	9.9	1.00
Overall	257	9.9	1.03	1348	10.1	1.03	1512	9.9	1.00

Horizon	Site 2	OBS 7			OBS 8			OBS 9	
	Npts	Trms (ms)	χ^2	Npts	Trms (ms)	χ^2	Npts	Trms (ms)	χ^2
1	739	10.0	1.01	721	10.0	1.00	168	10.0	1.01
2	247	10.0	1.00	231	10.0	1.00	50	9.9	1.00
3	139	10.0	1.00	148	10.0	1.00	44	9.9	1.00
4	176	10.0	1.00	185	10.0	1.00	32	9.9	1.00
5	158	10.0	1.00	197	10.0	1.00	28	9.8	1.00
6	107	10.0	1.00	108	10.0	1.00	37	9.9	1.00
7	106	10.0	1.00	86	10.8	1.17	25	9.8	1.00
8	124	10.0	1.00	115	10.0	1.00	50	9.9	1.00
9	158	10.0	1.00	138	10.0	1.00	51	9.9	1.00
10	53	9.9	1.00	51	9.9	1.00	36	9.9	1.00
Overall	2007	10.0	1.00	1980	10.0	1.02	521	9.9	1.00

Horizon	Site 2	OBS 10	
	Npts	Trms (ms)	χ^2
1	79	10.0	1.01
2	40	9.9	1.01
3	14	9.6	1.00
4	46	9.9	1.00
5	21	9.8	1.00
6	28	9.8	1.00
7	65	9.9	1.00
8	61	9.9	1.00
9	85	9.9	1.00
10	68	9.9	1.00
Overall	507	9.9	1.00

Table E.2 Misfit tables for 1D velocity models derived from Site 2 OBS data.